QUANTITATIVE MODELS OF CALCIUM-DEPENDENT PROTEIN SIGNALING IN NEURONAL DENDRITIC SPINES

by

Matthew Connor Pharris

A Dissertation

Submitted to the Faculty of Purdue University

In Partial Fulfillment of the Requirements for the degree of

Doctor of Philosophy

Weldon School of Biomedical Engineering

West Lafayette, Indiana

August 2019

THE PURDUE UNIVERSITY GRADUATE SCHOOL
STATEMENT OF COMMITTEE APPROVAL

Dr. Tamara L. Kinzer-Ursem, Chair
Weldon School of Biomedical Engineering
Dr. Edward L. Bartlett
Weldon School of Biomedical Engineering
Dr. Melanie I. Stefan
Centre for Discovery Brain Sciences, University of Edinburgh
Dr. David M. Umulis
Weldon School of Biomedical Engineering

Approved by:

Dr. George R. Wodicka
Head of the Graduate Program

To my wonderful parents, Tim and Anne.

ACKNOWLEDGMENTS

I must firstly acknowledge my outstanding advisor, Dr. Tamara Kinzer-Ursem. Since I first met her in 2013, Tami's mentorship has been unparalleled. Throughout my PhD, she was patient, understanding, and always made time to for us to discuss my data. She was remarkably supportive and encouraging when I decided to intern off-campus for a summer. She trusted me to accept the challenge of a short and stressful journal submission deadline. She showed me how to be a good "lab citizen". And she advocated for me on countless occasions. I will forever value her example as a hard-working, detail-oriented, and seemingly tireless scientist. I could not have asked for a better mentor and friend to guide me through graduate school.

Thank you to my thesis committee members, Dr. Ed Bartlett, Dr. David Umulis, and Dr. Melanie Stefan. Dr. Bartlett has offered invaluable insight into the neuroscience aspects of my thesis research. Also, in Fall 2011 Dr. Bartlett was my professor in a cell biology course, where I first learned about calmodulin and CaMKII, so I guess you could say this thesis started with him! Dr. Umulis has offered important systems biology insight on my work, challenging me to justify my computational models with biologically meaningful questions. Thank you lastly to Dr. Stefan, for being so open to a long-distance collaboration developing the rule-based CaMKII holoenzyme model, which has become a key component of this thesis.

I next want to acknowledge all of the excellent Purdue faculty and staff members who I've worked alongside these past years. Dr. Charlie Babbs invited me to teach and give guest lectures in BME 256 and other courses, landmark experiences of my graduate career. Mr. Asem Aboelzahab was a reliable and supportive officemate in Fall 2016 as I had my hands full coordinating the undergraduate laboratory course BME 205. Ms. Tricia Olinger and Dr. Tom Atkinson were delightful to work with—truly unsung heroes—over my years serving the Purdue Graduate Student Government. Ms. Sandy May and Ms. Tammy Siemers both worked tirelessly to coordinate workshops, seminars, and industry trips, especially my visit to Boston in Summer 2016. Dr. Kaisa Ejendal always offered the utmost insight and feedback on my work, especially during lab group meetings. Thank you to my teaching supervisors Dr. Andrew Brightman, Dr. Joseph Rispoli, Dr. Hugh Lee, Dr. Chi-Hwan Lee, Dr. Lester Smith, Mr. Corey Linkel, and Dr. Jacqueline Linnes.

Thank you to all of the members of the Kinzer-Ursem Laboratory. Dr. Katherine Clayton, Dr. Kaisa Ejendal, Dr. Joyatee Sarker, Yan Luo, Wes Salameh, Mrugesh Parasa, Scott Bolton, Aya Saleh, Julia Fraseur, Peter Brumm, and many others. I also want to mention the phenomenal undergraduate researchers I've been honored to mentor: Daniel Romano, Joseph Muskat, Neal Patel, Tyler VanDyk, Lakmini Wilson, Christopher Rust, and Eva Yezerets. I am so proud and appreciative for their hard work on projects related to this thesis.

The final year of my graduate studies was funded by the Robert F. Truitt Fellowship, for which I am immensely thankful. The Fellowship ensured that I could focus exclusively on my research as I approached graduation.

Thank you to my family and especially my parents, Tim and Anne Pharris. This thesis would not exist were it not for their constant faith and love. It is impossible to describe how thankful I am for their decades of sacrifice and commitment to my future. In short, they have taught me the value of hard work, determination, thoughtfulness, and so much else. They, along with my fantastic sisters Emily and Catherine, inspire and motivate me every day.

Lastly, I am forever grateful to my future wife Elizabeth Phillips for being in my corner throughout graduate school. Since our very first day of graduate school orientation, I have been blessed by her encouragement, enthusiasm, patience, determination, and sense of humor. Our countless hours traveling, hiking, golfing, cooking, and working together have been essential. Without her partnership and support, my graduate school experience would have been vastly less enjoyable. She motivates me to be my best, and I love her more than I can say.

TABLE OF CONTENTS

LIST OF TABLES

LIST OF FIGURES

ABSTRACT

Author: Pharris, Matthew, C. PhD
Institution: Purdue University
Degree Received: August 2019
Title: Quantitative Models of Calcium-dependent Protein Signaling in Neuronal Dendritic Spines
Committee Chair: Tamara Kinzer-Ursem

Worldwide, as many as 1 billion people suffer from neurological disorders. Fundamentally, neurological disorders are caused by dysregulation of biochemical signaling within neurons, leading to deficits in learning and memory formation. To identify better preventative and therapeutic strategies for patients of neurological disorders, we require a better understanding of how biochemical signaling is regulated within neurons.

Biochemical signaling at the connections between neurons, called synapses, regulates dynamic shifts in a synapse's size and connective strength. Called synaptic plasticity, these shifts are initiated by calcium ion (Ca^{2+}) flux into message-receiving structures called dendritic spines. Within dendritic spines, Ca^{2+} binds sensor proteins such as calmodulin (CaM). Importantly, Ca^{2+}/CaM may bind and activate a wide variety of proteins, which subsequently facilitate signaling pathways regulating the dendritic spine's size and connective strength.

In this thesis, I use computational models to characterize molecular mechanisms regulating Ca^{2+}-dependent protein signaling within the dendritic spine. Specifically, I explore how Ca^{2+}/CaM differentially activates binding partners and how these binding partners transduce signals downstream. For this, I present deterministic models of Ca^{2+}, CaM, and CaM-dependent proteins, and in analyzing model output I demonstrate in-part that competition for CaM-binding alone may be sufficient to set the Ca^{2+} frequency-dependence of protein activation. Subsequently, I adapt my deterministic models into particle-based, spatial-stochastic frameworks to quantify how spatial effects influence model output, showing evidence that spatial gradients of Ca^{2+}/CaM may set spatial gradients of activated proteins downstream. Additionally, I incorporate into my models the most detailed model to-date of Ca^{2+}/CaM-dependent protein kinase II (CaMKII), a multi-subunit protein essential to synaptic plasticity. With this detailed model of CaMKII, my analysis suggests that the many subunits of CaMKII provide avidity effects that significantly increase the protein's effective affinity for binding partners, particularly Ca^{2+}/CaM. Altogether, this thesis provides a

detailed analysis of Ca^{2+}-dependent signaling within dendritic spines, characterizing molecular mechanisms that may be useful for the development of novel therapeutics for patients of neurological disorders.

1. INTRODUCTION

1.1 Significance

Neurological disorders such as Alzheimer's Disease affect more than 15 million Americans and are currently neither preventable nor curable [1, 2]. Patients of neurological disorders experience deficits in learning and memory which arise from perturbations to biochemical signaling networks within neurons [3]. Developing therapeutics for neurological disorders requires a mechanistic understanding of these highly complex signaling networks. However, these signaling networks are highly dynamic, subject to biophysical noise, and occur within miniscule geometries [4]. Thus, experimental methods (e.g. protein knockout or fluorescent microscopy) currently lack the spatiotemporal resolution to fully describe how signaling pathways are regulated within neurons [5, 6]. To complement experimental methods, computational models can also identify and characterize mechanisms of molecular signaling. Therefore, in this work I use computational models to examine the molecular mechanisms regulating calcium ion (Ca^{2+})-dependent signaling networks within neurons. With these models, I quantify how parameters related to protein binding kinetics, competitive binding, spatial effects, and protein multivalence contribute to signaling outputs. By quantifying how these parameters effect signaling output, I identify and characterize mechanisms that may be targeted or accounted for by future therapeutics.

1.2 Synapses in the hippocampus

The human brain contains roughly 86 billion neurons [7]. Neurons may be classified as inhibitory neurons and excitatory neurons. Excitatory neurons are the most numerous and form large numbers of connections, or synapses, with neighboring neurons. Synapses facilitate electrochemical signaling from a presynaptic neuron's axon, towards the postsynaptic neuron's dendrite [3]. Dendrites compartmentalize individual synaptic connections at small, mushroom-shaped protrusions called dendritic spines [8]. At rest, ion channels embedded in a dendritic spine's plasma membrane move charged particles such as sodium and calcium (Ca^{2+}) to the extracellular space, creating a charge concentration gradient [9]. Meanwhile, the presynaptic axon prepares intracellular vesicles filled with neurotransmitter (mainly glutamate, for excitatory neurons). In the presence of a depolarizing action potential (AP), vesicles merge with the plasma membrane,

releasing neurotransmitter such as glutamate into the extracellular synaptic cleft. Neurotransmitters diffuse across the synaptic cleft and bind to ligand-gated receptors on the post-synaptic dendritic spine. Ligand-bound receptors allow ions to flux into the post-synapse, slightly depolarizing its membrane. Depending on the neurotransmitter, local depolarizations create excitatory or inhibitory postsynaptic potentials (EPSPs or IPSPs), which sum as they occur in succession [10]. Several repeated or concurrent EPSPs can lead to the postsynaptic neuron firing its own AP.

Synapses can be made more or less responsive to EPSPs via synaptic plasticity. Synaptic plasticity may elicit downward shifts in excitability called long-term depression (LTD) or upward shifts called long-term potentiation (LTP) [11]. LTP is characterized by an enduring increase in protein levels and structural remodeling within the postsynaptic density (PSD). The PSD, a cytoskeletal pseudo-organelle within the dendritic spine, has been observed to grow or shrink as a result of LTP or LTD. Together, LTP and LTD constitute the best-studied forms of synaptic plasticity in the hippocampus, which is essential to spatial learning and memory formation [10].

Although LTP and LTD yield distinct outcomes for a synapse, both depend on activation of the same type of postsynaptic glutamate receptor [12]. N-methyl-D-aspartate receptors (NMDARs) are coincidence detectors requiring two inputs: bound glutamate and a postsynaptic membrane depolarized by a back-propagating AP. Coincident input causes a conformational change and relieves a magnesium ion blocking the NMDAR pore, allowing Ca^{2+} influx to the dendritic spine. Importantly, Ca^{2+} influx at relatively high frequencies (10-100 Hz) often initiates LTP [5]. In contrast, lower frequencies (1-5 Hz) can initiate LTD. To distinguish between Ca^{2+} frequencies, Ca^{2+}-dependent proteins within the dendritic spine interpret and dynamically regulate distinct signaling networks [13].

1.3 Calcium-dependent signaling within dendritic spines

Synaptic plasticity begins with NMDAR-dependent influx of Ca^{2+}, which interacts with a range of protein buffers and sensors. Calmodulin (CaM) is the dominant Ca^{2+} sensor in the dendritic spine and has over 100 known binding partners. In hippocampal neurons, at least ten CaM binding partners (CBPs) are highly expressed [14, 15]. CaM is a dumbbell-shaped protein, with each of its two lobes cooperatively binding up to two Ca^{2+}. Depending on the number of Ca^{2+} bound, Ca^{2+}/CaM exhibits a distinct binding affinity for each of its downstream binding proteins.

A diagram of Ca^{2+}/CaM-dependent signaling interactions during early synaptic plasticity is provided in Figure 1.1.

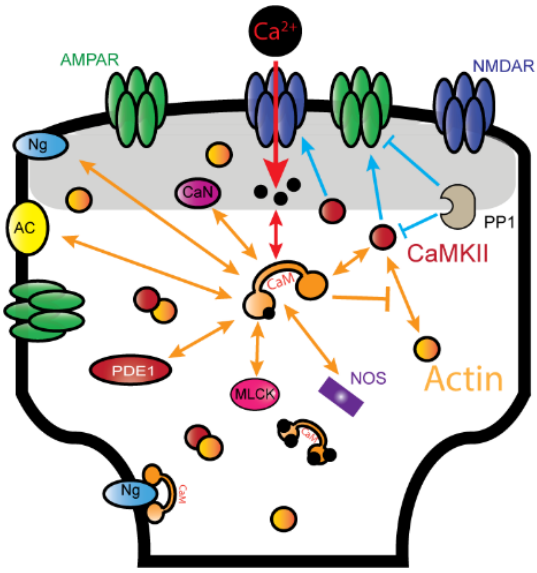

Figure 1.1. Ca^{2+}-dependent signaling in the dendritic spine. Ca^{2+} ions flux into the dendritic spine and bind to CaM (red arrows). Ca^{2+}/CaM is competed for by a variety of CaM binding partners (orange arrows). Activated CaM binding partners may regulate protein signaling downstream (blue arrows).

CBPs in the PSD include adenylate cyclase I and VIII (AC1, AC8), calcineurin (CaN), myosin light chain kinase (MLCK), nitric oxide synthase (NOS), phosphodiesterase 1 (PDE1), and neurogranin (Ng). AC1 and AC8 are membrane-associated enzymes that generate cyclic-AMP (cAMP) from ATP, following activation by CaM [16, 17]. CaM-activated CaN dephosphorylates proteins in the spine, lending CaN a putative role in LTD [18]. MLCK and NOS are under-characterized in hippocampal neurons, though still relevant to studies of competition among CBPs for CaM binding [19, 20]. CaM-activated PDE1 binds and degrades cAMP into AMP [21]. Ng, which strongly binds apo-CaM in the absence of Ca^{2+}, is thought to localize CaM to the dendritic spine's cell membrane [22]. Depending on the frequency, magnitude, and location of Ca^{2+} flux, CaM differentially activates these proteins to eventually elicit either LTP or LTD [23, 24]. It is important to emphasize, however, that no single CBP can elicit LTP or LTD in isolation; rather, many enzymes must together contribute to the fate of a synapse.

One essential CBP is Ca^{2+}/CaM-dependent protein kinase II (CaMKII). The abundance and structural complexity of CaMKII have made it a popular yet challenging research subject [24-27]. Comprising about 2% of all protein in the hippocampus, CaMKII is highly enriched in the PSD and is essential for LTP, though it also participates in LTD, by under-characterized mechanisms [28]. As shown in Figure 1.2A, CaMKII holoenzymes feature 12 catalytic subunits organized around a central hub, forming two parallel, radially-symmetric rings. Individual CaMKII subunits (Figure 1.2B) feature a catalytic and regulatory domain connected by a linker region. Ca^{2+}-bound CaM may bind the regulatory domain, holding it in an open conformation, exposing the catalytic domain. Critically, if a neighboring CaMKII subunit's catalytic domain is also exposed, that subunit can phosphorylate the other subunit's Thr-286 residue [29]. This so-called autophosphorylation causes prolonged subunit activation or "autonomy", as it allows the regulatory domain to remain open even in the absence of CaM. Notably, point mutation of Thr-286 to inert alanine prohibits LTP [5]. Understanding the timescales and patterns of CaMKII subunit activation may be essential for characterizing the regulation of synaptic plasticity induction.

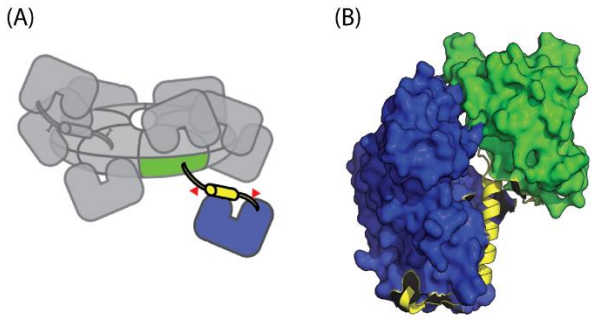

Figure 1.2. CaMKII holoenzyme and subunit structure. (A) Twelve CaMKII subunits (grey) arranged in two directly-apposed and radially symmetric rings. One subunit (colored) is illustrated in a possible extended conformation away from the holoenzyme central hub. (B) An individual CaMKII subunit in its closed conformation (PDB entry 3SOA). In both (A) and (B), the subunit's hub domain (green), kinase domain (blue), and linker region (yellow) are shown. (A) and (B) are not on the same scale.

CBPs regulate the downstream signaling events that adjust a synapse's cation conductivity [30]. For example, CaM-bound AC generates cAMP, which liberates the catalytic subunits of protein kinase A (PKA), and catalytic PKA can phosphorylate GluA1 subunits of AMPARs [31]. Phosphorylated AMPARs exhibit heightened conductivity and are considered hallmarks of LTP.

Notably, AMPAR phosphorylation is regulated by a variety of mechanisms. For instance, CaM-bound PDE1 will enzymatically convert cAMP into AMP, preventing PKA activation [32]. Similarly, cAMP is also degraded by phosphodiesterase 4 (PDE4), though PDE4 is not CaM-dependent. Another regulator is CaN, which when activated de-phosphorylates AMPARs at Ser-831, the site originally phosphorylated by PKA. However, the nearby Ser-845, which is phosphorylated by CaMKII, is not de-phosphorylated by CaN. Instead, Ser-845 is de-phosphorylated by less specific phosphatases than CaN, such as protein phosphatase 1 (PP1). PP1 binds and may de-phosphorylate a number of proteins, such as AMPARs at both Ser-831 and Ser-845, as well as auto-phosphorylated CaMKII. I especially explore the regulation of PP1-CaMKII binding in Chapter 5. Clearly, CBPs coordinate downstream events in a highly complex manner [33].

CBPs also regulate signaling events that determine a synapse's size. Indeed, AMPAR phosphorylation is but one of two classical hallmarks of LTP; the other hallmark is insertion, or localization, of AMPARs to the synaptic membrane [34]. Initially, AMPARs are uniformly distributed about the spine's plasma membrane or on intracellular vesicles. Following induction of LTP, AMPARs localize to the synaptic membrane, and it remains unclear how this localization is facilitated or preserved, or whether localization of AMPARs precedes or follows their phosphorylation. Simultaneously, the actin cytoskeleton is remodeled and other proteins become enriched in the PSD. Characterizing how these structural adjustments influence CBP-mediated signals will be essential to understanding early stages of synaptic plasticity. For instance, Ng is membrane-associated and strongly binds apo-CaM, meaning Ng could hypothetically pre-localize CaM to the PSD prior to Ca^{2+} influx [22, 35]. With CaM pre-localized to the PSD, subsequent Ca^{2+}/CaM could rapidly activate local CBPs such as AC1, thus perpetuating AMPAR phosphorylation specifically at the synaptic membrane. Similarly, pre-localized CaM could support CaMKII enrichment to the PSD, and, importantly, CaMKII can bind NMDARs, AMPARs, actin, and a number of other proteins thought to be involved in structural remodeling.

CaMKII has putative roles in both the enzymatic and structural aspects of synaptic plasticity. As previously stated, CaMKII phosphorylates AMPARs at Ser-845, one hallmark LTP. Additionally, CaMKII may provide a structural focal point in the intracellular actin scaffold [36, 37]. Initially, inactive CaMKII is uniformly distributed about the spine, with its subunits bound to actin filaments. Activated CaMKII subunits lose affinity to actin, causing the CaMKII to mobilize

and aggregate at the PSD by unidentified mechanisms [38]. Hypothetically, active CaMKII aggregates at the PSD as a consequence of CaM pre-localization and NMDAR binding. Additionally, CaMKII localization may be dependent on the CaMKII quaternary structure, which localizes its twelve subunits into large holoenzymes. Because CaMKII holoenzymes may be highly multivalent, CaMKII aggregation could also be attributed to avidity effects, increasing its effective affinity for its binding partners [39, 40].

Thus, the complexity of Ca^{2+}-dependent signaling limits our ability to intuit its regulation. That is, its regulation is highly dynamic, with oscillatory Ca^{2+} influx and many transient protein states. Moreover, its regulation may be spatially dependent, noting the localization of proteins such as CaMKII within the dendritic spine. Also, a number of convergent signaling pathways, such as PKA-mediated and CaMKII-mediated AMPAR phosphorylation, may further confound analysis of Ca^{2+}-dependent signaling *in vitro* and *in vivo*. Given this complexity within dendritic spines, it may be unsurprising that experimental methods such as genetic knockdown or fluorescent microscopy lack the spatiotemporal resolution needed to characterize the mechanisms regulating Ca^{2+}-dependent signaling.

1.4 Mathematical models of calcium-dependent signaling

Because experimental techniques lack sufficient spatiotemporal resolution, computational models are increasingly utilized to characterize molecular mechanisms regulating Ca^{2+}-dependent signaling in the dendritic spine [33, 41]. Models vary dramatically in sophistication and scope. For example, simple models describe the time-course dynamics of small or generalized sets of Ca^{2+}/CaM buffers. In contrast, complex models may explicitly describe many protein species, with each species exhibiting a variety of states, and with each state changing as a function of both time and space. While simplistic implementations can be valuable, complex models are increasingly utilized as practical and technical limitations are overcome.

Deterministic models are among the simplest mechanistic models used to describe protein kinetics. These models typically describe biochemical reactions using systems of time-dependent, ordinary differential equations (ODEs). Such systems of ODEs typically involve one equation per molecular state. To demonstrate, take the simple case of proteins A and B reversibly binding to form complex AB, $A + B \leftrightarrow AB$, according to the following equations. In Equations 1-3, brackets

denote protein concentrations, k_{bind} is the kinetic association rate for proteins A and B, and k_{rev} is the kinetic dissociation rate.

$$(1)\ \frac{d[A]}{dt} = k_{rev}[AB] - k_{bind}[A][B] \qquad (2)\ \frac{d[B]}{dt} = k_{rev}[AB] - k_{bind}[A][B]$$

$$(3)\ \frac{d[AB]}{dt} = k_{bind}[A][B] - k_{rev}[AB]$$

Many deterministic models of synaptic plasticity have been developed. For example, Lisman and Zhabotinsky used deterministic models to investigate how CaMKII autophosphorylation, which is necessary for LTP, endures for long timescales despite the presence of phosphatases [4]. To investigate this, they created a model network containing Ca^{2+}, CaM, monomeric CaMKII, and a small subset of other proteins within the PSD. Because their deterministic model system had low computational expense, they could rapidly compare output from a large parameter space. Sweeping through many Ca^{2+}/CaM concentrations, their results suggested that CaMKII could differentially reside in one of two stable states: predominantly inactive/unphosphorylated, and active/phosphorylated. In other words, CaMKII was able to function as a bistable switch. Subsequently, Hayer and Bhalla built another set of models, describing CaM, CBPs, and a larger variety of downstream regulatory proteins, with results that ultimately reinforced the view of CaMKII as a bistable switch [33]. In part to enable future exploration of CaMKII bistability, work by Pepke *et al*. developed a thermodynamically complete model in which sub-saturated CaM, with less than 4 bound Ca^{2+}, activates CBPs [42]. For this thesis, I began with an expansion of the model by Pepke *et al*., exploring how the conditions for CaMKII bistability may be more complicated than others have previously asserted.

Although time-dependent deterministic models are useful, spatial effects also contribute to signaling in the dendritic spine. Systems of partial differential equations (PDEs) can account for both spatial effects and time-course dynamics. Although PDEs involve significantly greater computational expense, the added spatial component is essential to understanding the interplay between enzymatic and structural regulation of synaptic plasticity. Note that experimental studies show spatial localizations of proteins within the spine, suggesting that space may limit the ability of some proteins to interact [38]. Otherwise put, if some proteins are localized and therefore highly concentrated at regions such as the PSD, their activation may be significantly different from deterministic model predictions. Thus, to account for and quantify how spatial effects impact Ca^{2+}-dependent signaling outputs, in this thesis I often compare deterministic model output to its spatial-

stochastic model equivalent. For this, I use the software platform MCell, which in-effect discretizes PDEs by describing individual molecules as particles diffusing about a model geometry of the dendritic spine [43]. As discussed in Chapter 4, aside from added spatial and stochastic components my MCell models are identical to my non-spatial deterministic models, accounting for Ca^{2+}, CaM, multiple CBPs, and multiple CBP-mediated downstream interactions. Notably, it is computationally complex to account for so many protein states, posing an interesting engineering problem.

Accounting for many protein states can cause conventional models to exhibit "combinatorial explosion", a key obstacle to detailed models of synaptic plasticity. Even in simple deterministic models but especially in spatial models, conventional systems of ODEs describing large numbers of proteins can incur state spaces that are intractable to specify or evaluate. For example, rigorously and explicitly accounting for multiple CaMKII subunits on the same holoenzyme can produce prohibitively extensive state spaces. Indeed, a multi-state CaMKII dodecamer model would conventionally require approximately 539 quintillion equations (See the Supplement to Chapter 5).

As described by Stefan *et al*., combinatorial explosion applies to models of CaMKII (and similar biomolecules) because the protein exhibits a large number of functionally significant and not necessarily inter-dependent states [24]. To avoid combinatorial explosion yet still account for all possible CaMKII states, a small number of options are available. First, Michalski and Loew have provided an infinite holoenzyme approximation (ISHA), that allows the holoenzyme to be described as independent subunits/monomers under specific conditions [44]. Unfortunately, because the ISHA model is valid only for CaMKII with fewer than 7 subunits per ring and requires exclusion of spatial information, it may not be adaptable into discretized, spatial-stochastic frameworks. Alternatively, Li and Holmes recently used the software Smoldyn to model multi-state CaMKII with a rule-based approach [45]. Rules are conditions, based primarily on experimental observations, that prescribe when an implicitly-defined reaction may occur. At a given iteration, only states that matter for the execution of a particular rule are explicitly declared. Rule-based states that do not matter to a particular rule can be omitted, a principle that has been paraphrased as "don't care, don't write" [30, 31]. By applying a sufficient set of rules, which is possible using a specialized syntax in MCell, combinatorial explosion becomes manageable. In Chapter 5, I present a rule-based model of CaMKII, and in contrast to Li and Holmes I use my

model to explore mechanisms of CaM- and PP1-binding to CaMKII. Further, in Chapter 6 I adapt my rule-based model of CaMKII into a larger network of Ca^{2+} signaling, and for the first time I begin to quantify how CaMKII multivalence may regulate the spatiotemporal dynamics of protein states in the dendritic spine.

1.5 Overview of thesis

My overall hypothesis for this thesis is that competition among Ca^{2+}-dependent proteins; spatial gradients of signaling molecules; and structural complexities of CaMKII are required to set the physiological Ca^{2+}-frequency dependence of activation for signaling pathways during early synaptic plasticity. Therefore, the major goals of thesis have been to create computational models of competition among CBPs for CaM-binding, protein diffusion within spatial models of the dendritic spine, and the mechanics of structurally complex proteins such as CaMKII. Using these models, I have addressed the following biophysical and physiological questions.

1. *Does competition for CaM-binding influence the activation of CaM-dependent enzymes?*

   In Chapter 2, I present a deterministic, non-spatial model of Ca^{2+} flux, Ca^{2+}/CaM-binding, and competition for Ca^{2+}/CaM among eight explicitly-defined CBPs. Unlike previously published computational models which generalize the pool of CBP competitors, my explicit definition of CBPs allows me to identify those which are most activated in response to particular Ca^{2+} stimuli. For this, I compare output from "isolated" models of Ca^{2+}, CaM, and individual CBPs versus "competitive" models of Ca^{2+}, CaM, and eight CBPs. My analysis reveals that competition alone may be sufficient to set *in silico* the Ca^{2+} frequency dependence of CBP activation observed *in vivo*. Moreover, I show that competition can explain counterintuitive effects of genetic knock-out of the CaM-buffer Ng. Specifically, I find that upon knock-out of Ng, competition mediates a shift in activation that results in reduced CaMKII activation, contrary to expectation but consistent with experimental results. Further, I find that when CaMKII activation is reduced, CaM activates increased AC1 and AC8, with implications that I explore in later chapters. Altogether, my results indicate that activation of CBPs is highly dependent on competition for CaM-binding.

2. *Are effects of competition transduced to outputs relevant to synaptic plasticity?*
   In Chapter 3, I present a more detailed deterministic, non-spatial model of Ca^{2+}, CaM, CBPs, and a set of CBP-mediated downstream pathways. This detailed deterministic model builds on that presented in Chapter 2, introducing downstream signaling pathways regulated by CBPs. Specifically, I model two CBP-mediated pathways that both lead to AMPAR phosphorylation, which is a hallmark of synaptic plasticity. First, I describe AMPAR GluA1 subunit phosphorylation at Ser-845 by CaMKII. Second, I describe GluA1 subunit phosphorylation at Ser-831 by PKA, which is activated by AC1 and AC8-Ct. With this expanded model, I perform a global sensitivity analysis to quantify the relative contributions of various parameters to model outputs. Also, I again simulate genetic knock-out of the CaM-buffer Ng. Here, I show that although Ng knock-down reduces CaMKII activity and its subsequent phosphorylation of AMPARs, the concomitant increase in AC activation is sufficient to compensate and provide robustness to overall AMPAR phosphorylation levels. Thus, I provide evidence that competition regulates outputs relevant to synaptic plasticity.
3. *Do spatial effects impact competitive tuning?*
   In Chapter 4, I adapt the detailed deterministic model into a particle-based, spatial-stochastic framework using the software MCell. With MCell, individual protein molecules randomly diffuse throughout a model dendritic spine geometry. In addition to more physiologically describing the dendritic spine, MCell allows me to quantify how spatial effects regulate CBP activation and downstream regulation. In Chapter 4, I show that the Ca^{2+} frequency-dependence of CBP activation provided by competition is mostly preserved in a spatial-stochastic environment. Interestingly, I also observe spatial dependence of CBP activation, which is sharpened and/or exaggerated in the presence of competition for CaM-binding. It appears that competition and spatial effects together are responsible for setting the location of activation for many CBPs. Notably, one CBP that does not exhibit spatial dependence in my models is AC8. While exploring AC8's lack of apparent spatial dependence, I find that the AC8 N-terminus, a non-enzymatic CBP, could be a significant regulator of the spatiotemporal dynamics of Ca^{2+}/CaM.

4. *How are signaling outputs affected when CaMKII is modeled as a detailed, multi-subunit holoenzyme?*

   In Chapter 5, I note that to proceed with detailed models of Ca^{2+}-dependent signaling in the spine, it may be necessary to account for the complex dodecameric structure of CaMKII. This is an important obstacle to address because conventional models using systems of differential equations must simultaneously monitor all possible protein states, and the number of states for CaMKII is prohibitively large. To bypass this obstacle, here I present a rule-based model of the CaMKII holoenzyme. With this rule-based model, I explore mechanisms regulating the maintenance of CaMKII activation and its potential role as a hypothetical bistable switch required for molecular memory. Specifically, I identify a Ca^{2+}/CaM stimulation threshold beyond which CaMKII activity is maintained on long timescales. While exploring this maintenance, I also identify a possible regulatory mechanism in which CaMKII-bound CaM may be sufficient to structurally exclude, or perhaps out-compete, the phosphatase PP1 for CaMKII-binding. In total, in Chapter 5 I show that rigorously describing multi-subunit, multi-state CaMKII can help provide insight into its regulation.

5. *How does CaMKII multivalence contribute to regulation of other Ca^{2+}-dependent proteins?*

   In Chapter 6, I combine modified versions of the models presented in Chapters 4 and 5 to describe Ca^{2+}-dependent signaling in the presence of a detailed CaMKII holoenzyme. Including the CaMKII holoenzyme allows me to quantify how CaMKII multivalence contributes to the spatiotemporal dynamics of protein activation in the spine. For example, I show that CaMKII multivalence may provide avidity effects that significantly increase its effective affinity for binding partners, especially influencing the spatiotemporal dynamics of Ca^{2+}/CaM states. In addition to multivalence, this model reaction network also distinguishes between distinct CaMKII subunit isoform interactions with actin binding sites (a new model feature in this Chapter). With this, I show that CaMKII mobility within the spine is likely regulated by the CaMKII beta subunit, and CaMKII localization to the PSD is likely regulated by the CaMKII alpha subunit, both consistent with previous studies. Altogether, the work in Chapter 6 lays the groundwork for future, currently unavailable modeling platforms to analyze how

CaMKII multivalence, along with competition and spatial effects, regulates Ca^{2+}/CaM-dependent signaling outputs.

2. COMPETITIVE TUNING: COMPETITION'S ROLE IN SETTING THE FREQUENCY-DEPENDENCE OF Ca^2+-DEPENDENT PROTEINS

2.1 Summary

A number of neurological disorders arise from perturbations in biochemical signaling and protein complex formation within neurons. Normally, proteins form networks that when activated produce persistent changes in a synapse's molecular composition. In hippocampal neurons, calcium ion (Ca^{2+}) flux through N-methyl-D-aspartate (NMDA) receptors activates Ca^{2+}/calmodulin signal transduction networks that either increase or decrease the strength of the neuronal synapse, phenomena known as long-term potentiation (LTP) or long-term depression (LTD), respectively. The calcium-sensor calmodulin (CaM) acts as a common activator of the networks responsible for both LTP and LTD. This is possible, in part, because CaM binding proteins are "tuned" to different Ca^{2+} flux signals by their unique binding and activation dynamics. Computational modeling is used to describe the binding and activation dynamics of Ca^{2+}/CaM signal transduction and can be used to guide focused experimental studies. Although CaM binds over 100 proteins, practical limitations cause many models to include only one or two CaM-activated proteins. In this work, I view Ca^{2+}/CaM as a limiting resource in the signal transduction pathway owing to its low abundance relative to its binding partners. With this view, I investigate the effect of competitive binding on the dynamics of CaM binding partner activation. Using an explicit model of Ca^{2+}, CaM, and seven highly-expressed hippocampal CaM binding proteins, I find that competition for CaM binding serves as a tuning mechanism: the presence of competitors shifts and sharpens the Ca^{2+} frequency-dependence of CaM binding proteins. Notably, I find that simulated competition may be sufficient to recreate the *in vivo* frequency dependence of the CaM-dependent phosphatase calcineurin. Additionally, competition alone (without feedback mechanisms or spatial parameters) could replicate counter-intuitive experimental observations of decreased activation of Ca^{2+}/CaM-dependent protein kinase II in knockout models of neurogranin. I conclude that competitive tuning could be an important dynamic process underlying synaptic plasticity. This work is published ([46]). Co-authors include two undergraduates who I supervised: Daniel Romano who developed the initial model and parameterization, and Neal Patel who helped with the analysis.

2.2 Introduction

Calcium (Ca^{2+}) is well-recognized as an important second messenger in cellular signaling. One of the most widely expressed Ca^{2+} binding proteins, calmodulin (CaM), is a highly conserved protein in the EF-hand family [14] (Figure 2.1A). CaM has over 100 reported downstream binding proteins, including enzymes that regulate a variety of cellular functions, such as neurotransmitter release in presynaptic neuronal axons [47], insulin secretion in the pancreas [48], and contractility in muscle [49]. Ca^{2+}-dependent signaling in postsynaptic dendrites of excitatory neurons has been the frequent subject of computational studies (see a recent review [29]). Indeed, it comprises an ideal system for mathematical modeling. Its parameters (molecular concentrations and kinetic rate constants) have been measured using controlled experiments, and experimental interest has produced an abundance of published values for model parameterization [49-65]. Two highly-studied functions of synaptic Ca^{2+} signaling are the induction and maintenance of long-term potentiation (LTP) and long-term depression (LTD) [66], which are correlated to learning processes and memory storage in various brain regions [67-70]. Both LTP and LTD are accompanied by persistent changes in postsynaptic gene transcription [71], actin polymerization [72], and AMPA receptor trafficking [19] that adjust cellular excitability and, in turn, synaptic strength. Among the best-studied forms of LTP and LTD are those initiated by transient, localized increases in intracellular Ca^{2+} through postsynaptic N-methyl-D-aspartate receptors (NMDARs). CaM translates Ca^{2+} signals into either LTP or LTD by forming Ca^{2+}/CaM complexes that bind and thereby activate downstream proteins (Figure 2.1C) [73]. Upon activation, these CaM-dependent proteins, which include a variety of enzymes—kinases, phosphatases, cyclases, and synthases—initiate protein signaling cascades that differentially modulate gene transcription, actin polymerization, and AMPA receptor trafficking.

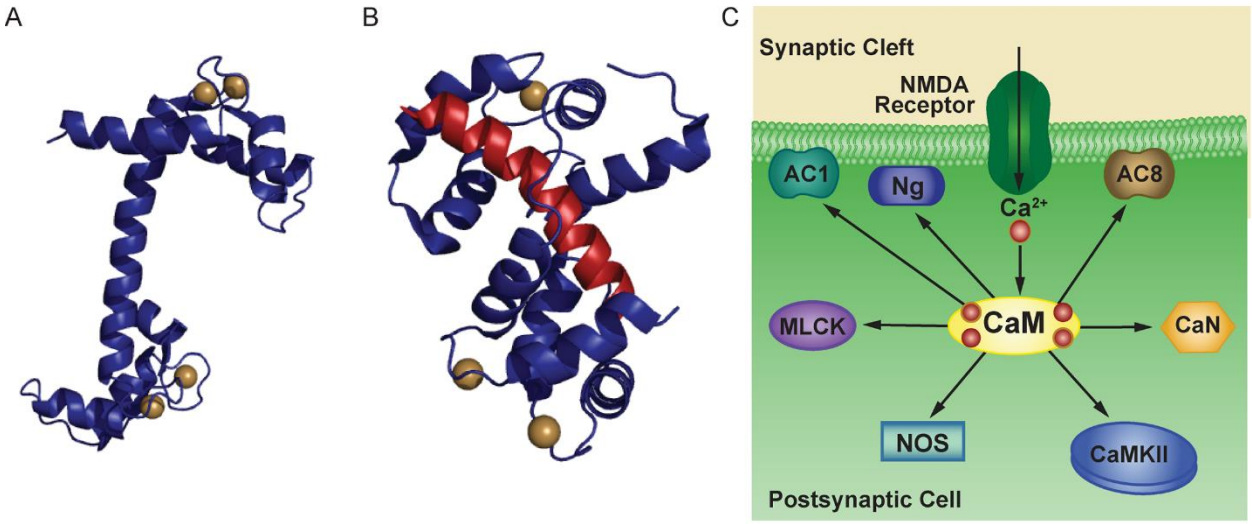

Figure 2.1. Schematic of CaM-binding. (A) Structure of CaM (PDB 1CLL), shown in blue, with two Ca^{2+} ions (gold) at each terminus. (B) Structure of Ca^{2+}/CaM (PDB 2JZI) bound to a calcineurin (CaN) peptide (red). (C) Schematic of CaM interactions with downstream binding partners. CaM may bind Ng in the absence of Ca^{2+}. In the presence of Ca^{2+}, CaM binds to CaN, CaMKII, NOS, MLCK, and AC1 and AC8 (AC1/8).

The frequency [74], amplitude, duration, and location [75] of Ca^{2+} fluxes determine the pattern of activation of CaM-dependent enzymes and, in turn, the fate of the synapse. For example, 1 Hz stimulation for 10-15 minutes both increases activation of the CaM-dependent phosphatase calcineurin (CaN, or PP3) [18] and induces NMDAR-dependent LTD [76]. On the other hand, 100 Hz stimulation for 1 second increases Ca^{2+}/CaM-dependent protein kinase II (CaMKII) activation and induces NMDAR-dependent LTP [77]. These and similar observations have led to the consensus that kinase cascades induce LTP, while phosphatase cascades induce LTD [78]. But more recent studies have found that CaN may also contribute to LTP induction [79], and that activated CaMKII can promote LTD [80]. These results suggest that normal initiation and maintenance of LTP and LTD do not simply depend on the Boolean activation of kinases or phosphatases in response to a given Ca^{2+} signal, but rather on the precise activation of a variety of often-counteracting proteins. Therefore, elucidation of the mechanisms that regulate NMDAR-dependent long-term plasticity depends on a complete understanding of the endogenous tuning mechanisms that pair precise patterns of enzyme activation to certain Ca^{2+} signals.

Computational studies have demonstrated the role of binding dynamics [81], feedback loops [82], and spatial effects [83] in regulating enzyme activation during synaptic Ca^{2+} signaling.

In this work, I hypothesize that competition among CaM binding proteins for access to CaM may serve as an additional tuning mechanism. The concentration of CaM binding partners in the cell far exceeds that of CaM itself [84], and *in vitro* studies have demonstrated competitive inhibition among neuronal CaM binding partners [85-87]. But, despite the implicit presence of competition in many computational models of Ca^{2+}/CaM signaling in neurons [4, 30, 83, 88-91] and cardiac myocytes [92-96], just one study [88] has had the explicit aim of investigating competition among CaM binding partners as a regulator of enzyme activation. Antunes *et al*. use such a model to investigate competitive binding as a potential facilitator of the frequency-dependence of CaM binding partners at low frequency Ca^{2+} fluxes (5 mHz to 5 Hz) for generalized sets of CaM binding partners. However, it is worth noting that both He *et al.* and Slavov *et. al.* both mention competition for CaM as a part of their broader studies on the frequency dependent behavior of networks of generalized CaM targets [30] and relative activation of kinase versus phosphatase signaling [91].

In this work I develop models of Ca^{2+} binding to CaM that explicitly include Ca^{2+}-binding to each of the two termini (N- and C-termini, Figure 2.1). Previous experimental work has shown that CaM is able to activate downstream binding proteins at sub-saturating levels of Ca^{2+}[97]. Moreover, a previous computational study explicitly including Ca^{2+}-binding to each of the two binding sites (N- and C-termini) of CaM has shown that Ca^{2+} bound at the C-terminus likely significantly contributes to activation of downstream binding partners [81]. My models also include seven experimentally-characterized postsynaptic CaM binding proteins expressed in CA1 hippocampal neurons. These mathematical models are used to investigate competition's potential role as a regulator of Ca^{2+}-dependent protein activation across a range of Ca^{2+} flux frequencies (0.1 Hz to 1000 Hz) that spans those found *in vivo* and oft employed experimentally *in vitro*. Specifically, I first develop a set of "isolated" models simulating CaM binding to Ca^{2+} and just one binding protein. I then combine the isolated models into a "competitive" model that simulates Ca^{2+} binding to CaM and CaM binding to its binding partners. The CaM binding proteins in this study have been chosen because they are known neuronal proteins with relatively well-characterized CaM-binding kinetics: adenylyl cyclase type I (AC1), the adenylyl cyclase type VIII N-terminus (AC8-Nt), the adenylyl cyclase type VIII C_{2b} domain (AC8-Ct), calcineurin (CaN, also known as PP2B and PP3), CaMKII, myosin light chain kinase (MLCK), neurogranin (Ng), and nitric oxide synthase (NOS) (Figure 2.1C). Because my model is devoid of feedback loops and spatial localization, the differences in CaM-binding between the competitive and isolated models

are solely due to competitive effects. I demonstrate the ability of competition to "tune" the binding and activation profiles of CaM-binding proteins at various Ca^{2+} flux frequencies and use the model to explain the counterintuitive role of neurogranin in CaMKII activation and LTP induction.

2.3 Results

2.3.1 Model Development

2.3.1.1 Model Structure

The interactions of Ca^{2+}, CaM, and CaM binding partners are quite complex. CaM binds a total of four Ca^{2+} ions, one pair at each of two EF-hand domains located at its N- and C-termini, respectively (Figure 2.1 and schematically in Figure 2.2A) [14]. Ca^{2+}-binding at each terminus is highly cooperative [98], but the Ca^{2+}-binding kinetics between these termini are distinct [65]. Moreover, the binding of Ca^{2+} to CaM changes its affinity for downstream binding partners. Similarly, the binding of CaM to its binding partners changes its affinity for Ca^{2+} (Figure 2.2B) [73]. I develop a mathematical model based on mass action kinetics that uses ordinary differential equations to simulate the dynamics of: Ca^{2+} ions binding reversibly to CaM, the dynamics of CaM binding reversibly to its binding partners, and the dynamics of Ca^{2+} ions binding reversibly to CaM when CaM is bound to a binding partner [81, 99] (Figure 2.2).

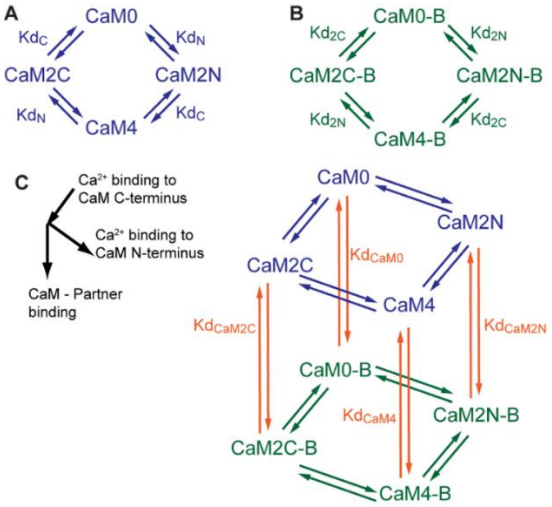

Figure 2.2. Model of Ca^{2+}-CaM binding. (A) Reversible binding of Ca^{2+} binding to CaM (blue). (B) Reversible binding of Ca^{2+} to CaM bound to a given binding partner, denoted with 'B' (green). (C) Reversible binding of a given binding partner to any state of Ca^{2+}/CaM (yellow).

A previous study by Pepke *et al*. offers two models for describing Ca^{2+}-CaM binding. First, they describe a four-state model in which it is assumed that binding of two Ca^{2+} at each CaM terminus can be treated as a single event due to the highly cooperative binding of Ca^{2+} at each terminus. Alternatively, a nine-state model is presented that explicitly accounts for each Ca^{2+} binding event, for which further details are discussed in the Supplement to Chapter 2. In the present study, I construct both model types and simulate CaM-binding of seven proteins implicated in hippocampal-dependent memory and long-term plasticity [77-79, 100-114]. I find that differences in the output of the four- and nine-state models are negligible for the purposes of this work (Figure 7.1 and elsewhere in the Supplement to Chapter 2). To reduce computational complexity, all model results are based on a four-state model of Ca^{2+}-CaM binding.

2.3.1.2 Model Parameterization

Initial concentrations of all proteins were either obtained directly from literature or calculated from published values. Equilibrium dissociation (K_D) constants not available in the literature are calculated (see [81, 115]) using the thermodynamic principle of microscopic reversibility. From the dissociation constants, any unmeasured kinetic rates are calculated using the equality: $K_D = k_{off}/k_{on,}$ and a pair of experimentally-supported assumptions regarding Ca^{2+}, CaM, and binding partner interactions.

First, it is well known that the affinity of Ca^{2+} for CaM is increased when CaM is bound to a binding partner (CaM-B) [58, 73]. The change in affinity could be represented by either an increase in the association rate constant of Ca^{2+} for CaM-B or a decrease in the dissociation rate constant of Ca^{2+} for CaM-B. Experimental work by Peersen *et al*. showed that the increased affinity of Ca^{2+} to target peptide-bound CaM was best explained by a reduction in Ca^{2+} dissociation rate constant [58]. More recent work has shown in the case of Ng binding to CaM, that the change in affinity for Ca^{2+} results primarily from a change in the dissociation rate constant [116]. Thus, I assume that the increase in affinity of Ca^{2+} for CaM when CaM is bound to a binding partner comes from a change in the dissociation, but not association, rate constant of Ca^{2+} from CaM-B.

Second, the binding of Ca^{2+} to CaM increases the affinity of CaM for most of its binding proteins [73, 117, 118], with the notable exception of Ng. Like others ([81, 83]), I note experimental observations showing that Ca^{2+} dissociation from CaM typically precedes CaM

dissociation from binding proteins [119], indicating that the increase in affinity of CaM for most of its binding proteins in the presence of Ca^{2+} may be due to an increase the association (and not the dissociation) rate constant of CaM binding to target proteins. Biophysically, Ca^{2+} binding to CaM induces a conformational change that exposes hydrophobic patches that then facilitate binding to hydrophobic residues on the target proteins [14, 120, 121]. These Ca^{2+}-binding induced structural changes on CaM could be thought of as increasing the probability of successful binding to a target protein, which would translate to an increased association rate. Thus, I implement an assumption that Ca^{2+}-binding changes the association, but not dissociation, rate of CaM to most of its binding partners (with the exception of Ng). It should be noted that it is likely that the increases in affinity discussed above come from changes in both the association and dissociation rate constant parameters. Current experimental techniques are unable to measure the kinetic rate constants of apo-CaM binding to target proteins (again, with the exception of Ng), and so the exact quantitative values or even relative changes in affinity and dissociate rate constants are unknowable at this time. The assumptions implemented here are my best-educated interpretation of current biophysical understanding of Ca^{2+}, CaM and CaM-target binding.

Published rate constant values that were obtained using full-length proteins are used preferentially over those for oligopeptides, but oligopeptide values are included in setting the physiological ranges for sensitivity analyses. Values for simulations are the geometric means of published values, or derived values (listed in Table 7.5). Geometric means were chosen as opposed to arithmetic means so that outlier values less significantly biased the parameter values in the simulations.

2.3.1.3 Adenylyl Cyclase Type I and VIII

AC1 and AC8 are 123 kDa and 135 kDa [122] membrane-spanning enzymes expressed in the CA1 pyramidal cells of mammalian hippocampus [123, 124]. The primary function of both AC1 and AC8 is the formation of the second messenger cyclic-AMP from ATP [125]. CaM activation of AC1 is dependent upon the binding of Ca^{2+}/CaM [126] to a single site in its C_{1b} domain [127]. Work by D. Cooper and colleagues has shown that CaM binding to the C_{1b} domain on AC1 requires participation from both the N- and C-lobes of CaM [50, 128]. CaM activation of AC8 is also dependent upon Ca^{2+}/CaM-binding [124], but unlike AC1, each AC8 enzyme contains binding sites at both its N-terminus and C_{2b} domain [129]. C_{2b}-binding is the major contributor to

CaM-dependent activation of AC8 and can be substantially activated by binding of the Ca^{2+}-bound N-lobe of CaM [50, 128]. A peptide derived from AC8-C_{2b} was able to pull down a CaM with mutations that prohibited Ca^{2+}-binding at the C-lobe at similar levels to WT CaM [50]; indicating that the N-lobe of CaM mediates most of the binding interaction between CaM and the C-terminus of AC8 (AC8-Ct). In contrast, similar pulldown experiments indicate that CaM binding to the N-terminus of AC8 (AC8-Nt) is mediated by the C-lobe of CaM [50]. CaM binding to AC8-Nt does not activate AC8's enzymatic activity [50], but has been suggested but CaM-binding at the N-terminus may support activation by increasing the local CaM concentration in a "CaM trapping" mechanism [129]. Each of these binding sites associates to Ca^{2+}/CaM in a 1:1 stoichiometry [130]. Therefore, I model AC8 as a pair of distinct targets, AC8-Nt and AC8-Ct. The concentrations of AC1 and AC8 in CA1 pyramidal cells have been estimated at 42.2 and 41.9 μM, respectively [83]. For all simulations, a concentration of 42 μM is used for AC1, AC8-Nt, and AC8-Ct. All kinetic parameters are either obtained from literature [50, 83] or calculated using previously-described assumptions.

2.3.1.4 Calcineurin

CaN is a 78 kDa [51], PSD-associated [131] enzyme expressed in the CA1 pyramidal cells of mammalian hippocampus [132]. As a heterodimer [133], CaN activation is dependent upon both the association of the catalytic subunit CaNA to the regulatory subunit CaNB as well as the binding of CaNA to Ca^{2+}/CaM [54] in a 1:1 stoichiometry [134]. Although CaNB is a Ca^{2+}-binding protein, Ca^{2+} binding to CaNB does not affect the affinity of CaNA for either CaNB [133] or Ca^{2+}/CaM [54]. For this reason, the binding of both CaNA and Ca^{2+} to CaNB are neglected in my model. CaN dephosphorylates the residues of many cellular proteins, including AMPA receptors, NMDARs, protein kinase A, and inhibitor-1 [135]. The concentration of CaN in the hippocampus is 36.4 mg of protein per kg of tissue [136]. Assuming an average protein concentration of 100 mg/mL, or 10% by mass [81], the density of CaN in hippocampus was calculated at 36.4 μg/mL, corresponding to a concentration of 0.47 μM. Here, a concentration of 0.5 μM is used. All kinetic parameters are either obtained from literature [51, 52, 54] or calculated based on previously-described assumptions.

2.3.1.5 Ca^{2+}/CaM-dependent Protein Kinase II

CaMKII is a PSD-associated [137] enzyme expressed in CA1 pyramidal cells of the mammalian hippocampus [138]. As a 650 kDa dodecamer, CaMKII is composed of twelve catalytic subunits [139]. In the hippocampus, the alpha isoform of CaMKII comprises approximately two-thirds of these subunits, while the beta isoform constitutes the remaining one-third [139]. The activation of each of these subunits is dependent upon the binding of Ca^{2+}/CaM [140] in a 1:1 stoichiometry [141], such that the full dodecamer binds Ca^{2+}/CaM in a 1:12 ratio [142]. CaMKII phosphorylates the residues of many cellular proteins, including synapsin I, pyruvate kinase, phenylalanine hydroxylase, tyrosine hydroxylase, phospholamban, MLCK, and MAP-2 [143]. CaMKII monomers can also phosphorylate intramolecular neighbors in an autophosphorylation process [144]. The resulting autophosphorylated CaMKII, termed autonomous CaMKII, remains partially active even after dissociating from Ca^{2+}/CaM [145]. Because my model is non-spatial and generally ignores catalytic processes, CaMKII is here modeled in its monomeric form (i.e., as separate, independent subunits). The local concentration of catalytic CaMKII subunits in the dendritic spines of CA1 pyramidal cells has been previously estimated at 74 μM [81]. All kinetic parameters are obtained from literature [81].

2.3.1.6 Myosin Light Chain Kinase

MLCK is a 146 kDa [146] enzyme expressed in CA1 hippocampal dendrites [109]. Its activation is dependent upon the binding of Ca^{2+}/CaM [147] in a 1:1 stoichiometry [148]. MLCK phosphorylates the regulatory light chain of the molecular motor myosin II [149]. The concentration of MLCK in the hippocampus has not been measured, but it has been observed to be much less than that in smooth muscle [150], where its concentration is about 50 μM [151]. Therefore, its concentration in CA1 pyramidal cells is estimated as one order-of-magnitude less, or 5 μM. Because the amino acid sequence of neuronal MLCK is almost identical to that of smooth muscle MLCK [150], I used the kinetic parameters of smooth muscle MLCK in my model. All kinetic parameters are either obtained from literature [49, 55, 57, 58] or calculated based on previously-described assumptions.

2.3.1.7 Neurogranin

Ng is a 7.8 kDa [152], membrane-associated [153] protein expressed in high quantities in the dendritic spines of CA1 pyramidal cells in the mammalian hippocampus [154]. Ng binds apo-CaM in a 1:1 stoichiometry [155]. It has no enzymatic function [156] but has been found to localize CaM to the cell membrane [22], theoretically resulting in the spatial coupling of CaM to both Ca^{2+} channels and CaM-dependent enzymes. The concentration of Ng in hippocampus has been estimated at 65 μM [113]. All kinetic parameters are obtained from literature [99].

2.3.1.8 Nitric Oxide Synthetase

NOS is a 155 kDa [157], PSD-associated [158] enzyme expressed in CA1 pyramidal cells of the mammalian hippocampus [159]. Its activation is dependent upon the binding of Ca^{2+}/CaM [160] in a 1:1 stoichiometry[63]. NOS catalyzes the formation of nitric oxide and citrulline from arginine [160]. The active form of NOS is a homodimeric complex [161]. However, because my model is non-spatial and generally ignores catalytic processes, NOS is modeled in its monomeric form. NOS is found in 100x diluted, homogenized rat striatum at a density of 0.7 μg/mL [162], corresponding to a concentration of 0.45 μM. Because the density of NOS is 1.5 times greater in the CA1 region of hippocampus than in striatum [163], and because NOS is localized to dendritic spines, a concentration of 1 μM is used. All kinetic parameters are either obtained from literature [59, 62], or calculated based on previously described assumptions.

2.3.1.9 Calcium

In response to a single presynaptic action potential, the transient opening of postsynaptic NMDARs in hippocampal dendritic spines generates a single spike in free Ca^{2+} concentration that peaks at 12 μM and, as Ca^{2+} is rapidly buffered, decays with a time constant of 12 milliseconds [164]. Therefore, free Ca^{2+} fluxes into the system by the equation, $[Ca](t)=12e^{-t/0.012}$. In my model, this function is a fixed boundary condition, meaning that the total Ca^{2+} concentration in the system is not conserved over the course of the simulation. Free Ca^{2+} is introduced into simulations at frequencies ranging from 0.1 Hz to 1 kHz, which spans one order-of-magnitude past the range of frequencies used in LTD- and LTP-inducing experimental protocols [18, 76]. Before the introduction of free Ca^{2+} into the system, all simulations are run to steady state for 600 seconds to equilibrate Ca^{2+}-independent binding events.

2.3.2 Model Analysis

I use the total concentration of CaM-bound protein as a primary output parameter. This is contrary to most published computational models, which investigate the concentration of Ca^{2+}-saturated CaM (CaM_4) bound to each protein. This approach is preferred for three main reasons. First, although most CaM-dependent enzymes are maximally activated by binding CaM_4, sub-saturated forms of CaM have also been found to activate these enzymes, albeit at a lower catalytic rate [97]. Therefore, the concentration of CaM_4-bound enzyme does not represent the total concentration of active enzyme. Second, not all binding sites in my model increase in catalytic activity upon CaM binding. For these proteins (Ng and AC8-Nt) the CaM_4-bound concentration is no more relevant than the concentration bound to apo-CaM or, for that matter, any other sub-saturated form. Third, CaM-binding to non-catalytic sites has been found to influence CaM availability to CaM-dependent enzymes [22, 129], suggesting an important physiological role for minimally-active, yet still CaM-bound, enzymes. Therefore, although the total concentration of CaM bound to each binding site is not a direct measure of its activation, it provides important information about patterns of enzyme activation that cannot be inferred from the concentration bound to CaM_4 alone. To obtain a representative measure of total CaM-binding during Ca^{2+} spiking at a particular frequency, the average value (henceforth designated the average bound concentration, C_b) is calculated by Equation 1:

$$(1)\ C_b = \frac{1}{t_f - t_0} \int_{t=t_0}^{t_f} \sum_{i=0}^{2} \sum_{j=0}^{2} \left[T_b CaMN_i C_j\right] dt$$

Where the subscript b indexes the binding partners, so the average bound concentration for a given binding partner (C_b) is found by integrating the total concentration of that binding partner (T_b) bound to each CaM state ($CaMN_iC_j$, i and j = 0, 1, or 2) over the stimulation period (t_o until t_f) and dividing by the stimulus duration (t_f - t_o). To measure relative levels of CaM-binding across various proteins and experimental conditions, for each binding partner I normalize C_b by its peak value from among all the Ca^{2+} frequencies simulated.

I observe that for competitive models, the frequency range at which C_b peaks may shift or narrow relative to the isolated case. To quantify this tuning, I define a metric of frequency specificity (S_b), where the subscript b indexes the binding partners. A binding partner with high frequency specificity is one that most significantly binds CaM over a narrow range of frequencies;

correspondingly, this binding partner's frequency-dependence curve would have a tall, narrow peak. First, the frequency-dependence curve is integrated and then normalized by the maximum C_b (Equation 2). I also divide by the total simulated frequency range and subtract from 1 to report S_b as a metric that identifies the most strongly tuned binding partners. In Equation 2, f denotes Ca^{2+} frequency.

$$(2)\ S_b = 1 - \frac{1}{(\log(f_f) - \log(f_0))\ \max[C_b]} \int_{f_0}^{f_f} C_b(f)\ df$$

2.3.2.1 Sensitivity Analysis

To determine which parameters most greatly impacted my models' outputs and, therefore, which may benefit most from further characterization in future experiments, I conducted two sets of global sensitivity analyses using Latin Hypercube sampling (LHS) to efficiently sample the input parameter space and partial rank correlation coefficients (PRCC) to quantify the results [115]. In one set, I fixed the kinetic rate constants and investigated the impact of variations in initial concentrations on the average bound concentrations (C_b) of the eight CaM binding partners. In the second, I fixed the initial concentrations and investigated the impact of variations in kinetic rate constants. Each of these analyses was performed at low (1 Hz), moderate (10 Hz), and high (100 Hz) frequency Ca^{2+} oscillations, allowing me to observe how the impacts of parameter variations change with frequency (available at [165]). To control for total Ca^{2+} introduced, oscillations were limited to 10 concentration spikes, regardless of frequency. In Table 2.1 and Table 2.2, I present the results of my 10 Hz sensitivity analysis, listing the parameters that most strongly influence each C_b.

Table 2.1. Significant PRCCs for initial protein concentration parameters.

Output	[Varied Input Parameter] PRCC Value			
C_{AC1}	[CaM] 0.9509	[AC1] 0.9204	[CaMKII] -0.8177	
$C_{AC8\text{-}Ct}$	[CaM] 0.9498	[AC8-Ct] 0.9209	[Ng] -0.8752	[CaMKII] -0.5186
$C_{AC8\text{-}Nt}$	[CaM] 0.9567	[AC8-Nt] 0.9116	[Ng] -0.7441	
C_{CaN}	[CaM] 0.9564	[CaN] 0.9442	[CaMKII] -0.8999	
C_{CaMKII}	[CaM] 0.9766	[CaMKII] 0.9177	[AC8-Nt] -0.6657	
C_{MLCK}	[CaM] 0.9381	[MLCK] 0.934	[CaMKII] -0.7392	[Ng] -0.6167
C_{Ng}	[CaM] 0.9759	[Ng] 0.8827		
C_{NOS}	[NOS] 0.996	[CaM] 0.8076	[Ng] -0.7238	

Enumeration of Partial Rank Correlation Coefficient (PRCC) values for variations in initial protein concentrations that most strongly affect each average CaM-bound protein concentration, C_b, for simulations with Ca^{2+} frequency of 10 Hz. Only inputs with absolute PRCC values greater than 0.5 are shown.

Table 2.2. Significant PRCCs for rate parameters.

Output	Varied Input Parameter PRCC Value				
C_{AC1}	$k_{on}^{AC1CaM4}$ 0.9243	k_{on}^{KCaM4} -0.8964	k_{on}^{1N} 0.5449	$k_{off}^{AC1CaM4}$ -0.5271	
$C_{AC8\text{-}Ct}$	$k_{on}^{AC8ctCaM4}$ 0.8295	k_{on}^{KCaM4} -0.7473	k_{on}^{1N} 0.6305	$k_{on}^{AC8ctCaM2N}$ 0.5914	$k_{on}^{NgCaM2N}$ -0.5065
$C_{AC8\text{-}Nt}$	$k_{on}^{AC8ntCaM2C}$ 0.8725 $k_{off}^{AC8ntCaM2C}$ -0.5663	k_{off}^{KCaM2C} 0.7294	k_{off}^{K2N} 0.703	k_{on}^{1N} -0.6864	$k_{on}^{NgCaM2C}$ -0.5816
C_{CaN}	k_{on}^{PPCaM4} 0.9649	k_{on}^{KCaM4} -0.8123			
C_{CaMKII}	k_{off}^{KCaM2C} -0.8187	k_{off}^{K2N} -0.7581	k_{on}^{KCaM4} 0.733	$k_{on}^{AC8ntCaM4}$ -0.5377	k_{on}^{1N} 0.5002
C_{MLCK}	k_{on}^{1N} 0.642	k_{on}^{KCaM4} -0.8983	k_{on}^{MKCaM4} 0.9376		
C_{Ng}	k_{off}^{NgCaM0} -0.6711 k_{on}^{2N} -0.6259	k_{on}^{Ng2C} -0.6645 $k_{off}^{NgCaM2C}$ -0.6093	k_{on}^{Ng1C} -0.6641 $k_{on}^{NgCaM2C}$ 0.5302	k_{off}^{Ng1C} 0.6444 k_{on}^{NgCaM0} 0.5021	k_{off}^{Ng2C} 0.6358
C_{NOS}	$k_{on}^{NOSCaM4}$ 0.8964	$k_{off}^{NOSCaM0}$ -0.6958	kon^{KCaM4} -0.5681		

Enumeration of Partial Rank Correlation Coefficient (PRCC) values for variations in rate parameters that most strongly affect each average CaM-bound protein concentration, C_b, for simulations with Ca^{2+} frequency of 10 Hz. Only inputs with absolute PRCCs greater than 0.5 are shown.

Although their experimental ranges span several orders of magnitude, the kinetic binding constants of CaM_4 binding to CaN (k_{on}^{PPCaM4} and k_{off}^{PPCaM4}), as well as CaM_4 binding to NOS ($k_{on}^{NOSCaM4}$ and $k_{off}^{NOSCaM4}$), only significantly affected the C_b of CaN and NOS, respectively. In contrast, the rate constant of CaM_4 binding to CaMKII (k_{on}^{KCaM4}), despite having an experimental range that varies only four-fold, significantly impacted almost all outputs of CaM binding partners at each of the three frequencies. Future competitive computational models may benefit from more accurate measurement of k_{on}^{KCaM4} than from the more accurate measurement of k_{on}^{PPCaM4}, k_{off}^{PPCaM4}, $k_{on}^{NOSCaM4}$, or $k_{off}^{NOSCaM4}$, despite the clear experimental uncertainty in measurements of the latter four.

2.3.3 Competition regulates CaM-binding dynamics

To investigate how competition alters the CaM-binding dynamics of each of the eight binding partners, I plotted the normalized concentrations of individual partners bound to different CaM states: apo-CaM (CaM_0), CaM bound to two Ca^{2+} ions at its N-terminus (CaM_{2N}), CaM bound to two Ca^{2+} ions at its C-terminus (CaM_{2C}), and CaM_4 (Figure 2.3). In each simulation, 10 Ca^{2+} fluxes (not plotted) were introduced at 10 Hz, corresponding to the logarithmic midpoint of my chosen frequency range. In Figure 2.3, the different colors of the plotted traces correspond to the concentration of binding partner bound to each of the four CaM states normalized to the total concentration of all CaM-bound binding partner (CaM_{tot}). The time-course of CaM binding partners bound to various states of CaM in micromolar for 1 second of 10 Hz Ca^{2+} flux is plotted in Figure 7.3 in the Supplement to Chapter 2.

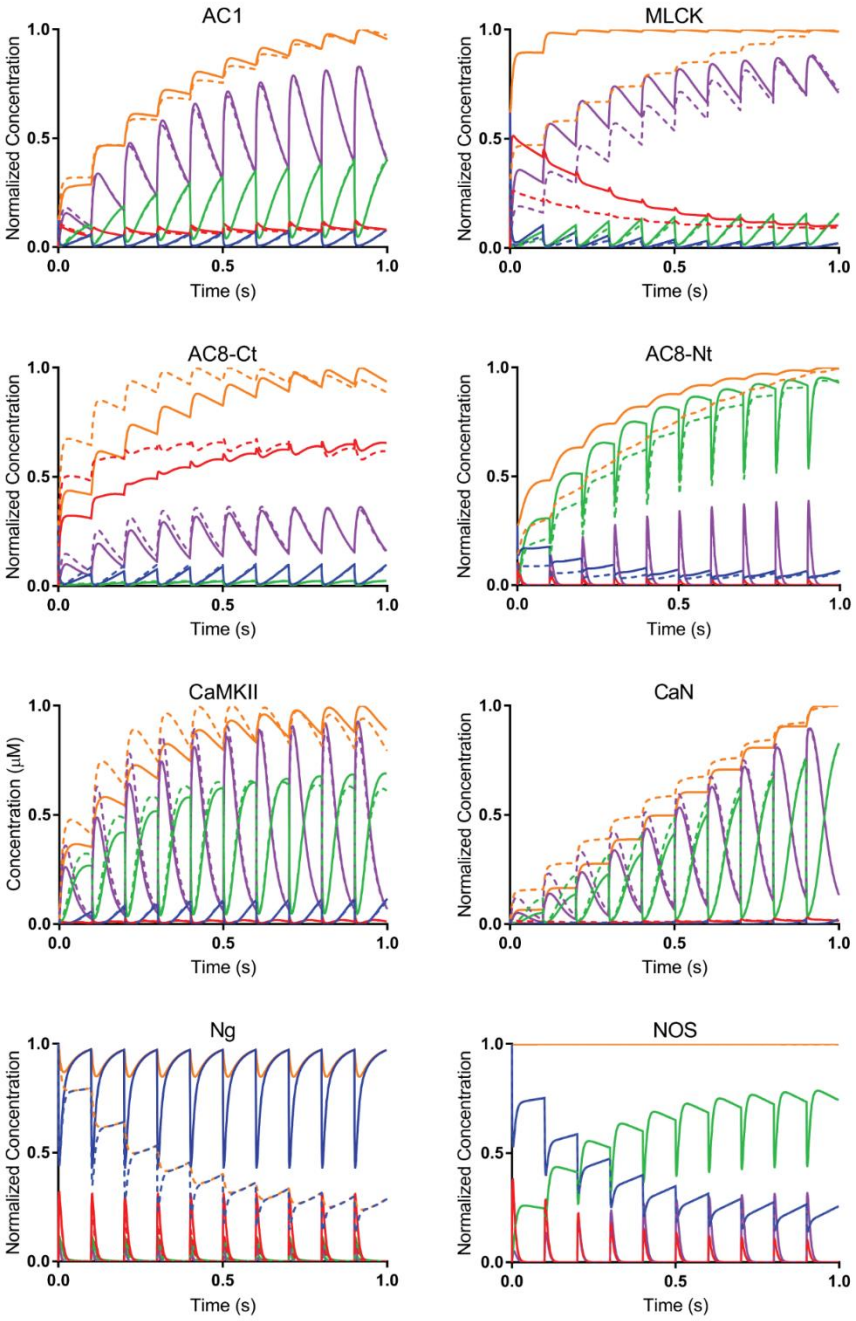

Figure 2.3. Competition for CaM alters binding dynamics. Time-course of CaM binding partners bound to various states of CaM for 1 second of 10 Hz Ca^{2+} flux: CaM_0 (blue), CaM_{2N} (red), CaM_{2C} (green), CaM_4 (purple), and CaM_{tot} (orange). CaM_{tot} is the sum of all CaM-bound states for a given protein. The concentration of each species is normalized against its maximum value of CaM_{tot}. Solid lines denote the isolated model. Dotted lines denote the competitive model. The differences between isolated and competitive behavior are more significant for some CaM binding partners than others.

As expected, the presence of competitors decreases the concentration of CaM bound to each binding partner. Because the relative contributions of the various CaM states to each binding partner's CaM_{tot} in the competitive model were similar to those in the isolated model, competition did not appear to have a disproportionately large effect on the binding of any one CaM state. This suggests that CaM, and not Ca^{2+}, is the major limiting factor in the activation of CaM-dependent enzymes in hippocampal dendritic spines. Furthermore, competition appears to change not just the concentration of CaM bound to each partner, but also the CaM-binding dynamics. To paraphrase, concentrations in the competitive model are not simply scaled versions of their counterparts in the isolated model. Instead, competition seems to change how each binding partner responds to rapid Ca^{2+} transients, including how CaM-binding changes with each subsequent Ca^{2+} flux. For example, after just three Ca^{2+} fluxes, the concentration of CaM-bound MLCK no longer changes in the isolated model, while it continues to increase in the competitive model. Conversely, while the CaM-binding of Ng decreases with each subsequent Ca^{2+} spike in the competitive model, it does not change in the isolated model. Therefore, the dynamic behavior of CaM targets in cellular environments cannot necessarily be inferred from computational studies that model them in isolation.

Finally, although competition attenuates the CaM-binding of all binding partners, the magnitude of their attenuation varies considerably in my model. For example, while NOS experiences virtually no change in CaM-binding in the presence of competitors, CaN experiences a more than 20-fold reduction in CaM-binding in the competitive model. Therefore, the binding partners are unequally competitive under the simulated conditions. From these observations, I hypothesize that the competitiveness of each binding partner (i.e., the ability of a binding partner to bind CaM in the presence of other binding partners) might not be absolute and, instead, that the competitiveness of each protein may change across environmental conditions. In this case, competition for CaM is well-positioned to serve as a tuning mechanism, suppressing the CaM-binding of each binding partner for all but a small range of internal conditions and external stimuli and allowing for the tight control of enzyme activation needed for the precise regulation of LTP, LTD, and other neurological processes. Therefore, I investigate how competition may tune the CaM-binding of each neuronal protein to certain Ca^{2+} frequencies.

2.3.4 Competition tunes CaM-binding to certain Ca^{2+} frequencies

To investigate my hypothesis that competition affects the frequency-dependence of CaM-binding, I construct frequency-dependence curves for all eight CaM binding sites (distinguishing between each AC8 terminus) using both the isolated and competitive models (Figure 7.2 in the Supplement to Chapter 2). The frequency dependence of C_b is then projected onto heat maps (Figure 2.4 A and B). For all simulations, Ca^{2+} oscillations consisted of 100 concentration spikes ranging from 0.1 Hz to 1 kHz.

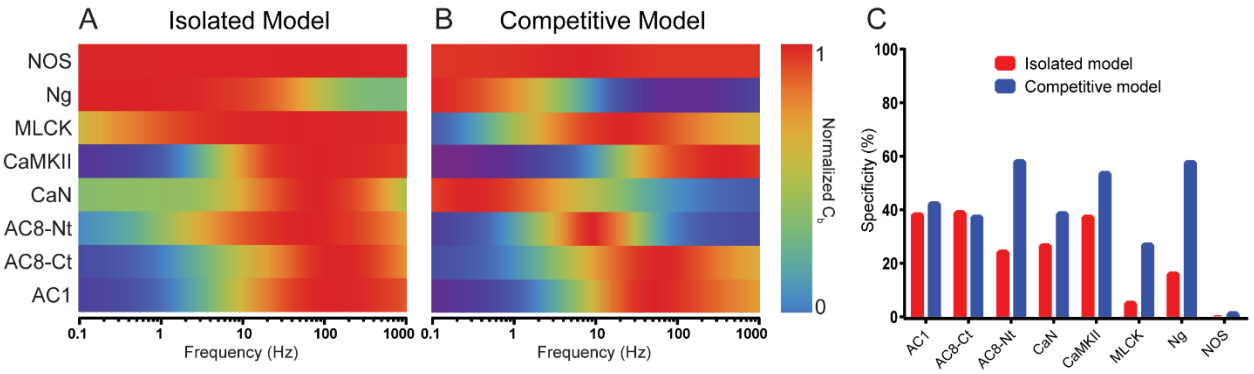

Figure 2.4. Competition tunes activation frequencies. (A) and (B) show normalized activation of CaM as a function of frequency for the isolated and competitive models, respectively. Red denotes peak activation; blue denotes minimal activation. Frequency windows of peak activation tend to narrow and shift for many of the binding partners in the competitive case. Indeed, (C) indicates a sharpening of activation frequency windows as an increase in specificity in the competitive model, at least for most proteins. Specificity is S_b multiplied by 100 percent.

The introduction of competition shifts the frequency-dependence curves of almost all binding partners. For some, such as AC1, AC8-Ct, CaMKII, and MLCK, this shift is slight, but apparent. For other partners, such as AC8-Nt and CaN, this shift is dramatic. In the competitive model, maximal CaM-binding occurs at frequencies almost one order of magnitude lower for AC8-Nt (10 Hz in the competitive model, as compared to 60 Hz in the isolated model). For CaN, maximal CaM-binding occurs at frequencies over two orders of magnitude lower (0.3 Hz in the competitive model, as compared to 80 Hz in the isolated model). For NOS, a frequency shift is present but not visible in Figure 2.4B.

Although, as stated earlier, total CaM-binding and enzymatic activation are not the same (particularly for CaN, which is subject to dual regulation by Ca^{2+}/CaM and CaNB), it is worth

noting that CaN is activated by low, but not high, frequency stimulation *in vivo* [18]. Therefore, it would be expected that maximal CaM-binding of CaN occurs at a similarly low frequency. The fact that this held true in the competitive, but not in the isolated, model suggests that the *in vivo* frequency-dependence of CaN may be reliant upon the presence of cellular competitors. Because of both the established role of CaN in LTD induction [78, 104] and the demonstrated ability of low frequency stimulation to induce LTD [18], my results further suggest that competition for CaM may be essential to normal LTD induction. Furthermore, because activated CaN downregulates LTP induction [103], competitive suppression of CaM-binding to CaN at high frequencies may be equally essential to normal LTP induction.

To investigate the effects of competition on each CaM binding partner's level of preference for a certain frequency range, I used the frequency-dependence curves to calculate the frequency specificity of each binding partner in both the isolated and competitive models as defined in Equation 2. If a binding partner were only active at one frequency, it would have a frequency specificity of 100 percent.

The introduction of competitors sharpens the frequency-dependence curves of almost all binding partners, as also indicated by increased frequency specificity values in the competitive models relative to the isolated models (Figure 2.4C); frequency specificities increased for AC1 (42.80%, as compared to 38.73%), AC8-Nt (58.55%, as compared to 24.79%), CaN (39.13%, as compared to 27.19%), CaMKII (54.17%, as compared to 37.89%), MLCK (27.45%, as compared to 5.70%), Ng (58.23%, as compared to 16.64%), and NOS (1.77%, as compared to 0.08%). The sole decrease, AC8-Ct, was small (37.86%, as compared to 39.50%). Therefore, competition for CaM not only regulates CaM-binding by changing the frequencies of maximal CaM binding, but also by narrowing the range over which appreciable CaM binding occurs.

2.3.5 Competition for CaM mediates Ng/CaMKII crosstalk

Two studies have reported decreased CaMKII autophosphorylation and CaMKII activity in CA1 hippocampal slices harvested from Ng genetic knockout ($Ng^{-/-}$) mice [166, 167]. Although both studies reported about a 30% decrease in CaMKII autophosphorylation and CaMKII activity, they were in disagreement concerning the effect of the genetic knockout ($Ng^{-/-}$) on LTP induction. Pak *et al.* (2000) found that wild type ($Ng^{+/+}$) mice required a single tetanus to achieve potentiation, while $Ng^{-/-}$ mice required multiple tetanic stimulations [166]. In direct contrast, Krucker *et al.*

(2002) found that $Ng^{-/-}$ mice required only a single tetanus to induce LTP [167]. Despite these inconsistent results, both sets of authors suggested that this phenomenon may be caused by abnormal regulation of local Ca^{2+} and CaM concentrations, a proposal that has since been supported by several studies.

For example, Huang *et al.* (2004) attributed diminished LTP in $Ng^{-/-}$ mice to lower levels of free Ca^{2+} following high frequency stimulation [113]. And using two sets of Ng mutants which, respectively cannot bind, and constitutively bind, CaM, Zhong *et al*. (2009) provided evidence that abnormal regulation of local CaM concentrations may also be responsible. Using a model of the interactions of Ca^{2+}, CaM, CaMKII, CaN, and AMPARs, Zhabotinsky *et al.* (2006) reproduced the effects of Ng knockout on LTP induction reported by Huang *et al*., but did not address the diminished CaMKII activity reported by both Pak *et al.* and Krucker *et al*. To date, no mathematical model has replicated the paradoxical effect of Ng genetic knockout on autonomous CaMKII activity.

I hypothesize that these phenomena could be explained by competitive tuning. I simulate autonomous CaMKII activation by extending my model according to a previously-published model of CaMKII autophosphorylation by Pepke *et al.* (see Fig 6 in [81]). In that work, two CaM-bound (active) CaMKII monomers form a complex that enzymatically catalyzes the phosphorylation of one of the monomers. I stimulate this extended model according to an LTP induction protocol followed by Krucker *et al*., in which hippocampal slices were subjected to two tetanic stimuli of 100 pulses at 100 Hz, 20 seconds apart. Using this protocol, I assess my isolated (Figure 2.5A) and competitive (Figure 2.5B) models' responses to simulated Ng knockout at 600 seconds after the last stimulus. Normalized results from the same experimental stimulation protocol by Krucker *et al*. are shown in Figure 2.5C (see activity data in Fig 1F in [167]).

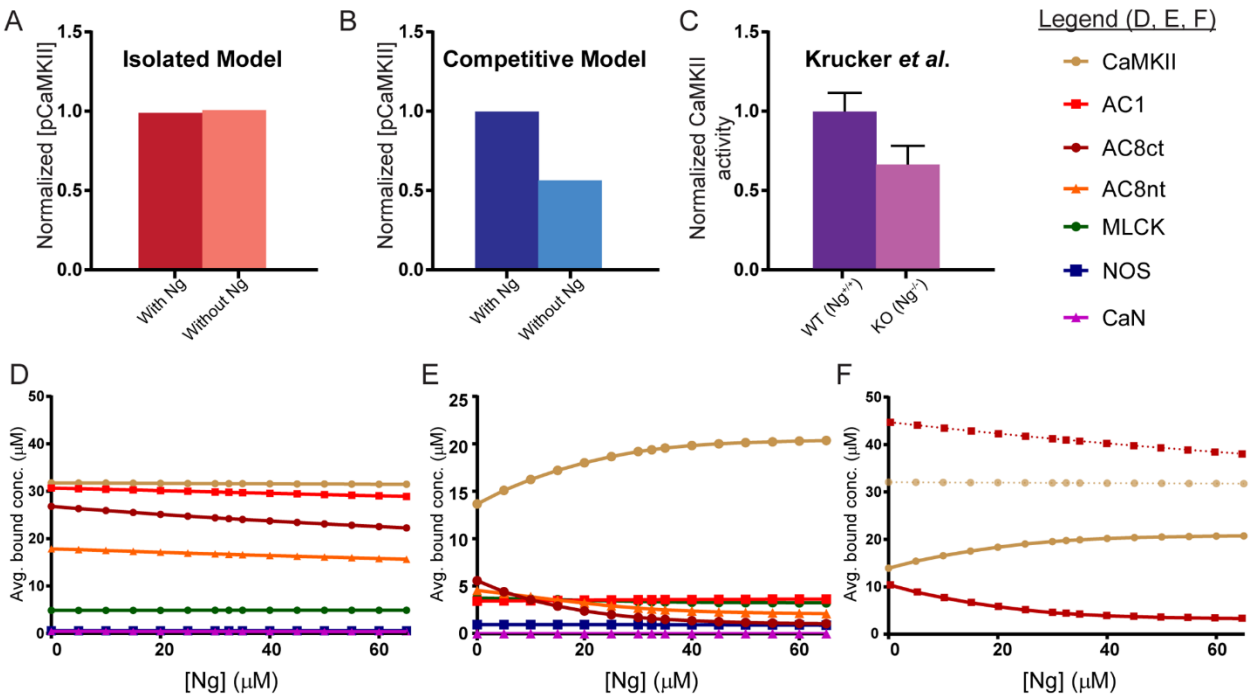

Figure 2.5. Competitive tuning explains intermolecular crosstalk. (A) Simulations of CaMKII phosphorylation in my isolated model with and without inclusion of Ng. (B) Simulations of CaMKII phosphorylation in my competitive model with and without Ng. (C) CaMKII activity in WT and $Ng^{-/-}$ knockout mice from Krucker *et al*. Simulations were performed to replicate the experimental method of Krucker *et al*. as closely as possible. (D) The average bound concentration (C_b) of each CaM binding protein in semi-isolated models as a function of Ng concentration. AC8-Ct and AC8-Nt exhibit the greatest relative change in CaM-binding (C_b, Eqn 1) as Ng concentration decreases. (E) The average bound concentration (C_b) of each CaM binding protein in the competitive model as a function of Ng concentration. For a decreasing Ng concentration, AC8-Ct and AC8-Nt again exhibit the greatest relative change in CaM-binding. (F) Comparing the semi-isolated (dotted traces) to the competitive (solid traces) model shows that only in the competitive model does summed AC8 (AC8-Nt + AC8-Ct, dark red) mirror the loss in CaM-CaMKII binding as Ng concentration decreases.

In the absence of other competitors, the isolated model elicits similar levels of CaMKII autophosphorylation (pCaMKII) whether in the presence or absence of Ng. That is, the complete removal of Ng, which competes with CaMKII for CaM, results in only a slight increase in pCaMKII (Figure 2.5A). In contrast, in the presence of competitors for CaM, simulated Ng knockout decreases pCaMKII levels by 44% compared to WT (Figure 2.5C). Notably, this decrease in pCaMKII is quantitatively similar to the roughly 33% loss of Ca^{2+}-independent CaMKII activity indicated by Krucker *et al*. [167]. Further, my competitive model results are also

consistent with Pak *et al*., who report a 40% decrease in pCaMKII in KO $Ng^{-/-}$ mice compared to WT ($Ng^{+/+}$) mice [166].

Because my model does not allow for either spatial effects or variations in free Ca^{2+} concentration, these results suggest that competition for CaM alone could explain the paradoxical effect of Ng genetic knockout on CaMKII autophosphorylation and activity. pCaMKII levels seem to be regulated, at least in-part, by the competition for CaM established by Ng. With Ng, an abundance of the CaM not bound to Ng preferentially binds CaMKII (at moderate Ca^{2+} levels) because CaMKII can out-compete the other candidate binding partners. Without Ng, as in $Ng^{-/-}$ knockout mice, this competitive advantage of CaMKII to bind CaM is reduced, likely because the CaM that would normally bind Ng instead binds other proteins that do not dissociate as readily when high levels of Ca^{2+} are introduced.

This interpretation predicts that the decreased CaMKII autophosphorylation and activity seen in the $Ng^{-/-}$ knockouts occurs as a result of increased CaM-binding to other partners. To identify which other partners most preferentially bind CaM upon decreasing Ng, I first employ "semi-isolated" models containing only Ng and one of the seven other CaM binding partners (Figure 2.5D). Semi-isolated models are utilized in Figure 2.5D to help ensure that shifts in binding partner activation with decreasing Ng are in fact due to decreasing Ng. The partners that experience the greatest relative increase in CaM-binding as Ng concentration is decreased are AC8-Ct and AC8-Nt (calculated according the average CaM bound concentration, C_b, in Eqn 1). A more pronounced increase in the average bound concentration of AC8-Ct and AC8-Nt is seen in full competitive model simulations at decreasing Ng concentrations (Figure 2.5E). This could indicate that the decrease in CaMKII autophosphorylation and activity in $Ng^{-/-}$ mice is due to the shift in availability of (that is, the competition for) CaM due to its increased binding to AC8 during high frequency stimulation. To investigate this, the average bound concentrations of AC8-Ct and AC8-Nt are summed together into AC8 in Figure 2.5E and plotted along with the average bound concentration of CaMKII as a function of initial Ng concentration for both isolated and competitive model simulations. CaM-binding to AC8 appears sufficient to explain these changes, with the amount of increase in the average bound AC8 concentration at decreasing Ng concentration closely mirroring the decrease in the average bound CaMKII concentration.

2.4 Discussion

In the present study, I use a system of ordinary differential equations to model the dynamic interactions of Ca^{2+}, CaM, and seven CaM target proteins implicated in LTP and LTD of hippocampal synapses. By developing both "isolated" and "competitive" models of this system, I observe competition among these target proteins for CaM-binding and investigate competition's role in regulating the frequency-dependent activation of downstream CaM binding proteins. The dynamic behavior of my model is largely determined by kinetic rate constants that describe the binding of CaM to Ca^{2+} and CaM binding to downstream binding to CaM binding proteins. My models are parameterized using published values where available and are calculated by applying experimentally supported assumptions and the thermodynamic principle of microscopic reversibility. Global sensitivity analyses are performed to determine the impact of these assumptions on my conclusions, and I find that very few of the parameters that significantly impacted my results are derived from these assumptions.

One of the major results of this work is that competitive binding could be among the mechanisms by which protein activation is dynamically tuned and regulated. I find that the presence of competitors affects not only the concentration of all respective CaM-bound proteins, but also the CaM-binding dynamics of these targets. Based on the results of the present work, I recommend at least the inclusion of Ng into models simulating the activation of CaM-dependent proteins in response to low frequency Ca^{2+} transients and the inclusion of CaMKII into models simulating the activation of CaM-dependent proteins in response to high frequency Ca^{2+} transients. Based on the results of my global sensitivity analyses, these two proteins appear to have the most significant impact on the CaM-binding of other CaM targets at these frequency ranges.

Another major result of this work is that competitive tuning may be able to explain the counter-intuitive results from studies of Ng knockouts in mice ($Ng^{-/-}$) in which CaMKII autophosphorylation and activity levels were seen to decrease in the $Ng^{-/-}$ compared to WT. My results suggest that under tetanic stimulation and normal initial Ng concentration, Ng buffers CaM from AC8 but not CaMKII. At low concentrations or in the absence of Ng, AC and particularly AC-Ct, is able to bind more CaM, while CaMKII binds less CaM (Figure 2.5F). Although the K_D value of CaM_4 binding to CaMKII and AC-Ct are only within 2-fold of each other (1.7 μM and 0.8 μM, respectively), they exhibit very different binding dynamics based on their binding of sub-saturated CaM (CaM_{2C} and CaM_{2N}). This is best seen in Figure 2.3. For AC-Ct, the dominant

species of CaM that binds is CaM_{2N}, making up greater than 50% of the total CaM species bound to AC-Ct. In contrast, for CaMKII there is no dominant species of CaM that binds; CaM_{2N} and CaM_4 are major contributors to the total CaMKII-CaM bound species. The binding dynamics of CaM-CaMKII interactions that are seen in the competitive model suggest, as previous work has suggested [81], that CaMKII binds to CaM_{2C} and this CaM_{2C} is then converted to CaM_4 while still bound to CaMKII, as noted by the coincident decline in CaMKII-CaM_2 and increase in CaMKII-CaM_4 in Figure 2.3 and Figure 7.3 in the Supplement to Chapter 2. The binding dynamics of AC8-Ct seem to indicate that AC8-Ct binds CaM_{2N} and stays bound until the next Ca^{2+} spike. Thus, I hypothesize that AC8-Nt is able to out compete CaMKII for CaM binding in absence of Ng because of its relatively high affinity for CaM_{2N}. Since the dynamic behavior that I see in the competitive model is so dependent on the rate parameters it would be ideal if more of them could be experimentally determined in the future. To test the hypothesis that AC8 activity would be increased in a $Ng^{-/-}$ model, I suggest an experiment in which cAMP production is measured in CA1 hippocampal slices from $Ng^{+/+}$ and $Ng^{-/-}$ mice while employing forskolin and specific AC1 blockers to control for cAMP production by AC1 and G protein activation, respectively. If my proposed model is accurate, then increased cAMP production will be observed in $Ng^{-/-}$ mice.

Protein networks for which the initiating ligand is a limiting resource, such as the Ca^{2+}/CaM network studied here, are common in biology. As *in vivo* ligand concentrations often approach the dissociation constants of their binding partners, the concentration of bound ligand could exceed that of free ligand, resulting in the phenomenon of ligand depletion [168]. Ligand depletion, as described by Edelstein *et al*., reduces cooperative interactions and broadens the range of signals to which the ligand is most responsive. It may be that I observe ligand depletion phenomena in my isolated models (Figure 2.4A), given the broad range of Ca^{2+} frequencies at which many binding partners are activated, especially for AC8 and MLCK. However, if ligand depletion really were the predominant regulatory phenomenon, I would expect that by introducing more binding partners (Figure 2.4B), the broadening effect of ligand depletion would become more conspicuous. Instead, I see a shift and narrowing of the Ca^{2+} frequencies over which the binding partners are activated. Thus, I am confident that it is competition among the CaM-binding proteins that is the mechanism underlying this tuning behavior.

Because competition seems to be important in my neuron-based model, I sought to compare my results to a different biological system with Ca^{2+}/CaM-dependent signaling. The 2008

publication by Saucerman and Bers examines activation of CaMKII and CaN in a compartmentalized model of cardiomyocytes, stimulated at Ca^{2+} frequencies ranging from 0-4 Hz [92, 93]. Although this frequency range is much narrower than that used in my competitive model, I can still compare trends of frequency-dependent protein activation. For example, CaMKII activation increases with frequency for both models. Additionally, my isolated model agrees with the Saucerman-Bers model without CaM buffers, in which CaN activation dramatically increases over 0-4Hz. In my competitive model CaN activation is attenuated, in agreement with the Saucerman-Bers model with CaM buffers. This agreement lends further confidence to my model, as the Saucerman-Bers results were subsequently verified experimentally [169]. It appears my model using explicitly-defined CaM buffers (binding proteins) is consistent with the Saucerman-Bers implementation of generalized, unidentified CaM buffers.

The 2008 model by Saucerman and Bers, though not explicitly spatial, highlights how protein localization may affect model output. In Saucerman's model, Ca^{2+} frequency-dependent activation levels are different for the cytosolic and membrane-localized (dyadic) CaN sub-populations. My current model excludes spatial effects in order to scrutinize competitive binding in the absence of confounding factors. However, I acknowledge that spatial effects likely alter competition for CaM, especially in the PSD. Future work would investigate the effect of spatial localization on competition for CaM binding; in particular instantiating membrane-localized proteins such as AC1, AC8, NOS and especially Ng at or near the membrane. Sub-populations of CaN may also be localized to the PSD through binding with scaffolding proteins such as AKAP79 [170-172]. Indeed, because I describe Ng as freely diffusing, it is possible my model exaggerates the ability of Ng to compete for CaM relative to other proteins in my model. Therefore, it would be interesting to assess whether a competitive model accounting for membrane localization can still explain the paradoxical effect of $Ng^{-/-}$ on CaMKII autophosphorylation.

Together, my results suggest that the frequency-dependence of CaM targets observed *in vivo* is not an inherent property of these proteins, but rather may be an emergent property of their competitive environment. This competitive tuning may provide a mechanism by which otherwise-independent protein pathways can engage in crosstalk through the limited availability of CaM. I propose that competitive tuning, alongside binding dynamics, feedback loops, and spatial localization, may serve as a major regulator of CaM target protein activation. Furthermore, I have attempted to explain the paradoxical decrease in CaMKII activity seen in $Ng^{-/-}$ mice as a result of

the dysregulation of this competitive tuning mechanism. In the absence of spatial effects or aperiodic variations in free Ca^{2+} concentration, competitive tuning is able to offer an explanation for this phenomenon. It is important to note that other proteins, mechanisms, or pathways not included in this model likely lend robustness and further regulatory mechanisms of this phenomenon. Further, it is unlikely that seven CaM-target proteins studied here are the only CaM target proteins that engage in this type of crosstalk through limiting CaM. If competitive tuning facilitates crosstalk among CaM binding proteins, then genetic disorders, neurological diseases, normal aging processes, and therapeutics that disrupt any one CaM target protein may have non-intuitive effects that extend into other signaling pathways. Computational modeling and analysis will continue to play a large role deciphering these oft counter-intuitive regulatory mechanisms that when disrupted, give rise to complex neurological disorders and other important diseases.

2.5 Methods

All numerical integration and data manipulation were performed in Mathematica as described in Model Analysis. Reaction equations were implemented using Mathematica [173] with the XCellerator package [174]. XCellerator uses the Law of Mass Action to create ordinary differential equations describing the time rate of change in concentration for each binding partner and their respective CaM-bound states. In Equation 3 I monitor the concentration of a generalized Ca^{2+}/CaM state complexed with an arbitrary binding partner, T_b:

$$(3)\ \frac{d\left[T_bCaMN_iC_j\right]}{dt} = k_{on}^{T_bCaMN_iC_j}[T_b]\left[CaMN_iC_j\right] - k_{off}^{T_bCaMN_iC_j}\left[T_bCaMN_iC_j\right] + k_{on}^{T_bjC}[Ca^{2+}]\left[T_bCaMN_iC_{j-1}\right] + k_{on}^{T_biN}[Ca^{2+}]\left[T_bCaMN_{i-1}C_j\right] + k_{off}^{T_b(i+1)N}\left[T_bCaMN_{i+1}C_j\right] + k_{off}^{T_b(i+1)C}\left[T_bCaMN_iC_{j+1}\right] - \left[T_bCaMN_iC_j\right]\left(k_{off}^{T_biN} + k_{off}^{T_bjC} + k_{on}^{T_b(i+1)N}[Ca^{2+}] + k_{on}^{T_b(j+1)C}[Ca^{2+}]\right)$$

where i and j = 0, 1, or 2.

For simulations involving autophosphorylation of CaMKII, I extend the system of differential equations generalized in Equation 3 to describe formation of a complex between two

active (CaM-bound) CaMKII monomers (Equation 4). Finally, complexes of CaMKII monomers react such that one monomer behaves as an enzyme and the other becomes the phosphorylated substrate (Equation 5). As stated, I refer directly to the previously-published model of CaMKII autophosphorylation by Pepke *et al.* (see Fig 6 in [81]).

$$(4)\ \frac{d\left[\mathrm{Dimer_{CaMKII}N_{1,i}N_{2,m}C_{1,j}C_{2,n}}\right]}{dt} = k_{on}^{Dimer}\left[\mathrm{CaMKIICaMN_{1,i}C_{1,j}}\right]\left[\mathrm{CaMKIICaMN_{2,m}C_{2,n}}\right] - k_{off}^{Dimer}\left[\mathrm{Dimer_{CaMKII}N_{1,i}N_{2,m}C_{1,j}C_{2,n}}\right]$$

$$(5)\ \frac{d\left[\mathrm{pCaMKIICaMN_iC_j}\right]}{dt} = k_p^{\mathrm{CaMN_iC_j}}\left[\mathrm{Dimer_{CaMKII}N_{1,i}N_{2,m}C_{1,j}C_{2,n}}\right]$$

Where i, j, m, and n = 0, 1, or 2. Phosphorylated CaMKII monomers may also be one of the two participating species in Equation 4.

All the equations for this model can be found in S3 Appendix. Mathematica files for the complete models can be found on the Purdue PURR database: Romano, D.; Pharris, M. C.; Patel, N.; Kinzer-Ursem, T. L. (2017), "Mathematica Files: Competitive tuning: competition's role in setting the frequency-dependence of Ca^{2+}-dependent proteins." (DOI: 10.4231/R7154F7Q). My model code is also being uploaded to the BioModels Database [175-177].

Despite my best efforts to constrain my models' parameter values to those that have been experimentally-measured or those which can be calculated by the principle of thermodynamic equilibrium, it was still a valuable exercise to investigate the effects of the previously-described calculations and assumptions on model conclusions. Therefore, a global sensitivity analysis was used to investigate how uncertainty in parameter values impacted model outputs. Latin hypercube sampling (LHS) was used to simultaneously sample input parameter spaces, and partial rank correlation coefficients (PRCC) were calculated to measure the correlation between variation in parameter values and variation in model outputs. These methods have been previously described (see [81, 115]). In short, for each CaM target, a uniform probability distribution of input parameter values was assumed to either span the experimental range specified in Table 7.5 (a more detailed version of this table is available at [46]) or, if a range of experimental values is not present, 50-200% of experimental, calculated, or assumed values. A perfect positive correlation gave a PRCC

of 1, whereas a perfect negative correlation gives a PRCC of -1. A threshold of 0.5 was used to select for only the parameters that significantly impacted (either positively or negatively) the average bound concentration of each binding partner, and parameters were then ranked by the absolute value of their PRCCs. For the sake of completeness, the sensitivity analysis was done for the nine-state model of Ca^{2+}-CaM binding.

3. COMPETITIVE TUNING AMONG CA2+/CALMODULIN-DEPENDENT PROTEINS: ANALYSIS OF IN SILICO MODEL ROBUSTNESS AND PARAMETER VARIABILITY

3.1 Summary

Calcium/calmodulin-dependent (Ca^{2+}/CaM-dependent) regulation of protein signaling has long been recognized for its importance in a number of physiological contexts. Found in almost all eukaryotic cells, Ca^{2+}/CaM-dependent signaling participates in muscle development, immune responses, cardiac myocyte function and regulation of neuronal connectivity. In excitatory neurons, dynamic changes in the strength of synaptic connections, known as synaptic plasticity, occur when calcium ions (Ca^{2+}) flux through NMDA receptors and bind the Ca^{2+}-sensor calmodulin (CaM). Ca^{2+}/CaM, in turn, regulates downstream protein signaling in actin polymerization, receptor trafficking, and transcription factor activation.

The activation of downstream Ca^{2+}/CaM-dependent binding proteins (CBPs) is a function of the frequency of Ca^{2+} flux, such that each CBP is preferentially "tuned" to different Ca^{2+} input signals. I have recently reported that competition among CBPs for CaM binding is alone sufficient to recreate *in silico* the observed *in vivo* frequency-dependence of several CBPs. However, CBP activation may strongly depend on the identity and concentration of proteins that constitute the competitive pool; with important implications in the regulation of CBPs in both normal and disease states.

Here, I extend my previous deterministic model of competition among CBPs to include phosphodiesterases, AMPAR receptors that are important in synaptic plasticity, and enzymatic function of CBPs: cAMP regulation, kinase activity, and phosphatase activity. After rigorous parameterization and validation by global sensitivity analysis using Latin Hypercube Sampling (LHS) and Partial Rank Correlation Coefficients (PRCC), I explore how perturbing the competitive pool of CBPs influences downstream signaling events. In particular, I hypothesize that although perturbations may decrease activation of one CBP, increased activation of a separate, but enzymatically-related CBP could compensate for this loss, providing a homeostatic effect.

First I compare dynamic model output of two models: a two-state model of Ca^{2+}/CaM binding and a four-state model of Ca^{2+}/CaM binding. I find that a four-state model of Ca^{2+}/CaM binding best captures the dynamic nature of the rapid response of CaM and CBPs to Ca^{2+} flux in

the system. Using global sensitivity analysis, I find that model output is robust to parameter variability. Indeed, although variations in the expression of the CaM buffer neurogranin (Ng) may cause a decrease in Ca^{2+}/CaM-dependent kinase II (CaMKII) activation, overall AMPA receptor phosphorylation is preserved; ostensibly by a concomitant increase in adenylyl cyclase 8 (AC8)-mediated activation of protein kinase A (PKA). Indeed phosphorylation of AMPAR receptors by CaMKII and PKA is robust across a wide range of Ng concentrations, though increases in AMPAR phosphorylation is seen in at low Ng levels approaching zero. My results may explain recent counter-intuitive results in neurogranin knockout mice and provide further evidence that competitive tuning is an important mechanism in synaptic plasticity. These results may be readily translated to other Ca^{2+}/CaM-dependent signaling systems in other cell types and can be used to suggest targeted experimental investigation to explain counter-intuitive or unexpected downstream signaling outcomes. This work is published ([165]).

3.2 Introduction

Worldwide, as many as 1 billion people suffer from neurological disorders [178]. In the US alone, neurological disorders affect more than 1 in 7 households [179]. At the most basic level, these neurological disorders arise from perturbations in protein signaling networks within neuronal synapses. Normal synaptic function requires dynamic, short-timescale regulation of the connective strength of the synapse. This regulation is initiated within the post-synapse by the influx of calcium ions (Ca^{2+}) through NMDA receptors [27]. Intracellular Ca^{2+} binds the Ca^{2+} sensor protein calmodulin (CaM), which subsequently activates a variety of Ca^{2+}/CaM-dependent protein signaling pathways. Ca^{2+}/CaM-dependent pathways may either potentiate synaptic connective strength via AMPA receptor (AMPAR) phosphorylation and trafficking to the synapse, or they may depress synaptic strength by regulating AMPAR de-phosphorylation and removal from the synapse (recently reviewed in Huganir and Nicoll [180]). Although many of the proteins that are involved in Ca^{2+}/CaM-dependent AMPAR regulation are well known, the dynamics of the pathway(s) are far from understood. With computer-guided studies, I begin to characterize the dynamics and cross-talk inherent to the protein interactions in these pathways, possibly enabling the identification of new therapeutic targets for treating neurological disorders.

Calmodulin (CaM) regulates synaptic plasticity by selectively activating a number of downstream proteins, termed calmodulin binding proteins (CBPs), within the signaling networks

responsible for either the dynamic strengthening or weakening of synaptic connections. The binding of CaM to its many downstream binding partners [20, 181-183] depends on the kinetic rates with which different CaM species bind CBPs, such that each CBP is preferentially activated by, or "tuned" to, different input Ca^{2+} signals. Aside from binding dynamics, other mechanisms that regulate this tuning include feedback loops, spatial localization, and a recently described phenomenon called competitive tuning [92, 184, 185]. I have recently reported that competitive tuning is sufficient to recreate, *in silico*, the *in vivo* Ca^{2+} frequency-dependence of several CBPs [184]. One prediction from competitive tuning is that, in the absence of other mechanisms, signaling outcomes may strongly depend on the abundance and binding dynamics of individual CBPs; parameters susceptible to perturbation either by genetic regulation or by post-translational modification. It follows then that signaling outcomes may lack robustness if competitive tuning occurs in isolation of other regulatory mechanisms.

Indeed, modulating just one parameter (e.g. a protein's concentration) could cause a shift in competition that influences the signaling outcomes of other proteins in the system, perhaps leading to non-intuitive effects. I have previously shown that simulated knockout of the CaM buffer neurogranin (Ng) shifts the competition for CaM, non-intuitively decreasing Ca^{2+}/CaM-dependent kinase II (CaMKII) activation and concomitantly increasing adenylyl cyclase (AC) activation [184]. My previous results may explain a surprising experimental observation by Krucker *et al*. (2002) in which Ng knockout (Ng KO) mice retain the ability to acquire long-term potentiation (LTP), despite a considerable reduction in CaMKII activity [186]. In this present work I further explore how competitive tuning regulates LTP, hypothesizing that although reduced CaMKII activation in the Ng KO should reduce the phosphorylation of AMPA receptor GluA1 subunits at residue S831, a coincident increase in AC activation may cause an increase in GluA1 subunit phosphorylation at residue S845. This would lead to robustness in the overall level of GluA1 phosphorylation. Although there is still some debate about the precise roles of phosphorylation at S831 and S845, it is well accepted that phosphorylation of these sites is involved in the function and location of AMPARs and in synaptic plasticity (recently reviewed in [31, 180]). Thus, competitive tuning alone could provide the mechanism by which overall GluA1 phosphorylation levels are maintained and provide a homeostatic effect on synaptic plasticity.

Here, I compare two models of Ca2+/CaM-dependent activation of CBPs; a 2-state Ca2+/CaM binding model and a four-state Ca2+/CaM-binding model. I include well documented

CBPs that are highly expressed in neurons, and also include signaling events downstream of Ca2+/CaM binding, including CaM-dependent enzymatic activity, PKA kinase activation, phosphatase regulation, and AMPAR receptor phosphorylation. After validating the model, I use a global sensitivity analysis to quantify the effect of parameter perturbations on model outcomes. I also find that at short timescales, competitive tuning provides robustness in overall GluA1 phosphorylation levels via upregulation in the activation of PKA-mediated phosphorylation of GluA1 in conditions that simulate the Ng KO. My results provide further evidence that competitive tuning could be an important mechanism in the regulation and maintenance of synaptic plasticity.

3.3 Results and Discussion

3.3.1 Model Development

3.3.1.1 Model Structure

Similar to my previous work [184], I constructed models of CaM binding to a number of downstream CBPs and allowed the CBPs to compete for the various states of Ca^{2+}/CaM. CaM has four binding sites for Ca^{2+} ions, two in EF-hand domains in the amino (N) terminus, and two in EF-hand domains in the carboxy (C) terminus. The binding of Ca^{2+} within each terminus is highly cooperative, for example upon binding of the first Ca^{2+} ion at the N-terminus, a second Ca^{2+} ion binds rapidly to the N-terminus. But binding between the termini is independent (i.e. Ca^{2+}-binding at the N-terminus does not change the binding of Ca^{2+} at the C-terminus). Many models of Ca^{2+} signaling cascades in neurons and cardiomyocytes have employed a simplified, yet still relevant model of Ca^{2+} ions binding to CaM where all four Ca^{2+} ions are assumed to bind simultaneously (outlined in Figure 1A). These models have been used extensively and are thought to be quite accurate, at least for scenarios in which the overall magnitude of Ca^{2+} flux is large, such as in Ca^{2+}-dependent Ca^{2+} release phenomena or high frequency Ca^{2+} flux. However, more detailed descriptions of CaM that account for its intermediate, sub-saturated states (outlined in Figure 1B) may be more appropriate for situations in which Ca^{2+} flux occurs at moderate to low frequencies, or in conditions of limiting Ca^{2+} [187]. It has been shown that several CBPs (MLCK, CaMKII, AC1 and AC8) produce CaM-dependent activity even with small increases in Ca^{2+} concentration [97, 188, 189]. Additionally, CaMKII has been shown to be enzymatically active with only two Ca^{2+} ions bound to CaM [190], and AC8 has been shown to bind CaM with only two Ca^{2+} ions

bound to CaM [189]. These observations and the fact that binding of Ca^{2+} to CaM is highly cooperative within each terminus, but not between termini, together have led some to develop models that include more intermediate states of Ca^{2+} binding to CaM [42, 92, 184].

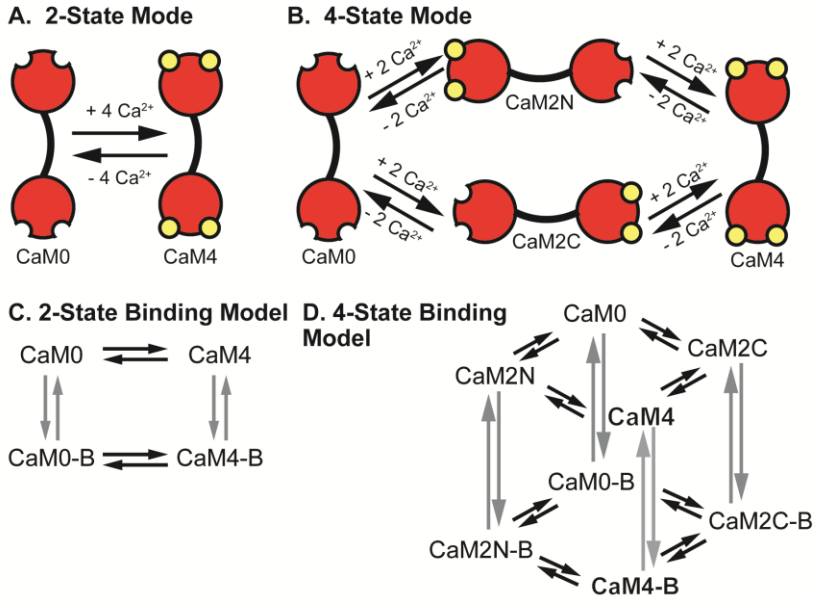

Figure 3.1. Schematic representations of binding models. (A-B) Binding models of Ca2+-binding to calmodulin. Four Ca2+ ions (yellow circles) bind to CaM at binding sites in the amino (N) and carboxyl (C) termini. A) 2-state model of Ca2+ binding to CaM. CaM with no Ca2+ ions bound (CaM0) is assumed to simultaneously bind four Ca2+ ions forming a fully saturated Ca2+ bound CaM (CaM4). B) 4-state model of Ca2+ binding to CaM where two Ca2+ ions bind simultaneously to either the N- or C- termini of CaM (CaM2N or CaM2C, respectively). In a subsequent reaction two Ca2+ ions bind to either termini to form fully saturated Ca2+-bound CaM (CaM4). (C-D) Models of Ca2+ binding to CaM and CaM binding to downstream binding partners. C) 2-state binding model where CaM0 with no Ca2+ ions bound binds to downstream binding partners (represented by CaM0-B). CaM4 can also bind to downstream binding partners (CaM4-B). D) 4-state binding model where all states of CaM (CaM0, CaM2N, CaM2C, and CaM4) may bind downstream binding partners (CaM0-B, CaM2N-B, CaM2C-B, and CaM4-B).

I compare a 2-state CaM model to a 4-state CaM model (Figure 3.1 A and B). For both models I view CaM as a limiting resource. There are many more CBPs than CaM itself. Thus CBPs compete simultaneously for binding to CaM in its different states (overview in Figure 3.1C-D and Figure 3.2). Listed below, the CBPs that are included in this work are highly expressed in neurons and widely reported to interact with CaM (see [20] for a review). The reactions that describe these

interactions are listed in Table 7.1, given in the Supplement to Chapter 3. To study downstream events in Ca^{2+}/CaM-dependent signaling I additionally include enzymatic activation of CBPs and the relevant proteins and nucleotides that are downstream of CaM-binding. These include the generation of cAMP by AC1 and AC8, hydrolysis of cAMP by PDE1 and PDE4, activation of PKA by cAMP, phosphorylation of GluA1 by PKA and CaMKII, and de-phosphorylation of GluA1 by CaN and PP1 (summarized in Table 7.2; reactions listed in Table 7.1). The interactions among Ca^{2+} ions, proteins, and nucleotides described above and shown schematically in Figure 3.2 and the corresponding differential equations are found in the Supplement to Chapter 3. In total there are 91 equations and 225 parameters for the 2-state model and 151 equations and 447 parameters for the 4-state model.

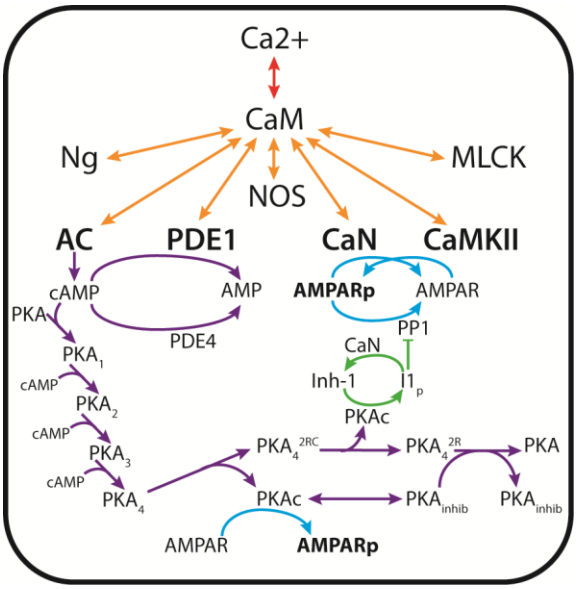

Figure 3.2. Schematic of the CaM-dependent protein signaling network. Ca2+ ions flux through the NMDA receptor, initiating a cascade of signaling that results in phosphorylation of the AMPA receptors. CaM-binding proteins (neurogranin (Ng), muscle light chain kinase (MLCK), neuronal nitric oxide synthetase (NOS), calcineurin (CaN, also known as protein phosphatase 3), Ca2+/calmodulin-dependent kinase II (CaMKII), phosphodiesterase 1 (PDE1), adenylyl cyclase 1 (AC1) and adenylyl cyclase 8 (AC8)) simultaneously compete for CaM binding. CaM binding activates the catalytic activity of CaMKII, which phosphorylates the AMPA receptor GluA1 subunit at site S831. Generation of cAMP by CaM-bound adenylyl cyclases activates the catalytic activity of protein kinase A (PKA, also known as cAMP-dependent kinase), which phosphorylates Inh-1 as well as GluA1 at site S845. Phosphodiesterases (both CaM-dependent PDE1 and constitutively active PDE4) regulate intracellular levels of cAMP by hydrolysis, thereby regulating PKA activity. PP1 may additionally de-phosphorylate CaMKII or GluA1. PP1 may become sequestered by Inh-1, until Inh-1 is de-phosphorylated by CaN.

Table 3.1. Calmodulin binding proteins.

Protein	Description and Chemical Reactions
Adenylyl Cyclase 1 (AC1)	A prominent adenylyl cyclase isoform in hippocampal neurons. Binds CaM at its C_{1b} domain and, when activated, converts ATP to cAMP [16, 17, 191, 192].
Adenylyl Cyclase 8 (AC8)	A prominent adenylyl cyclase isoform in hippocampal neurons. Binds Ca^{2+}/CaM at both its N- and C-termini, which are explicitly accounted for in this work [189, 193]. Ca^{2+}/CaM-AC8ct (C-terminus-bound AC8) may bind ATP for conversion to cAMP [16].
Ca^{2+}/CaM-dependent kinase II (CaMKII)	Ca^{2+}/CaM-dependent kinase. Highly expressed in brain, and especially hippocampal tissue [194]. In this work, CaMKII is modeled as monomers which, when active, may dimerize and subsequently become Ca^{2+}/CaM-independent via autophosphorylation [195]. Active CaMKII phosphorylates many downstream proteins such as the GluA1 subunit of AMPA receptors [196].
Calcineurin (CaN)	A Ca^{2+}/CaM-dependent serine/threonine phosphatase [197, 198]. CaN dephosphorylates GluA1 at S845 [199].
Myosin Light Chain Kinase (MLCK)	A putatively abundant CBP in dendritic spines, which we model using kinetic parameters derived from studies on smooth muscle [200-202].
Neurogranin (Ng)	A membrane-associated protein, and one of the few proteins that strongly binds CaM in absence of Ca^{2+} [35, 155, 203, 204].
Nitric Oxide Synthetase (NOS)	Typically a membrane-associated protein that binds tightly to CaM and generates Nitric Oxide from citrulline and arginine [159, 161, 205].
Phosphodiesterase 1 (PDE1)	A Ca^{2+}/CaM dependent phosphodiesterase that cleaves cAMP into AMP [21].

Table 3.2. Non-calmodulin binding proteins in this model.

GluA1	One of four subunits of α-amino-3-hydroxy-5-methyl-4-isoxazolepropionic acid receptor (AMPA receptor). Is phosphorylated at amino acid residue S831 by CaMKII and residue S845 by PKA [32, 33]. Increase AMPA phosphorylation is implicated in synaptic plasticity, and GluA1-p845 may be necessary for exocytosis of AMPARs to the synaptic membrane [33].
Inhibitor 1 (Inh-1)	When phosphorylated by active PKAc, Inh-1 may bind PP1, inhibiting the ability of PP1 to de-phosphorylate GluA1. Inh-1 is de-phosphorylated by CaM-activated CaN [33].
Phosphodiesterase 4 (PDE4)	PDE4 is not Ca^{2+}/CaM dependent but plays a significant role in regulating the levels of cAMP in cells by cleaving cAMP into AMP. Phosphorylation by active PKAc increases the enzymatic activity of PDE4 [206].
PKA Inhibitor	A generic model species representative of many unspecified off-target binding partners for PKA. These binding partners sequester PKA, preventing its phosphorylation of GluA1, and they additionally participate in the pathway restoring PKAc to the original four-subunit, auto-regulated PKA heteromer [207].
Protein kinase A (PKA, also known as cAMP-dependent kinase)	Binds up to four cAMP, liberating catalytic subunits that bind and phosphorylate a number of downstream targets such as PDE4, Inh-1, and GluA1 [21, 32].
Protein Phosphatase 1 (PP1)	PP1 de-phosphorylates GluA1 subunits at both S831 and S845, in addition to CaMKII T286 [33]. In this model, PP1 may only bind CaMKII when CaMKII is un-bound to Ca^{2+}/CaM.

3.3.1.2 Model Parameterization

Model parameters are either obtained directly from literature or are calculated from published values using the principle of microscopic reversibility and implementing the assumption that Ca^{2+} binding does not affect the rate of protein dissociation from CaM k_{off}, but rather the association rate (k_{on}) such that the general equation $K_D = \frac{k_{off}}{k_{on}}$ can be used to calculate rate constants. These assumptions have been used regularly in the modeling literature by myself and others [42, 184, 208, 209] and have been shown to be experimentally validated [58]. For the Ca^{2+}/CaM-dependent enzymes AC, PDE1, and CaN the catalytic activity is assumed to scale with the amount of Ca^{2+} bound to CaM, similar to what has been shown with CaMKII [97]. Thus I calculate scaled values for the catalytic activity of sub-saturated Ca^{2+}-bound CaM-CBPs similar to my previous model of CaMKII auto-phosphorylation [184]. For example, the catalytic activity of Ca^{2+}/CaM_{2C}-CaN is slower than that of Ca^{2+}/CaM_4-CaN. In the absence of experimental measurement of catalytic rate constants for AC, PDE1, and CaN activity when bound to sub-saturated CaM, I calculated these scaled catalytic rate constants such that the rate of activity of the CaM_{2C}-bound state relative to that CaM_4-bound state was decreased by a similar proportion to that of the phosphorylation rate CaM_{2C}-CaMKII to CaM_4-CaMKII which has been previously measured [97]. Catalytic rate constants for CaM_{2N}-bound state of AC, PDE1, and CaN was similarly scaled relative to the ratio of phosphorylation rate constants of CaM_{2N}-CaMKII to CaM_4-CaMKII. The values of all parameters are provided in Table 7.5 in the Supplement to Chapter 3.

Prior to executing Ca^{2+} flux, each simulation was run for a time course of 30 seconds at a basal level of 5 nM Ca^{2+} to allow for steady state binding of CaM to CBPs [34, 210]. The concentrations of all species at the end of this preliminary simulation were used as the input for simulations in which Ca^{2+} flux was initiated at varying frequencies.

3.3.2 2-State vs 4-State CaM Binding Models

In previous work I have shown that a thermodynamically complete, 9-state model of Ca^{2+} binding to CaM did not significantly change model output relative to a 4-state binding model [184]. In this work my first task was to compare a 2-state binding model to that of a 4-state binding model (Figure 3.1C and D) to validate the hypothesis that the dynamics of CBP binding by CaM are optimally represented by a 4-state binding model. For this, I analyzed model output when

stimulated at a frequency of 10 Hz (see Methods). In Figure 3.3 I used two metrics to show how the 2-state model (Figure 3.3 A and C) and 4-state model (Figure 3.3 B and D) each responded to 10 Hz Ca^{2+} stimulation. The first metric (Figure 3.3 A and B) monitored CBP binding only to fully-saturated CaM_4 over time. The second metric (Figure 3.3 C and D) monitored the total CBP binding to all Ca^{2+}/CaM states. The only difference between metrics for the 2-state model is that the second metric additionally accounts for each CBP bound to apo-CaM (CaM_0), if any. Similarly, using the second metric for the 4-state model involves summing the concentrations of each CBP bound to each Ca^{2+}/CaM state: CaM_0, CaM_{2N}, $CaM_{2C,}$ and CaM_4.

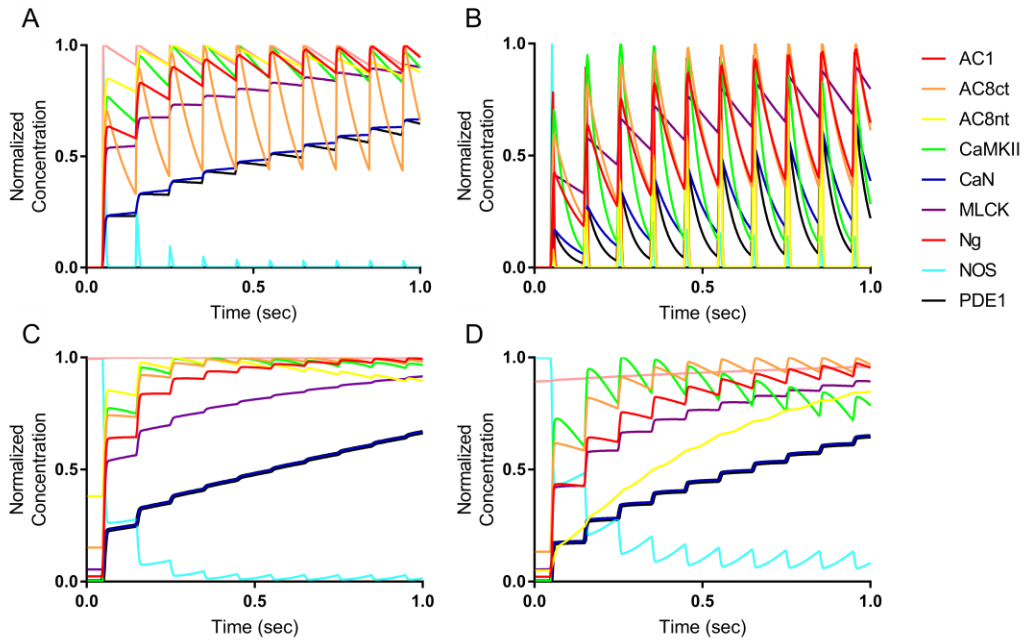

Figure 3.3. Time-course comparison of Ca2+/CaM binding models. (A,B) Response of binding models to 10Hz Ca2+ frequency stimulation, monitoring each CBP bound to Ca2+-saturated CaM4. (C, D) Response of binding models to 10 Hz Ca2+ frequency stimulation, monitoring the cumulative concentration of each CBP bound to any Ca2+/CaM state. Similar data for models stimulated at 50 Hz Ca2+ is provided in the Supplement to Chapter 3.

By monitoring either CaM_4-bound or all CaM-bound CBP, I assessed the added value of a relatively detailed 4-state model to the simpler 2-state model of Ca^{2+}/CaM. In Figure 3.3A, each CBP-CaM_4 trace exhibited wavelets implying a frequency detection inherent to CBP activation. For most CBPs such as CaN (blue) and AC8ct (black), relative activation by CaM_4 generally increased over time, which was consistent with expectation for CBPs exposed to a continuous,

frequency-based stimulus. In contrast, Ng (cyan) rapidly decreased in relative CaM_4 binding over time though this was also expected due to the high affinity of Ng for CaM_0 compared to CaM_4. In Figure 3.3C, the 2-state model elicited similar time-course trends for each CBP compared to Figure 3.3A, and because the traces lack frequency-associated wavelets, it appears that CaM_0 was significantly bound to CBPs, particularly during inter-spike intervals of Ca^{2+}. The differences between monitoring solely CaM_4- versus all CaM-bound CBPs were further evidenced by Figure 7.4 in the Supplement to Chapter 3, which shows equivalent output but for a model stimulated at 50 Hz.

For the 4-state model, the Ca^{2+} frequency-associated waveforms were much more prominent than in the 2-state model (compare Figure 3.3B and D to Figure 3.3A and C), indicating that the 4-state model is much more responsive to Ca^{2+} than the 2-state model (some data obscured by the highly dynamic traces). See also results from 50 Hz stimulation in Figure 7.4. Of note, there is a significant difference in the dynamics of binding of CaM to $AC8_{nt}$ and NOS between the 2-state and 4-state models (compare Figure 3.3A and C to Figure 3.3B and C) at 10 Hz. Additionally, the 4-state model is altogether more responsive to rapid changes in Ca^{2+} concentration, even when all the CaM-bound CBPs are summed (Figure 3.3D). Taken together this data provides a strong motivation to move forward with the 4-state model as the best model to simulate the frequency-dependent response of CBPs.

3.3.3 Frequency Analysis

Because my current 4-state model dramatically expands on previous work, I wanted to assess the frequency-dependence of CBP activation. I define two metrics in order to compare the frequency response of all CBPs. In the first metric, Normalized C_{b1}, the time-averaged integration of all CaM_4-bound CBPs (Equation S1) is normalized to the highest C_{b1} value of each CBP, respectively. In the second metric, Normalized $C_{b2,}$ the time-averaged integration of all CaM species-bound CBPs (Equation S2) is normalized to the highest C_{b2} value of each CBP, respectively. Normalized C_{b1} and C_{b2} values for each CBP are plotted at various Ca^{2+} flux frequencies (Figure 3.4).

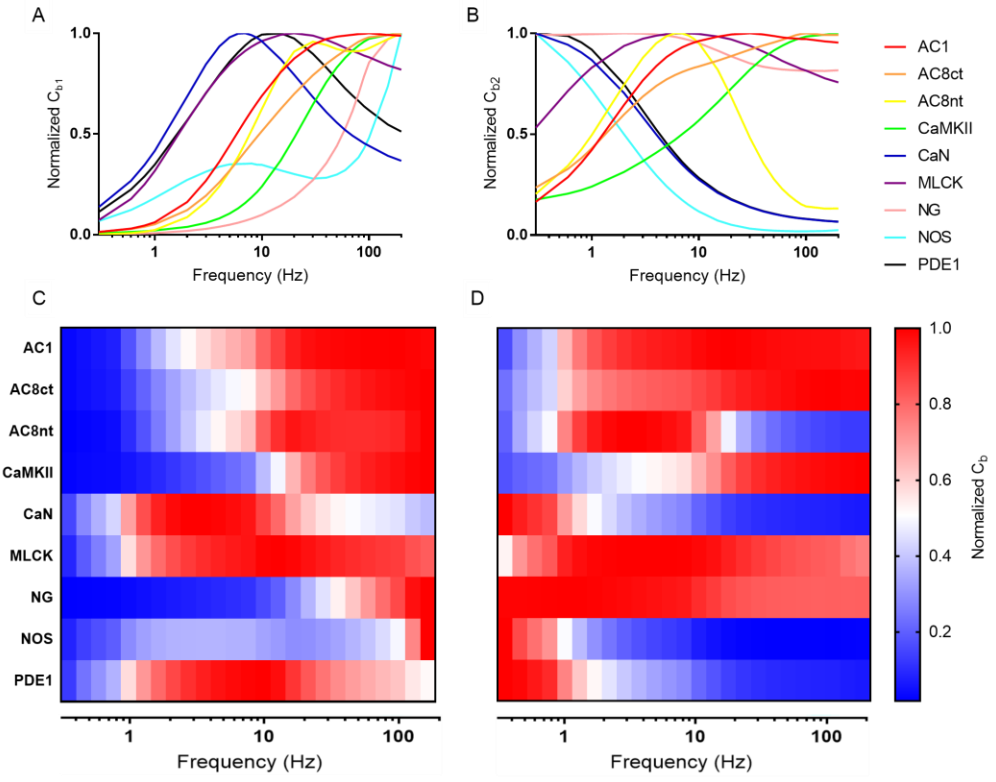

Figure 3.4. Frequency-dependence of CBPs. **(A,B)** Relative time-averaged concentrations of CaM_4-bound CBPs (C_{b1}) and all CaM-bound CBPs (C_{b2}), respectively, for the 4-state model. **(C,D)** Heatmap representations of data shown in A and B, where each row denotes the CaM_4- and total CaM-binding to each CBP. Blue denotes minimal relative activation of CBP, and red denotes maximal relative activation of CBP. Note the shifts in the frequencies of peak CBP activation when accounting only for CaM_4-binding (C) and all CaM-CBP binding (D).

The frequency responses of the various CBPs, when accounting for all CaM-binding, are in good agreement with previously published results. For example, CaMKII (green trace) exhibited its highest CaM_4-binding (and thus, activation) at high frequencies, peaking around 100 Hz (Figure 3.4 A and B). High frequency activation of CaMKII coincides with the protein's putative role in long-term potentiation, which is initiated under high-frequency (~100 Hz) Ca^{2+} flux. Interestingly, Ng, which has a higher affinity for CaM_0 than CaM_4, exhibited relatively little CaM_4-binding across most frequencies, before spiking at about 80 Hz (Figure 3.4 A and C). This spike in average CaM_4-bound Ng is explained by the full saturation of CaM_4 at high frequencies. Indeed, when accounting for all CaM-binding (Figure 3.4B), Ng exhibits a peak activation at lower frequencies, which is more consistent with expectation [4]. Most notably, when analyzing Normalized C_{b1}

(Figure 3.4 A and C) many CBPs such as AC1, AC8, Ng, and NOS have highly similar peak activation frequencies. If distinct Ca^{2+} signals/frequencies elicit activation of distinct Ca^{2+}/CaM-dependent pathways and were in-part dependent on competitive tuning, then I would have expected each CBP to have a more distinguishable frequency of peak activation.

The frequency dependence of the CBPs is clearer when I analyze the data using the second metric, Normalized C_{b2}. As seen in Figure 3.4B and Figure 3.4D, this analysis revealed how CaM_0 and the intermediate Ca^{2+}/CaM states can, in conjunction with saturated CaM_4, contribute to the frequency-dependence of CBP activation. This is additional evidence that suggests that a 4-state model of Ca^{2+}/CaM binding is able to capture the frequency dependent changes in CBP activation. These results also compare favorably with my previous work [184]. However, in my previous work the adenylyl cyclase CBPs (AC1, $AC8_{nt}$, and $AC8_{ct}$) generally exhibits activation that peaked at higher-frequencies (greater than 50 Hz). In Figure 3.4B and Figure 3.4D, it appears that incorporating the additional CPB (PDE1) caused a downward shift and sharpening in peak activation frequency for $AC8_{nt}$.

3.3.4 Sensitivity of GluA1 Phosphorylation to Variation in Key Input Parameters

Global sensitivity analysis was performed to assess how variation in input parameters contributed to variation in the overall phosphorylation of GluA1. Latin Hypercube Sampling (LHS) was used to efficiently sample the input parameters over 4-fold range (2-fold increased and decreased). Partial Rank Correlation Coefficients (PRCC) was used to quantify how the variation in each input parameter contributed to overall phosphorylation of GluA1 (sum of all phosphorylated GluA1 species). To test the hypothesis that CaMKII significantly contributes to GluA1 phosphorylation under normal Ng concentrations, and PKA (via AC1/8 activation of cAMP) significantly contributes to GluA1 phosphorylation when Ng is knocked down, I performed LHS/PRCC analysis under a both wild-type Ng condition and a total Ng KO condition. For both conditions, the parameters with absolute PRCC's greater than my threshold of 0.5 are shown in Table 3.3.

Table 3.3. Sensitivity analysis results for kinetic parameters at 100Hz Ca^{2+}.

Parameter	PRCC	Parameter	PRCC [Ng]=0
$k_p^{AC1CaM4}$	0.808	$k_p^{PKAcGluA1}$	0.785
$k_{on}^{AC1CaM4}$	0.758	$k_p^{AC1CaM4}$	0.763
$k_p^{PKAcGluA1}$	0.597	$k_{on}^{PKAcGluA1}$	0.636
$k_p^{KCaM4GluA1}$	0.584	$k_p^{AC8ctCaM4}$	0.618
$k_{on}^{CaMKIIGluA1}$	0.527	$k_p^{PDE4cAMP}$	-0.864
k_{on}^{KCaM4}	-0.732		
$k_p^{PDE4cAMP}$	-0.805		

In the WT Ng condition at 100 Hz Ca^{2+} flux, all association and catalytic rate parameters (k_{on}^{B} or k_p^{B}, where B represents the different CBPs) were varied simultaneously. As expected, I find that the phosphorylation rate constant of CaMKII-mediated phosphorylation of GluA1 $k_p^{KCaM4GluA1}$ is highly correlated with total GluA1 phosphorylation (Table 3.3). Additionally, the catalytic rate constant for AC1-CaM_4 production of cAMP ($k_{on}^{AC1CaM4}$) and that of the downstream output of AC1 activation (PKA, $k_p^{PKAcGluA1}$) were also highly correlated with phosphorylation of GluA1. This indicates that at 100 Hz and WT Ng conditions, increases in the rate of CaM_4 binding to AC1 leads to increases in phosphorylation of GluA1.

For the second set of conditions the concentration of Ng was set to zero to simulate Ng KO. In comparison to the WT Ng case, it is first interesting to note that the phosphorylation rate constant $k_p^{KCaM4GluA1}$ is no longer highly correlated with GluA1 phosphorylation (PRCC value = 0.467, below my threshold of 0.5). Though admittedly this PRCC value for $k_p^{KCaM4GluA1}$ is still somewhat high, its reduction in the Ng KO analysis suggests a diminished importance for CaMKII-mediated phosphorylation of GluA1 subunits. In accordance with my over-arching hypothesis that competitive tuning mediates a shift in pathway activation, I refer again to Table 3.3 for clues as to the alternative proteins contributing to GluA1 phosphorylation. Indeed, both the association and catalytic rates of PKAc for GluA1 ($k_{on}^{PKAcGluA1}$ and $k_p^{PKAcGluA1}$, respectively) have significantly greater PRCC values in the Ng KO compared to the WT case. Furthermore, the catalytic rate of cAMP production by $AC8_{ct}$-CaM_4 ($k_p^{ACtctCaM4}$) also exhibits a significant PRCC in the Ng KO case.

Altogether, the results of my sensitivity analysis indicate that, at least for 100 Hz Ca^{2+} and short timescales (<2 sec), competition for Ca^{2+}/CaM-binding may support a shift in signaling in which Ng perturbation causes AC to overtake CaMKII as the primary activator of pathways leading to GluA1 subunit phosphorylation.

3.3.5 Potential Robustness Provided by Competitive Tuning

Having seen in the preceding sections that my expanded model exhibits similar frequency dependence to a previous result, and that perturbing Ng causes a shift in the parameters most strongly associated with GluA1 phosphorylation, I now explore the functional consequences of competitive tuning in this simplified model of synaptic plasticity. One hallmark of synaptic plasticity is the phosphorylation of AMPAR GluA1 subunits at two residues: S831 and S845. S831 is phosphorylated by CaM-bound CaMKII or pCaMKII, and S845 is phosphorylated by catalytic PKA (PKAc).

Previously I have shown that competitive tuning was able to explain counter-intuitive experimental results showing that Ng genetic knock-out (Ng KO) results in decreased CaMKII activation/autophosphorylation [184]. This same work also predicted that knocking out Ng concentration would cause a shift in CaM binding away from CaMKII in favor of AC8. Noting that activated AC1 and AC8ct generate cAMP, which in turn activates PKA, it seemed that competitive tuning could provide a mechanism for the system to account for perturbations in Ng expression. That is, because Ng KO reduces CaMKII-facilitated phosphorylation of GluA1 S831, competitive tuning could drive the alternative activation of more AC8ct, increasing PKA activation and in turn, phosphorylation of GluA1 S845.

In Figure 3.5, I explore this potential mechanism by simulating Ng knockdown, while monitoring the time-averaged concentration of phosphorylated AMPARs (pGluA1) under three different Ca^{2+} flux frequencies. Note that because the number of Ca^{2+} pulses is conserved with varying Ca^{2+} frequency, the scales in Figure 3.5 exaggerate the total GluA1 phosphorylation seen at 10 Hz compared to 100 Hz, due to differences in stimulation time. For all three stimulation frequencies in Figure 3.5, GluA1 subunits phosphorylated by CaMKII at S831 (p831, red) decrease with decreasing Ng concentration. As expected, GluA1 phosphorylation by PKAc at S845 (p845, blue) increases with decreasing Ng concentration. However, only for 10 Hz stimulation (Fig 5A) does the cumulative GluA1 phosphorylation remain relatively constant for all Ng concentrations.

Surprisingly, Ng KO caused phosphorylation at S845 to significantly increase at higher frequencies, whereas the decrease in S831 phosphorylation was relatively modest. It would appear that while competitive tuning could facilitate robustness to perturbations in Ng expression, the system tends to over-correct at early timescales in the absence of additional regulatory mechanisms.

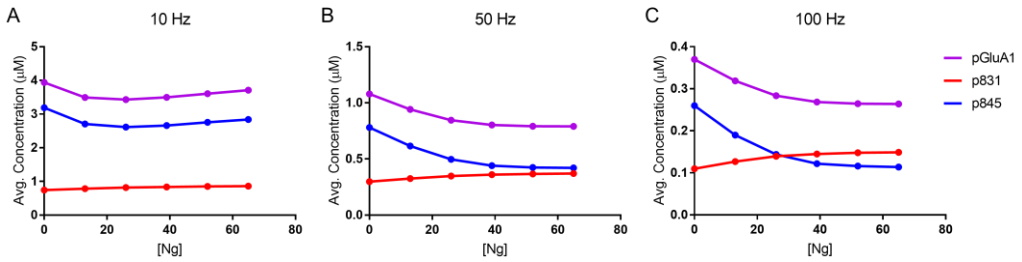

Figure 3.5. Phosphorylation of AMPAR GluA1 Subunits at S831 and S845. Time-averaged concentrations of total phosphorylation (pGluA1, purple), CaMKII-mediated phosphorylation at S831 (p831, red), and PKA-mediated phosphorylation at S845 (p845, blue) against Ng concentration. For each panel, the 4-state Ca^{2+}/CaM binding model was stimulated at either (A) 10 Hz, (B) 50 Hz, or (C) 100 Hz Ca^{2+} stimulation.

These results imply that high frequency stimulation such as those that elicit LTP (100 Hz) should be more easily attainable upon Ng KO. This result is consistent with Krucker *et al*. (2002), who showed that even though CaMKII activation/phosphorylation is reduced upon Ng KO, long-term potentiation can be achieved following stimulation by only a single 100Hz tetanus. Further, it is worth noting that for all Ca^{2+} frequencies presenting in Figure 3.5, shifts in overall pGluA1 levels with decreasing Ng concentration were largely negligible until Ng expression was reduced by more than half. Thus, it appears that the system is robust to modest perturbations to Ng expression, such as what might be seen in Ng heterozygous animals.

3.4 Conclusions

Competitive tuning is a recently-described phenomenon in which signaling molecules compete for binding of a common activator. Although others have either alluded to or invoked competition as being important in signal transduction [4, 24, 30, 211], my work shows that competition may play a larger role in informing signaling outcomes than previously thought. In this work I first compare a 2-state and 4-state model of competitive binding for Ca^{2+}/CaM and

determined that a 4-state model is best-suited to accurately detect the frequency dependence of a competitive CaM-CBP reaction network under dynamic stimulation. I also verify that expanding my 4-state model network to include an additional CBPs and downstream species preserves the overall competitive tuning phenomenon. I explore the functional implications of competitive tuning by using sensitivity analysis to identify the parameters most strongly correlated with a hallmark of synaptic plasticity, AMPAR GluA1 subunit phosphorylation. I further explore the implications of competitive tuning by building on a previous result showing that Ng KO counter-intuitively decreases CaMKII activation and autophosphorylation. Because competitive models indicate that Ng KO causes an increase in Ca^{2+}/CaM binding to AC8, I hypothesize that competitive tuning could provide a mechanism that compensates for a loss in CaMKII-mediated phosphorylation of GluA1 by promoting (via AC) PKA-mediated phosphorylation of GluA1. Indeed, in Figure 3.5 I observe that for high Ca^{2+} flux frequencies, Ng knockdown results in a switch between CaMKII and PKA in cumulative kinase activity.

Interestingly, stimulating at an LTP-inducing Ca^{2+} frequency of 100 Hz (Figure 3.5C) further causes an upregulation of GluA1 phosphorylation by PKA in the Ng KO case. This upregulation could explain results by Krucker *et al*. who observed that LTP could be elicited by just a single tetanus of stimulation at 100 Hz in brain slices of Ng KOs. Note that the current model includes both PP1- and CaN-dependent dephosphorylation of GluA1. Contrary to expectation, the combined action of PP1 and Ca^{2+}/CaM-dependent dephosphorylation by CaN seemingly did not dramatically decrease GluA1 phosphorylation levels in the presence of compensation facilitated by competitive tuning. Of course, other regulatory mechanisms could additionally be affecting GluA1 phosphorylation levels. For example, spatial localizations of proteins such as Ng and PP1, or perhaps A-kinase-anchoring proteins (AKAPs), could be required to increase, through avidity effects, the local concentrations of CaMKII, AC, and/or CaN in the dendritic spine. Alternatively, it may be required to analyze the reaction network presented here on longer timescales in order to discern the complete downstream effects of competitive tuning. As it currently stands, my current results are focused on short-term effects of Ca^{2+}-dependent signaling. Future work is needed to analyze longer term processes (e.g. receptor localization, other feedback mechanisms, receptor trafficking). It remains unclear whether increased GluA1 phosphorylation in Ng KO is an expected consequence of Ng perturbation and represents an example how competitive tuning can impart robustness to model outcomes across a wide range of Ng concentrations, or whether the

maintenance of GluA1 phosphorylation is a result of missing layers of model regulation. Future work will include these additional mechanisms of regulation and will explore other protein activation dynamics in GluA1 phosphorylation. A key prediction from my model that could be readily experimentally tested is that the relative level of phosphorylation of GluA1 at p845 would increase in Ng KO mice and phosphorylation of GluA1 at p831 would decrease.

3.5 Methods

Chemical reactions between species were written and converted to ordinary differential equations according to laws of mass action using the XCellerator package [212]. Mathematica was used to solve the differential equations using the NDSolve command. All other data analysis (including integration of species concentration over time and the LHS/PRCC sensitivity analysis) were performed in Mathematica (Wolfram Research, Mathematical version 11). Model output is plotted in the 2D graphing program GraphPad Prism (GraphPad, version 7).

Ca^{2+} stimulation was implemented as a boundary condition forcing function for the system of differential equations solved in Mathematica. To control for the magnitude of Ca^{2+} exposure from a single Ca^{2+} pulse, Ca^{2+} spike half widths are set to 5 msec regardless of frequency. To reduce computational complexity and control for the cumulative magnitude of Ca^{2+} exposure across all simulations, total magnitude of calcium flux is conserved at 100 pulses regardless of Ca^{2+} frequency.

All the equations for this model can be found in the Supplement to Chapter 3. Mathematica files for the complete models can be found on the Purdue PURR database: Pharris, M. C., Patel, N. M., Kinzer-Ursem, T. L. (2018). Competitive Tuning of Ca^{2+}/Calmodulin-Activated Proteins Provides a Compensatory Mechanism for AMPA Receptor Phosphorylation in Synaptic Plasticity. Purdue University Research Repository. doi:10.4231/R7ST7N11.

A global sensitivity analysis was used to investigate how variation in input parameter values contributed to variation in model output. Latin hypercube sampling (LHS) was used to efficiently sample input parameters over a range of values that were determined by experimental measurement or calculated by thermodynamic equilibrium (see Section *Model Parameterization* for a more in-depth discussion of model parameterization). In all variations of my sensitivity analysis, each parameter was sampled at least 250 times using values within 2-fold of each parameter's listed value (results available at [165]). Partial rank correlation coefficients were used

correlate the rank contribution of parameter variation on the variation in desired model output as described in my previous work [42, 184, 208]. I have previously shown that allowing the K_d of an interaction to vary by either varying the k_{on} or k_{off} (but not both simultaneously) produced similar results in the sensitivity analysis [208]. Therefore only association rate constants (k_{on}) and catalytic rate constants (k_p) were varied. PRCC analysis produces correlation factors over a range of 1 to -1, where 1 indicates perfect positive correlation and -1 indicates perfect negative correlation. In order to show the parameters whose variation most greatly impacted model output (total phosphorylation of GluA1 AMPAR subunits), a threshold PRCC value of absolute magnitude of 0.5 was used to generate the parameter list in Table 3.3.

4. COMPETITION FOR CALMODULIN BINDING REGULATES THE IN SILICO SPATIAL GRADIENTS OF DOWNSTREAM PROTEIN ACTIVATION IN THE DENDRITIC SPINE

4.1 Summary

Dendritic spines are small neuronal structures that dynamically shift in size and excitability in response to calcium ion (Ca^{2+}) influx. Depending on Ca^{2+} influx frequency, location, and other factors, the intracellular Ca^{2+} sensor calmodulin (CaM) differentially activates enzymes and other CaM-binding proteins (CBPs) that subsequently set the dendritic spine's size or excitability. For example, at high frequency Ca^{2+} flux CaM may activate kinases such as Ca^{2+}/CaM-dependent protein kinase II (CaMKII), while low frequency Ca^{2+} flux CaM may activate phosphatases such as calcineurin (CaN). Characterizing the molecular mechanisms regulating differential Ca^{2+}/CaM activation of CBPs may be essential to understanding Ca^{2+} signal transduction in the dendritic spine. Indeed, computational studies have shown using non-spatial frameworks how competition among CBPs for CaM binding is alone sufficient to recreate the observed Ca^{2+} frequency-dependence of many CBPs. However, the dendritic spine is highly spatially organized, which likely additionally influences the competitive environment. Therefore, here I present a computational model that describes competition for binding to Ca^{2+}/CaM among multiple explicitly-defined CBPs and downstream proteins in a spatial-stochastic framework. With this model, I quantify how competition and spatial effects co-regulate the dynamics of Ca^{2+}/CaM-dependent signaling. My results suggest that spatial effects alone are insufficient to set the Ca^{2+} frequency-dependence of CBP activation, and the frequency-dependence set by competition is mostly independent of spatial effects. Instead, spatial dependence of CBP activation and regulation of downstream proteins such as AMPA receptors (AMPARs) appears to be enhanced by competition. Notably, the spatial location of protein activation could be important to how Ca^{2+}-dependent signals are transduced. To explore this transduction, I use the spatial-stochastic model to explore the effects of adenylyl cyclase (AC) knock-outs on the spatiotemporal dynamics of Ca^{2+}/CaM and AMPAR phosphorylation. Interestingly, my results suggest how the adenylyl cyclase 8 (AC8) N-terminus may regulate the predominant states and locations of Ca^{2+}/CaM in the dendritic spine. This chapter will soon be submitted for publication. The co-authors include a number of undergraduates I have supervised: Neal Patel, who developed and parameterized the

model; Christopher Rust, who performed statistical analysis of the spatial gradient results; and Lakmini Wilson and Eva Yezeretz, who explored the effects of adenylyl cyclase knockouts.

4.2 Introduction

Synaptic plasticity, the process by which neuronal connections dynamically shift in size and connective strength, occurs within specialized neuronal structures called dendritic spines. Two long-studied outcomes of synaptic plasticity include long-term potentiation (LTP) and long-term depression (LTD), both of which are essential to healthy learning and memory formation. Both LTP and LTD depend on calcium ion (Ca^{2+}) flux through N-methyl-D-aspartate glutamate receptors (NMDARs), and the magnitude and timing of these excitatory changes are regulated by Ca^{2+}-dependent signaling pathways [3]. Dysregulation of Ca^{2+} signaling pathways disrupts synaptic plasticity within dendritic spines, putatively leading to disorders as wide ranging as Alzheimer's disease and epilepsy [1, 213]. To better understand neuronal Ca^{2+} signaling and its regulation of downstream proteins, experimental techniques such as genetic knock-down and super-resolution microscopy are frequently used [5, 6, 214]. However, experimental techniques lack the spatiotemporal resolution needed to characterize precise regulatory mechanisms within the dendritic spine. The dendritic spine's volume (femtoliters) and the molecular concentrations therein (micromolar) produce a highly stochastic environment in which signaling events also occur on small timescales (microseconds) [185]. Therefore, to complement experimental techniques, computational models are increasingly used to help characterize signaling mechanisms in synaptic plasticity (reviewed in [215]). In the computational model presented here I explore how the Ca^{2+} signaling pathways involved in synaptic plasticity induction may be regulated by spatial and stochastic effects.

A dendritic spine's response to NMDAR-mediated Ca^{2+} influx is determined by many factors. The frequency, magnitude, duration, location, and pattern of Ca^{2+} flux each contribute to how Ca^{2+} sensor proteins, namely calmodulin (CaM), integrate and transduce Ca^{2+} signals [23, 216, 217]. For example, high frequency and short-term Ca^{2+} flux (100Hz, 1sec) classically elicits LTP in hippocampal neurons, in-part due to heightened activation of Ca^{2+}/CaM-dependent protein kinase II (CaMKII) [29, 218, 219]. In contrast, low frequency and longer-term Ca^{2+} flux (1Hz, many minutes) classically elicits LTD, in-part due to heightened activation of Ca^{2+}/CaM-dependent enzymes such as phosphodiesterase 1 (PDE1) and the phosphatase calcineurin (CaN)

[3, 4, 24, 186, 220, 221]. Importantly, LTP is not solely dependent on kinase activity, and LTD is not solely dependent on phosphatase activity. Indeed, CaMKII activation has been shown to be involved in LTD promotion, and a separate study suggests that CaN contributes to LTP [80, 222]. It may therefore be necessary for computational models to explicitly account for CaMKII and CaN in addition to many other downstream CaM-binding partners (CBPs). Explicitly accounting for multiple CBPs highlights the fact that the concentration of CBPs in the dendritic spine (tens of micromolar each) cumulatively exceeds that of CaM (33 μM), resulting in competition for Ca^{2+}/CaM binding [46]. Thus, in addition to factors such as Ca^{2+} influx frequency, competition for Ca^{2+}/CaM may further regulate, or tune, the activation of CBPs.

Competition for Ca^{2+}/CaM appears in previous computational models [30, 211, 221], but few expressly aim to quantify the effect of competition on CBP activation. Some models implicitly create competition by including a generalized CaM-buffering species, though such implicit models obscure how the activation of specific CBPs may depend on competition [92, 185]. Alternatively, some models account for competition by explicitly defining multiple CBPs, though these models often restrict the competitive pool to only two or three CBPs and focus on other regulatory mechanisms [24, 33, 211]. Romano *et al*. (2017) was the first model aiming to quantify the effect of competition on the Ca^{2+} frequency-dependence of multiple (eight) explicitly-defined CBPs [46]. Romano *et al*. found that in a deterministic model void of spatial parameters or feedback mechanisms, competition alone could recreate the *in vivo* Ca^{2+} frequency-dependence of CBP activation. For example, whereas an isolated model of Ca^{2+}, CaM, and CaN alone predicts maximal activation of CaN at high Ca^{2+} frequencies (>100Hz), a competitive model of Ca^{2+}, CaM, CaN, and seven other CBPs predicts a maximal activation of CaN at low Ca^{2+} frequencies (1-10Hz), which is consistent with experimental observations [104, 220]. Pharris *et al*. (2018) extend upon the work by Romano *et al*., adding the CBP PDE1, as well as a variety of downstream proteins including protein kinase A (PKA), protein phosphatase 1 (PP1), and AMPA receptor (AMPAR) GluA1 subunits. The deterministic model by Pharris *et al*. examines how competitive tuning, in the presence of feedback mechanisms, regulates downstream signaling events relevant to synaptic plasticity [165].

In addition to feedback mechanisms, spatial effects may further regulate the effect of competitive tuning. Because Ca^{2+} ions flux through NMDARs at the top of a spine, the diffusion of Ca^{2+} may lead to spatial gradients of Ca^{2+} and Ca^{+}/CaM along the major axis of the dendritic

spine [41, 185]. Moreover, these spatial gradients may be enhanced by CaM-buffering proteins such as the membrane-associated protein neurogranin (Ng), which distinctly binds apo-CaM in the absence of Ca^{2+} [155, 204]. Additionally, spatial gradients may also be set by interactions with cytosolic proteins such as PSD-95 or synGAP, which are major components of a membrane-less organelle located at the intracellular synaptic membrane called the post-synaptic density (PSD) [37, 223]. The observed localization of CBPs motivates my hypothesis that competition regulates the location of CBP activation within the dendritic spine. Therefore, I aim to quantify how competition and spatial effects co-regulate the frequency-dependence and localization of CBPs. By quantifying this co-regulation in a computational model, it may also be possible to characterize how localized CBPs could subsequently transduce signals to downstream CBP-dependent pathways. Indeed, characterizing CBP-dependent protein localizations could help elucidate how downstream signaling leads to various outputs such as changes in protein expression [224, 225], post-translational modifications [226, 227], or molecular trafficking [228].

In this work, I again adopt the view of Romano *et al.* that CaM is a limiting resource in the dendritic spine and that competition for CaM in-part tunes the selection of CBPs by Ca^{2+}/CaM. I also adapt the previous work by Pharris *et al*. (2018) to explicitly account for downstream signaling events, in particular the phosphorylation of AMPARs by CaMKII and PKA. In contrast to these previous deterministic and non-spatial models, here I use the software MCell to implement a spatial-stochastic model of Ca^{2+} flux, 9-state CaM activation, nine explicitly-defined CBPs, and CBP-mediated downstream signaling [229]. In my spatial-stochastic model, I again find that competition alone may be sufficient to set the Ca^{2+} frequency-dependence of CBP activation by CaM. Also, I find that many CBPs exhibit robust spatial gradients of activation at multiple Ca^{2+} frequencies. Interestingly, although the spatial gradients do not seem to require competition, competition for CaM-binding consistently increases spatial gradient steepness. Importantly, increased steepness in the spatial gradient of a CBP's activation may support the localization of a CBP's downstream effectors. For example, I show evidence that spatial gradients of CaMKII activation sets gradients of phosphorylation at the AMPAR GluA1 subunit residue Ser-831 (GluA1-p831). However, I do not observe spatial gradients of GluA1 phosphorylation at residue Ser-845 (GluA1-p845), which is mediated by PKA, despite consistent formation of spatial gradients of AC isoforms. Therefore, I finally simulate the effect of various AC isoform knockouts on GluA1-p845. My results suggest a role for the AC8 N-terminus (AC8-Nt) as a regulator of the

distribution of Ca^{2+}/CaM states in the dendritic spine. Ultimately, this work provides a framework for quantifying how competition and space co-regulate protein activation during synaptic plasticity induction.

4.3 Results

4.3.1 Model Development

4.3.1.1 Model Structure

The spatial-stochastic model presented in this study is created with the open-source software MCell and its complementary Blender plug-in called CellBlender [185, 230]. I use CellBlender to approximate the geometry of a single dendritic spine, and with this geometry I use MCell to simulate the diffusion and interactions of individual molecular species. The molecular species, mostly proteins, are shown in Figure 4.1 and described in Model Parameterization. With this setup, the input to my model is the frequency of NMDAR-mediated Ca^{2+} flux. Although the magnitude, location, and patterning of Ca^{2+} flux may influence the selection of distinct CBPs by Ca^{2+}/CaM, these parameters are held constant throughout all simulations in order to observe differences in signaling as a function of Ca^{2+} frequency alone.

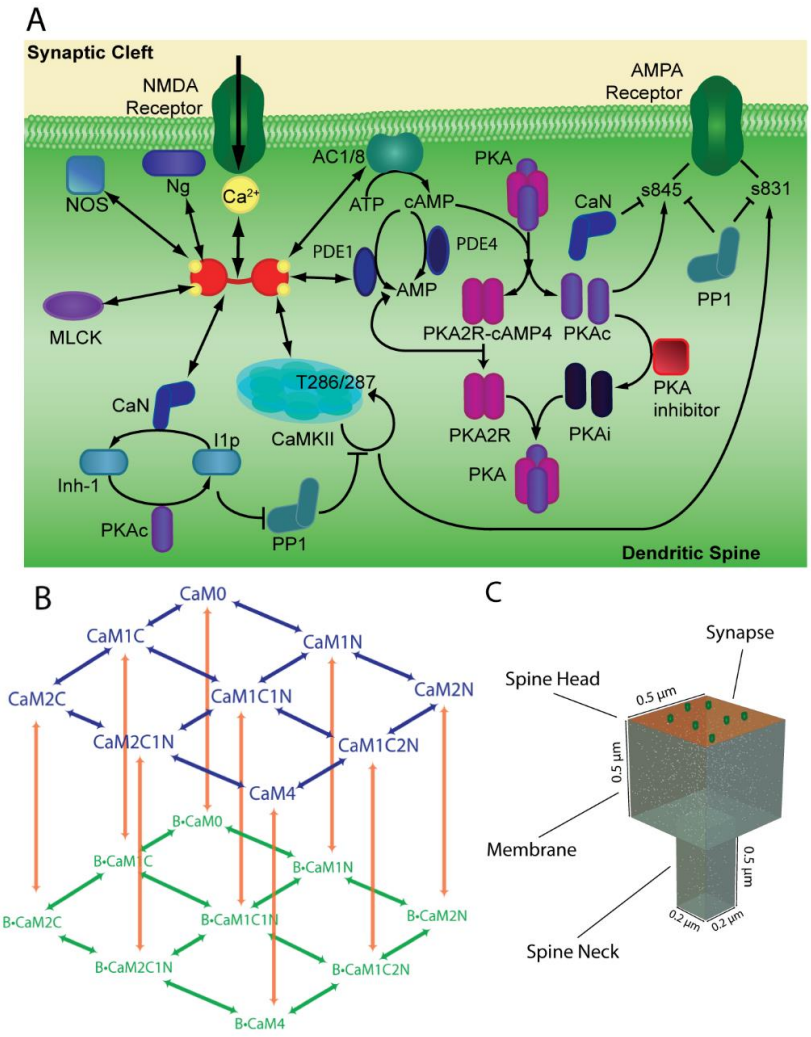

Figure 4.1. Model reaction networks and simulation framework. (A) The complete reaction network of NMDAR-mediated Ca^{2+} flux, Ca^{2+} binding to CaM, Ca^{2+}/CaM activation of CBP's, and CBP-mediated downstream pathways regulating AMPAR phosphorylation at Ser-831 and Ser-845. (B) Nine-state Ca^{2+}/CaM activation. Ca^{2+} reversibly binds CaM (blue), Ca^{2+}/CaM reversibly binds CBP's (denoted 'B') (orange), and Ca^{2+} also reversibly binds CaM-CBP's (green). (C) Model dendritic spine constructed using CellBlender.

In my model, intracellular Ca^{2+} binds exclusively the Ca^{2+} sensor protein CaM. CaM has two globular EF-hand domains, one at the N- and C-terminus, and each domain cooperatively binds up to two Ca^{2+} [15]. Interestingly, sub-saturated Ca^{2+}/CaM states (with fewer than four Ca^{2+} bound) may predominate and exhibit non-negligible binding affinities for CBPs, as suggested in experiments by Shifman *et al.* [97] and as-modeled first by Pepke *et al.* (2010) [42]. Pepke *et al.*

present two models of Ca^{2+}/CaM activation: a coarse four-state model and a detailed nine-state model. The four-state model assumes that due to cooperativity, the binding of 2 Ca^{2+} to each CaM terminus can be modeled as a single event. In contrast, the nine-state model explicitly accounts for individual Ca^{2+}-CaM binding events and is thus thermodynamically complete [208]. The four-state model is relatively simple and more convenient compared to the nine-state model, and it may be appropriate for use depending on a study's timescales of interest or simulation framework. For example, Romano *et al*., using a deterministic framework of ordinary differential equations, compare the utility of a four- versus nine-state model of Ca^{2+}/CaM in a competitive scenario [46]. The results of Romano *et al*. suggest that for their analysis, there is little difference in output for the four- and nine-state models, and they therefore defer to the simpler four-state model. Pharris *et al*., using a similar deterministic framework, also utilize the four-state model [165]. However, for the present study the four-state model is inappropriate because the spatial-stochastic, particle-based framework in MCell causes trimolecular reactions to exhibit unrealistically small probabilities (MCell developers encourage use of bimolecular reactions only—see mcell.org). Consequently, the model presented here utilizes a nine-state model of Ca^{2+}/CaM activation (Figure 4.1B).

4.3.1.2 Model Parameterization

The initial concentrations and kinetic parameters, listed in the Supplement to Chapter 4, are all adopted from previous literature [21, 33, 42, 46, 165]. The majority of these parameters are based on experimental measurements. Kinetic parameters not measured experimentally, such as affinities of Ca^{2+} for sub-saturated Ca^{2+}/CaM or of sub-saturated Ca^{2+}/CaM for CBPs, are determined using the thermodynamic principle of microscopic reversibility [42, 208], the definition of the dissociation constant ($K_D = k_{off}/k_{on}$), and two biophysical assumptions.

First, I assume that the affinity of Ca^{2+} for CaM increases upon CaM-binding to a CBP [20], and this increase in affinity is primarily due to a reduction in the Ca^{2+} dissociation rate constant [58]. Second, I assume that because Ca^{2+}-binding to CaM induces structural changes that stabilize CaM and expose its hydrophobic patches [14, 231], Ca^{2+}-binding to CaM increases the association (but not dissociation) rate constant of CaM to a CBP. These assumptions are discussed in detail by Romano *et al*. [46].

MCell uses a Monte Carlo algorithm to approximate the Brownian motion of molecules in space. Diffusion coefficients for all molecular species, listed in Table 4.1 and Table 7.6, are adapted from experimental measurements or calculated using the Stokes-Einstein relation (see the Supplement to Chapter 4). The Stokes-Einstein relation describes a molecule's diffusion coefficient as a function of its hydrodynamic radius. If I assume that proteins in solution are roughly spherical and that hydrodynamic radius is proportional to molecular weight, I can approximate diffusion coefficients for unmeasured proteins and for all protein-protein complexes in my model [232, 233].

Table 4.1. Model protein classifications and initial localizations.

Protein/Molecule	**Class**	**Diffusion Coeff. (cm^2/s)**	**Localization**
Calcium (Ca^{2+})	Stimulator	3.55e-6	Cytosol
Calmodulin (CaM)	Stimulator	8.48e-9	Cytosol
Adenylyl Cyclase 1 (AC1)	CBP (Enzyme)	2.41e-9	Spine membrane
Adenylyl Cyclase 8 (AC8)	CBP (Enzyme)	1.89e-9	Spine membrane
Calcineurin (CaN)	CBP (Enzyme)	1.83e-9	Cytosol
Ca^{2+}/CaM-dependent Kinase II (CaMKII subunit)	CBP (Enzyme)	2.5e-10	Cytosol
Myosin Light Chain Kinase (MLCK)	CBP	6.76e-10	Cytosol
Neurogranin (Ng)	CBP	8.14e-9	30% spine membrane; 70% cytosol [112]
Nitric Oxide Synthetase (NOS)	CBP	9.19e-10	Spine membrane
Phosphodiesterase 1 (PDE1)	CBP (Enzyme)	3.39e-9	Cytosol
AMPA Receptor (AMPAR)	CBP-dependent	4.45e-10	Spine membrane
Cyclic Adenosine Monophosphate (cAMP)	CBP-dependent	4.33e-7	Cytosol
Inhibitor 1 (Inh-1)	Downstream	7.5e-9	Cytosol
Protein Kinase A (PKAc)	Downstream	3.75e-9	Cytosol
Protein Phosphatase 1 (PP1)	Downstream	3.8e-9	Cytosol
Phosphodiesterase 4 (PDE4)	Downstream	2.1e-9	Cytosol

4.3.1.3 Model Stimulation

The input to every model simulation is NMDAR-dependent Ca^{2+} flux at a particular frequency. In this model, NMDAR receptors are surface molecules constrained to the synaptic membrane at the top of the model geometry. All other components of Ca^{2+} flux, such as magnitude

and the inter-spike intervals (patterning), are held uniform regardless of Ca^{2+} frequency as described in Methods. In short, Ca^{2+} influx is controlled in MCell according to time-dependent variables informing the forward rate of the reactions $NMDAR \rightarrow NMDAR + Ca^{2+}$ and $Ca^{2+} \rightarrow NULL$. The combined effect of these reactions is to produce global free Ca^{2+} dynamics obeying the equation $[Ca](t)=12e^{-t/0.012}$ as used by Romano *et al.*

4.3.1.4 Calmodulin-binding proteins

CBPs in this model are the set of eight proteins (nine CaM binding sites) which directly compete for and reversibly bind CaM. CBPs are here classed as either enzymatic or non-enzymatic.

Enzymatic CBPs include AC1, AC8 (C-terminus; AC8-Ct), CaN, CaMKII, and PDE1. AC1 and AC8 are membrane-associated which, when activated upon Ca^{2+}/CaM-binding, catalytically generate cAMP [191]. Note that only the C-terminus, and not the N-terminus, of AC8 exhibits Ca^{2+}/CaM-dependent catalysis [193]. CaN is a serine/threonine phosphatase which, when activated upon Ca^{2+}/CaM binding, de-phosphorylates CaMKII, Inhibitor 1 (Inh-1), and AMPAR GluA1 subunits [33, 199, 234]. CaMKII is a homomeric holoenzyme consisting of twelve identical catalytic subunits arranged in two directly-apposed, symmetric rings [3]. However, for simplicity I here model CaMKII as monomers, which activate only upon binding by Ca^{2+}/CaM. In addition to CaMKII activation, I account for CaMKII auto-phosphorylation at Thr-286 according to the mechanism described by Pepke *et al*. (see Figure 6 in [42]) [46, 218]. Auto-phosphorylated CaMKII monomers remain active even in the absence of bound CaM. Finally, PDE1 is a phosphodiesterase which, upon Ca^{2+}/CaM binding, catalytically converts cAMP into AMP [21]. Note that for all enzymatic CBPs, catalytic rate parameters are adapted from literature where available. Any un-measured catalytic rates, such as those for CBPs bound to sub-saturated Ca^{2+}/CaM, are assumed to scale identically to the ratio of catalytic rates for sub-saturated Ca^{2+}/CaM-CaMKII to fully-saturated Ca^{2+}/CaM_4-CaMKII (calculated by Pepke *et al*. and used by Romano *et al.* and Pharris *et al*.). Consequently, each CBP's catalytic activity is greatest when activated by fully-saturated CaM_4.

Non-enzymatic CBPs in this model include AC8 (N-terminus; AC8-Nt), Myosin Light Chain Kinase (MLCK), Neurogranin (Ng), and Nitric Oxide Synthetase (NOS). Note that although MLCK and NOS are in fact enzymes *in vivo*, the model presented here does not account for their downstream enzymatic activity. Note also that I model the N- and C-termini of AC8 on the same

particle in MCell, though I reiterate that only AC8-Ct catalyzes ATP into cAMP. Explicitly accounting for both AC8 termini is important to the AC isoform knockouts I explore at the end of this paper. Furthermore, it is important to include these non-enzymatic CBPs because they enhance the competitive environment for CaM binding.

4.3.1.5 CBP-dependent downstream signaling

Activated CBPs initiate downstream signaling pathways Figure 4.1. Here, I focus on pathways leading to AMPAR GluA1 subunit phosphorylation, a hallmark of synaptic plasticity. For example, CaM-activated AC1 and AC8-Ct both generate cAMP, which subsequently binds either CaM-PDE1 or PKA [207]. PKA binds up to four cAMP, and fully-saturated PKA (PKA_4), may disassemble yielding 2 catalytic PKA (PKA_c) subunits. PKA_c binds the generic target PKA Inhibitor (PKA_I), and it also may phosphorylate GluA1 subunits (at Ser-845) and Inh-1 [32, 209]. Inh-1 phosphorylated at Ser-35 (I_{p35}) may bind and inhibit the phosphatase PP1. Note that PKA_c has one catalytic rate per substrate, each adopted from previous literature.

The CBPs CaN and CaMKII also regulate GluA1 phosphorylation. Active CaMKII phosphorylates GluA1 at Ser-831 [196]. Active CaN and PP1 may de-phosphorylate GluA1 at either Ser-831 or Ser-845 [33]. Active CaN additionally may also bind and de-phosphorylate $I_{p35.}$ All kinetic rate constants for these pathways are taken directly from literature. Note that PP1 has one catalytic rate per substrate, each adopted from previous literature.

4.3.2 Model Validation

I first quantify any differences in global CaM activation between my nine-state spatial-stochastic model and its deterministic equivalent. The nine-state deterministic model is implemented using the software Mathematica. For both the deterministic and spatial-stochastic models, I allow the model system to equilibrate for 10 sec of simulation time prior to initiating Ca^{2+} flux. Ca^{2+} flux begins at t=10 sec, proceeding at 10 Hz of evenly-spaced Ca^{2+} peaks for an additional 10 sec (a total of 100 Ca^{2+} pulses). Each panel in Figure 4.2 monitors a distinct Ca^{2+}/CaM state (whether CBP-bound or -unbound) as a function of time for both the deterministic and spatial-stochastic models. In comparison, the deterministic and spatial-stochastic models respond to 10 Hz Ca^{2+} flux very similarly, suggesting that fundamental model behavior is preserved when implemented in a spatial-stochastic framework.

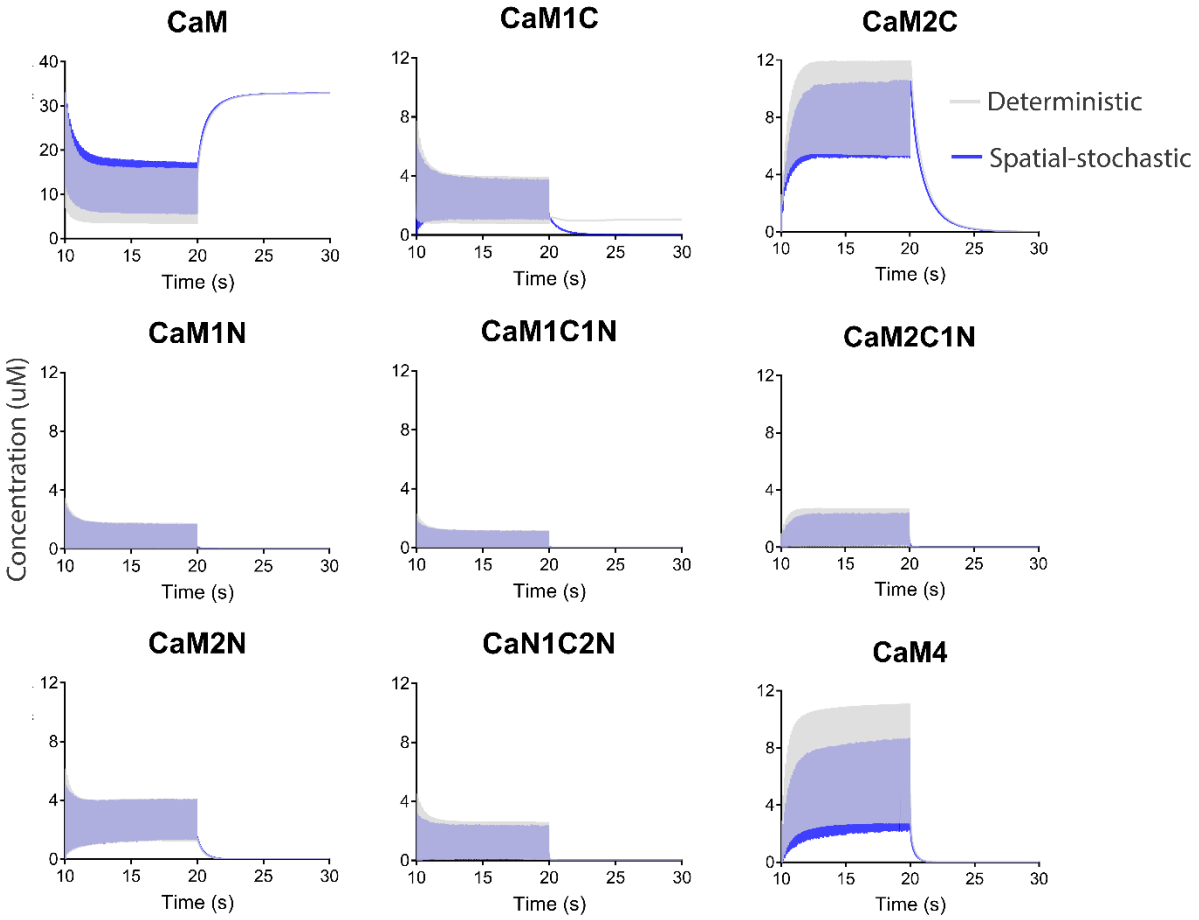

Figure 4.2. Ca^{2+}/CaM states in deterministic versus spatial-stochastic frameworks. Ca^{2+}/CaM activation for 10 Hz Ca^{2+} flux in deterministic (grey) and spatial-stochastic (blue) frameworks. Spatial-stochastic traces are the averaged output representative of N=50 executions. For the same comparison at 100 Hz Ca^{2+} flux, see Figure 7.5.

Comparing 10 Hz (Figure 4.2) and 100 Hz (Figure 7.5) Ca^{2+} flux reveals considerable differences in levels of various Ca^{2+}/CaM states as a function of Ca^{2+} frequency. For example, apo-CaM (top left panel) is much more dynamic and on time-average more abundant under 10 Hz than 100 Hz Ca^{2+}. The same is also true, although to a lesser extent, for the CaM_{1C} and CaM_{1N} states. Note that apo-CaM, CaM_{1C}, and CaM_{1N} have relatively high affinities for CBPs that are conventionally LTD-associated such as CaN. Also, CaM_4 (bottom right panel) is on time-average much less abundant under 10 Hz compared to 100 Hz Ca^{2+}, and note that CaM_4 has a high affinity for CBPs that are conventionally LTP-associated such as CaMKII. Finally, in addition to CaM_4,

CaM_{2C} is a highly predominant Ca^{2+}/CaM state, especially at 100 Hz Ca^{2+} flux, consistent with previous results [42, 45]. Taken together, I interpret these results as consistent with experimental observations [20, 97, 188, 189].

Having benchmarked my spatial-stochastic model against its deterministic equivalent, as a further validation I next ask how spatial and stochastic effects impact the global frequency-dependence of CBP activation. To compare CBP activation at distinct Ca^{2+} frequencies, I use a metric also utilized by Romano *et al.* [46]. This metric, denoted C_b, describes the normalized time-averaged active concentration of a particular CBP ('b') at a particular Ca^{2+} frequency. I calculate C_b for each CBP and display this as a function of Ca^{2+} frequency for the deterministic (Figure 4.3A) and spatial-stochastic models (Figure 4.3B). Comparing Figure 4.3A and Figure 4.3B reveals that the Ca^{2+} frequencies of peak CBP activation are similar in both the deterministic and spatial-stochastic frameworks. The slight differences, perhaps most notably for CaN and PDE1, are attributed to the fact that CaN and PDE1 are expressed at very low concentrations and thus susceptible to stochastic effects. That is, because fewer than 50 total particles of CaN are instantiated in each spatial-stochastic execution, the relative levels of CaN activation are highly variable even when averaged over many (N = 50) equivalent executions. Despite such variability, CaN exhibits peak activation at relatively low Ca^{2+} frequencies (~20 Hz) in Figure 4.3B, roughly consistent with the deterministic results (Figure 4.3A) and its putative role in LTD. Similarly, other proteins such as CaMKII exhibit peak activation at high Ca^{2+} frequencies (about 100 Hz), consistent with the known importance of CaMKII to LTP [27]. Overall, my results in Figure 4.3 further suggest that my model output is biophysically realistic.

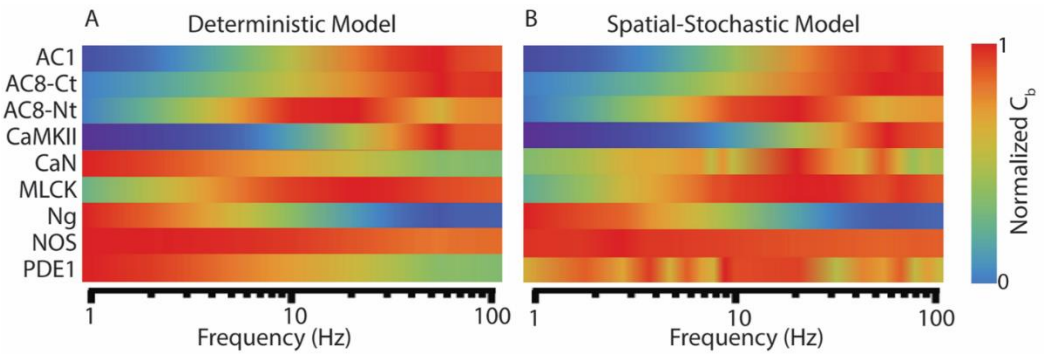

Figure 4.3. Ca^{2+} frequency-dependence of CBP activation. (A) and (B) show relative levels of CBP activation by Ca^{2+}/CaM as a function of Ca^{2+} frequency for a deterministic and spatial-stochastic framework, respectively. Red denotes maximal CBP activation, and blue denotes minimal CBP activation. Heatmap rows pertain to a particular CBP, and the horizontal axis is Ca^{2+} frequency on a logarithmic scale. Spatial-stochastic results are the averaged output of N=50 executions.

4.3.3 Competition steepens spatial gradients of CBP activation

MCell provides a framework to monitor the spatial locations of Ca^{2+}/CaM and CBP activations. Others use MCell similarly, namely Keller *et al*. (2008) who model Ca^{2+} buffering in the dendritic spine [185]. With their MCell model, Keller explores how Ca^{2+} channel positions, Ca^{2+} patterning, and initial localizations of CaM influence the spatial distributions of Ca^{2+}/CaM states within the dendritic spine. Their results show a predomination of CaM_{2C} that becomes even more exaggerated when CaM is artificially localized to the PSD, suggesting that the location of CaM in the spine can influence its state. Building on this previous work, my model's addition of multiple explicitly-defined CBPs allows me to determine if spatial dependence of Ca^{2+}/CaM states subsequently influences the spatial dependence of CBPs and CBP-dependent proteins.

Therefore, I explore how different Ca^{2+}/CaM states may exhibit both spatial and temporal dynamics. To monitor Ca^{2+}/CaM states in space, I construct three equal-volume compartments in my model of the dendritic spine (Figure 4.4C). The compartments are used to monitor model proteins in the top (purple), middle (yellow), and bottom (red) of the dendritic spine. All proteins can freely move between each compartment. Each compartment monitors total levels of both cytosolic (units of concentration) and membrane-bound (units of density) proteins, so I report model output in terms of total number of protein particles in each compartment.

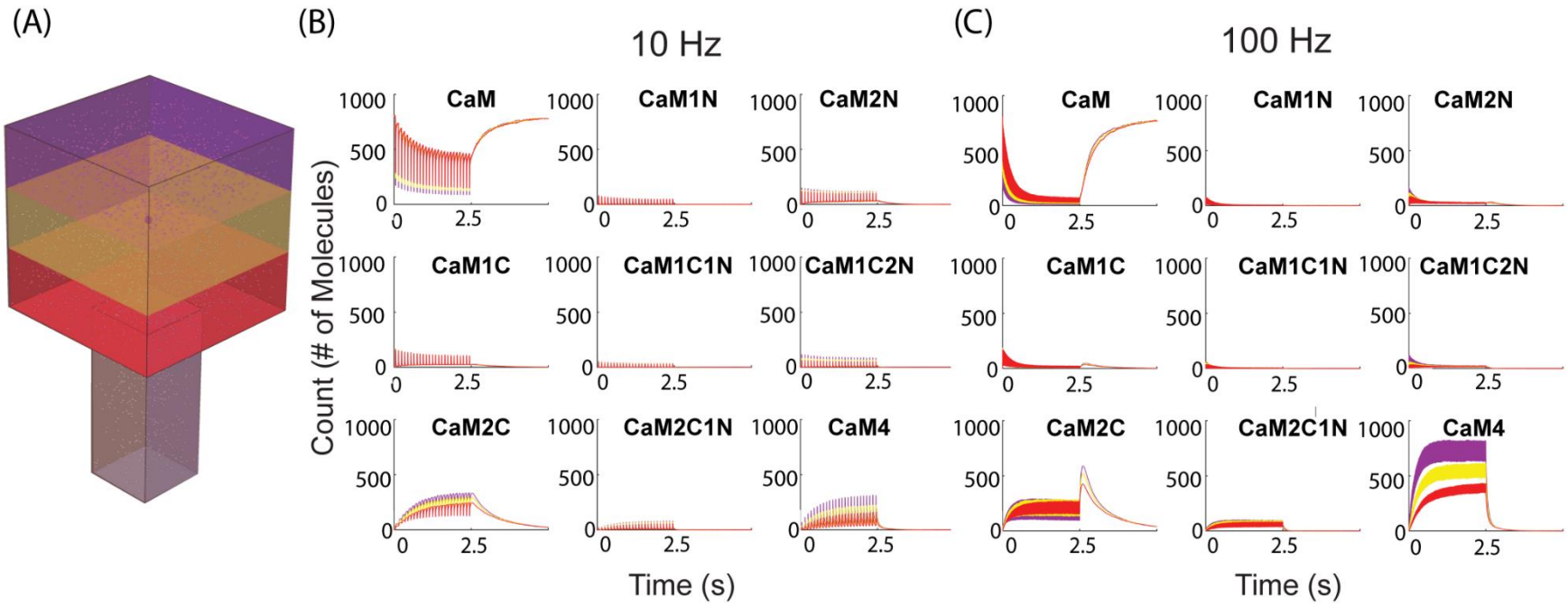

Figure 4.4. Ca^{2+}/CaM states at distinct spatial locations. (A) Equal-volume compartments arranged along the major axis of the dendritic spine, each monitoring protein counts at the top (purple), middle (yellow), or bottom (red) regions. (B) CBP-bound Ca^{2+}/CaM states in each compartment as a function of time under 10 Hz Ca^{2+} flux. (C) CBP-bound Ca^{2+}/CaM states in each compartment as a function of time under 100 Hz Ca^{2+} flux. Each trace is the average of N=50 executions.

For Figure 4.4B and Figure 4.4C, I simulate my model at 10 Hz and 100 Hz Ca^{2+} flux, respectively, and monitor each Ca^{2+}/CaM state bound to a CBP in each compartment. I observe that all bound Ca^{2+}/CaM states exhibit spatial dependence, in which the numbers of a particular state in each compartment are almost always different. For example, apo-CaM (top left panels) exhibits spatial dependence during Ca^{2+} flux regardless of Ca^{2+} frequency. Specifically, apo-CaM is always most abundant in the bottom (red) compartment, which is reasonable because that compartment is furthest from the site of Ca^{2+} flux. CaM_{2C} and CaM_4 also exhibit clear spatial dependence, even at 10Hz Ca^{2+} flux. At 100Hz Ca^{2+} flux, CaM_4 exhibits such strong spatial dependence that its traces (Figure 4.4C bottom-right panel) never overlap during stimulation, which I regard as a fully-developed spatial gradient. My observation of spatial dependence and spatial gradients among Ca^{2+}/CaM states at multiple Ca^{2+} frequencies may suggest that distinct CBPs may be activated at distinct locations within the spine.

I next explore whether the spatial dependence of Ca^{2+}/CaM states observed in Figure 4.4 is transduced as spatial locations of active CBPs and how localization may influence Ca^{2+} frequency-dependence of CBP activation. For this, I compare my standard, or "competitive", version of the model against a non-competitive, or "isolated", version. The competitive model contains Ca^{2+}/CaM and all nine CBPs simultaneously competing for CaM-binding, whereas the isolated models contain Ca^{2+}/CaM and only one of the respective CBPs. In Figure 4.5, I compare these model versions to quantify how competition sets CBP activation (using the C_b metric) as a function of Ca^{2+} frequency in each compartment of the model dendritic spine.

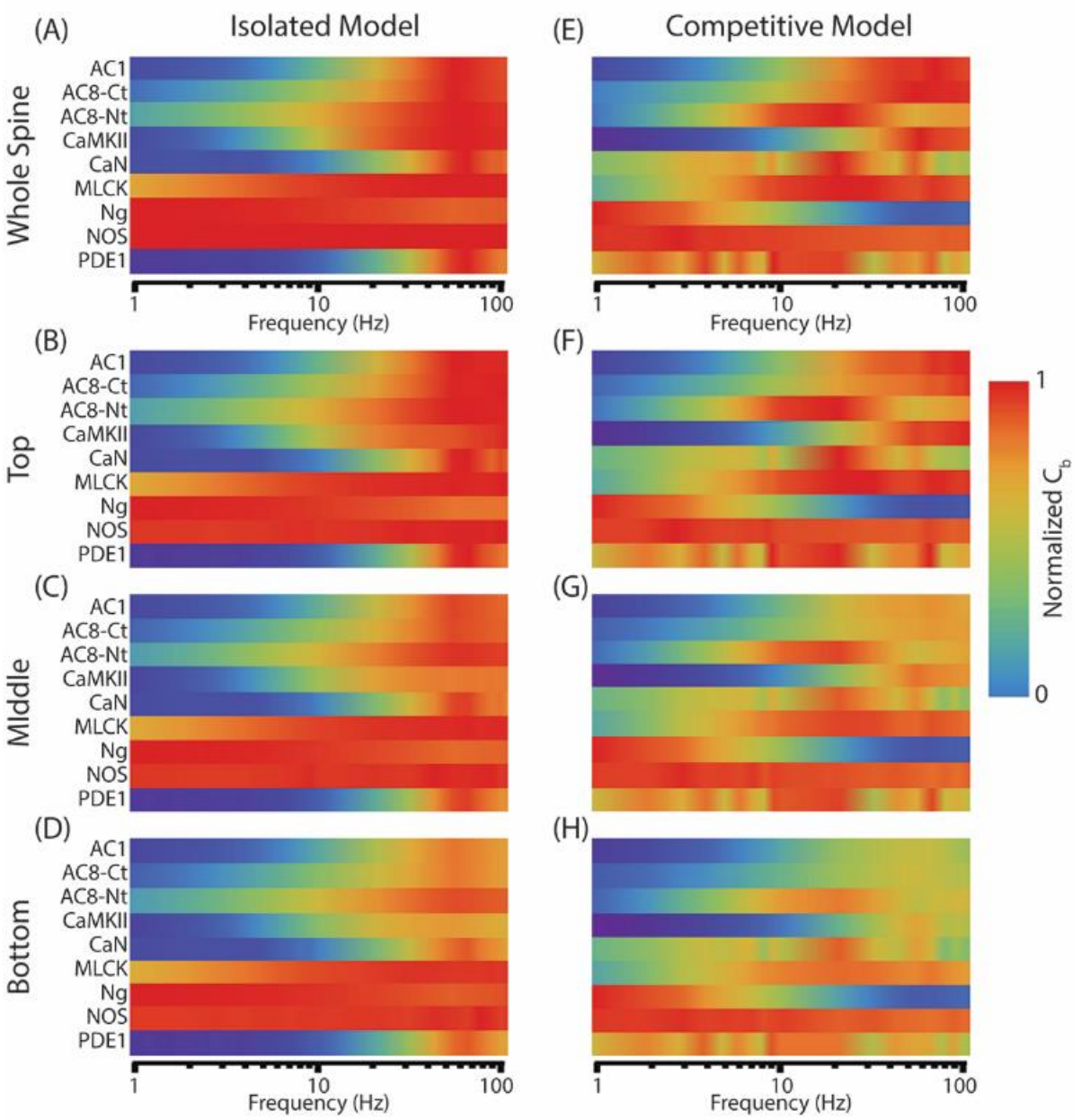

Figure 4.5. Spatial gradients of CBP activation are regulated by competition. (A) and (E) show normalized global activation of CBPs time-averaged over the entire dendritic spine geometry as a function of Ca^{2+} frequency for the isolated and competitive models, respectively. (B-D) show the normalized compartmental activation of CBPs in isolated model. (F-H) show the normalized compartmental activation of CBPs in the competitive model. Red denotes peak activation; blue denotes minimal activation. All data points are the average of N=50 executions.

First, I compare the isolated and competitive versions of my spatial-stochastic model "globally"; for Figure 4.5A and Figure 4.5E, C_b values are calculated for each CBP and then plotted as a function of Ca^{2+} frequency. The global-isolated model (Figure 4.5A) predicts most CBPs to be preferentially activated at relatively high (>50 Hz) and broad ranges of Ca^{2+} frequencies. In contrast, the global-competitive model (Figure 4.5E; identical to Figure 4.3B) predicts CBPs to be activated at distinct and relatively narrower Ca^{2+} frequencies. Indeed, just as in the deterministic-competitive model (Figure 4.3A), the spatial-competitive model predicts CaN to be most active at relatively low Ca^{2+} frequencies, unlike the isolated models. These results further indicate that, even in a spatial-stochastic environment, competition remains an emergent property that seems to tune the Ca^{2+} frequency-dependence of CBPs.

Second, I compare the isolated and competitive versions of my spatial-stochastic model "compartmentally". For this, I calculate C_b values for each CBP in only the top (Figure 4.5 B and F), middle (Figure 4.5 C and G), or bottom (Figure 4.5 D and H) compartments of the dendritic spine. Notably, the C_b-frequency heat-band for a particular CBP in these panels is normalized to itself and also across spine compartments. This compartmental normalization helps convey how C_b's vary with Ca^{2+} frequency in addition to spatial location. The compartmental-isolated results (Figure 4.5B-D) reveal similar Ca^{2+} frequency-dependence compared to the global-isolated results. Similarly, the compartmental-competitive results (Figure 4.5F-H) also reveal similar Ca^{2+} frequency-dependence compared to the global-competitive results. However, peak C_b values are highest in the top compartment for both the isolated and competitive models. C_b peaks appear to decline with increasing distance from the top compartment, which is reasonable given that the Ca^{2+} source is at the top compartment. Notably, this decrease in C_b magnitude is much more apparent in the competitive model. Overall, these results indicate that spatial effects alone do not elicit physiological Ca^{2+} frequency-dependence of CBP activation, and the Ca^{2+} frequency-dependence set by competition for CaM is largely independent of spatial effects. However, because the decrease in C_b with increasing distance from the Ca^{2+} source is greater in the competitive model, it appears that competition may sharpen possible spatial gradients of activation for certain CBPs.

Spatial gradients of CBP activation may influence the localization of CBP-dependent proteins downstream. For example, I hypothesize that spatial gradients of active CaMKII might lead to gradients of phosphorylated CaMKII (pCaMKII) or AMPARs phosphorylated by CaMKII

at Ser-831 ($GluA1_{p831}$). Similarly, gradients in AC1 or AC8 might elicit gradients in catalytically-active PKA_c, and perhaps subsequently set gradients of AMPARs phosphorylated by PKA at Ser-845 ($GluA1_{p845}$). Given the results in Figure 4.5, these hypothetical gradients of downstream protein states might only occur, or perhaps become exaggerated, in a competitive CaM-binding environment. Because these hypothetical gradients could be dynamic, I forgo the time-averaging C_b metric and return to time-dependent plots of protein states. In Figure 4.6 and Figure 4.7, I monitor CaMKII-relevant and AC-relevant protein states, respectively, in response to 100 Hz Ca^{2+} flux and in each spine compartment. Equivalent plots of protein states in response to 10 Hz Ca^{2+} flux are found in the Supplement to Chapter 4.

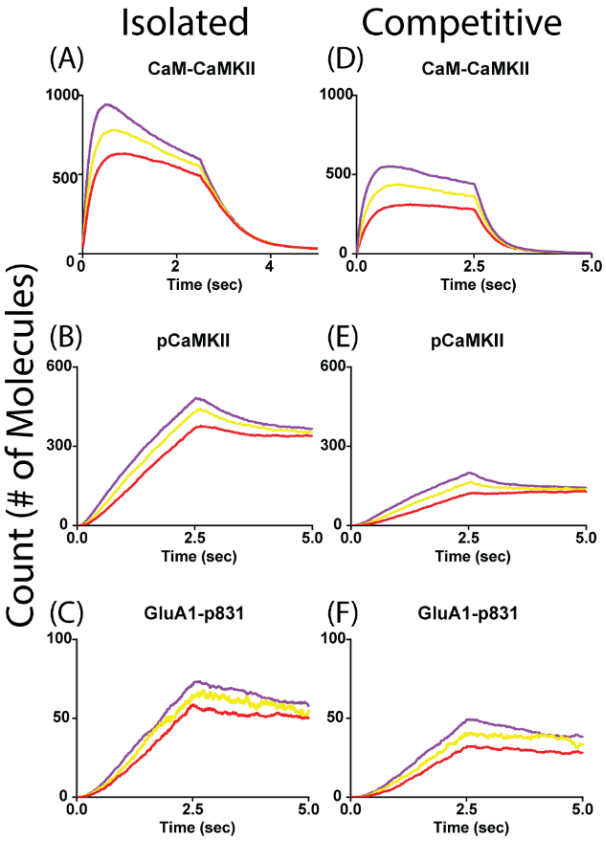

Figure 4.6. CaMKII-associated state gradients depend on competition for CaM. In response to 100Hz Ca^{2+} flux from time t = 0 until t = 2.5 sec, Ca^{2+}/CaM activates CaMKII to elicit the complex CaM-CaMKII (A & D). Active CaM-CaMKII may become auto-phosphorylated into pCaMKII (B & E), and both CaM-CaMKII and pCaMKII may bind and phosphorylate GluA1 subunits, leading to GluA1-p831 (C & F). For each protein state, I monitor the number of states in the spine head's top (purple), middle (yellow), and bottom (red) compartments. (A-C) Are the isolated model, and (D-F) are the competitive model. All traces are the average of N=50 executions.

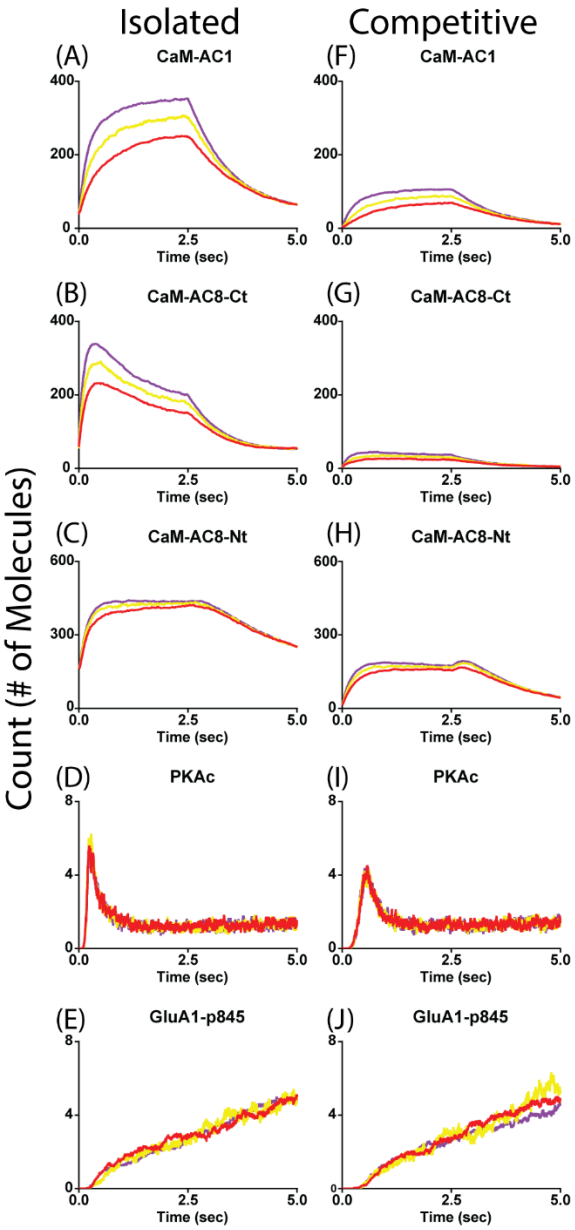

Figure 4.7. AC-associated state gradients depend on competition for CaM. In response to 100Hz Ca^{2+} flux from time t = 0 until t = 2.5 sec, Ca^{2+}/CaM activates AC1 (A & F), AC8-Ct (B & G), and AC8-Nt (C & H). Active AC1 and AC8-Ct are catalytically active, leading to PKA activation into PKAc (D & I). PKAc may bind and phosphorylate GluA1 subunits, leading to GluA1-p845 (E & J). For each protein state, I monitor the number of states in the spine head's top (purple), middle (yellow), and bottom (red) compartments. (A-E) Are the isolated model, and (F-J) are the competitive model. All traces are the average of N=50 executions.

Comparing the isolated and competitive model results shown in Figure 4.6 & Figure 4.7 reveals a clear effect of competition on the spatial gradients of protein states. Indeed, the compartmental traces (in purple, yellow, and red) for almost all protein states never overlap, at least during Ca^{2+} stimulation. To verify that I in fact observe distinct spatial gradients in these stochastic model results, in the Supplement to Chapter 4 (Table 7.7) I test for statistically significant differences in the number of protein states in each spine compartment. I find that at the termination of 100 Hz Ca^{2+} flux (t = 2.5sec), the only protein states not exhibiting a statistically significant spatial gradient were PKAc and p845. The same is true at the termination of 10 Hz Ca^{2+} flux (see Table 7.7). Interestingly, regardless of Ca^{2+} frequency, the spatial gradients that do occur all steepen when moving from an isolated to a competitive environment.

To quantify the increased steepness in spatial gradients of protein states, I measure the percent difference in the average number of protein states at the top and bottom compartments of the spine. Therefore, Table 4.2 enumerates the number of proteins at the top and bottom compartments at t = 2.5sec (as shown in Figure 4.6 and Figure 4.7), and the corresponding percent differences (far-right column). For every protein for which a statistically significant spatial gradient is observed, the spatial gradient is steeper in the presence of competition for CaM-binding. Furthermore, it is notable that the relative shift in steepness for each protein state is fairly independent of Ca^{2+} frequency, not changing by more than about ten percent. This is further evidence that competition-sharpening of spatial gradients is not an anomalous phenomenon but instead a distinct regulatory mechanism.

Table 4.2. Quantifying spatial gradient steepness in isolated and competitive environments.

100Hz Ca2+ flux		**Average count (#)**		**Percent Change (%)**	
		Isol.	Comp.	Isol.	Comp.
CaM-CaMKII	Top	597.98	441.6		
	Bottom	494.78	278.7	17%	**37%**
pCaMKII	Top	479.4	197.94		
	Bottom	374.6	120.52	22%	**39%**
p831	Top	70.84	48.96		
	Bottom	54.28	29.72	23%	**39%**
AC1	Top	352.48	105.26		
	Bottom	231.9	65	34%	**38%**
AC8ct	Top	200.02	37.48		
	Bottom	140.86	21.72	30%	**42%**
AC8nt	Top	437.08	173.6		
	Bottom	390.96	145.02	11%	**16%**

10Hz Ca2+ flux		**Average count (#)**		**Percent Change (%)**	
		Isol.	Comp.	Isol.	Comp.
CaM-CaMKII	Top	555.74	175.72		
	Bottom	459.78	114.07	17%	**35%**
pCaMKII	Top	120.62	15.06		
	Bottom	92.60	9.25	23%	**39%**
p831	Top	24.32	8.84		
	Bottom	17.76	4.64	27%	**48%**
AC1	Top	149.72	52.24		
	Bottom	113.94	32.52	24%	**38%**
AC8ct	Top	223.38	25.1		
	Bottom	164.5	17.28	26%	**31%**
AC8nt	Top	413.92	206.82		
	Bottom	355.22	159.7	14%	**23%**

4.3.4 N-terminus of AC8 as a regulator of spatial distributions of Ca^{2+}/CaM

Given that Figure 4.7 and Table 4.2 indicate consistent spatial gradients of active AC1 and AC8, it is surprising that these spatial gradients seemingly do not produce gradients of PKAc or GluA1-p845. Indeed, LTP *in vivo* elicits increased levels of GluA1-p845 and GluA1 localization

(gradients) to the synaptic membrane [180, 228]. To explore why my detailed model elicits increased levels but not localization of GluA1-p845, I refer to experiments by Wong *et al*. who show that mice with single knock-out of AC1 or AC8 retain the ability to achieve LTP [235]. Wong *et al*. further show that abolishing LTP requires double knockout of both AC1 and AC8. Therefore, I hypothesize that spatial gradients of LTP, and in particular GluA1-p845, may somehow depend on expression levels of AC1 and AC8.

To test the effect of AC1 and AC8 expression levels on spatial gradients GluA1-p845, I present two alternative versions of my model. The first alternative simulates knock-out (KO) of the AC8 N-terminus (AC8-Nt), chosen because although AC8-Nt binds Ca^{2+}/CaM it has no known enzymatic activity [189, 193]. The second alternative simulates knock-out of AC8 altogether. I simulate my standard (wild-type; WT) and alternative models at 10Hz and 100Hz Ca^{2+} at various initial concentrations of AC1, and I then calculate the time-averaged concentration of GluA1-p845 observed in each compartment of the spine. Figure 4.8 reveals that for the WT and AC8-Nt-KO cases, average GluA1-p845 levels are robust to decreasing concentrations of AC1. Furthermore, the AC8-KO case is similarly robust until AC1 concentrations fall below ~10μM. It appears that, at multiple Ca^{2+} frequencies, decreasing concentrations of AC1 causes a shift in competition such that Ca^{2+}/CaM increasingly binds and activates AC8, allowing the system to maintain overall PKAc and GluA1-p845 levels. Only the double KO of AC1 and AC8 abolishes GluA1-p845, which is consistent with Wong *et al*. However, I continue to observe no spatial gradients of GluA1-p845.

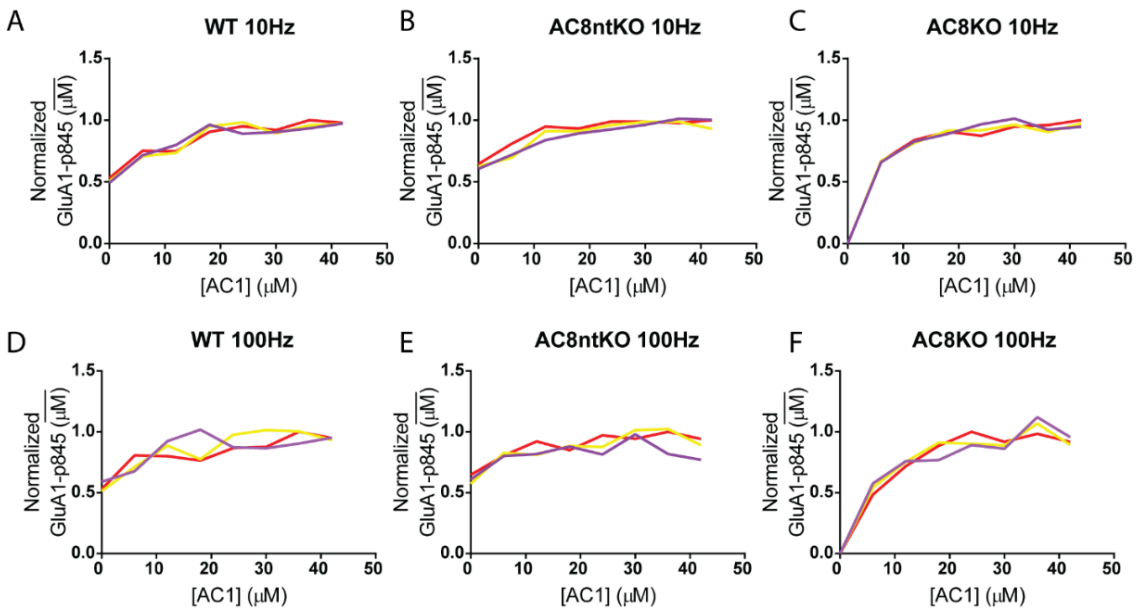

Figure 4.8. Normalized time-averaged GluA1-p845 for various AC-knockouts. Wild-type (A & D), AC8-Nt-KO (B & E), and AC8-KO (C & F) model responses to 10Hz Ca^{2+} (100 pulses; A-C) and 100Hz Ca^{2+} (250 pulses; D-F) as a function of AC1 concentration. Time-averaged GluA1-p845 levels are monitored in the top (purple), middle (yellow), and bottom (red) compartments. The data in each panel are normalized to the maximum average concentration observed in the top (purple) compartment. All traces are the average of N=50 executions.

The persistent lack of GluA1-p845 spatial gradients in Figure 4.8 and elsewhere in this paper is likely evidence that such gradients are regulated on longer timescales and/or by mechanisms not accounted for by this model. For example, my model may produce excessive cAMP/PKA levels or effective diffusivities, despite inclusion of cAMP- and PKA-sequestering mechanisms. These considerations can be accounted for in future work. Although in this model AC KO has seemingly no effect on spatial gradients of GluA1-p845, KO of AC (or any CBP) could still disrupt the competitive environment for CaM-binding and thereby perturb the spatiotemporal dynamics of other proteins in the system. For instance, Romano *et al*. identify how decreasing concentrations of the CBP Ng causes a shift in competition for CaM-binding, resulting in decreased CaMKII activation and a concomitant increase in AC1 activation [46]. Similarly, perturbing the concentration of AC isoforms as in Figure 4.8 could likely shift the spatiotemporal dynamics of Ca^{2+}/CaM in the spine.

Therefore, I next examine how various AC isoform KO scenarios influence the spatiotemporal dynamics of Ca^{2+}/CaM. In Figure 4.9, I monitor CBP-bound CaM_{2N}, CaM_{2C}, and

CaM_4 in each spine compartment at 100Hz Ca^{2+} flux. Each row in Figure 4.9 pertains to a distinct AC isoform KO scenario. Note that the WT Ca^{2+}/CaM (Figure 4.9A-C) dynamics are consistent with those observed in Figure 4.4B. Specifically, the levels of the CaM_{2N} state, with its high association and dissociation rate constants for Ca^{2+}, rapidly climb and then decline as Ca^{2+}/CaM moves into the higher-affinity CaM_{2C} state. Moreover, the fully-saturated CaM_4 state eventually predominates, consistent with expectation under 100Hz Ca^{2+} flux. Also, each Ca^{2+}/CaM state exhibits at least some spatial dependence, with distinct levels of each state in each spatial compartment. And the CaM_4 state exhibits a clear spatial gradient as before. Importantly, these general spatiotemporal dynamics are conserved in every AC KO shown in Figure 4.9. Notably, the spatiotemporal dynamics of Ca^{2+}/CaM are also conserved in every AC KO under 10Hz Ca^{2+} flux, as shown in Figure 7.7 in the Supplement to Chapter 4. However, under both 10Hz and 100Hz Ca^{2+} flux, absence of the AC8-Nt (Figure 4.9G-I) halves the levels of CaM_{2C} observed during Ca^{2+} stimulation. AC8-Nt changes the activation levels and spatial dependence of CBP-bound CaM_{2C}, and leading to a concomitant increase in CaM_4. This observation holds for the AC8-KO (Figure 4.9K) and double KO (DKO; Figure 4.9N) scenarios. These results suggest that one consequence of AC8-Nt-KO, or equivalent perturbations, *in vivo* could be a reduction in the dynamic activation of CBPs with high affinities for CaM_{2C} and increase in activation of CBPs with high affinities for CaM_4.

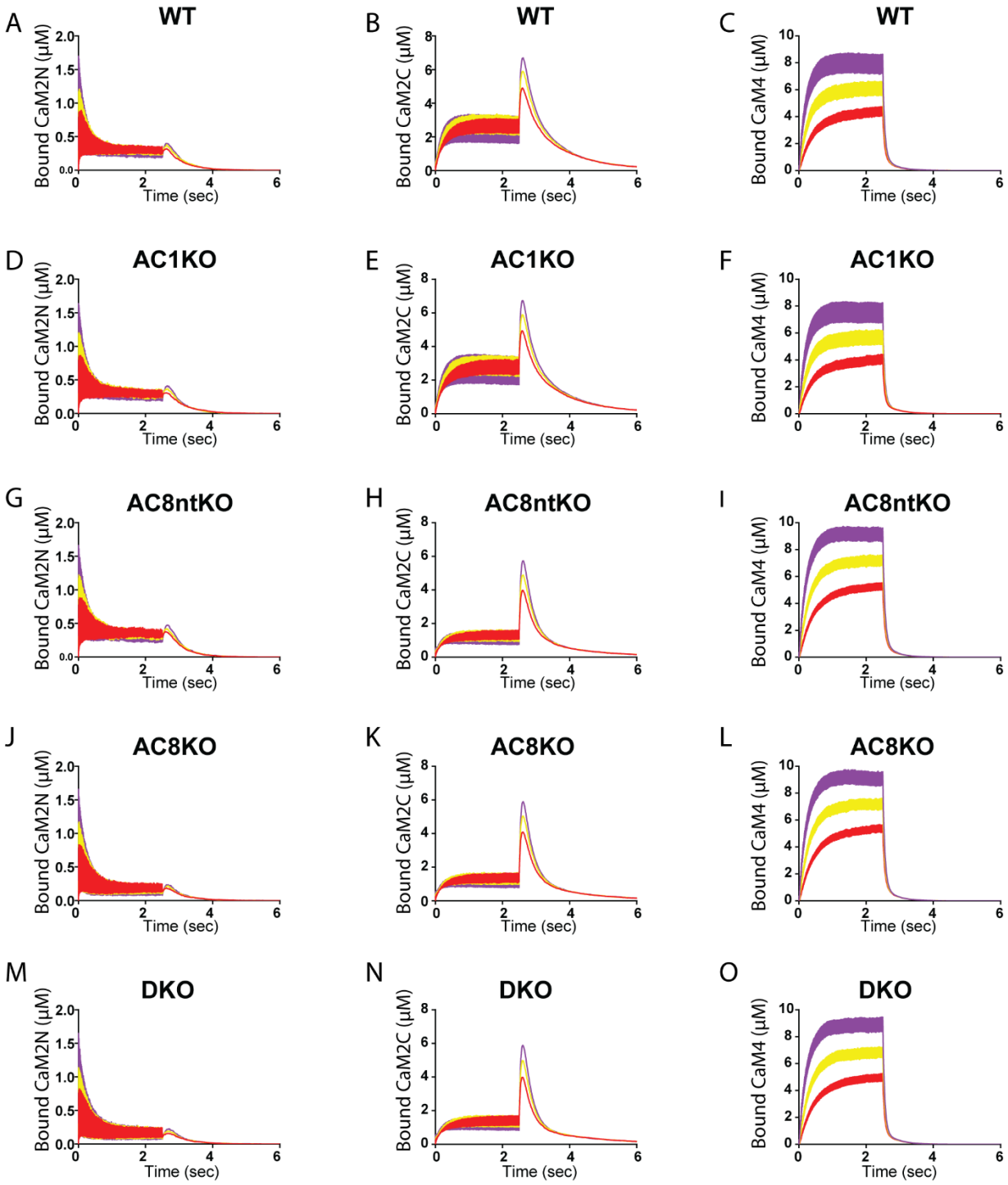

Figure 4.9. Spatiotemporal dynamics of CBP-bound Ca^{2+}/CaM under 100Hz stimulation for various AC isoform KO's. CBP-bound CaM_{2N} (left column), CaM_{2C} (middle column), and CaM_4 (right column) in each compartment in response to 100Hz Ca^{2+} flux. Ca^{2+}/CaM states in the top (purple), middle (yellow), and bottom (red) compartments may overlap and are therefore plotted from top to bottom, with bottom at the foreground. Ca^{2+} flux begins at t=0 and proceeds until t=2.5sec. All traces are the average of N=50 executions.

Having explored the effects of AC KO on CBP-bound Ca^{2+}/CaM in Figure 4.9, I next examine the effects on free Ca^{2+}/CaM. During active Ca^{2+} flux, the concentration of free Ca^{2+}/CaM can be quite low, especially at high Ca^{2+} frequencies and in the presence of many CBPs. Yet examining free Ca^{2+}/CaM (as opposed to CBP-bound or global Ca^{2+}/CaM), particularly in a spatial-stochastic model, might better elucidate how perturbing competition for CaM-binding changes where individual CBPs bind or unbind Ca^{2+}/CaM. Figure 4.10 is identical to Figure 4.9 but instead of monitoring bound Ca^{2+}/CaM in each spine compartment under 100Hz Ca^{2+}, I monitor free Ca^{2+}/CaM. Again, each row in Figure 4.10 is a distinct AC KO scenario. For each AC KO scenario in Figure 4.10, the spatiotemporal dynamics of CaM_{2N} and CaM_{2C} are both unchanged. However, the AC8-Nt- and AC8-KO scenarios both exhibit noticeable reductions in the levels of CaM_4 in the middle (yellow) compartment. This surprising result is remarkably not observed at 10Hz Ca^{2+} flux, shown in Figure 7.8. Instead, free Ca^{2+}/CaM under 10Hz causes a noticeable shift in CaM_{2C} location only observed upon AC8-Nt-KO. That is, AC8-Nt-KO results in consistently *higher* levels of CaM_{2C} in the middle compartment than the top compartment. Given these results, I further speculate that AC8, and especially AC8-Nt, is an essential regulator of the type and location of CBPs activated by CaM.

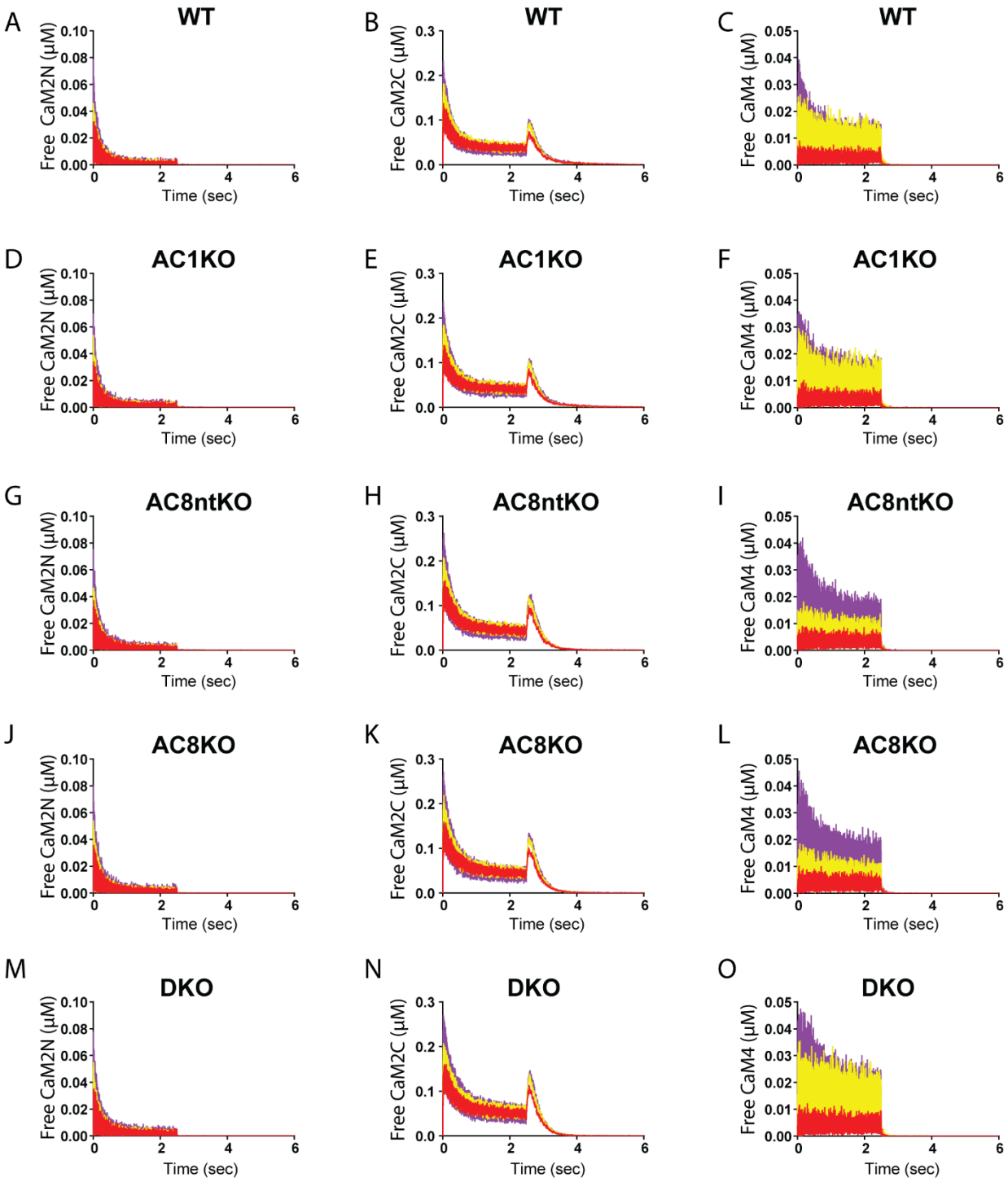

Figure 4.10. Spatiotemporal dynamics of free Ca^{2+}/CaM under 100Hz stimulation for various AC isoform KO's. Free CaM_{2N} (left column), CaM_{2C} (middle column), and CaM_4 (right column) in each compartment in response to 100Hz Ca^{2+} flux. Ca^{2+}/CaM states in the top (purple), middle (yellow), and bottom (red) compartments may overlap and are therefore plotted from top to bottom, with bottom at the foreground. Ca^{2+} flux begins at t=0 and proceeds until t=2.5sec. All traces are the average of N=50 executions.

Finally, I aim to explain my results in Figure 4.9 and Figure 4.10 by identifying the CBP to which CaM-binding shifts upon AC8-Nt-KO. For this, I leverage the fact that my model explicitly accounts for each CBP, whereas other models may lump CBPs into a single term. Specifically, I monitor the activation of each CBP by the major Ca^{2+}/CaM states CaM_{2N}, CaM_{2C}, and CaM_4 in each spine compartment, and then I calculate (see Methods) the dynamic changes in these activations between the WT and AC8-Nt-KO scenarios. My results in Figure 4.11 indicate that upon AC8-Nt-KO, there is a marked increase in CaMKII and AC1 activation by CaM_4 during Ca^{2+} flux and by CaM_{2C} following Ca^{2+} flux (which terminates at t=2.5 sec). It appears that without AC8-Nt, which has a high affinity for CaM_{2C}, Ca^{2+} flux leads to a greater abundance of CaM_4. Consequently, this increase in CaM_4 appears to increase the activation of CBPs with high affinities with CaM_4. Indeed, the CBPs in my model with the highest affinities for CaM_4 are CaMKII, AC1, and MLCK.

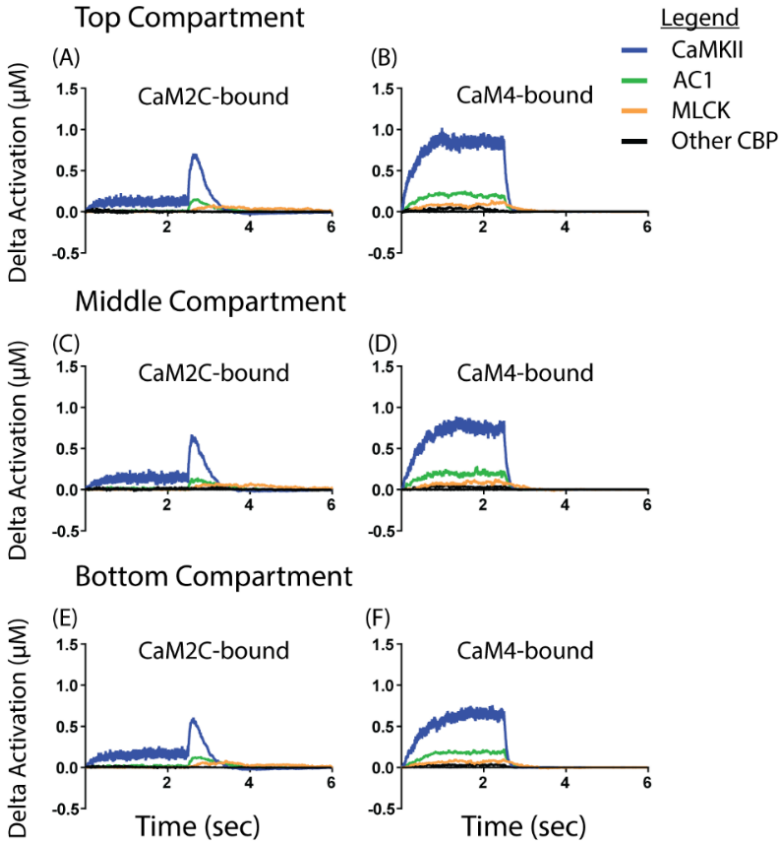

Figure 4.11. Shifts in individual CBP activations upon AC8-Nt-KO. Changes in individual CaM_{2C}-activated (left column) and CaM_4-activated (right column) CBPs in the top (A-B), middle (C-D), and bottom (E-F) compartment of the spine in response to 100Hz Ca^{2+} flux. The CBPs that shift by at least 20% are colored non-black as shown in the legend. All traces are the average of N=50 executions.

4.4 Discussion

This study uses MCell to simulate a system of differential equations in a particle-based spatial-stochastic framework, modeling the dynamic interactions of Ca^{2+}/CaM with nine explicitly-defined CBPs and a set of CBP-dependent signaling pathways relevant to early synaptic plasticity. My spatial-stochastic model accounts for competition among multiple CBPs for binding to CaM. With my model, I analyze how competition and spatial effects co-regulate signaling outputs relevant to synaptic plasticity.

I validate my spatial-stochastic model by comparing its output against the deterministic equivalent. Note that the equivalent deterministic model, which I implement using the software Mathematica, is not the same as that published by Pharris *et al*. (2018), although the model species and parameters are mostly identical [165]. In contrast to this previous publication, the deterministic equivalent used in my validation models 9-state Ca^{2+}/CaM to match the spatial-stochastic model. Recall that my spatial-stochastic model requires 9-state Ca^{2+}/CaM because the 4-state Ca^{2+}/CaM alternative calls for trimolecular reactions to which MCell assigns unreasonably low reaction probabilities. Comparing the dynamics of Ca^{2+}/CaM between my deterministic and spatial-stochastic models in Figure 4.2 reveals that both models agree and exhibit Ca^{2+}/CaM states consistent with past experimental and computational results [42, 45]. Furthermore, in Figure 4.3 I show that the Ca^{2+} frequency-dependence of CBP activation is preserved upon inclusion of spatial effects. The minor differences between Figure 4.3A and B are likely a consequence of both stochasticity and space. First, weakly expressed proteins such as CaN (0.5 μM) and PDE1 (2.25 μM) are most susceptible to stochastic effects and therefore exhibit noise despite averaging over many executions [21]. Second, spatial effects may localize active CBPs to distinct compartments in the spine. Protein localization, compounded by the particle-based methods in MCell, creates a scenario in which not all CBPs simultaneously compete for binding to the same CaM particle. Indeed, the Ca^{2+} frequency-dependence shown in Figure 4.3B can be regarded as a hybrid of the isolated and competitive results from a deterministic model (compare to Fig 4 in [46]). Thus, I proceed with my validated model and analyze how spatial effects and competition together regulate CBP activation.

A major outcome of this work suggests that competition is the predominant mechanism for setting the physiological Ca^{2+} frequency-dependence of CBP activation. Figure 4.5A indicates that spatial effects alone, in the absence of competition for CaM-binding, do not influence the Ca^{2+}

frequency-dependence of any CBP (for example, compare to Fig 4A in [46] which is a deterministic model with a similar reaction network). Moreover, Figure 4.5F-H indicate that the frequency-dependence, specifically the frequencies of peak activation, for each CBP are unchanged by location within the dendritic spine. However, although the frequency-dependence is seemingly independent of spatial effects, spatial effects do seem to influence the magnitudes of CBP activation. For example, while CaMKII is most activated at 100Hz Ca^{2+}, the magnitude of CaMKII activation at 100Hz is much higher in the top compartment (Figure 4.5F) than the bottom compartment (Figure 4.5H). Notably, this decrease in peak activation magnitude is reduced in the isolated model (Figure 4.5B-D), suggesting how competition regulates the localization of CBPs in the spine.

To further examine how localization of active CBPs is regulated by competition for CaM, in Figure 4.6 & Figure 4.7 I show spatiotemporal dynamics of protein states in CaMKII- and AC-mediated signaling pathways. Both pathways exhibit statistically significant spatial gradients during Ca^{2+} stimulation at multiple frequencies, for multiple protein states, in both the presence and absence of competition. Critically, inclusion of competition increases the percent change in spatial gradient height for every protein state (Table 2). I can be confident this increase in gradient height is not merely due to the pre-localization of CBPs such as Ng to the PSD, because I observe that all spatial gradients become more pronounced during Ca^{2+} flux, while Ca^{2+}/CaM states (non-apo-CaM) have low affinity for Ng. Although Ng likely localizes apo-CaM to the PSD prior to Ca^{2+} flux, Ng's affinity for Ca^{2+}/CaM is so low (and the diffusion of Ca^{2+}/CaM is sufficiently fast) that it likely does not interact with Ca^{2+}/CaM during Ca^{2+} flux, given the presence of other CBPs competing for CaM-binding. Thus, during Ca^{2+} flux it appears that competition alone is responsible for the enhancement of the spatial localization of proteins such as CaMKII, as depicted in Figure 4.12.

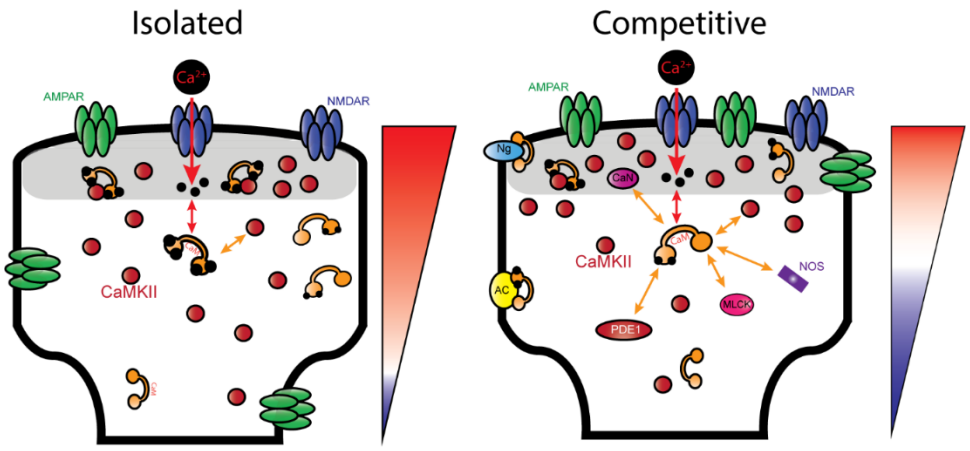

Figure 4.12. Schematic depiction of CaMKII spatial gradient enhancement by competition for CaM. (Left) Isolated CaMKII (red circles) binds CaM (orange dumbbells) along a spatial gradient throughout the spine. (Right) Competition for CaM-binding reduces CaMKII activation overall, causing most CaMKII to occur locally to the Ca^{2+} source, resulting in a steeper spatial gradient. Gradient bars are non-quantitative, illustrating shifts from high (red) to low (blue) local concentrations of CaMKII along the spine.

Competition's apparent influence on spatial localization highlights its importance as a regulatory mechanism. Although competition for CaM-binding has long been a known phenomenon [14, 30], the effect of competition on other regulatory mechanisms is now becoming understood. In addition to setting the Ca^{2+} frequency-dependence of CBPs through competitive tuning [46], competitive tuning may, in the presence of feedback loops, provide a compensatory mechanism that lends robustness to Ca^{2+}-dependent outputs of synaptic plasticity induction [165]. Now, I identify how competition could enhance spatial microdomains of CBP activation, helping to ensure that active CBPs transduce their downstream signals at correct/consistent locations within the spine (Figure 4.6 and Figure 4.7). And note that activating CBP-dependent pathways at the appropriate location may be important to ensure, for example, that CaMKII is predominantly active in the PSD and able to phosphorylate or localize GluA1 receptors at the synaptic membrane [236, 237]. Alternatively, inactivating CaMKII and other CBPs at the appropriate location may also be important; as, for example, CaMKII inactivation at the PSD and subsequent re-binding to actin may be essential to the structural remodeling following LTP [37, 238-242].

The final section of my results explores various AC isoform KO scenarios in an attempt to explain to why, despite robust gradients of AC activation, I observe no spatial gradients of GluA1-

p845. First, I observe that only AC DKO abolishes GluA1-p845 (Figs 8C & 8F), consistent with experiments by Wong *et al*. that individual knockouts of either AC1 or AC8 are insufficient to abolish LTP [235]. I also observe robust GluA1-p845 levels across a wide range of AC concentrations, perhaps consistent with experiments in insular cortex, where LTP is observed as long as AC1 alone is at least weakly expressed [243]. However, despite my model's agreement with these experimental results, none of my simulated AC KOs affect the distribution of GluA1-p845 in space. Thus, I speculate that this aspect of my model could be under-regulated in a variety of ways. For example, my parameterization of cAMP generation by AC, cAMP degradation by PDE1 and PDE4, or the binding of cAMP to PKA could be incomplete. To quantify how these parameters influence the spatial dependence of GluA1-p845, future studies could implement a global sensitivity analysis, though this may be computationally impractical for a spatial-stochastic model such as ours. Moreover, my representation of diffusion for small cytosolic molecules such as cAMP and PKA may be incomplete. If diffusion is too rapid for molecules such as cAMP, the spatial gradients of AC activation may not be efficiently transduced downstream. Future work could explore reports by previous studies that propose how actin filaments, molecular crowding, spine geometry, and high affinity interactions may reduce the effective diffusion of particles in the spine [185, 244-246]. I note, of course, that if the model presented here were to more rigorously account for diffusion, the spatial gradients currently observed would likely become more pronounced. Finally, my model excludes structural mechanisms that might restrict bound or phosphorylated AMPARs to the synaptic membrane. Therefore, my results may provide further evidence that intracellular interactions involving PSD-95 or A-kinase-anchoring proteins (AKAPs) might be necessary to encumber the trafficking of AMPARs to the synaptic membrane [19, 37, 180]. To further explore the regulation of AMPAR trafficking, it might be interesting to combine my MCell model with that recently published by Antunes *et al*., who use MCell to explore AMPAR trafficking in response to generic LTP and LTD inputs [228].

Although my AC KO scenarios do not influence the spatial dependence of GluA1-p845, they did impact the spatiotemporal dynamics of Ca^{2+}/CaM. Indeed, levels of CBP-bound CaM_{2C} are roughly halved in the absence of the AC8-Nt (Figure 4.9H, K, and N). Interestingly, when CaM_{2C} levels halve, CaM_4 levels increase by roughly the same amount, and this result is consistent at multiple Ca^{2+} frequencies (see the 10Hz scenario in Figure 7.7). I attribute this result mainly to the differences in my kinetic parameters for CaM binding each AC isoform. First, with my

parameterization each AC isoform binds CaM_{2N} and CaM_4 at affinities all within roughly one order of magnitude. Second, AC8-Nt binds CaM_{2C} at a higher affinity than the other AC isoforms (K_D = 0.8μM). Thus, it is reasonable that AC8-Nt-KO causes a reduction in dynamic CaM_{2C} levels; one of the most abundant CBPs (42μM) with a relatively high affinity for CaM_{2C} is no longer in the system. So, in the absence of AC8-Nt, other CBPs with high affinities for CaM_{2C} may either become less activated or become activated by different Ca^{2+}/CaM states instead. Determining the full impact of AC8-Nt-KO may require a rigorous examination of individual CBP dynamics in future work. While others have explored how Ca^{2+}/CaM influences AC isoforms [247, 248], there has been less work on how the AC isoforms influence the spatiotemporal dynamics of Ca^{2+}/CaM.

In this study I distinguish between CBP-bound Ca^{2+}/CaM and free (unbound) Ca^{2+}/CaM. In Figure 4.10, I examine free Ca^{2+}/CaM under identical conditions to Figure 4.9, again revealing a seemingly critical role for the AC8-Nt. First, at 100Hz Ca^{2+} AC8-Nt-KO (Figure 4.10I) causes a reduction in the levels of free CaM_4 in the middle compartment of the spine. This reduction persists upon AC8-KO (Figure 4.10L) but is recovered upon AC DKO (Figure 4.10O), likely due to a shift in competition for CaM_4 upon removal of AC1. The results in Figure 4.10 I and L reveal a critical function for AC8, and AC8-Nt in particular. Specifically, AC8-Nt-KO may cause CBPs with high affinity for CaM_4 (such as AC1 and CaMKII) to excessively bind CaM_4 at the top of the spine, instead of more uniformly as Figure 4.9C implies. Secondly, at 10Hz Ca^{2+} (Figure 7.8) AC8-Nt-KO uniquely causes higher levels of CaM_4 in the middle than the top compartment of the spine. This surprising result implies how AC8-Nt-KO may cause some CBP(s) not necessarily localized to the PSD (such as CaMKII, AC1, or MLCK as identified in Figure 4.11) to perhaps pathologically predominate in CaM_4 binding. Especially given that Figure 4.11 implicates dysregulation of AC1 upon AC8-Nt-KO, it would be interesting to explore my results in light of results by Garelick *et al*. who show that young mice with excess AC1 ($AC1^+$) have improved spatial memory, while older $AC1^+$ mice show deficient spatial memory [249, 250]. Based on my results, it could be that old mice have under-expressed AC8 or some other perturbation specific to AC8-Nt.

Ca^{2+} signaling is important in virtually every cell type in addition to hippocampal neurons. Because CaM has over 100 downstream binding partners, it is reasonable to expect that competition provides an added layer of regulation to how different cell types respond to Ca^{2+}/CaM [14]. Certainly, my view of Ca^{2+}/CaM as a limiting resource could also be adopted in a

computational model of Ca^{2+}/CaM-regulated neurotransmitter release in presynaptic neurons, cardiac muscle contractility, or insulin secretion in the pancreas [251, 252]. The methods used for this model, such as the principle of microscopic reversibility, may be useful in estimating other parameter values (e.g. the as-yet unmeasured kinetic rates of sub-saturated Ca^{2+}/CaM for binding AC3 in olfactory receptors) [253]. My results motivate further examination of the influence of competition on spatial effects, and such future studies could build on my and others' use of MCell and CellBlender. Indeed, it would be interesting to return to work by Saucerman *et al*. (2008) or Antunes *et al*. (2018), expanding those models with added spatial detail, thermodynamically-complete Ca^{2+}/CaM binding, and/or multiple explicitly-defined CBPs [92, 228].

4.5 Methods

All model code and associated files are available at the Purdue University Research Repository. The model is written using MCell 3.3 with syntax documented at mcell.org. MCell 3.3 accepts geometry files exported from the open-source software Blender using the plug-in CellBlender. In my model, I use the same dendritic spine geometry as Keller *et al*. (2008) [185], excluding their dendrite shaft. The spine head is a 0.5 μm cuboid.

Prior to Ca^{2+} flux, all model simulations are run for t=10sec to allow model species to equilibrate. I forgo showing this equilibration period in all time-course plots. At t=10sec, Ca^{2+} flux begins according to time-variable rates informing the reactions $NMDAR \rightarrow NMDAR + Ca^{2+}$ and $Ca^{2+} \rightarrow NULL$. The combined effect of these reactions is to produce global free Ca^{2+} dynamics obeying the equation $[Ca](t)=12e^{-t/0.012}$ as used by Romano *et al.* [46]. To implement this equation in MCell as time-variable reaction rates, I numerically differentiate as shown in Ca_train.m provided in the code repository. This equation controls for Ca^{2+} magnitude and patterning by ensuring that all Ca^{2+} pulses are evenly spaced and consistently peak at 12μM. Note that NMDARs are constrained to the synaptic membrane, or the top surface of my dendritic spine geometry. Thus, Ca^{2+} magnitude, patterning, and location are all controlled, allowing me to observe model output as a function of Ca^{2+} frequency alone.

To calculate the changes in dynamic activation of individual CBPs between WT and AC8-Nt-KO scenarios as shown in Figure 4.11, I define the metric ‘delta activation’. Here, I define this metric as shown in equation 1. Note that positive delta activation implies an increase in a CBP’s activation upon AC8-Nt-KO.

$$(1)\ DeltaActivation(t) = AC8_{NTKO}(t) - WT(t)$$

5. A MULTI-STATE MODEL OF THE CAMKII DODECAMER SUGGESTS A ROLE FOR CALMODULIN IN MAINTENANCE OF AUTOPHOSPHORYLATION

5.1 Summary

Ca^{2+}/calmodulin-dependent protein kinase II (CaMKII) accounts for up to 2 percent of all brain protein and is essential to memory function. CaMKII activity is known to regulate dynamic shifts in the size and signaling strength of neuronal connections, a process known as synaptic plasticity. Increasingly, computational models are used to explore synaptic plasticity and the mechanisms regulating CaMKII activity. Conventional modeling approaches may exclude biophysical detail due to the impractical number of state combinations that arise when explicitly monitoring the conformational changes, ligand binding, and phosphorylation events that occur on each of the CaMKII holoenzyme's twelve subunits. To manage the combinatorial explosion without necessitating bias or loss in biological accuracy, I use a specialized syntax in the software MCell to create a rule-based model of the twelve-subunit CaMKII holoenzyme. Here I validate the rule-based model against previous measures of CaMKII activity and investigate molecular mechanisms of CaMKII regulation. Specifically, I explore how Ca^{2+}/CaM-binding may both stabilize CaMKII subunit activation and regulate maintenance of CaMKII autophosphorylation. Noting that Ca^{2+}/CaM and protein phosphatases bind CaMKII at nearby or overlapping sites, I compare model scenarios in which Ca^{2+}/CaM and protein phosphatase do or do not structurally exclude each other's binding to CaMKII. My results suggest a functional mechanism for the so-called "CaM trapping" phenomenon, such that Ca^{2+}/CaM structurally excludes phosphatase binding and thereby prolongs CaMKII autophosphorylation. I conclude that structural protection of autophosphorylated CaMKII by Ca^{2+}/CaM may be an important mechanism for regulation of synaptic plasticity. This chapter has been submitted for publication and is currently in revision. Co-authors include Dr. Melanie Stefan of the University of Edinburgh, a collaborator with our laboratory who introduced us to the idea of rule-based modeling. Other co-authors include Drs. Tom Bartol and Terrence Sejnowski of the Salk Institute, who helped with the development of MCell, and Dr. Mary Kennedy of the California Institute of Technology, who provided key insight into the possibility for Ca^{2+}/CaM to structurally exclude PP1 from CaMKII-binding.

5.2 Introduction

CaMKII is a protein of interest because of its crucial role in synaptic plasticity [5, 254-257]. In the hippocampus, synaptic plasticity in the post-synapse occurs within mushroom-shaped protrusions called dendritic spines [258]. Synaptic plasticity is dependent on calcium ion (Ca^{2+}) flux through N-methyl-D-aspartate receptors (NMDARs) located on the dendritic spines of the post-synaptic neuron [23]. Depending on the magnitude, frequency, and location of Ca^{2+} flux, synaptic plasticity may produce increases or decreases (or neither) in synaptic strength [3, 259]. Large, higher-frequency Ca^{2+} spikes can induce an enduring up-regulation of synaptic strength, called long-term potentiation (LTP); while weak, lower-frequency Ca^{2+} spikes can induce an enduring down-regulation of synaptic strength, called long-term depression (LTD) [29, 259]. Whether Ca^{2+} spikes induce LTP or LTD depends on relative activation of intracellular protein signaling networks. When Ca^{2+} first enters the dendritic spine, it interacts with a variety of buffer and sensor proteins, chiefly calmodulin (CaM), which has many protein targets in the spine, including CaMKII [20, 46, 257].

The CaMKII holoenzyme contains at least twelve subunits [260-263] arranged as two rings of six. As shown in Figure 5.1, each CaMKII subunit features an N-terminal kinase domain and C-terminal hub domain [218]. Between the kinase and hub domains is a flexible regulatory domain which lends to the subunit a wide range of movement away from the holoenzyme's central hub. A crystal structure of human alpha-CaMKII expressed in *E. coli* published by Chao *et al*. (2011) shows CaMKII subunits as able to rapidly and stochastically pivot between a "docked" and "undocked" conformation, seemingly mediated by residues on the kinase domain's activation loop and a spur structure on the hub domain (see Fig 3C in [218]), such that a docked subunit may be inaccessible to CaM binding. In contrast, a more recent work using electron microscopy with rat alpha-CaMKII expressed in Sf9 cells suggests that less than 3 percent of subunits exhibit a compact (or docked) conformation [264]. Given the uncertainty in the field, I include subunit docking and undocking in my model, allowing for future exploration of this possible subunit functionality. In addition to docking and undocking, each subunit can be in an "inactive" conformation when the regulatory domain is bound to the kinase domain (Fig 1B), or an "active" conformation when this binding is disrupted by the binding of Ca^{2+}/CaM or phosphorylation at Thr-286 [218, 265]. In the active conformation the catalytic domain of a subunit is able to bind and phosphorylate enzymatic

substrates. A subunit may spontaneously return to an inactive conformation in the absence of Ca^{2+}/CaM or phosphorylation at Thr-286 [265].

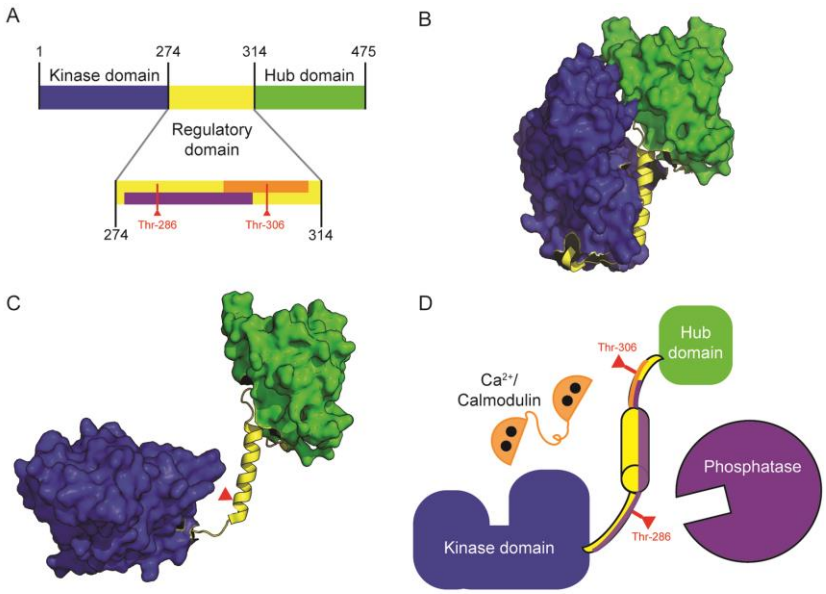

Figure 5.1. Schematic of CaMKII Subunit Structure. (A) Map of amino acid residues in a CaMKII subunit. The N-terminal kinase domain (blue) approximately spans residues 1-274. The regulatory domain (residues 275-314, yellow) binds to the kinase domain autoinhibiting the kinase activity of the each CaMKII subunit. The putative phosphatase binding site is also shown purple. The Ca^{2+}/CaM binding site is shown in orange. Subunits self-associate via the hub domain (residues 315-475, green) to form multimeric complexes of 12-14 subunit holoenzymes. (B) The "inactive" CaMKII subunit (PDB: 3SOA) in which the regulatory domain (yellow) is closely associated with the kinase domain (blue). (C) A schematic of the "active" CaMKII subunit. The regulatory domain (yellow) is not bound to the kinase domain (blue). This schematic was generated by manually modifying PDB entry 3SOA to illustrate how the regulatory domain may be available for Ca^{2+}/CaM binding and the kinase domain open for substrate binding. (D) Cartoon depiction of all protein species in my model, in which Ca^{2+}/CaM (orange) or phosphatase (purple) may bind to the regulatory domain (yellow) of a CaMKII subunit.

CaMKII activity can become Ca^{2+}/CaM-independent through phosphorylation at Thr-286, which is required for LTP [5, 26]. Importantly, this phenomenon is an autophosphorylation: it is thought to occur when an active subunit phosphorylates neighboring subunits within the same holoenzyme [195, 266]. Autophosphorylation at Thr-286 ("pThr-286") is thought to provide structural stability to a subunit's active conformation (reviewed in [267]) [42]. Because CaMKII plays a key role in the induction of LTP, and ultimately learning and memory (reviewed in [3,

256]), I seek to better understand the biochemical regulation of CaMKII activation and autophosphorylation via computational modeling.

To characterize the spatiotemporal regulation of CaMKII, experimental studies are increasingly complemented by computational models [45, 218, 262, 268]. Computational models of Ca^{2+}-dependent signaling implicate competition, binding kinetics, feedback loops, and spatial effects in regulating enzyme activation [23, 33, 42, 46, 185]. However, fully characterizing these and other mechanisms of CaMKII regulation is impeded by the challenge of accurately portraying the CaMKII holoenzyme. As described by previous work, combinatorial explosion applies to models of CaMKII (and similar biomolecules) because the protein exhibits a large number of functionally significant and not necessarily inter-dependent states [24, 42, 45, 269, 270]. The large number of possible states of CaMKII can neither be explicitly specified nor efficiently evaluated with conventional mass action-based methods. Indeed, for just one CaMKII hexamer ring, I estimate a state space of ~32 billion states, and for the full dodecamer approximately 10^{20} possible states (see the Supplement to Chapter 5). The numbers of possible CaMKII states far exceeds the number of CaMKII molecules in a dendritic spine, suggesting that some states never occur and are therefore not functionally important. Previous models leverage this observation to reduce the model state space and provide valuable insight to CaMKII binding and autophosphorylation dynamics [4, 24, 42, 245, 271]. However, for CaMKII it remains unclear which states functionally participate in synaptic plasticity. Reduced models can inadvertently obscure key mechanisms regulating CaMKII activation and autophosphorylation. To elucidate complex regulatory mechanisms, it may be necessary for models to provide for all possible states *ab initio*.

In this work, I use rule-based model specification and particle-based rule evaluation methods to overcome combinatorial explosion [45, 270, 272]. Rules are conditions, based primarily on experimental observations, that prescribe when an implicitly-defined reaction may occur. At a given iteration, only states that matter for the execution of a particular rule are explicitly declared. States that do not matter to a particular rule can be omitted, a principle that has been paraphrased as “don’t care, don’t write” [273]. I use rule- and particle-based methods within the spatial-stochastic software MCell 3.3 [185, 274] to present a comprehensive multi-state model of the CaMKII dodecamer. Other simulation platforms can also overcome combinatorial explosion through rule-based model specification (e.g. BioNetGen [275]) or network-free approaches (e.g. NFsim [276]). Unlike other platforms, MCell 3.3 provides both spatial-stochastic and rule-based

modeling, although multi-state molecules in MCell 3.3 cannot diffuse. I use MCell 3.3 in anticipation of future MCell versions accounting for multi-state molecule diffusion, and to eventually build on simulations with physiological dendritic spine geometries such as those by Bartol *et al*. (2015) [230].

Here, I validate this rule-based MCell model of CaMKII regulation against current descriptions of the Ca^{2+} frequency-dependence of CaMKII activation. By varying the rules and model parameter values I can simulate different experimental manipulations of CaMKII interaction with Ca^{2+}/CaM and phosphatase and thereby explore various mechanisms regulating CaMKII activity. In particular, I show that Ca^{2+}/CaM is important not only for regulating activation of CaMKII but may also contribute to the maintenance of CaMKII phosphorylation at Thr-286. I hypothesize that by limiting access of phosphatases to CaMKII Thr-286 (perhaps by steric hindrance), Ca^{2+}/CaM may prolong the lifetime of the auto-phosphorylated state.

5.3 Results

5.3.1 Model Development

5.3.1.1 Molecular Species

The model contains three protein species: CaM, protein phosphatase, and CaMKII. Ca^{2+}/CaM facilitates CaMKII activation, which leads to autophosphorylation at Thr-286, and phosphatase activity facilitates de-phosphorylation at Thr-286. Both protein phosphatase 1 (PP1) and protein phosphatase 2A (PP2A) have been shown to dephosphorylate Thr-286, though in different subcellular fractions (reviewed by [266, 277-279]). Here I refer to them generally as protein phosphatase (PP).

CaM and PP are modeled in MCell as conventional cytosolic molecules. CaM is modeled as having one of two states: un-bound apo-CaM and fully-saturated Ca^{2+}/CaM (four Ca^{2+} bound to CaM). Although I and others have described the importance of sub-saturated Ca^{2+}/CaM states with fewer than 4 Ca^{2+} [24, 42, 46, 97, 190, 215], the dynamics of Ca^{2+}-CaM binding and the binding of sub-saturated Ca^{2+}/CaM to CaMKII are beyond the scope of this current work. Indeed, accounting for sub-saturated Ca^{2+}/CaM would here require a multi-state representation, and because multi-state molecules cannot diffuse in MCell 3.3, I simplify my Ca^{2+}/CaM model to allow CaM and CaMKII to interact. Thus, similarly to previous models [33, 216], I assume that apo-

CaM has a negligible affinity for CaMKII; only fully-saturated Ca^{2+}/CaM binds CaMKII. In contrast to CaM, PP is modeled as single-state protein that is constitutively active and able to bind auto-phosphorylated CaMKII subunits. My representation of constitutively active PP is consistent with previous models such as that by Lisman and Zhabotinsky (2001) [280].

CaMKII is modeled as a multi-subunit complex, defined using a specialized model syntax for complex molecules (COMPLEX_MOLECULE) in MCell 3.3 [43]. This syntax allows for explicit representation of individual CaMKII dodecamers with distinguishable subunits. As shown in Figure 5.2, the holoenzyme is arranged as two directly-apposed, radially-symmetric rings each with six subunits. Each subunit features five "flags", each standing for a particular state that each CaMKII subunit can adopt. Flags are used in rule evaluation, which occurs at each time step and for each individual subunit. That is, MCell repeatedly evaluates model rules against a given subunit's flags (and those of the neighboring subunits) to determine which state transitions a subunit undertakes at each time step. In the following sub-sections, I describe all CaMKII model flags, the state transitions that apply to each flag, the conditions and rate parameters for each state transition, and related model assumptions. In Figure 5.2, I visually convey how CaMKII subunits transition between states according to my model's rules. In Table 7.8 I summarize the state transition rules and rate parameter values.

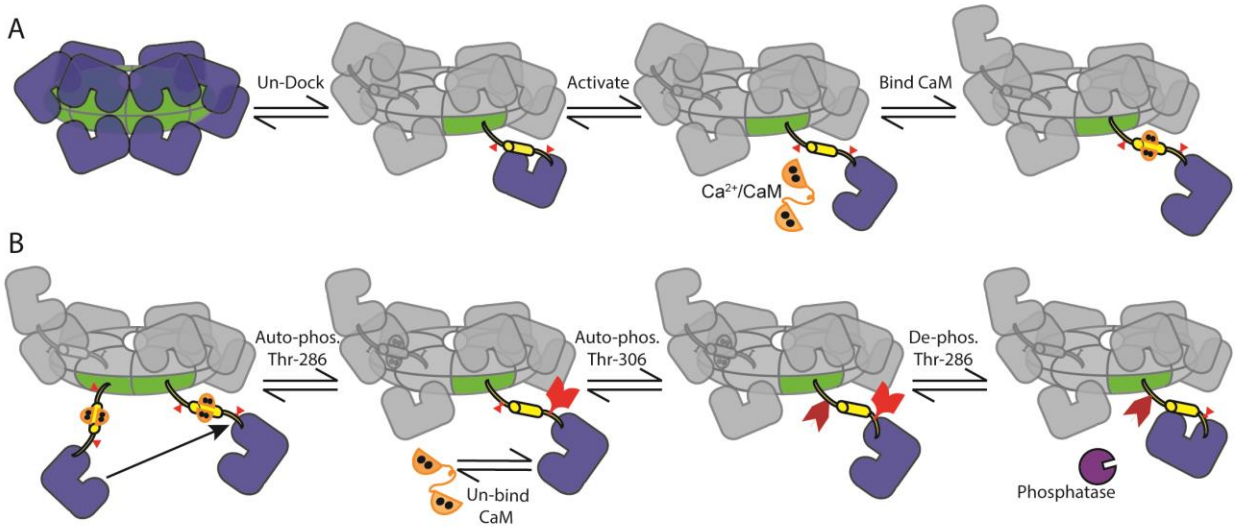

Figure 5.2. CaMKII holoenzyme state transitions. (A) CaMKII has twelve subunits arranged in two radially symmetric, directly apposed rings. Subunits may spontaneously undock/extend from the central hub or dock/retract (if inactive). When undocked, subunits may spontaneously open/activate. (B) If two neighboring subunits are active, one may auto-phosphorylate the other at Thr-286. If auto-phosphorylated (pThr-286), a subunit may remain active even upon un-binding of CaM. A pThr-286 subunit un-bound to CaM may additionally phosphorylate at Thr-306, blocking subsequent re-binding of Ca^{2+}/CaM. A pThr-286 subunit may also bind and become de-phosphorylated by PP (purple).

5.3.1.2 Subunit Docking

Docking is a binary flag that describes subunits as either "docked" or "undocked" to the CaMKII central hub. Subunits are instantiated in a docked state but may undergo numerous transitions between docked and undocked over the course of a simulation. At each time step, I assess a rule governing the subunit's transition from a docked to undocked state. If this rule is satisfied, meaning that the subunit's docking flag is verified as "docked", then the transition is considered. Similarly, I assess a separate rule governing a transition from an undocked to docked state, which requires that the subunit not be bound to CaM and not phosphorylated at Thr-306 [218].

Subunit docking follows the structural model of Chao *et al.*, who showed that a subunit cannot bind CaM as long as the subunit is in a compact conformation, docked to its central hub [218]. Docking implies a two-step process in which the subunit must first un-dock before subsequent CaM-binding, which accounts for the reported difference in binding rate for CaM to CaMKII-derived peptide (1×10^8 $M^{-1}s^{-1}$ [281]) and for CaM to full-length CaMKII-T286A ($1.8 \times$

10^6 $M^{-1}s^{-1}$ [282]). Taking the ratio of these two rates gives an equilibrium constant for docking of 0.018, which is consistent with estimates by Chao *et al*., who assumed $K_{docking}$ to fall between 0.01 and 100 [218]. With this equilibrium constant, I estimate kinetic rates for docking and undocking. For this estimation, I first note that subunit docking involves a structural conformation change on a relatively large scale. Referring to a separate, and notably smaller-scale, conformational change in my model, in which CaM quickly transitions from an initially- to fully-bound state (see Flag 3: CaM Binding), I assume the docked-to-undocked transition to proceed at an order of magnitude slower. I therefore arrive at an assumed rate for k_{dock} of 35 s^{-1}. In turn, this gives an undocking rate $k_{undock}=k_{dock} \times K_{docking}$ of 0.63 s^{-1}, which lies within the range of 0.01 s^{-1} and 100 s^{-1} for k_{undock} assumed by Chao *et al*.

5.3.1.3 Subunit Activation

The activation flag describes subunits as either "active" or "inactive". An inactive subunit has no catalytic activity because the regulatory domain is bound to the subunit's catalytic site; others may refer to it as a closed subunit. Conversely, an active subunit has catalytic activity because the regulatory domain's inhibition of the kinase domain is disrupted; in other words, an active subunit is an open subunit. When a subunit is active, Ca^{2+}/CaM and/or other proteins may access and bind CaMKII. In my model, the transition reaction from inactive to active (opening) involves no explicit rules (but rather occurs unconditionally and as governed by rates described below). In contrast, two rules inform the conditions for subunit inactivation: that the subunit is 1) not fully-bound to CaM, and 2) not phosphorylated at Thr-286.

To assign rate parameters for this flag, I first note that subunits can fluctuate between inactive and active states rapidly in the absence of Ca^{2+}/CaM (on the order of hundreds of nanoseconds) [116, 265]. Noting this, I set the rate parameter for subunit inactivation at 1×10^7 s^{-1}. Further, Stefan *et al*. determined that the activation probability (in the absence of CaM and phosphorylation) is 0.002, leading me to set my activation rate parameter to 2×10^4 s^{-1} [269]. Thus, I arrive at a model in which CaMKII subunit activation is unstable until stabilized by CaM-binding or autophosphorylation.

5.3.1.4 CaM binding

CaM binding is a ternary flag meaning that each CaMKII subunit displays one of three states, where CaM may be "unbound", "initially-bound", or "fully bound". My model adapts previous work by Stefan *et al*. (2012) to describe CaM-binding to CaMKII as a two-step process [269]. First, CaM binds to the regulatory domain of a CaMKII subunit (residues 298-312), resulting in a low-affinity "initially bound" CaMKII state, which is compatible with both the closed and open subunit conformation. Second, if the initially bound CaMKII opens it may transition to a "fully bound" state that describes the complete, higher-affinity interaction between CaM and CaMKII along residues 291-312 (see Figure 5 in [269]). I specify three rules to govern the transition from an unbound to initially bound state: the subunit must be 1) undocked, 2) not PP-bound, and 3) un-phosphorylated at Thr-306. The transition reaction from initially bound to a fully bound state is governed by a single rule that the subunit already be active/open. Dissociation of CaM from a fully bound CaM-CaMKII state proceeds through the initially bound state before becoming completely unbound from CaMKII.

In order to determine the parameters governing initial binding of CaM to CaMKII, I use data on CaM binding to CaMKII-derived peptides, rather than full-length CaMKII. This is done to separate the intrinsic binding constants from the parameters governing subunit activation/inactivation and docking/undocking. The microscopic k_{on} for CaM binding to CaMKII has been measured, using a CaMKII peptide and fluorescently labeled DA-CaM, as 1×10^8 $M^{-1}s^{-1}$ [281]. For the K_D governing initial CaM binding, I use the K_D reported by Tse *et al*. for CaM binding to a low-affinity peptide (CaMKII residues 300-312), which is 5.9×10^{-6} M [283]. From these two parameters, I can compute the dissociation rate of initially-bound CaM from CaMKII: $k_{off\_CaM\_ini} = K_{d\_CaM\_ini} \times k_{on\_CaM} = 590\ s^{-1}$.

In order to determine the parameters governing the transition from initially-bound to fully-bound CaM to CaMKII, I note that this transition involves a structural compaction of the CaM molecule, which has been measured using fluorescent labels [281, 282]. Using fluorescent labels to analyze the structural compaction of CaM is convenient in its exclusion of effects due to conformational changes within CaMKII subunits or the CaMKII holoenzyme. Thus, I use these measurements as a proxy for CaM binding to a CaMKII peptide and to estimate parameters governing the transition between initially- and fully-bound CaM-CaMKII. Taken from experimental measurements by Torok *et al*., I identify a transition rate from initially- to fully-

bound CaM-CaMKII (compaction of CaM) of 350 s^{-1} and from fully- back to initially-bound CaM-CaMKII (de-compaction of CaM) of 4×10^{-3} s^{-1} [281]. This means that, in the absence of obstructions to binding, the likelihood of a bound CaM molecule being in the initial binding state (rather than the fully bound state) is $4 \times 10^{-3} / 350 = \sim 1.1 \times 10^{-5}$. This is consistent with a probability of CaM being bound to the high-affinity site of 0.99999 which was derived by Stefan *et al*. (2012) [269].

5.3.1.5 Phosphorylation at Thr-286

Phosphorylation at the residue Thr-286 is a ternary flag that describes this site as either "un-phosphorylated (uThr-286)", "phosphorylated (pThr-286)", or "phosphatase-bound". I specify three rules to govern the reaction that transitions a subunit from uThr-286 to pThr-286: the subunit 1) be uThr-286, 2) be active, and 3) have an active neighbor subunit in the same holoenzyme ring. The neighboring subunit's activation flag is considered because autophosphorylation is facilitated by its catalytic site. My model only considers the counter-clockwise neighbor subunit because, in the absence of experimental observations to the contrary, I assume that steric effects cause autophosphorylation to occur in only one direction about a CaMKII ring, similar to previous work [284, 285]. The rate of autophosphorylation, 1 s^{-1}, at Thr-286 is taken from an earlier study of CaMKII autophosphorylation in the presence of CaM [97].

De-phosphorylation of pThr-286 is facilitated by binding and enzymatic activity of protein phosphatases PP1 and PP2A, here referred to generally as PP [277, 278]. Two rules govern PP binding to a CaMKII subunit (the transition from pThr-286 to a phosphatase-bound state): that the subunit be 1) pThr-286 and 2) un-bound to CaM. It has been shown that a majority of autophosphorylated CaMKII in the PSD is dephosphorylated by PP1 [286, 287]; while in brain extracts autophosphorylated CaMKII is mostly dephosphorylated by PP2A [277]. The requirement that CaM be unbound from CaMKII in order for PP to bind to CaMKII is motivated by the observation that simultaneous binding of CaM and PP to the CaMKII regulatory domain may be mutually exclusive due to steric hindrance. CaM, having molecular weight 18 kDa, binds to the CaMKII regulatory domain around residues 290–309 [284, 288, 289], which is at least 4 residues, and at most 23 residues away from Thr-286 (again, see also Figure 5 in [269]). To the best of my knowledge, the peptide binding footprint of neither PP (PP1 nor PP2A) onto CaMKII is not yet fully described. However, both PP1 and PP2A are widely known to target pThr-286 [104, 286,

287] and de-phosphorylate threonine residues nearby alpha helices in other substrates [290, 291]. Additionally, the catalytic subunit of PP1 has a molecular weight of 37 kDa, which is nearly twice that of CaM and more than half that of a CaMKII subunit. Taken together, I hypothesize that the PP binding footprint likely overlaps with the CaM binding site, such that the presence of bound PP likely structurally excludes or impedes upon a subsequent binding of CaM to CaMKII. Similarly, the presence of bound Ca^{2+}/CaM structurally would exclude coincident binding of PP. In the Supplement to Chapter 5, I further discuss the quantitative basis of this structural exclusion hypothesis in light of the crystal structure of the PP1-spinophilin interaction (PDB: 3EGG) [292]. In short, PP1 tends to bind substrates at a site >20Å from the PP1 active site. Thus, if the PP1 binding footprint does not actually contain T286, then the furthest likely CaMKII residue of PP1 binding (at least on the hub domain side of T286) is G301, well within the CaM binding footprint (see the Supplement to Chapter 5). I examine the regulatory implications of this hypothesis by relaxing the rules of PP binding and requiring only that the subunit be pThr-286. The association, dissociation, and catalytic rates of PP for CaMKII are taken from Zhabotinsky (2000), using a Michaelis constant of 6 μM and a catalytic rate of 2 s^{-1} [216].

5.3.1.6 Phosphorylation at Thr-306

Phosphorylation at the residue Thr-306 is a binary flag that describes this site as either un-phosphorylated ("uThr-306") or phosphorylated ("pThr-306"). I model the transition from uThr-306 to pThr-306 using three rules: that that the subunit be 1) uThr-306, 2) active, and 3) un-bound by CaM. My model uses a forward rate parameter 50-fold slower than that of phosphorylation at Thr-286, based on past experimental measurements [271, 293]. Over the course of my simulation times, I observe very few pThr-306 transitions and therefore exclude the reverse transition reaction describing de-phosphorylation of pThr-306 into uThr-306.

5.3.2 Stimulation frequency correlates with subunit activity

To validate my model, I assessed a variety of model outputs under various regimes of Ca^{2+}/CaM stimulation. As a first assessment, I simulated a persistent Ca^{2+}/CaM bolus, similar to experiments by Bradshaw *et al*. (2002), who monitored CaMKII autophosphorylation over time [285]. In Figure 5.3 I simultaneously monitored the time-course concentration of CaMKII subunit flags indicating: initially-bound Ca^{2+}/CaM, fully-bound Ca^{2+}/CaM, active CaMKII, and pThr-286.

In the persistent, continuous presence of Ca^{2+}/CaM, the concentration of subunits with initially-bound Ca^{2+}/CaM (orange trace) is noisy and consistently low, implying that Ca^{2+}/CaM transiently binds subunits in an initially-bound conformation. That is, initially-bound Ca^{2+}/CaM seems rapidly to either dissociate or proceed to a fully-bound conformation. Fully-bound Ca^{2+}/CaM (red trace) subunit concentrations closely follow those of active CaMKII subunits (dark blue trace) over time, providing evidence that Ca^{2+}/CaM stabilizes CaMKII activation. Indeed, because the difference in concentrations of fully-bound Ca^{2+}/CaM and active CaMKII is always small, I observe that although unbound CaMKII may spontaneously activate, these activated subunits rapidly return to an inactive state and are not likely to progress to a phosphorylated (pThr-286) state. I next observe that the increase of CaMKII autophosphorylation at Thr-286 (cyan trace) over time is strongly associated with increases in the number of subunits that are fully-bound to Ca^{2+}/CaM and active subunits (dark blue and red traces, respectively). This is consistent with previous work showing that Ca^{2+}/CaM must be bound to CaMKII for pThr-286 to occur [284] and CaMKII Ca^{2+}-independent activity is strongly associated CaMKII autophosphorylation at Thr-286 [218, 282, 294, 295]. Furthermore, I observe in Figure 5.3A that more than 80 percent of CaMKII subunits are autophosphorylated at t=20sec, which is of similar magnitude and timescale as observed by Bradshaw *et al*. (see Figure 2A in [285]).

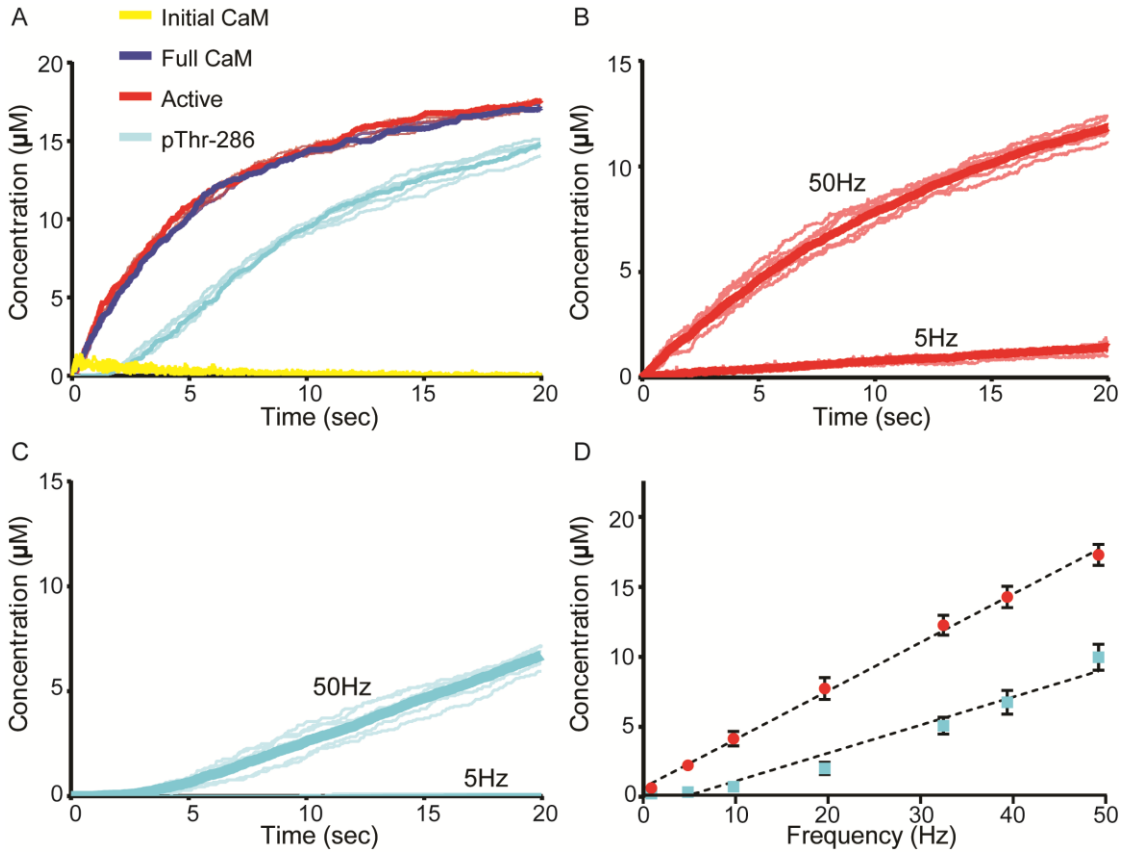

Figure 5.3. Validation of the Rule-based Model. Bold traces (A-C) and solid circles (D) are the average of N = 50 executions. For each species (A-C), six representative traces are also shown (semi-transparent lines). (A) Model output resulting from stimulation with a large continuous bolus of Ca^{2+}/CaM. Concentrations of active (red), initially CaM-bound (yellow), fully CaM-bound (blue), and pThr-286 (cyan) subunits. (B) Time-course average concentration (bold trace) of active subunits stimulated by 5 Hz or 50 Hz Ca^{2+}/CaM. (C) Time-course concentration of pThr-286 subunits stimulated continuously by 5 Hz or 50 Hz Ca^{2+}/CaM. (D) Frequency-dependent activation (red) and pThr-286 (cyan) of CaMKII subunits, with SEM error bars. Black dotted traces are linear fits.

Next, I assessed model behavior under low- and high-frequency stimulating conditions. CaMKII activation and autophosphorylation at Thr-286 in response to 5Hz and 50Hz Ca^{2+}/CaM is plotted in Figure 5.3 B and C, respectively; 50 seeds were run for each condition, with 6 representative traces (transparent lines) and the average response (bold) plotted. As expected, the data showed significantly greater levels of CaMKII activation and autophosphorylation at 50Hz [26, 46]. Indeed, I compared my result in Figure 5.3C to work by Shifman *et al.* (2006), who observed much lower autophosphorylation at low Ca^{2+}/CaM concentrations (less than 2 μM) than at high concentrations (see Figure 4D in [97]). Therefore, because my 50Hz model cumulatively

exposes CaMKII to approximately ten times as much Ca^{2+}/CaM per second as my 5Hz model, my results in Figure 5.3C are consistent with Shifman *et al.*, showing much higher autophosphorylation at 50Hz than 5Hz.

To further determine how stimulation frequency affects CaMKII activity, the model was stimulated at frequencies ranging from 1Hz to 50 Hz. At each frequency, models were sampled at 20 seconds of simulation time. I observe a nearly linear correlation between both subunit activation (R^2 = 0.99) and pThr-286 (R^2 = 0.96) and stimulation frequency (Figure 5.3D). This result is consistent with computational results from Chao *et al.*, who developed a stochastic model that also yielded a linear relationship between pThr-286 and stimulation frequency for frequencies greater than 1 Hz [15]. Additionally, my results in Figure 5.3D show that the model elicits ~10% (~2μM out of 21μM total) CaMKII pThr-286 in response to 10Hz stimulation, which is in agreement with experimental results given my relatively short pulse width of 10msec (see Figure 4A in [296]). Taken together, these results show that my model behaves as expected and is able to produce CaMKII activity and autophosphorylation behaviors similar to previous computational and experimental results.

5.3.3 A thresholded response of CaMKII to Ca^{2+}/CaM

CaMKII has long been theorized to exhibit switch-like or bistable behavior, which could underlie the importance of pThr-286 to learning and memory formation [216, 256, 280, 297, 298]. However, experimental efforts have struggled to identify a bistability between CaMKII and phosphatase activity. Though recently, Urakubo *et al*. used the chelator EGTA to control single pulses of Ca^{2+} in a mixture of CaM, CaMKII, PP1, and NMDAR peptides, leading to what seemed to be the first direct observation of CaMKII bistability [299]. Referring to Urakubo *et al.*, I explored whether a spatial stochastic model of the CaMKII dodecamer would exhibit near bistability or switch-like behavior for concentration parameters of Ca^{2+}, CaM, CaMKII, and PP known to exist in hippocampal spines. To explore this bistability, I stimulated the model with a set of short Ca^{2+}/CaM input pulses (which could also be reproducible *in vitro*). Importantly, I did not aim to identify true bistability because exploring the many combinations of Ca^{2+}, kinase, and phosphatase concentrations was outside the scope of this paper. Instead I wondered if, by stimulating with brief pulses of Ca^{2+}/CaM of variable duration, my model would exhibit switch-

reminiscent pThr-286 behavior. Specifically, I predicted a Ca^{2+}/CaM stimulation threshold below which pThr-286 was unachievable and above which pThr-286 was maintained.

In Figure 5.4 I exposed my model to single Ca^{2+}/CaM pulses of constant magnitude but of variable duration (similar to Figure 1B in [299]). The model was stimulated with single Ca^{2+}/CaM input pulses of magnitude 26 μM and varying duration (0.05, 0.1, 0.2, 0.3, 0.4, or 0.5 sec). Different pulse durations resulted in distinct levels of subunit activation, where longer pulse durations resulted in greater activation and autophosphorylation (p-Thr286) levels, (Figure 5.4 A and B, respectively). Interestingly, subunits stimulated by even the shortest pulses of 0.05 or 0.1 sec, appeared to sustain their activation for the complete simulation period (120 sec). However, these short-pulse (0.05-0.1 sec) stimulations rarely resulted in autophosphorylation (pThr-286, Fig 4B). Longer (0.2-0.5 sec) Ca^{2+}/CaM pulses resulted in greater levels of subunit activation that started declining immediately after the Ca^{2+}/CaM pulse ended (Figure 5.4A), but elicited pThr-286 levels that were generally sustained for the duration of a simulation (Figure 5.4B). Taken together, I found that CaMKII may be thresholded at a level of Ca^{2+}/CaM exposure below which pThr-286 is unobserved and above which pThr-286 is achieved and subsequently sustained across several minutes even in the presence of phosphatase.

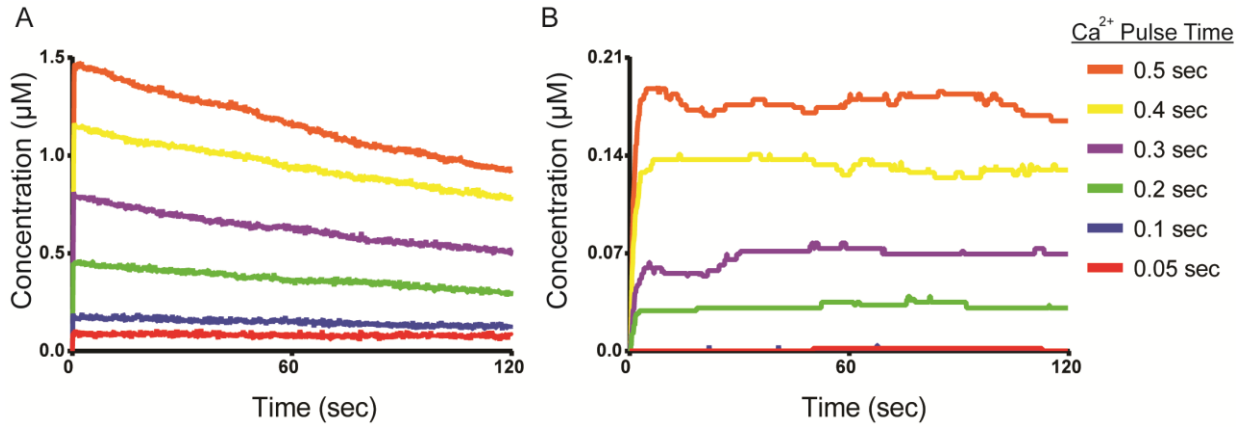

Figure 5.4. Response to short Ca^{2+}/CaM pulse stimulation. Average concentration of (A) active and (B) pThr-286 CaMKII subunits over time, following Ca^{2+}/CaM stimulating pulses of length 0.05 (red), 0.1 (blue), 0.2 (green), 0.3 (purple), 0.4 (yellow), and 0.5 (orange) seconds. Each trace represents the average of N=50 executions.

I briefly explored how this Ca^{2+}/CaM threshold may depend on the number of directions by which subunits can autophosphorylate their neighbors. Note that in the results up to this point,

autophosphorylation was limited to occurring in a single direction, or degree of freedom. That is, subunits could only autophosphorylate their adjacent neighbors [218]. I therefore created alternative versions of my model in which autophosphorylation could occur with multiple degrees of freedom, both intra- and/or trans- holoenzyme ring. I used these higher-degree of freedom models to monitor the rates of pThr-286 formation both in bulk and on an individual subunit basis. As expected, pThr-286 formation and intra-holoenzyme propagation rates increased with increasing degrees of freedom (see S1 Appendix, Figure S2.2), though the differences would likely not be distinguishable by bench-top experimentation. In addition, the length of time in which consecutive subunits remained autophosphorylated also increased with increasing degrees of freedom. This implied that subunits may be more frequently autophosphorylated on time-average with increasing degrees of freedom (See Figure 7.12 and Figure 7.13). Future experimental and computational studies could perhaps explore autophosphorylation with higher degrees of freedom.

Figure 5.4 suggested a threshold of Ca^{2+}/CaM activation beyond which CaMKII remains autophosphorylated, implying a balance between kinase and phosphatase activity. I wondered how a putative balance between CaMKII autophosphorylation and phosphatase activity might be regulated. In the previous experimental work by Urakubo *et al.*, maximally-phosphorylated CaMKII was maintained in the presence of PP1 and GluN2B peptide for as long as 8 hours (at 4°C). In that work, addition of the kinase inhibitor K252a to phosphorylated CaMKII resulted in a steady decline in pThr-286 towards basal levels, suggesting that maintenance of pThr-286 over time was not due to low phosphatase activity, but rather a recovery of de-phosphorylated subunits back a phosphorylated state. To recreate inhibition of kinase activity in my model, at time t=30 sec I introduced a high concentration (21 μM) of K252a, enough to bind all CaMKII subunits in the model. K252a binding results in a blocked CaMKII state that cannot be autophosphorylated (see Flag 2 in Table 7.8). Importantly, the blocked CaMKII subunit can still be de-phosphorylated at pThr-286. In separate simulations I explored the effects of a phosphatase inhibitor, which was also introduced at t=30sec. To simulate the introduction of a phosphatase inhibitor, I defined the catalytic rate of de-phosphorylation by PP1 (k_{cat}^{PP1}) as a time-dependent variable that assumed a value of zero at t = 30sec. This implementation of kinase and phosphatase inhibition preserved normal CaM and PP1 binding dynamics.

I compared non-inhibited, control versions of my model to versions in which kinase activity or phosphatase activity was inhibited after stimulating with Ca^{2+}/CaM for 2 sec (Figure

5.5). As expected, inhibiting phosphatase activity (green trace) caused kinase activity to dominate, resulting in a steady increase in pThr-286 compared to the control (black trace). Surprisingly, the kinase-inhibited model (blue trace) showed little difference compared to the control. Instead of causing phosphatase activity to dominate, simulated kinase inhibition caused pThr-286 activity to persist as if no kinase inhibitor were present. Because pThr-286 persisted even in the presence of kinase inhibitor, I hypothesized that some other, non-enzymatic mechanism in my model was contributing to the maintenance of pThr-286.

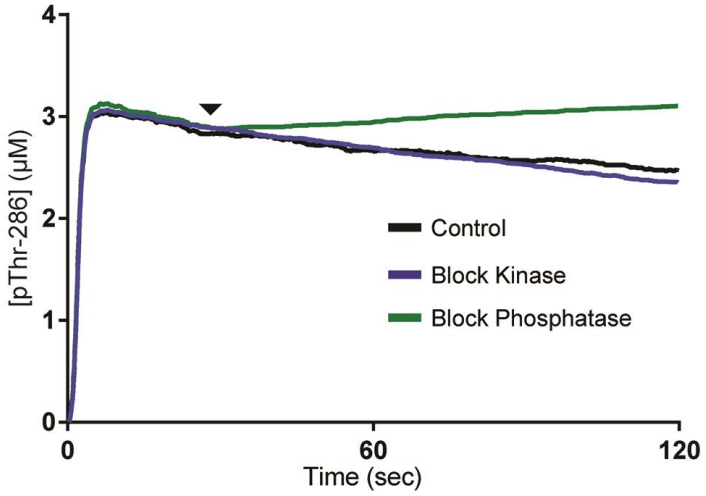

Figure 5.5. Blocking kinase or phosphatase activity. Average concentration of pThr-286 CaMKII subunits over time. For all traces, the model is stimulated by a 2 sec pulse of Ca^{2+}/CaM. At time t=30 sec (arrowhead), either a kinase inhibitor (blue trace) or phosphatase inhibitor (green trace) is introduced. No inhibitor is introduced in the control (black trace). Each trace represents the average of N=50 executions.

5.3.4 CaM-dependent exclusion of PP1 binding stabilizes autophosphorylation

To understand why my model as-presented in Figure 5.5 showed no significant response to kinase inhibition, I wondered if another mechanism was regulating the putative balance between kinase and phosphatase activity. In every simulation presented thus far, I assumed that CaM binding to the CaMKII regulatory domain sterically hinders PP binding to the regulatory domain, and vice-versa. This was implemented in the model via a rule that requires a subunit be unbound by CaM in order for PP to bind.

To test the role of PP exclusion by CaM, I created a second version of my model in which PP binding would become allowable regardless of the presence of CaM. In contrast to my original

"exclusive" model, the "non-exclusive" model required only that a subunit be pThr-286 in order for PP binding to be allowable. In other words, the non-exclusive model allowed Ca^{2+}/CaM and PP to bind CaMKII agnostically of each other. Aside from this rule adjustment, my exclusive and non-exclusive models utilized identical parameters. As in Figure 5.5, I selected a Ca^{2+}/CaM bolus time of 2 sec. Again, I monitored both CaMKII activation (Figure 5.6 A and B) and pThr-286 (Figure 5.6 C and D) over 120 seconds of simulated time. Critically, both the exclusive and non-exclusive models were examined with high (purple trace) and low (orange trace) association rate parameter values for PP binding to CaMKII. Increasing and decreasing the association rate of PP (k_{on}^{PP} is normally set to 3 $\mu M^{-1}sec^{-1}$) to CaMKII by one order of magnitude accounted for parameter uncertainty and provided a magnified view of the signaling effects of CaM-mediated exclusion of PP binding.

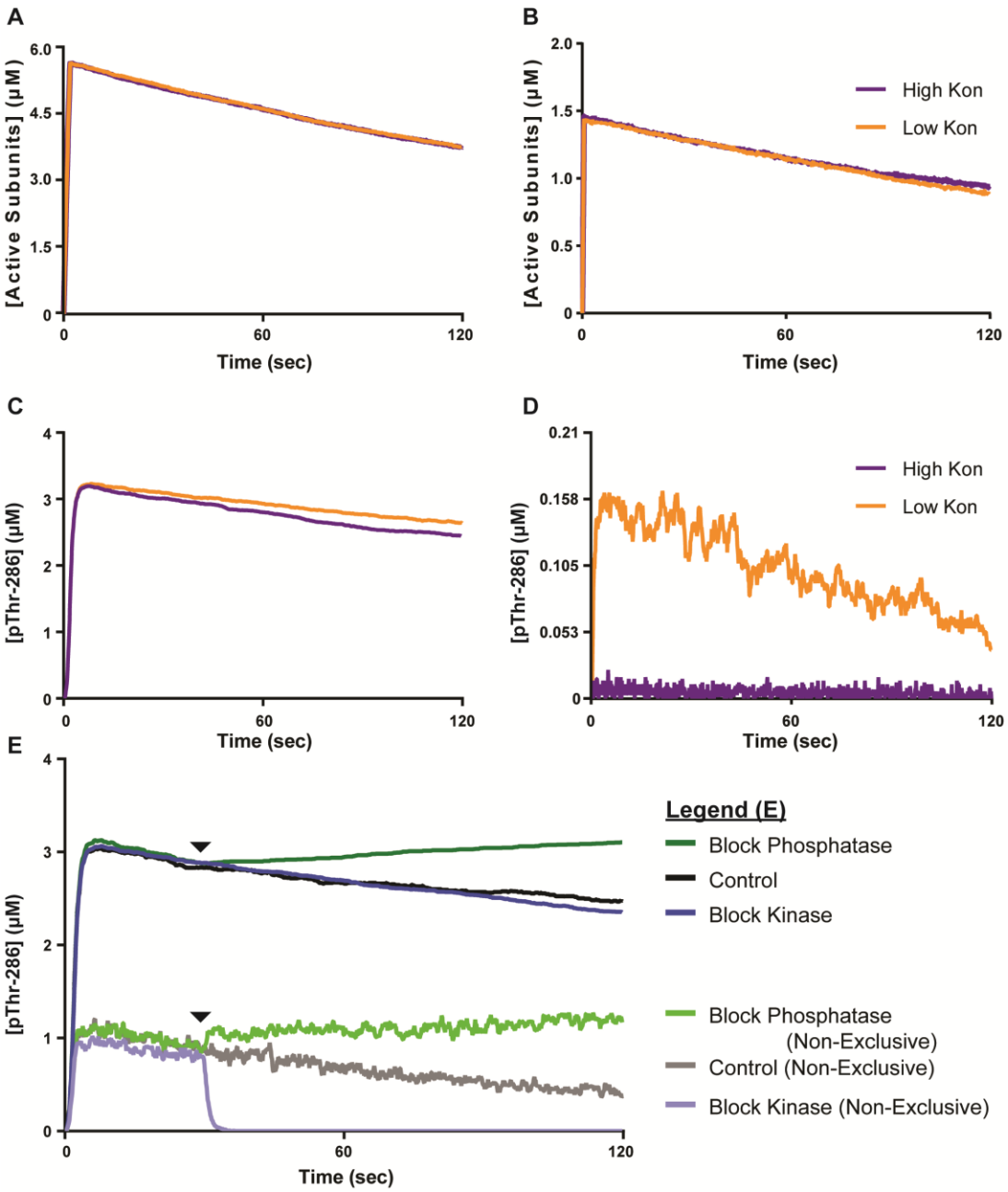

Figure 5.6. Comparison of Exclusive and Non-exclusive Models. For all traces, models are stimulated by a 2sec pulse of Ca^{2+}/CaM**.** (A) Active CaMKII subunits over time in my exclusive model. (B) Active CaMKII subunits over time in my non-exclusive model. (C) pThr-286 subunits over time in my exclusive model. (D) pThr-286 subunits over time in my non-exclusive model. (A-D) The parameter value for the rate of PP association (k_{on}^{PP1}) with CaMKII is either increased (purple traces) or decreased (orange traces) by one order of magnitude. (E) Extension of Figure 5.5 to include non-exclusive model results. At time t=30sec (arrows), either a kinase inhibitor (light blue trace) or phosphatase inhibitor (light green trace) is introduced. No inhibitor is introduced in the control (grey trace). All traces are the average of N=50 executions.

My results suggested that CaM-dependent exclusion of PP is an important regulatory mechanism for maintaining CaMKII autophosphorylation levels. While the PP exclusion rule had little to no effect on CaMKII subunit activation (Figure 5.6 A and B), pThr-286 (Figure 5.6 C and D) was highly influenced by the PP exclusion rule. In the exclusive model (Figure 5.6C), pThr-286 levels were steady and stable despite varying the PP association rate parameter by two orders of magnitude. In contrast, the non-exclusive model (Figure 5.6D) showed that for a high PP association rate, significant pThr-286 levels were never achieved. Moreover, for a low PP association rate, the non-exclusive model briefly attained pThr-286 levels similar to those achieved in the exclusive model, but the pThr-286 levels then declined while also displaying a high level of noise. It seemed that in order to maintain pThr-286 over longer time periods, CaMKII required a mechanism regulating phosphatase access, and a regulator of phosphatase access could be CaM itself.

To reinforce my assertion that CaM-dependent structural exclusion of PP binding stabilizes pThr-286, I repeated simulations shown in Figure 5.5, but with my non-exclusive model. In Figure 5.6E, I stimulated my non-exclusive model with a 2sec pulse of Ca^{2+}/CaM and then monitored pThr-286 over time. For these simulations, k_{on}^{PP1} was restored to its standard value of 3 $\mu M^{-1}sec^{-1}$. As in Figure 5.5, in separate simulations I inhibited at t=30sec either phosphatase activity, kinase activity, or neither (control). The control (grey trace) was reminiscent of results in Figure 5.6D, in which pThr-286 was achieved but then slowly declined on a steady yet noisy basis. Notably, all non-exclusive model variants were much noisier than their exclusive model counterparts in Figure 5.6E. Inhibiting phosphatase activity (light green trace) in the non-exclusive model again caused kinase activity to dominate and pThr-286 levels to generally increase over time, similarly to the exclusive model. In contrast to the exclusive model, inhibiting kinase activity (light blue trace) in the non-exclusive model rapidly and totally abolished pThr-286. It seemed that for the non-exclusive model, in which CaM and PP could bind simultaneously, inhibiting kinase activity caused phosphatase activity to dominate. Taken together, these results suggested that in addition to supporting CaMKII subunit activation, CaM also has a role in maintaining CaMKII activity by blocking phosphatase access and thereby slowing down dephosphorylation.

CaM-dependent exclusion of PP1 binding may depend significantly on how I model Ca^{2+}/CaM. Until this point, I have modeled Ca^{2+}/CaM as "2-state-2-step", existing as either Ca^{2+}-unbound apo-CaM or CaM_4 (2-state), which binds CaMKII in an initially- then fully-bound

conformation (2-step). However, previous experimental and computational studies have determined that sub-saturated Ca^{2+}/CaM, with fewer than four Ca^{2+} bound, may significantly bind CaM-binding partners such as CaMKII [42, 97]. Indeed, Pepke *et al*. [42] and others use a "9-state-1-step" model of Ca^{2+}/CaM, which explicitly accounts each mode of Ca^{2+}-binding at the CaM N- and C-termini. Importantly, each Ca^{2+}/CaM state in the 9-state model has unique binding kinetics for CaMKII. However, I emphasize that these 9-state binding kinetics, which were measured using wild-type CaMKII *in vitro*, are incompatible with my 2-step CaM-binding model. In other words, a 9-state-2-step CaM-CaMKII model is difficult to parameterize because the 9-state parameter values inherently account for 2-step CaM-binding (if it in fact occurs physiologically). Moreover, the 9-state-2-step model would likely require a multi-state, rule-based model of CaM. And problematically, MCell 3.3 prohibits diffusion for rule-based species. Still, it is important to consider whether sub-saturated Ca^{2+}/CaM states might still be able to structurally exclude, or kinetically out-compete, PP1-CaMKII binding.

Although a 9-state-2-step model of CaM-CaMKII binding is currently impractical with MCell 3.3, a 9-state-1-step model of CaM-CaMKII binding is practical, at least to verify my PP1-exclusion mechanism when accounting for sub-saturated Ca^{2+}/CaM. For the 9-state-1-step model, I again use MCell 3.3 to describe the multi-state CaMKII holoenzyme, but I modify three of the flags described earlier in this paper. First, I remove the subunit docking and activation flags to reduce model noise and ensure the 9-state CaM-binding parameters remain valid. Second, I modify the CaM-binding flag to allow all nine Ca^{2+}/CaM states (including apo-CaM) to bind a CaMKII subunit. Thus, whereas in the 2-state-2-step CaMKII model subunit activation is equivalent to subunit opening, in the 9-state-1-step model activation is equivalent to CaM-binding. The parameters and reaction network for Ca^{2+}-CaM binding and CaM-CaMKII binding may be found in Pepke *et al*. (see Figure 2C in [42]). With my 9-state-1-step model in place (MCell code provided in the PURR repository—see Methods), I simulate using identical conditions to those used for Figure 5.6A-D. My 9-state-1-step model results are shown in Figure 5.7, where I again show that CaMKII subunit activation and pThr-286 levels are maintained on significantly longer timescales when CaM and PP1 cannot bind CaMKII simultaneously (Figure 5.7 A and D). Note the increased activation and pThr-286 levels and reduced output noise are almost certainly due to the absence of the docking and activation flags, which pose significant obstacles to CaM-binding in the 2-state-2-step model presently in the rest of this paper. Finally, I observe that when only

fully-saturated CaM_4 but no other Ca^{2+}/CaM state is allowed to exclude CaM (Figure 5.7 B and E), model output is virtually identical to the non-exclusive case (Figure 5.7 C and F). This suggests that sub-saturated Ca^{2+}/CaM states may significantly contribute to PP1 exclusion. Indeed, this may be unsurprising given the affinity of states such as CaM_{2C} for CaMKII (7.4μM), which is only one order of magnitude larger than that of PP1 for CaMKII (0.166μM). Notably, because I explicitly account for CaM-trapping in my 9-state-1-step model, the CaM_{2C}-CaMKII affinity increases by 1000-fold when a CaMKII is subunit is pThr-286 [300]. Therefore, sub-saturated Ca^{2+}/CaM states, including apo-CaM, are very likely to out-compete PP1 and prevent its binding to pThr-286 subunits, at least from a kinetics perspective.

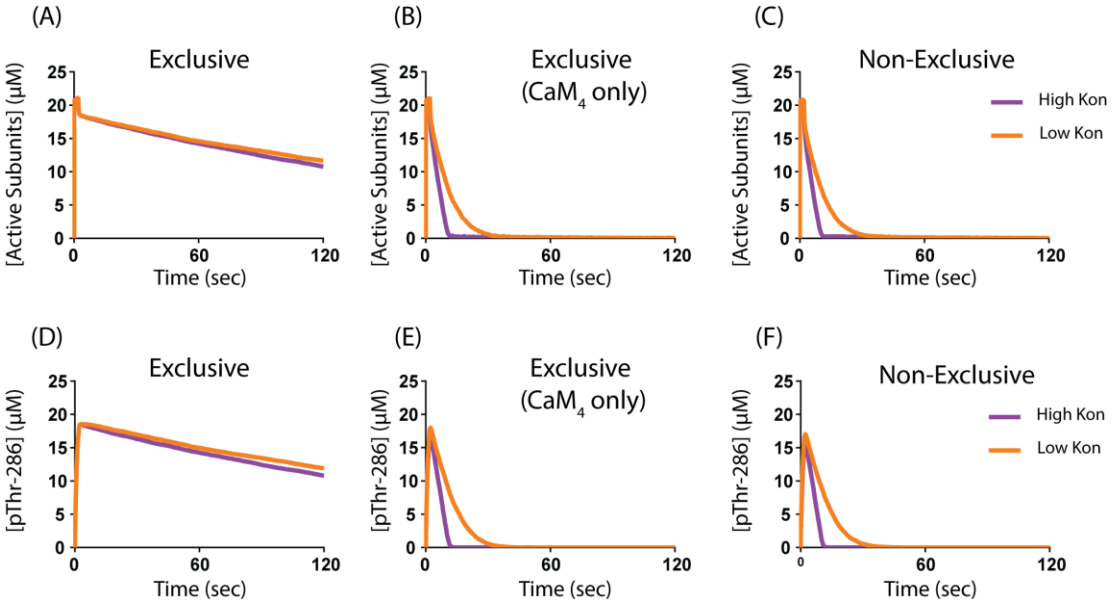

Figure 5.7. Exclusion in a 9-state-1-step CaM-CaMKII model. For all traces, models are stimulated by a 2sec pulse of Ca^{2+}/CaM**.** (A-C) Active CaMKII subunits over time in my 9-state-1-step model. (D-F) pThr-286 subunits over time. The parameter value for the rate of PP association (k_{on}^{PP1}) with CaMKII is either increased (purple traces) or decreased (orange traces) by one order of magnitude. Because this model version has inherently less output noise, all traces are the average of N=20 executions.

5.3.5 Discussion

In this work, I use rule- and particle-based methods with the software MCell to model the complete CaMKII holoenzyme. Rule-based modeling allows me to account for and monitor multiple CaMKII states simultaneously without eliciting combinatorial explosion. By explicitly

accounting for multiple CaMKII states, I can use this model to explore regulatory mechanisms such as the CaM-dependent maintenance of pThr-286 by structural exclusion of phosphatase binding to CaMKII.

Previous multi-state models of CaMKII exist but are different in focus and in scope from the present model. For example, my model is based on an earlier multi-state model by Stefan *et al*. (2012) [269] implemented in the particle-based stochastic simulator StochSim [301]. StochSim accounts for subunit topology (i.e. the user can specify whether a subunit is adjacent to another, and reactions can be neighbor-sensitive), but StochSim does not explicitly account for spatial information. MCell, as a spatial simulator, offers more possibilities to precisely account for spatial effects and to situate models in spatially realistic representations of cellular compartments. In addition, the model by Stefan *et al*. provides only for interactions between adjacent CaMKII molecules on the same hexamer ring and therefore models CaMKII as a hexamer, not a dodecamer. Similarly, another previous model of CaMKII by Michalski and Loew (2012) uses the softwares BioNetGen and VCell to offer an infinite subunit holoenzyme approximation (ISHA) of the CaMKII hexamer [44, 302, 303]. The ISHA asserts that under certain enzymatic assumptions, the output of a multi-state CaMKII model is independent of holoenzyme size when the number of subunits exceeds six. However, Michalski's ISHA model is most suitable for systems containing only one holoenzyme structure-dependent reaction such as the autophosphorylation at Thr-286. Additional reactions to describe actin binding [244] or subunit exchange [261, 262] may invalidate Michalski's ISHA, whereas my model can in the future readily accommodate additional, holoenzyme structure-dependent phenomena. Finally, a more recent rule-based model of the CaMKII holoenzyme by Li and Holmes [45] offers a detailed representation of how CaM binds to Ca^{2+} and subsequently activates CaMKII subunits, based on earlier results of CaM regulation [15]. Li and Holmes offer valuable and detailed insight into how CaM binding to CaMKII depends on Ca^{2+} dynamics. While my model is less detailed in representing the regulation of CaM itself, my model is much more detailed in representing other aspects of CaMKII regulation, including multiple modes of CaM binding, conformational change, detailed holoenzyme structure, multiple phosphorylation sites, and dephosphorylation. I can in the future expand my MCell model to account for multiple holoenzyme structure-dependent phenomena and simultaneously incorporate this model into the broader Ca^{2+}-dependent signaling network.

This work in-part demonstrates the value of MCell as a rule-based modeling framework. Rule-based modeling accommodates much larger state spaces than is possible using conventional systems of differential equations. Admittedly, not all models (including models of CaMKII) require extensive state spaces, but rule-based modeling results can help justify the assumptions typically used to reduce a state space. For example, my model conditions yield, as shown in Figure 5.3A, negligible levels of initially-bound CaM compared to other states such as fully-bound CaM or pThr-286. Therefore, it might sometimes be appropriate to exclude an initially-bound CaM state from future implementations in frameworks for which combinatorial explosion is a concern. Aside from addressing combinatorial explosion, rule-based models are especially well-suited to discern otherwise concealed mechanisms, as exemplified by Di Camillo *et al*. who used rule-based models to identify a robustness-lending negative feedback mechanism in the insulin signaling pathway [49]. Furthermore, MCell describes CaMKII holoenzymes as discrete particles in space, which will lend realism to future spatial-stochastic models of Ca^{2+}-dependent signaling networks in the dendritic spine, a compartment in which the Law of Mass Action is invalid [24]. This particle-based framework also allows for individual subunit monitoring, which works in conjunction with the Blender software plugin, CellBlender (see S1 Movie).

One of the results of this work is the identification of distinct levels of CaMKII activation and pThr-286 in response to distinct pulses of Ca^{2+}/CaM stimulation. Distinct levels of CaMKII activation could tune the selectivity of CaMKII for certain downstream binding targets such as AMPA receptors or the structural protein PSD-95. If stimulation-dependent tuning of CaMKII activation were observed, it would be reminiscent of other studies that have implicated feedback loops [33] and binding dynamics [42] as regulators of Ca^{2+}-dependent enzyme activation. For example, a recent study suggests that competition is an emergent property that tunes the Ca^{2+} frequency dependence of CaM binding to downstream targets, leading Ca^{2+}/CaM to set distinct levels of calcineurin- and CaMKII-binding [46]. Similarly, CaMKII itself could preferentially select downstream binding partners as a function of its level of activation by Ca^{2+}/CaM, possibly providing a mechanism by which CaMKII facilitates certain LTP-related molecular events. Additionally, my observation of distinct levels of CaMKII activation and thresholded pThr-286 could be an indication of long-hypothesized switch-like behavior in synaptic plasticity [256, 297]. If switch-like behavior in fact occurs, then pThr-286 is likely maintained by a balance in kinase and phosphatase activity.

While investigating a putative interplay in CaMKII kinase and PP phosphatase activity in maintaining pThr-286 levels, I may have identified a CaM-dependent mechanism that blocks PP binding to CaMKII. In a model that excludes simultaneous binding of CaM and PP to CaMKII, pThr-286 significantly increases upon phosphatase inhibition, yet in the same model kinase inhibition causes little change in pThr-286 over time (Figure 5.5). In contrast, a non-exclusive model that allows simultaneous binding of CaM and PP shows that introduction of a kinase inhibitor rapidly abolishes pThr-286. These results suggest that CaM-dependent exclusion of PP may provide a stabilizing mechanism. Additionally, I use my MCell-based implementation of the model to monitor transitions between multiple states of distinct subunits within holoenzymes (Figure 5.8).

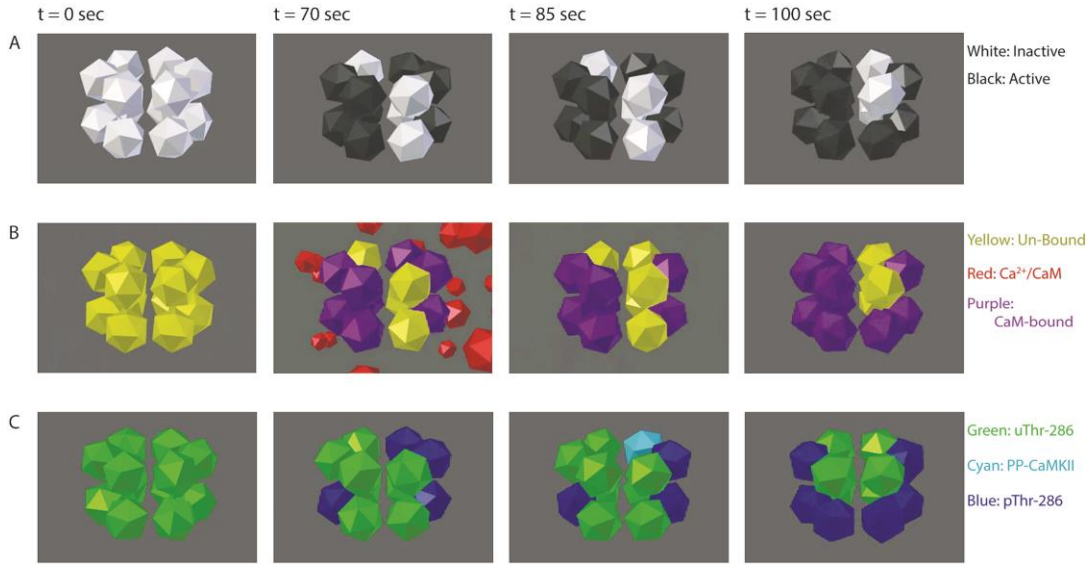

Figure 5.8. Visualizing Individual Subunits with MCell and CellBlender. In the exclusive model, PP does not bind a pThr-286 subunit until Ca^{2+}/CaM dissociation (see t = 85 sec, comparing rows B and C). Each frame depicts the same CaMKII holoenzyme, from the same perspective, at identical time points under 50Hz Ca^{2+}/CaM stimulation. Each dodecahedron is a single CaMKII subunit. (A) Inactive CaMKII subunits (white) spontaneously become active (black) and remain active while bound to Ca^{2+}/CaM. (B) Un-bound CaMKII subunits (yellow) will not bind Ca^{2+}/CaM (red) and become Ca^{2+}/CaM-bound (purple) unless the subunit had previously activated. (C) uThr-286 subunits (green) become pThr-286 (blue). If Ca^{2+}/CaM dissociates from a pThr-286 subunit, then PP can bind and form a PP-CaMKII complex (cyan).

The major outcome of this work is a proposed mechanism in which bound Ca^{2+}/CaM could exclude PP from accessing CaMKII subunits, thereby protecting pThr-286. I assert that CaM-

dependent exclusion of PP could provide a functional role for so-called "CaM trapping" [284] and possibly contribute to CaMKII bistability. Indeed, a model by Zhabotinsky (2000) explored CaMKII bistability, indicating that two stable states of pThr-286 would in-part require very high CaMKII concentrations, seemingly to bolster kinase activity in the system [216]. However, the Zhabotinsky model assumes that CaM and PP1 could bind CaMKII simultaneously, possibly exaggerating the ability of PP1 to de-phosphorylate at Thr-286. If PP1 binding were to be encumbered in the Zhabotinsky model, perhaps through CaM-dependent exclusion, then bistability might be achievable at lower CaMKII concentrations.

Previous studies have sought to explore the dependence of CaMKII de-phosphorylation on the presence of Ca^{2+}/CaM. An experiment by Bradshaw *et al*. (2003) quantifies PP1-mediated de-phosphorylation rates of pThr-286 *in vitro*, in the presence or absence of the Ca^{2+} chelator EGTA (see Figure 4B in [304]). The Bradshaw results suggest that PP1 activity at 0°C is unaffected by the presence of bound-CaM to CaMKII, seemingly at odds with the results of my model. However, the Bradshaw results show that regardless of the presence of CaM, CaMKII activation persists for at least tens of minutes. The persistence of CaMKII activity on relatively long timescales is consistent with separate experimental results [195, 285, 297, 300], and I emphasize that with my model, CaMKII activity persists for many minutes only when CaM excludes PP1. Indeed, the effect of CaM exclusion on the timescale of CaMKII activation is even more pronounced in my 9-state 1-step CaM-binding model results. Moreover, my 9-state-1-step model suggests that following termination of Ca^{2+} flux, sub-saturated Ca^{2+}/CaM states may significantly contribute to PP1-exclusion. Thus, because the Bradshaw experiments use EGTA to chelate Ca^{2+}, but not remove CaM, the Bradshaw experiments may be confounded.

In the Supplement to Chapter 5, I show that the Ca^{2+}/CaM state predominantly responsible for PP1-exclusion following termination of Ca^{2+} stimulation in the 9-state-1-step model is apo-CaM (Figure 7.17). Apo-CaM remaining bound to CaMKII is consistent with results by Brown *et al*., who determine that when free Ca^{2+} levels decrease, Ca^{2+} dissociates from CaM before CaM dissociates from its binding partner [119]. Of course, the affinity of apo-CaM for CaMKII (1.45mM) should be insufficient to out-compete PP1-CaMKII binding (1.6μM). Yet because the 9-state-1-step model explicitly accounts for CaM-trapping by increasing the affinity of pThr-286 subunits for Ca^{2+}/CaM by 1000-fold [300], the affinity of pThr-286 CaMKII for apo-CaM (1.45μM) is on the same order of magnitude as that of PP1. Thus, apo-CaM may be able to

significantly compete with PP1 for CaMKII-binding, but it now remains for future experimental studies to directly quantify the kinetics and/or structure of the apo-CaM interaction with pThr-286 CaMKII.

Further structural studies of the CaM-CaMKII and PP1-CaMKII interaction are needed. Also, because this work could only model multi-state CaMKII (but not also multi-state CaM) due to limitations in MCell 3.3, perhaps a future version of MCell should provide for the diffusion of multiple multi-state proteins. With a platform that can handle multiple multi-state proteins, a model could much more explicitly handle Ca^{2+}/CaM-binding and further explore my results.

CaM-dependent PP exclusion could provide an added layer of robustness to similar mechanisms that may protect pThr-286 from de-phosphorylation. For example, Mullasseril *et al*. (2007) observe that endogenous, PSD-resident PP1 cannot de-phosphorylate CaMKII at pThr-286, whereas adding exogenous PP1 does cause de-phosphorylation [298]. The results by Mullasseril *et al*. suggest that endogenous PP1 is somehow sequestered by the PSD scaffold, and only upon saturation of this scaffold by exogenous PP1 does pThr-286 become de-phosphorylated. My results indicate that perhaps in addition to saturating the PSD scaffold, the added exogenous PP1 could be out-competing CaM for binding to CaMKII, thereby terminating protection of pThr-286 by CaM. As another example, Urakubo *et al*. suggest that pThr-286 could be protected from PP activity by GluN2B binding, showing that GluN2B peptides are necessary for an apparent CaMKII bistability *in vitro* [299]. Notably, Urakubo *et al*. observe a decline in pThr-286 upon kinase inhibition, in contrast with my exclusive model, though this is likely due to differences in the conditions and timescales between Urakubo's experiments and my model. Moreover, it could be that the GluN2B-dependent PP exclusion suggested by Urakubo could operate on a longer timescale than CaM-dependent exclusion, and I again note that the Urakubo study did not remove CaM from any reaction mixture. Overall, it seems scaffold-dependent sequestration of PP1 [298], GluN2B-dependent PP exclusion [299], and CaM-dependent PP exclusion could together provide considerable robustness of pThr-286 to phosphatase activity.

5.4 Methods

In each MCell execution, proteins are instantiated at time zero having random positions within a 0.32 μm^3 (0.32 fL) cube. All proteins are described as three-dimensional volume molecules having the following concentrations: 1.52 μM CaMKII (30 holoenzymes, 360 subunits),

22.8 μM CaM (450 discrete proteins), and 0.86 μM PP1 (17 discrete proteins). Because CaMKII particles are modeled using the specialized COMPLEX_MOLECULE syntax and MCell 3.3 does not accommodate diffusion for such particles, CaMKII is given no diffusion constant. In contrast, CaM and PP1 are simple volume-type molecules that move about the model space with a diffusion constant 6×10^{-6} μm^2/sec, so chosen to minimize the effects of any possible spatial localizations that may arise during a simulation. I emphasize that because this model does not explore spatial effects and, indeed, does not utilize a physiological spine geometry, using such a relatively fast diffusion parameter ensures that spatial effects do not confound my results. All models are run at a time step of 0.1 μs for a total of either 20 or 120 seconds of simulation time, depending on the model variant.

MCell is a particle-based spatial-stochastic simulation engine. In a particle-based framework, individual protein species are modeled as discrete objects in space, rather than bulk/well-mixed fluids. At each model timestep, MCell calculates each protein particle's subsequent diffusion distance and trajectory, in addition to the particle's probabilities for reacting with any nearby particles. More information about MCell's internal algorithms may be found at mcell.org and in publications such as those by Bartol *et al*. [43]. In short, the particle-based framework in MCell provides for spatial and stochastic considerations because each protein particle has unique spatial coordinates that proceed along random (stochastic) trajectories. Importantly, I assert that spatial-stochastic frameworks may be essential to characterizing CaMKII regulation, because 1) proteins in the spine are spatially organized and 2) protein copy numbers in the spine are low (tens to hundreds each), possibly invalidating the Law of Mass Action. Because MCell models are stochastic and change with each simulation, I average the output of many identical simulations. To ensure that the averaged output converges and is statistically significant, all model variants are repeated 50 times each.

CaM activation/inactivation is modeled by a pair of forcing functions which serve as a proxy for Ca^{2+} flux. Both forcing functions are time-dependent square waves and inform the rates at which free CaM transitions between states. Equation 1 rapidly transitions all free CaM towards an active (Ca^{2+}/CaM) state, and Equation 2 rapidly transitions all free CaM towards an inactive (apo-CaM) state.

$$(1) F_{activation}(t) = \begin{cases} 100000000, t = n_i \\ 0, t \neq n_i \end{cases}$$

$$(2) F_{inactivation}(t) = \begin{cases} 0, t = n_i \\ 100000000, t \neq n_i \end{cases}$$

For both Equations 1 and 2, n = i/f where i is the number of time step iterations and f is frequency. Time t iterates at 0.01sec intervals for the complete duration of a simulation. Equations 1 and 2 therefore yield a peak width of 0.01sec regardless of frequency, which allows me to directly compare the effect of different Ca^{2+}/CaM frequencies on CaMKII activity, without having to account for variable amounts of Ca^{2+}/CaM exposure per pulse. In separate simulations without frequency dependence (i.e. Ca^{2+}/CaM is continuously available to CaMKII), Equation 1 is adjusted to always fulfill the $t=n_i$ condition. Similarly, for pulse simulations in which Ca^{2+}/CaM becomes withdrawn or blocked, Equations 1 and 2 are given abbreviated time domains.

All MCell code and associated files are available online at Github, the Purdue University Research Repository, and the University of Edinburgh Repository.

6. USING MCELL TO QUANTIFY THE EFFECTS OF CAMKII MULTIVALENCE ON PROTEIN SPATIOTEMPORAL DYNAMICS IN THE DENDRITIC SPINE

6.1 Summary

Following initiation of long-term potentiation (LTP), proteins localize to distinct sub-regions within the dendritic spine. Indeed, in Chapter 4 I demonstrate how Ca^{2+}, Ca^{2+}/CaM, and other protein states exhibit spatial dependence within the dendritic spine. For example, one protein state that exhibits strong spatial dependence is CaMKII. That is, in the presence of Ca^{2+} flux, I observe steep gradients of CaMKII activation along the major axis of the dendritic spine, with most active CaMKII in the top compartment of the spine. Because CaMKII is essential to synaptic plasticity and LTP, it may be important to characterize the mechanisms regulating CaMKII localization to the top of the spine, or post-synaptic density (PSD). CaMKII localization or mobility is likely regulated by its diffusion, interactions with the actin cytoskeleton, and affinity for its many enzymatic substrates, as others have previously explored. However, most studies do not account for, or are unable to quantify, the dependence of CaMKII localization on the protein's dodecameric quaternary structure. Otherwise put, CaMKII has a multivalence that could potentially increase its effective affinity for binding partners, perhaps significantly impacting its mobility within the spine. Therefore, here I combine modified versions of the models presented in Chapters 4 and 5 of this thesis, to quantify how CaMKII multivalence may contribute to the spatiotemporal dynamics of proteins within the dendritic spine. For this quantification, I compare output from a deterministic, non-spatial model of Ca^{2+}-dependent signaling against output from an equivalent but spatial-stochastic model of Ca^{2+}-dependent signaling. The spatial-stochastic model initially describes CaMKII as monomers, and then I incorporate a rule-based model of the CaMKII holoenzyme based on that first presented in Chapter 5. By comparing output from models with deterministic, spatial-stochastic, and rule-based frameworks, I show that CaMKII multivalence may significantly influence the spatiotemporal dynamics of cytosolic proteins in the spine, especially Ca^{2+}/CaM.

6.2 Introduction

The dendritic spine is a specialized structure on the message-receiving side of a neuronal connection, or synapse [27, 180]. The dendritic spine contains proteins that control synaptic plasticity, the process by which synapses dynamically shift in size and excitability [257, 305]. Downward shifts are called long-term depression (LTD), and upward shifts are called long-term potentiation (LTP). Both LTD and LTP elicit remodeling of the dendritic spine's actin cytoskeleton and membrane-associated receptors [3, 12, 256]. For example, LTP elicits actin cross-linking and remodeling close to the synaptic membrane, at a protein-rich region called the post-synaptic density (PSD). LTP also induces AMPA receptor (AMPAR) phosphorylation and trafficking to the synaptic membrane. Interestingly, both LTP- and LTD-associated actin and receptor regulation and are thought to be directly regulated by calcium/calmodulin-dependent protein kinase II (CaMKII) [219, 280]. CaMKII is one of the most highly expressed neuronal proteins and is essential to synaptic plasticity [260, 306, 307]. Characterizing the complex and dynamic interactions between CaMKII, actin, AMPARs, and other proteins is likely necessary for understanding the molecular regulation of synaptic plasticity.

CaMKII holoenzymes have twelve subunits, each of which can bind and/or phosphorylate a variety of proteins in the dendritic spine [218, 260, 262]. In a naïve spine, CaMKII subunits are generally inactive and therefore bound to F-actin throughout the dendritic spine head [37, 244]. Following influx of Ca^{2+} through NMDA receptors (NMDARs), the Ca^{2+}-sensor calmodulin (CaM) activates CaMKII, terminating the actin-CaMKII interaction [239, 240]. Termination of this interaction allows the F-actin scaffold to structurally remodel and CaMKII to translocate to the PSD [237, 308], both by unclear mechanisms. Once localized to the PSD, active CaMKII has a variety of targets such as NMDARs [236] and AMPARs [33, 199]. The mechanisms and conditions by which AMPARs subsequently become phosphorylated and localized to the synaptic membrane remain unclear. When intracellular Ca^{2+} levels decrease and CaMKII returns to an inactive state, CaMKII re-binds the remodeled F-actin filaments near the synaptic membrane, seemingly acting as a cross-linking or actin-bundling agent [239, 242, 309].

Previous experimental studies have explored CaMKII localization in the dendritic spine. Notably, this CaMKII localization is essential to synaptic plasticity [256]. For instance, studies have determined that CaMKII localization at the spine head in response to Ca^{2+} influx is due to both diffusion and protein binding [237]. More recently, single-molecule photoactivated

localization microscopy (PALM) has been used to identify immobilized sub-populations of CaMKII at not only the PSD but other microdomains in the spine [38].

In particular, there is strong evidence that CaMKII localization is dependent on subunit isoform [38]. In the brain, CaMKII holoenzymes are heteromers of the alpha and beta subunit isoforms, which are expressed at a ratio of approximately 3:1 [260]. This ratio may be important to synaptic plasticity because of the distinct kinetics of alpha and beta CaMKII for actin binding sites, as determined by Hoffman *et al*. [310]. To quantify these distinct kinetics, Khan *et al*. use total internal reflection fluorescence (TIRF) microscopy to track single molecules and subsequently measure the kinetics of both alpha and beta CaMKII binding to actin [244]. The dissociation constant for beta CaMKII binding actin (0.5 μM) is one order of magnitude smaller than that of alpha CaMKII (1.4 μM). Thus, the question of how CaMKII holoenzymes become localized and select phosphorylation targets becomes even more complex.

To help understand the highly dynamic and crowded signaling pathways in the dendritic spine, bench-top studies can be complemented by computational models. For example, Byrne *et al*. use Monte Carlo simulations to describe discrete CaMKII monomer particles in a spine, showing how spine geometry, binding interactions at the PSD, and encumbrance by F-actin contribute to the Ca^{2+}-induced accumulation of CaMKII at the PSD [245]. The study determines that individual CaMKII monomers are likely too diffuse to remain localized to the PSD, even if their binding affinities are assumed to be high. Byrne *et al*. therefore conclude that either an F-actin barrier and/or multivalent interactions may be necessary to prevent CaMKII escape. To quantify how F-actin and multivalence contribute to CaMKII localization, the field requires further computational modeling to account for both the complex Ca^{2+}/CaM-CaMKII signaling dynamics and complicated CaMKII structure. Currently, models describing Ca^{2+}/CaM signaling dynamics are available [21, 32, 42, 46, 92, 165], but these generally describe CaMKII as non-multivalent monomers. Notably, models of the multivalent CaMKII holoenzyme exist but do not explicitly account for distinct CaMKII subunit kinetics or quantify the specific contributions of CaMKII multivalence on spatiotemporal dynamics of proteins in the spine [44, 45].

Thus, here I demonstrate a strategy for quantifying the effects of CaMKII multivalence and subunit isoform type on the spatiotemporal dynamics of Ca^{2+}-dependent proteins in the dendritic spine. For this, I model with three distinct frameworks a reaction network consisting of Ca2+, CaM, nine CaM-binding proteins (CBPs), CaMKII interactions with actin binding sites, CaMKII

autophosphorylation, and CaMKII phosphorylation of NMDARs and AMPARs. My first model framework is a deterministic system of ordinary differential equations describing the time-rate of change of each protein state independently of spatial effects. Importantly, the deterministic model framework provides for rapid model validation and computationally tractable global sensitivity analysis. My second model framework is a spatial-stochastic implementation in MCell 3.3, which describes each protein, including CaMKII, as discrete monomers in space. Finally, my third model framework is a spatial-stochastic implementation incorporating the rule-based model syntax of MCell 3.3, allowing me to describe multi-state proteins such as the twelve-subunit CaMKII holoenzyme. By comparing my MCell 3.3 and rule-based model results, I can quantify how CaMKII multivalence might impact the activation and/or localization of CaMKII and other proteins in the dendritic spine.

6.3 Results

6.3.1 Model Development

6.3.1.1 Model Structure

The reaction network accounts for Ca^{2+} flux, Ca^{2+}-CaM binding, CaM-dependent activation of CBPs such as CaMKII, CaMKII interactions with actin binding sites, and CaMKII-mediated phosphorylation of membrane-associated receptors.

Ca^{2+} fluxes into the dendritic spine at a range of frequencies. Low frequency (<10Hz) Ca^{2+} flux results in Ca^{2+}/CaM states that may predominantly activate LTD-associated CBPs. In contrast, high frequency (~100Hz) Ca^{2+} flux results in Ca^{2+}/CaM states that may predominantly activate LTP-associated CBPs. Notably, besides Ca^{2+} frequency, the magnitude, location, and pattern of Ca^{2+} flux can also influence intracellular Ca^{2+} signaling within the spine [23, 41, 311]. However, for simplicity this study excludes Ca^{2+} flux through voltage-gated and other Ca^{2+} channels, and I ignore Ca^{2+}-buffering by proteins besides CaM. Therefore, I control Ca^{2+} flux in all simulations to have constant magnitude (12 μM [164]), location (in spatial models, via NMDARs at the top of the spine), and uniformly-spaced patterning. Thus, all model output is a function of Ca^{2+} frequency alone.

Up to four Ca^{2+} can bind CaM, two at each of the EF-hand domains located at the CaM N- and C- termini [14]. Both CaM termini bind Ca^{2+} cooperatively but with distinct kinetics.

Importantly, these distinct kinetics may cause sub-saturated Ca^{2+}/CaM states (with fewer than four bound Ca^{2+}) to predominate at various Ca^{2+} frequencies. Because sub-saturated Ca^{2+}/CaM states exhibit distinct affinities for various CBPs, it may be important to explicitly account for them in computational models [97]. Here, I use a thermodynamically-complete, nine-state model of Ca^{2+}-CaM binding first presented by Pepke *et al*. (see Fig 2C in [42]). Although other models [46, 165] use a simpler, four-state model of Ca^{2+}-CaM binding also presented by Pepke *et al*., my usage of MCell as a spatial-stochastic framework requires the more complex nine-state model. Specifically, I use the nine-state model because the alternative four-state model causes MCell to calculate inaccurately small probabilities for trimolecular reactions (2 Ca^{2+} plus 1 CaM; see mcell.org and [43, 229]).

Each of the nine Ca^{2+}/CaM states (including apo-CaM [35, 116]) in my model have distinct, explicitly-defined binding kinetics for each of my nine CBPs. These CBPs include adenylyl cyclase 1 (AC1) [235], adenylyl cyclase 8 N- and C-termini (AC8-Nt and -Ct) [189], calcineurin (CaN), CaMKII, myosin light chain kinase (MLCK) [231], neurogranin (Ng), nitric oxide synthetase (NOS) [205], and phosphodiesterase 1 (PDE1) [21, 198]. I emphasize that with the exception of CaMKII, this model does not include the known enzymatic functions of these CBPs, each of which are discussed by Pharris *et al*. [165]. Explicitly defining CBPs helps in accurately accounting for competition for CaM-binding, which may be important because there are more than 100 known CaM-binding partners [312]. The CBPs included in my model are enriched in the dendritic spine, with a cumulative concentration (tens of micromolar each) exceeding that of CaM (33 μM). And indeed, recent computational studies have shown that competition alone, in the absence of spatial effects or feedback loops, may be sufficient to set the Ca^{2+} frequency-dependence of CBP activation observed *in vivo* [46]. Although competition is not the focus of this study, I again describe competition for CaM-binding to help ensure that model stimulation at a particular Ca^{2+} frequency results in physiological CaMKII activation levels.

In this study, I model CaMKII in two distinct ways. First, I describe monovalent CaMKII monomers similarly to Pepke *et al*. [42]. In my model, CaMKII monomers become activated by Ca^{2+}/CaM, and active CaMKII are able to bind and subsequently phosphorylate AMPARs and NMDARs (my first two model frameworks, Figure 6.1 A and B). I also account for CaMKII phosphorylation by allowing CaMKII monomers to dimerize (see Figure 6 in [42]). Importantly, by modeling active CaMKII monomers as monovalent, they can only bind one other protein

(AMPAR, NMDAR, or another monomer) at a time. In contrast, I secondly describe multivalent CaMKII holoenzymes using a specialized rule-based syntax (Figure 6.1C). In this rule-based framework, each CaMKII holoenzyme has twelve subunits, and each subunit can be activated by Ca^{2+}/CaM and a bind one other protein target. I note that rule-based (multi-state) molecules cannot diffuse due to limitations in MCell 3.3, an obstacle I address later in this paper. Therefore, my rule-based CaMKII holoenzymes do not interact with NMDARs or AMPARs. However, I can still describe CaMKII monomer and holoenzyme interactions with actin binding sites, which strongly depend on CaMKII subunit isoform.

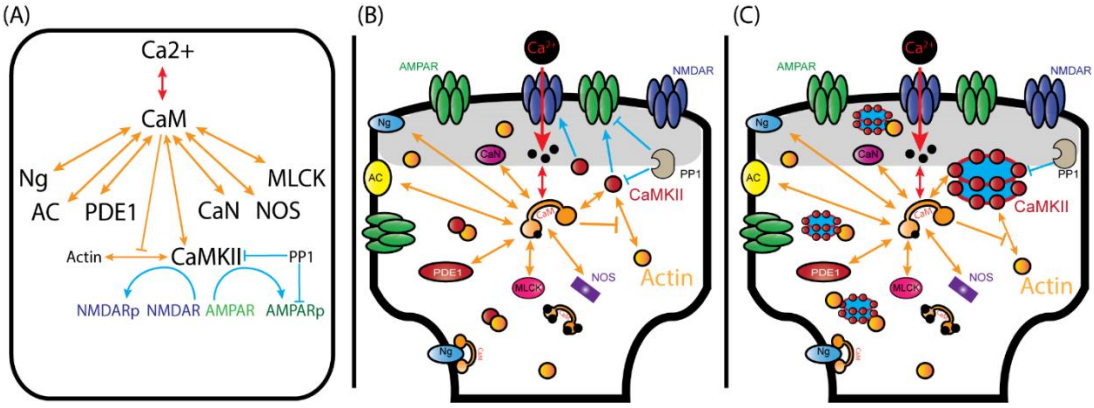

Figure 6.1. Model frameworks for comparing effects of CaMKII subunit type and multivalence. (A) The deterministic (non-spatial) model of Ca^{2+}-CaM binding (red arrows), Ca^{2+}/CaM-dependent activation of CBPs (orange arrows), and regulation of receptor proteins by CaMKII monomers and the phosphatase PP1 (blue arrows). (B) The spatial-stochastic (MCell 3.3) model equivalent to the deterministic model, with monomer CaMKII. Note that I model actin binding sites as diffuse particles (orange circles). (C) The rule-based equivalent to the MCell 3.3, which describes CaMKII as twelve-subunit holoenzymes. Double-edged arrows are reversible reactions. Blunt-ended arrows denote PP1-mediated de-phosphorylation.

In all model frameworks, I distinguish between CaMKII subunit isoforms. Although at least four CaMKII isoforms are known, the alpha and beta isoforms are most abundant in the hippocampus, expressed at a ratio of 3:1 [260]. In this study, alpha- and beta-CaMKII are modeled identically, with the exception of their binding affinities for actin binding sites. Whereas I model alpha- and beta-CaMKII as having identical affinities for Ca^{2+}/CaM, NMDARs, and AMPARs, I account for observations by Khan *et al*. that both the alpha and beta isoform bind actin in the absence of Ca^{2+}/CaM, and that the affinity of alpha-CaMKII for actin (1.4 μM) is one order of magnitude weaker than that of beta CaMKII (0.5 μM) [244]. To minimize confounding model

output, I note that my model requires Ca^{2+}/CaM binding to CaMKII as a condition for CaMKII-actin dissociation.

Finally, I emphasize my model describes neither G-actin, F-actin, nor actin polymerization or degradation. Because actin regulation is not the main focus of this study, I instead model only actin binding sites. To model actin binding sites, I make a number of model assumptions. First, I assume that the number of actin binding sites is non-limiting, which ensures that actin binding sites are always available to bind inactive CaMKII, given the dendritic spine's extensive actin scaffold. Thus, I set the concentration of actin binding sites at 100 μM, which is greater than the total concentration of CaMKII subunits (74 μM). Second, I assume that the number of actin binding sites is constant, which is valid given my model timescales (seconds) [245]. Third, I assume that CaM-bound CaMKII is unable to re-bind actin, which could be due either to steric hindrance of the CaMKII-actin binding site by CaM or because CaM-binding changes the conformation of the CaMKII subunit.

6.3.1.2 Model Parameterization

Ca^{2+} flux and the kinetics of Ca^{2+}-CaM and CaM-CBP binding are identical to those used in previously published computational models [42, 46, 165]. Briefly, Ca^{2+} flux is a model boundary condition defined by the function $[Ca](t) = 12e^{-t/0.012}$ where t is time, the coefficient is the peak magnitude, and the exponent's denominator is a decay time constant for a single Ca^{2+} pulse. As mentioned, Ca^{2+} pulses are uniformly spaced in order to control model output as a function of Ca^{2+} frequency. Ca^{2+}-CaM and CaM-CBP binding kinetic parameters (including those for CaMKII autophosphorylation) are taken directly or derived from experimental measurements as described in the previous publications. CaMKII binding and phosphorylation kinetics of AMPARs and NMDARs are also taken directly from experimental measurements as listed in Table 7.5 and Table 7.9. The deterministic, spatial-stochastic, and rule-based models presented in this study all use identical kinetic parameters. The only exception to this pertains to CaMKII autophosphorylation in the rule-based model, which I discuss later in this paper.

Diffusion coefficients are also used to parameterize the spatial-stochastic and rule-based models. Almost all diffusion coefficients for unbound proteins are taken from experimental measurements as listed in Table 7.6. For diffusion coefficients of proteins and protein-protein complexes not measured experimentally, I use the Stokes-Einstein relation [233]. The Stokes-

Einstein relation describes a protein's diffusion as a function of its hydrodynamic radius. As also discussed in the Supplement to Chapter 5, if I assume hydrodynamic radius to be proportional to molecular weight, I can determine diffusion coefficients for all protein states in my models. Throughout this paper, diffusion coefficients taken directly from experimentation or calculated by the Stokes-Einstein relation are referred to as "standard" diffusion parameters.

Diffusion in the dendritic spine is difficult to characterize. Indeed, experimental measurements and the Stokes-Einstein relation both assume proteins obey Brownian motion in a dilute medium. However, the dendritic spine is a small and crowded space in which 1) proteins may no longer diffuse according to Brownian motion, and 2) effective diffusion coefficients may be reduced. Fortunately, work by Regner *et al*. suggests that diffusion in the spine is reasonably well modeled in the dendritic spine by a continuous-time random walk [246]. To reproduce a continuous-time random walk in MCell, my spatial-stochastic and rule-based models use a small time-step of 0.5 μsec. To account for possible reductions in effective diffusion coefficients, I refer to experiments by Blanpied *et al*. [38] and Heidarinejad *et al*. [313], who experimentally determine that particles in the dendritic spine diffuse on average approximately one order of magnitude more slowly than simulations predict. Therefore, throughout this paper I compare model results using "standard" against "reduced" diffusion parameters, in which diffusion coefficients are all reduced by one order of magnitude.

6.3.2 Deterministic, Monovalent CaMKII Model Analysis

First, I implement my reaction network in a deterministic framework. Using my deterministic framework, I can validate my reaction network and model parameters, rapidly perform global sensitivity analysis, and set a non-spatial benchmark against which to compare spatial versions of my model.

To validate my model, I first explore my model's Ca^{2+}/CaM dynamics in response to various Ca^{2+} frequencies. Although this study's Ca^{2+}/CaM reaction network is similar to previously published work, it is important to ensure that new model features added in this study, such as CaMKII interactions with actin binding sites, preserve fundamental model behavior. Therefore, shown in Figure 6.2, I monitor global Ca^{2+}/CaM dynamics in response to 10Hz and 100Hz Ca^{2+} flux. Starting with the top-left panels in Figure 6.2 A and B, apo-CaM (with no Ca^{2+} bound) levels rapidly drop in the presence of Ca^{2+}. Unsurprisingly, the drops in apo-CaM under

10Hz Ca^{2+} are more dynamic because the period of Ca^{2+} oscillation is much longer compared to the 100Hz case. Next, in the bottom-left panels CaM_{2N} (2 Ca^{2+} bound to the CaM N-terminus) levels peak very shortly after initiation of Ca^{2+} flux, consistent with the high association and dissociation rate parameters for Ca^{2+} binding to the CaM N-terminus. The CaM_{2N} levels steadily decline later during Ca^{2+} stimulation (by t=8sec), as Ca^{2+}/CaM shifts into the CaM_{2C} state shown at the top-right panels. Again, late predomination of CaM_{2C} is consistent with expectation because the CaM C-terminus has a higher affinity (but slower association rate) for Ca^{2+} than the N-terminus. Finally, the fully-saturated CaM_4 state most highly predominates during Ca^{2+} flux, again consistent with expectation, especially in the 100Hz case. Indeed, 100Hz Ca^{2+} flux is associated with LTP, and LTP is known to involve the CBPs with highest affinity for CaM_4 (CaMKII and AC1) [3, 27, 250, 256].

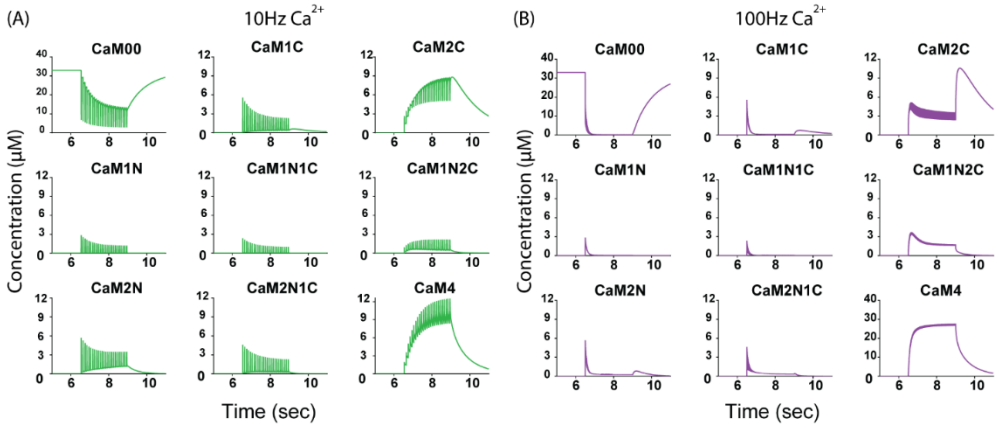

Figure 6.2. Deterministic Ca^{2+}/CaM dynamics. (A) All nine Ca^{2+}/CaM states in response to 10Hz Ca^{2+} flux (green). (B) All nine Ca^{2+}/CaM states in response to 100Hz Ca^{2+} flux (purple). Here, Ca^{2+} flux begins at t=6.5sec and terminates after 2.5sec regardless of Ca^{2+} frequency. Note differences in scale for apo-CaM (CaM00) panels and the CaM_4 panel in (B).

In addition to analyzing Ca^{2+}/CaM dynamics as shown in Figure 6.2, validation can also be achieved through global sensitivity analysis. Using global sensitivity analysis, it is possible to quantify the model parameters that most significantly influence model output. If a particular model output is significantly affected by parameters as-expected, it could be further evidence the model output is valid. For my sensitivity analysis, it is necessary to quantify the influence of 162 distinct model parameters (all K_D's, catalytic rates, and initial concentrations). Problematically, quantifying a parameter's influence relative to all other model parameters requires sampling each parameter over a relatively wide range of values (two orders of magnitude). To minimize

computational expense, I restrict my sensitivity analysis to the deterministic model and systematically vary all parameters simultaneously using Latin hypercube sampling (LHS) [208]. With LHS, I can subsequently calculate partial rank correlation coefficients (PRCCs) to quantitatively rank each parameter's impact on model output (see Methods). In my analysis, I calculate PRCCs for two model outputs: the concentration of CaMKII-bound NMDARs following stimulation, and the cumulative number of actin-CaMKII dissociations. In particular, using LHS-PRCCs to identify parameters important to NMDAR-binding could also help elucidate mechanisms relevant to CaMKII localization to the PSD.

In Table 6.1, I present LHS-PRCC results for end-time CaMKII-bound NMDARs. I first group results for simulations varying initial protein concentrations. While varying initial concentrations, I also consider model output at 10Hz and 100Hz Ca^{2+} flux. I find that regardless of Ca^{2+} frequency, the end-time bound NMDARs are most dependent on the concentrations of CaM, actin binding sites, and (of course) NMDARs. Notably, these results match intuition; as the CaM concentrations (PRCC > 0.76) increase, actin-CaMKII complexes are more readily terminated, leading to increased NMDAR-binding. And as the actin concentration (PRCC < -0.68) increases, actin out-competes CaM for CaMKII binding, reducing opportunities for CaMKII to bind NMDARs.

Table 6.1. Global sensitivity analysis by LHS-PRCC.

Varying Initial Concentrations									
Output Variable	Ca2+ frequency	Alpha:Beta							
End-time bound NMDARs	100Hz	1a:1b	Parameters:	**concCaM**	**concActin**	**concNMDAR**			
			PRCC value:	0.766176922	-0.68759582	0.776849323			
End-time bound NMDARs	10Hz	1a:1b	Sig. Parameters:	**concCaM**	**concActin**	**concNMDAR**			
			PRCC value:	0.785320279	-0.69298301	0.77669873			
Varying Kinetic Parameters									
Output Variable	Ca2+ frequency	Alpha:Beta							
End-time bound NMDARs	100Hz	1a:1b	Parameters:	**konNg2C**	**konKCaM4**	**koffAlphaActin**	**koffBetaActin**		
			PRCC value:	0.533317695	0.810042637	0.968025072	0.851005754		
End-time bound NMDARs	100Hz	1a:0b	Parameters:	**konNg2C**	**konKCaM4**	**koffAlphaActin**			
			PRCC value:	0.528466089	0.787735837	0.981058808			
End-time bound NMDARs	100Hz	0a:1b	Parameters:	**konNg2C**	**konKCaM4**	**koffBetaActin**			
			PRCC value:	0.56535111	0.825029887	0.986898838			
End-time bound NMDARs	10Hz	1a:1b	Parameters:	**konNg1C**	**konNg2C**	**konKCaM4**	**kcatGluN2Bphos**	**koffAlphaActin**	**koffBetaActin**
			PRCC value:	0.670819777	0.811708542	0.794176764	-0.62127195	0.903539074	0.688161823
End-time bound NMDARs	10Hz	1a:0b	Parameters:	**konNg1C**	**konNg2C**	**konKCaM4**	**kcatGluN2Bphos**	**koffAlphaActin**	
			PRCC value:	0.692816713	0.827943014	0.772165805	-0.627392718	0.950889559	
End-time bound NMDARs	10Hz	0a:1b	Parameters:	**konNg1C**	**konNg2C**	**konKCaM4**	**kcatGluN2Bphos**	**koffBetaActin**	
			PRCC value:	0.629175299	0.798228385	0.768403709	-0.552920502	0.959586706	

LHS-PRCC values are calculated from deterministic model simulations varying initial concentrations and kinetic parameters. I also consider model output in response to 10Hz and 100Hz Ca^{2+} flux and distinct CaMKII subunit isoform ratios. Here, I list only parameters with significant PRCCs having absolute values greater than 0.5. Complete PRCC results are provided in the research repository cited in Methods.

In my sensitivity analysis, I also vary the model's kinetic parameters. While varying the kinetic parameters, I again analyze scenarios at 10Hz and 100Hz Ca^{2+} flux and at variable CaMKII subunit isoform ratios. Here, in all scenarios, the association rate for CaM_4-CaMKII binding (k_{on}^{KCaM4}) is shown to significantly impact the concentration of CaMKII-bound NMDARs (PRCC > 0.77). Again, this is consistent with intuition as CaM_4 is the Ca^{2+}/CaM state with highest affinity for CaMKII and therefore is most able to outcompete actin for CaMKII-binding. Also, I observe that the catalytic rate for CaMKII-mediated phosphorylation of NMDARs ($k_{cat}^{GluN2Bphos}$) significantly impacts model output at 10Hz but not 100Hz Ca^{2+} flux (PRCC < -0.55). Note that in my model, phospho-NMDARs have reduced affinity for CaMKII. Therefore, I attribute the importance of $k_{cat}^{GluN2Bphos}$ at 10Hz to the fact that Ca^{2+} levels, and therefore CaMKII activation, are more dynamic at low frequencies. Because CaMKII activation is more dynamic at low frequencies, NMDAR-binding is likely more dependent on the phosphorylation status of NMDARs rather than the activation of CaMKII.

Next, I observe that high association rates for Ng-CaM binding (k_{on}^{Ng1C} and k_{on}^{Ng2C}) have a surprisingly positive impact on model output (PRCC > 0.52). Intuitively, one would expect Ng, which strongly binds apo-CaM, to sequester Ca^{2+}/CaM away from CaMKII, reducing NMDAR-CaMKII binding. However, my LHS-PRCC results indicate that increasing the affinity of Ng for sub-saturated CaM_{1C} and CaM_{2C} (k_{on}^{Ng1C} and k_{on}^{Ng2C}) leads to increased NMDAR-CaMKII binding. This result is reminiscent of results by Krucker *et al*., who showed that Ng knock-down *in vivo* leads to reduced CaMKII activity [186]. Romano *et al*. subsequently explained the Krucker *et al*. results by demonstrating that Ng knock-down may cause a shift in competition for CaM-binding leading to decreased CaMKII activation and concomitantly increased AC1 activation. I speculate that my results here show that increasing the Ng affinity for the CaM C-terminus causes a similar shift in competition, perhaps reducing the activation of CBPs with high affinity for CaM_{2C} such as AC1. Having reduced AC1 activation, more CaM_{2C} may bind CaMKII, ultimately leading to increased CaMKII-NMDAR binding.

My sensitivity analysis also identifies a strong dependence on CaMKII subunit composition. Regardless of Ca^{2+} frequency, when concentrations of alpha- and beta-CaMKII are equal (1:1 alpha-beta) the actin dissociation rate constants for both subunits types are important to NMDAR-CaMKII binding (PRCC > 0.68). In the absence of alpha-CaMKII, the beta subunit's dissociation from actin remains important. Similarly, in the absence of beta-CaMKII, the alpha

subunit's dissociation from actin remains important. Based on these results, I speculate that CaMKII-NMDAR binding is strongly regulated by CaMKII subunit composition, despite the fact that I model alpha- and beta-CaMKII as having identical affinities for NMDARs. To explore this regulation, in Figure 6.3 I monitor CaMKII-actin complexes, CaMKII-NMDAR binding in the presence of actin binding sites, and CaMKII-NMDAR binding in the absence of actin binding sites in response to 100Hz Ca^{2+} flux, at various CaMKII subunit isoform ratios. My results demonstrate that, in the absence of spatial effects, that CaMKII-NMDAR is highly dependent on the CaMKII subunit isoform ratio. In Figure 6.3A I show that increasing levels of alpha-CaMKII (which has a weaker affinity for actin) relative to beta-CaMKII increases CaMKII-actin dissociations during Ca^{2+} flux. Increased CaMKII-actin dissociations leads to increased levels of free CaM-CaMKII, which subsequently bind increased levels of NMDARs (Figure 6.3B). However, in the absence of actin binding sites, CaMKII-NMDAR binding is totally independent of CaMKII subunit isoform ratio (Figure 6.3C).

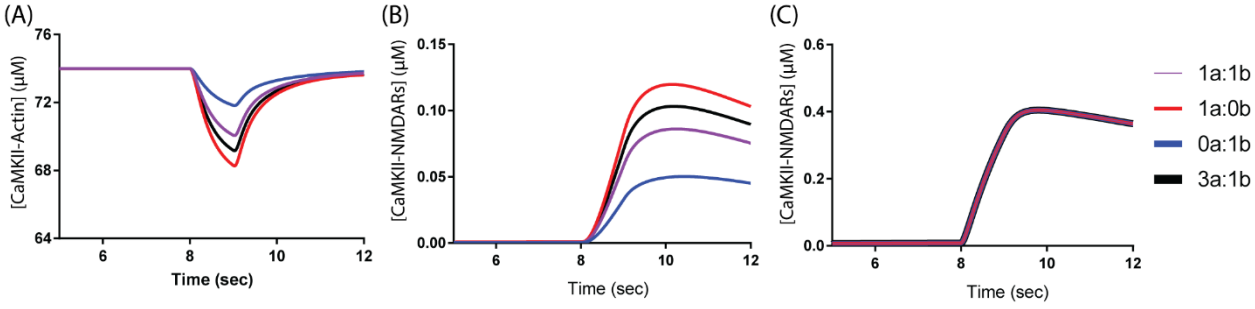

Figure 6.3. CaMKII-NMDAR dependence on CaMKII subunit composition. CaMKII-actin complexes (A), CaMKII-NMDAR complexes in the presence of actin binding sites (B), and CaMKII-NMDAR complexes in the absence of actin binding sites (C). Model output is shown for equal (purple), alpha-only (red), beta-only (blue), and physiological (black) CaMKII subunit isoform ratios. I monitor deterministic model output as a function of time in response to 100Hz Ca^{2+} flux. Here, Ca^{2+} flux begins at t=8sec and terminates after 1sec of stimulation.

6.3.3 Spatial-stochastic, Monovalent CaMKII Model Analysis

Because NMDARs are spatially localized to the synaptic membrane *in vivo*, the results shown in Figure 6.3 may constitute evidence that CaMKII subunit composition regulates its localization to the PSD. To further explore this regulation, I shift from my non-spatial deterministic framework to an equivalent spatial-stochastic model framework. In my spatial-stochastic implementation, I use MCell 3.3 to simulate each model species as a discrete particle diffusing

about a cuboidal dendritic spine geometry as described in Methods. Ca^{2+} flux is identical to my deterministic model except that Ca^{2+} ions enter the spine via NMDARs located at the synaptic membrane, at the top of my model geometry.

As a first validation of my spatial-stochastic model, I again monitor CaMKII-NMDAR binding. As shown in Figure 6.4 A and B, I monitor CaMKII-NMDAR binding in the presence and absence of actin binding sites, respectively, and at various CaMKII subunit isoform ratios. As in Figure 6.3, CaMKII-NMDAR binding is highly CaMKII subunit isoform-dependent, increasing with an increasing alpha-beta CaMKII ratio, but only in the presence of actin binding sites. In Figure 6.4C, I again monitor CaMKII activation but with "reduced" diffusion conditions, for which all model diffusion coefficients are reduced by one order of magnitude, as described in Model Parameterization. Even with reduced diffusion, isoform-dependence of CaMKII-NMDAR binding requires the presence of actin binding sites. Thus, my deterministic results in Figure 6.3 appear to be preserved in my spatial-stochastic model as shown in Figure 6.4. Specifically, because NMDARs are localized to the synaptic membrane and because CaMKII-NMDAR binding is subunit isoform-dependent, my results may suggest an isoform-dependence for CaMKII localization overall.

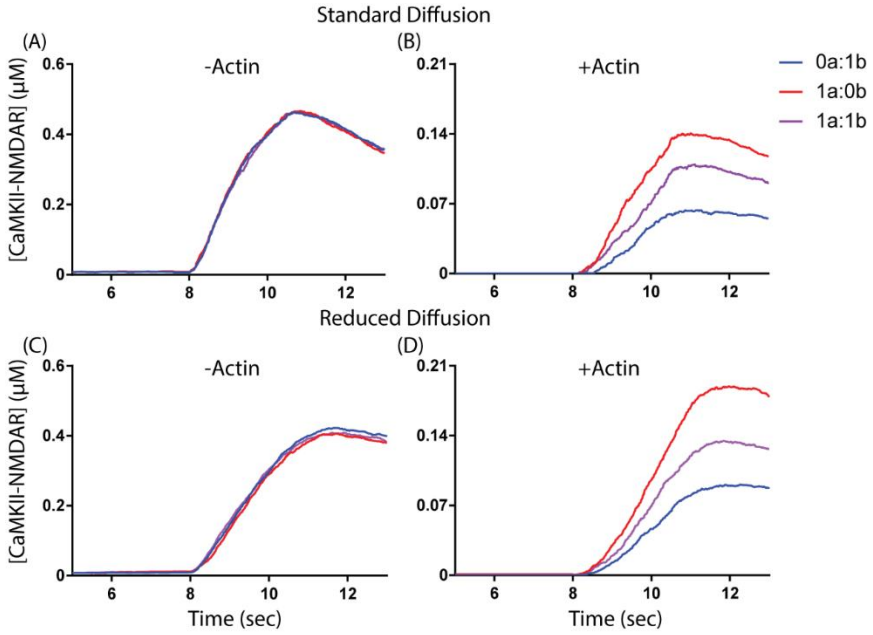

Figure 6.4. Spatial-stochastic CaMKII-NMDAR dependence on CaMKII subunit composition. CaMKII-NMDAR complexes in the absence of actin binding sites (A & C) and CaMKII-NMDAR complexes in the absence of actin binding sites (B & D). Model output is shown for equal (purple), alpha-only (red), and beta-only (blue) CaMKII subunit isoform ratios. I monitor spatial-stochastic model output as a function of time in response to 100Hz Ca^{2+} flux. Here, Ca^{2+} flux begins at t=8sec and terminates after 1.5sec of stimulation. Equivalent model output in response to 10Hz Ca^{2+} is provided in Figure 7.18..

To further ensure that transitioning to a spatial-stochastic framework preserves fundamental model behavior, I simulate my model as previously shown in Figure 6.2. However, in addition to monitoring major Ca^{2+}/CaM states as a function of time, I use MCell to monitor Ca^{2+}/CaM states in space. For this, I partition the dendritic spine geometry into three transparent, equally-spaced, equal-volume compartments distributed along the spine's major axis. Within these compartments, I monitor local concentrations of protein states (see Methods). As shown in Figure 6.5, I monitor the major Ca^{2+}/CaM states in response to 10Hz and 100Hz Ca^{2+} flux. As in the non-spatial deterministic model, CaM_{2N} peaks early upon initiation of Ca^{2+} flux due to that terminus' high association rate for Ca^{2+} binding. Subsequently, the CaM N-terminus' high dissociation rate and the C-terminus' high affinity for Ca^{2+} cause a shift from CaM_{2N} to CaM_{2C}. The fully-saturated CaM_4 state ultimately predominates, especially under 100Hz Ca^{2+}. Importantly, using the spatial-

stochastic framework allows me to observe clear spatial dependence of Ca^{2+}/CaM states. That is, there are distinct concentrations of Ca^{2+}/CaM across each compartment at multiple Ca^{2+} frequencies. In particular, during 100Hz Ca^{2+} flux the CaM_4 state exhibits a clear spatial gradient, in which the levels of CaM_4 in each compartment never appear to overlap. In the Supplement to Chapter 6, I provide equivalent results to Figure 6.5 demonstrating that spatiotemporal dynamics of Ca^{2+}/CaM are independent of CaMKII subunit isoform ratios and the presence of actin binding sites. Because the spatiotemporal dynamics of Ca^{2+}/CaM are preserved in my spatial-stochastic framework, I proceed to use this framework to explore CaMKII localization.

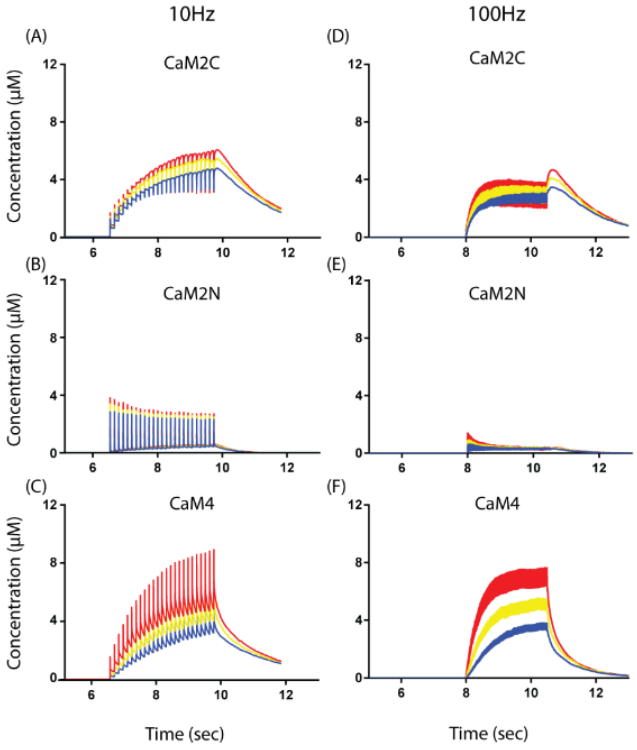

Figure 6.5. Spatial-stochastic Ca^{2+}/CaM dynamics. CaM_{2C} (A & D), CaM_{2N} (B & E), and CaM_4 (C & F) in response to 10Hz (left column) and 100Hz (right column) Ca^{2+} flux at standard diffusion conditions. Ca^{2+}/CaM states are monitored in the top (red), middle (yellow), and bottom (blue) spine compartments. Here, 10Hz Ca^{2+} flux begins at t=7sec and terminates after 3sec of stimulation. Also, 100Hz Ca^{2+} flux begins at t=8sec and terminates after 2.5sec of stimulation. Differences in stimulation are meant to enhance visualization of model dynamics. All traces are the average of N=50 executions.

Because my results in **Figure 6.5** show clear spatial dependence of Ca^{2+}/CaM states, I next explore how this spatial dependence may be transduced to CBPs. Specifically, I explore the extent

to which the location of CaMKII activation by Ca^{2+}/CaM may influence CaMKII localization. Therefore, in Figure 6.6 I monitor the spatiotemporal dynamics of active CaMKII in response to 100Hz Ca^{2+} flux. In Figure 6.6A, I show that CaMKII activation exhibits clear spatial gradients that are seemingly unaffected by the presence of actin binding sites or the CaMKII subunit isoform ratio. With reduced diffusion in Figure 6.6B, I observe exaggerated spatial gradients of CaMKII activation, again mostly unaffected by actin binding sites or subunit isoform ratio.

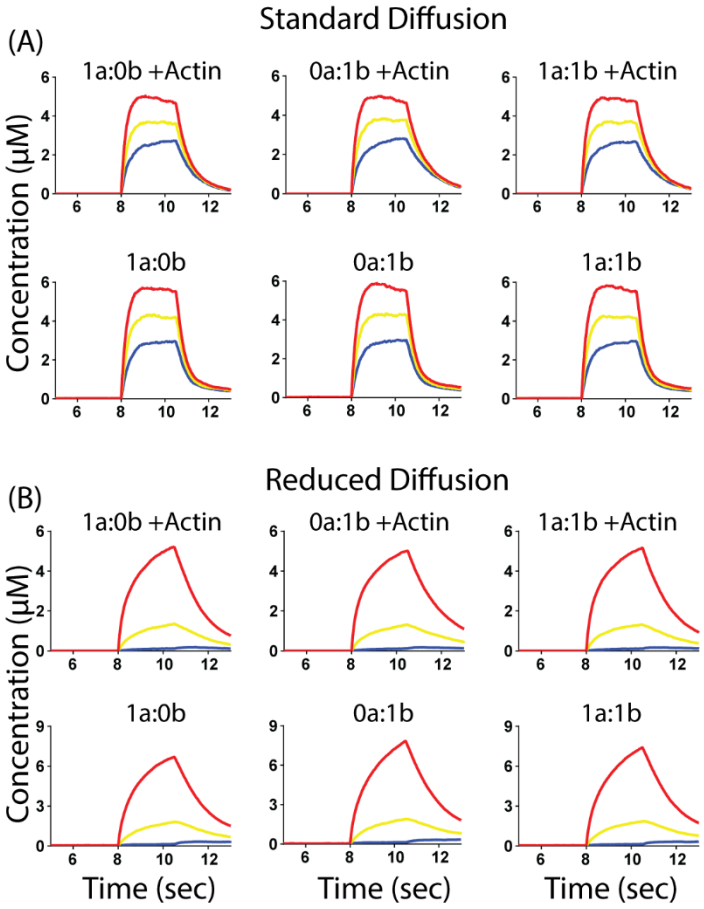

Figure 6.6. Spatiotemporal dynamics of monovalent CaMKII. Active CaMKII in the top (red), middle (yellow), and bottom (blue) spine compartments in response to 100Hz Ca^{2+} flux. Output is shown for various CaMKII subunit isoform ratios, in the presence or absence of actin binding sites, and with standard (A) and reduced (B) diffusion conditions. Here, Ca^{2+} flux begins at t=8sec and terminates after 2.5sec of stimulation. All traces are the average of N=50 executions.

Although CaMKII activation levels are unaffected by subunit isoform type and the presence of actin binding sites, I next explore whether these factors regulate CaMKII binding to AMPAR GluA1 subunits. For this I monitor GluA1-CaMKII binding complexes in each spine

compartment in response to 100 Hz Ca^{2+} flux. Similarly to Figure 6.6, in Figure 6.7 I compare model output for GluA1-CaMKII complexes for scenarios in the presence and absence of actin binding sites and with various CaMKII subunit isoform ratios. Critically, I observe GluA1-CaMKII complex formation dependence on subunit isoform, and only in the presence of actin binding sites (Figure 6.7A, top row). This is understandable given my model setup, because the only difference between alpha and beta subunits in this model is their affinity for actin binding sites. Indeed, in the presence of actin binding sites, CaMKII-GluA1 levels are highest with a high alpha:beta isoform ratio. I attribute this to the relatively low affinity of alpha CaMKII for actin binding sites—if CaMKII can rapidly dissociate from actin, it can more readily interact with its substrates. Notably, this result is exaggerated when diffusion coefficients are reduced (Figure 6.7B).

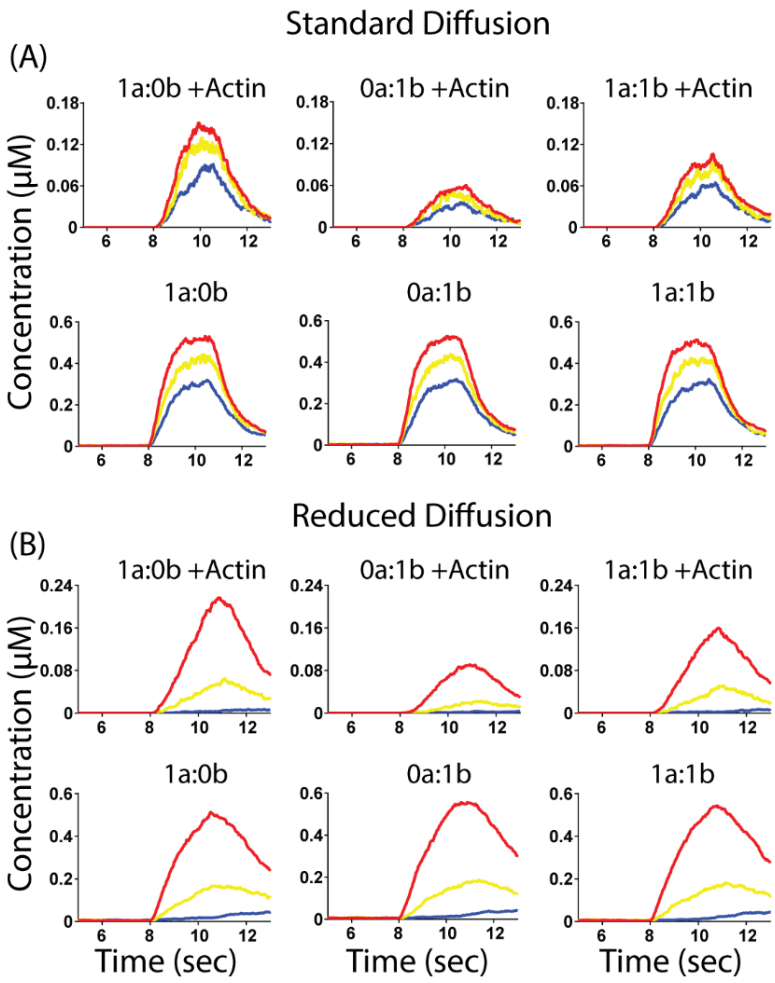

Figure 6.7. Spatiotemporal dynamics of GluA1-CaMKII complexes. GluA1-CaMKII complexes in the top (red), middle (yellow), and bottom (blue) spine compartments in response to 100Hz Ca^{2+} flux. Output is shown for various CaMKII subunit isoform ratios, in the presence or absence of actin binding sites, and with standard (A) and reduced (B) diffusion conditions. Here, Ca^{2+} flux begins at t=8sec and terminates after 2.5sec of stimulation. All traces are the average of N=50 executions.

The differences in CaMKII dynamics observed in Figure 6.5-7 may also be a result of my dendritic spine volume. Although my dendritic spine head geometry (0.5 μm cuboid) is roughly physiological, its volume may be large relative to the average diffusion of molecules in my model. To verify whether my results in Figure 6.5-7 could be preserved in small model geometry, I repeated my analysis in Figure 6.5. As in Figure 6.5, in Figure 6.8 I monitor CaMKII-NMDAR complexes in response to 100Hz Ca^{2+} flux with various CaMKII subunit isoform ratios, but in a model geometry in which each dimension is reduced 2-fold. All other parameters, including initial

protein concentrations, are the same as previous simulations in this Chapter. I find that in the absence of actin binding sites (Figure 6.8 A and C), CaMKII-NMDAR complex formation is independent of CaMKII subunit isoform ratio, consistent with Figure 6.5. In the presence of actin binding sites (Figure 6.8 B and D), CaMKII-NMDAR complex formation increases with increasing alpha:beta subunit ratio, also consistent with Figure 6.5. Note that due to axis scaling in Figure 6.8B, the differences between each subunit ratio trace are visually obscured. Still, the differences with subunit ratio are quite evident with reduced diffusion in Figure 6.8D. Altogether, my results indicate that even in a reduced-volume spine geometry, CaMKII may still exhibit spatial localizations that depend on its subunit isoform composition.

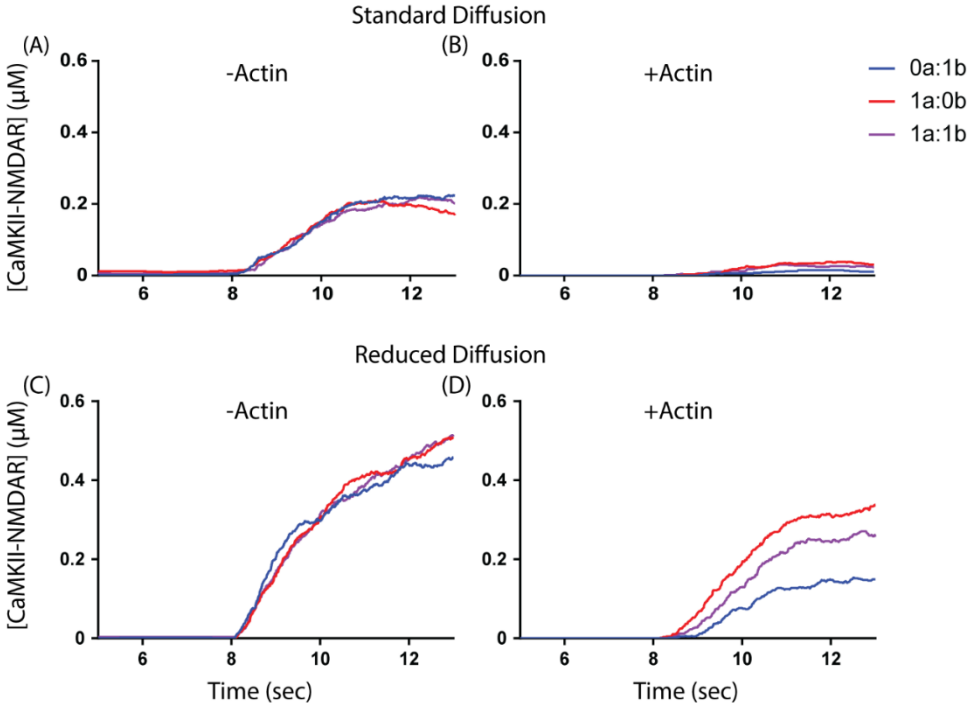

Figure 6.8. CaMKII-NMDAR complex formation with reduced spine volume. CaMKII-NMDAR complexes in the absence of actin binding sites (A & C) and CaMKII-NMDAR complexes in the absence of actin binding sites (B & D). Model output is shown for equal (purple), alpha-only (red), and beta-only (blue) CaMKII subunit isoform ratios. I monitor spatial-stochastic model output as a function of time in response to 100Hz Ca^{2+} flux. Here, Ca^{2+} flux begins at t=8sec and terminates after 1.5sec of stimulation. Simulations are identical to those in Figure 6.5 except with a re-scaled dendritic spine geometry in which each dimension is reduced by 2-fold.

6.3.4 Spatial-Stochastic, Multivalent CaMKII Model Analysis

The deterministic and spatial-stochastic models in the preceding sections both describe CaMKII as a simple monomer. However, CaMKII is of course a twelve-subunit holoenzyme. It may be important to account for intra-holoenzyme subunit interactions and/or the avidity effects created by co-localizing such a high number of subunits. Few computational models have been able to satisfactorily describe the CaMKII holoenzyme because of the combinatorial problem of specifying and evaluating the large CaMKII state space. As shown in Chapter 5, though, it is possible to use rule-based modeling as an alternative to conventional systems of differential equations, thereby bypassing the combinatorial problem typically posed by CaMKII. Here, I extend on the CaMKII holoenzyme model in Chapter 5 by incorporating it into the larger Ca^{2+}-dependent signaling network used in this chapter.

As discussed in Chapter 5, that CaMKII holoenzyme model uses a so-called "2-state-2-step" model. "2-state-2-step" refers to two states of CaM (apo-CaM and fully-saturated CaM_4), wherein only CaM_4 is allowed to bind CaMKII, and the CaM_4-CaMKII binding interaction occurs in two steps. First, CaM_4 assumes an "initially bound" conformation which is compatible with a closed CaMKII subunit (see Chapter 5 for a discussion of CaMKII subunit docking and opening). When the CaMKII subunit opens, the initially-bound CaM_4 can proceed to a high affinity "fully bound" conformation. Although the 2-state-2-step model of CaM-CaMKII binding was useful for parameterization and analysis of CaMKII in Chapter 5, the challenge for this chapter is to make the 9-state Ca^{2+}/CaM model compatible with a similar rule-based CaMKII holoenzyme model.

To reconcile the 9-state Ca^{2+}/CaM model with my existing description of the CaMKII holoenzyme, a new "9-state-2-step" model would be ideal. Problematically, the parameters for the 9-state model are mainly derived from experimental measurements by Shifman *et al.*, who use wild type rat CaMKII *in vitro* [97]. So, the 9-state kinetic parameters inherently account for CaMKII subunit docking, opening, and two-step CaM-binding. Therefore, without a total re-parameterization, a 9-state-2-step model of CaM-CaMKII binding would likely predict non-physiologically small probabilities for CaM binding to CaMKII. Indeed, preliminary data not presented in this thesis indicates that a naïve 9-state-2-step model exhibits virtually no CaM-CaMKII binding.

To reconcile 9-state CaM and the CaMKII holoenzyme, I therefore present a "9-state-1-step" model. In this model, I eliminate CaMKII subunit docking and opening, and I simplify the

process of CaM-CaMKII binding. Specifically, I allow *any* Ca^{2+}/CaM state (including apo-CaM) to bind CaMKII, and as elsewhere in this thesis, I define CaM-CaMKII binding as equivalent to CaMKII activation. Note that the 9-state-1-step model remains developmental, primarily because of how it accounts for subunit auto-phosphorylation and CaM-trapping [145]. That is, the 2-state-2-step model implicitly accounts for CaM-trapping because CaMKII autophosphorylation stabilizes the high-affinity "fully bound" CaM state. In contrast, the 9-state-1-step model explicitly accounts for CaM-trapping by uniformly imposing a 1000-fold higher affinity of CaM-CaMKII binding whenever the CaMKII subunit is phosphorylated. Determining which model better accounts for CaM-trapping remains for future experimental studies and/or a rigorous computational sensitivity analysis. Still, for the purposes of this thesis I here present preliminary output from my 9-state-1-step model.

A primary reason for incorporating the CaMKII holoenzyme into larger models of Ca^{2+}-dependent signaling is to quantify the effect of CaMKII multivalence. Proteins with high multivalence, such as CaMKII, may exhibit avidity affects that result in increased effective affinities for binding partners. Increasing the effective affinity for CaMKII binding could significantly impact the spatial dependence of many proteins in the dendritic spine. For example, increasing the actin-CaMKII affinity could reduce the mobility of CaMKII in the spine, or at least increase the Ca^{2+} stimulation threshold required to initiate CaMKII mobilization. Additionally, increasing the CaMKII affinity for membrane receptors could enhance the localization of CaMKII and/or membrane receptors to the synaptic membrane or other regions of the spine. However, because MCell 3.3 prohibits diffusion of my multivalent CaMKII holoenzymes, I can only analyze the effects of CaMKII multivalence on the CaM-CaMKII interaction. Therefore, in Figure 6.9 I monitor the all major Ca^{2+}/CaM states (whether CaMKII-bound or unbound) in response to 100Hz Ca^{2+} flux in each spine compartment. Because here CaMKII cannot diffuse, I further compare model output when holoenzymes are uniformly distributed about the spine head (Figure 6.9A-C), to output when holoenzymes are localized only to the PSD (Figure 6.9D-F).

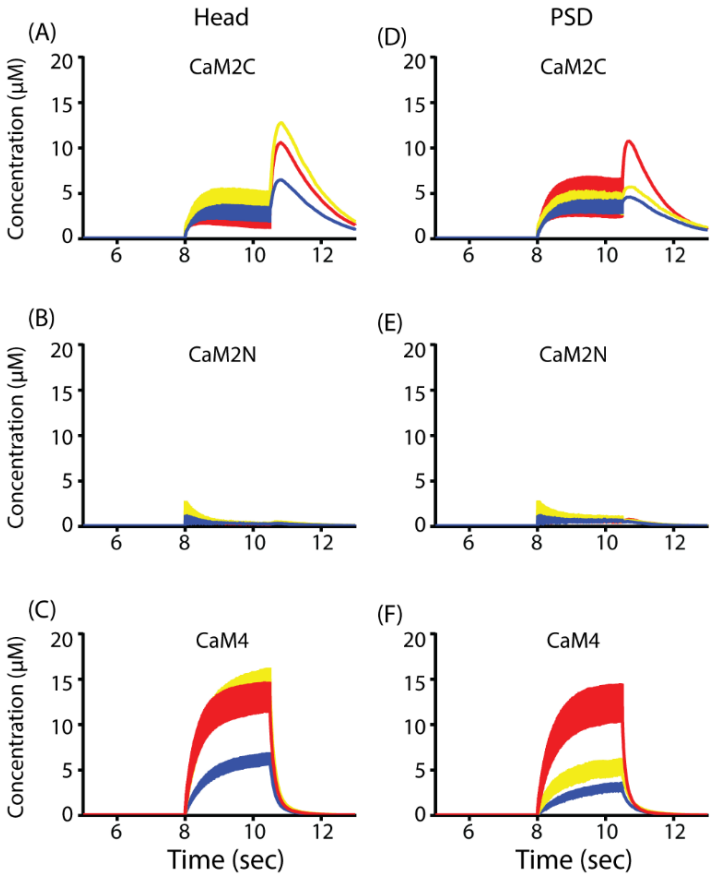

Figure 6.9. Spatial-stochastic Ca^{2+}/CaM dynamics with multivalent CaMKII. CaM_{2C} (A & D), CaM_{2N} (B & E), and CaM_4 (C & F) in response to 100Hz Ca^{2+} flux at standard diffusion conditions. Ca^{2+}/CaM states are monitored in the top (red), middle (yellow), and bottom (blue) spine compartments. CaMKII holoenzymes are uniformly distributed about the entire spine head (A-C) or localized to the PSD (D-F). Ca^{2+} flux begins at t=8sec and terminates after 2.5sec of stimulation. All traces are the average of N=50 executions.

Figure 6.9 indicates that CaMKII multivalence could significantly effect the spatiotemporal dynamics of Ca^{2+}/CaM in the spine. I compare Figure 6.9A-C to Figure 6.5D-F, which are identical simulations except that Figure 6.9 describes CaMKII holoenzymes. Whereas in Figure 6.5 all Ca^{2+}/CaM states are highest in the top spine compartment (PSD), in Figure 6.9 all Ca^{2+}/CaM states are markedly increased in the middle spine compartment. In particular, fully-saturated CaM_4 levels are almost the same in the middle and top compartments when CaMKII holoenzymes are uniformly distributed about the spine head (Figure 6.9 A-C). This may be explained by the high affinity of CaMKII for CaM_4, which is effectively increased when I describe CaMKII as holoenzymes. By increasing the effective affinity of CaMKII for CaM_4, the

predomination of CaM_4 becomes even more pronounced. Notably, in Figure 6.9C CaM_4 no longer exhibits a clear spatial gradient as seen in the presence of monomer CaMKII (Figure 6.5F). Interestingly, when I localize CaMKII holoenzymes only to the top spine compartment, or PSD, CaM_{2C} and especially CaM_4 also predominantly localize to the PSD (Figure 6.9D-F). Thus, it seems that prior to CaMKII localization to the PSD, CaMKII holoenzymes reduce spatial gradients of CaM_4, but prior to CaMKII localization to the PSD (by unidentified mechanisms), CaMKII holoenzyme multivalence may be essential to setting significant spatial gradients of Ca^{2+}/CaM.

6.4 Discussion

This study provides a framework for quantifying the effects of CaMKII subunit isoform composition and multivalence in early synaptic plasticity.

First, I present a deterministic and non-spatial model of Ca^{2+}, CaM, nine explicitly-defined CBPs including CaMKII, and CaMKII interactions with membrane receptors and actin binding sites. I validate the deterministic model by comparing the temporal dynamics of Ca^{2+}/CaM to previously published data. I explore the deterministic model using global sensitivity analysis (using LHS-PRCC) to quantify how various model parameters contribute to model output. Interestingly, I find that parameters associated with actin-CaMKII interactions may significantly regulate CaMKII interactions with membrane receptors. Because membrane receptors are often localized to the synaptic membrane (at the PSD), it could therefore be that CaMKII localization to the PSD is regulated by its subunit isoform composition, also suggested in Figure 6.3.

Because the deterministic model suggests that actin interactions with CaMKII subunits could regulate CaMKII localization to the PSD, I adapt the deterministic model into a spatial-stochastic framework. Notably, this spatial-stochastic framework describes CaMKII as monomers. The spatial-stochastic model output again indicates the temporal dynamics of Ca^{2+}/CaM are consistent with previously published results, and the spatial dependence of Ca^{2+}/CaM is consistent with output from a similar (but distinct) model presented in Chapter 4 of this thesis. Moreover, the spatial gradients of Ca^{2+}/CaM are transduced as gradients of CaMKII activation. Significantly, these spatial gradients of CaMKII activation are preserved at multiple diffusivities and dendritic spine geometries. Interestingly, although the deterministic model suggests that CaMKII localization could depend on subunit isoform composition, the results in Figure 6.6 indicates no dependence on isoform composition in the spatial-stochastic model. Further analysis will be

required to verify whether this lack of dependence persists when monitoring *all* CaMKII, rather than solely the active CaMKII monomers. Still, in Figure 6.7 and Figure 6.8 I monitor CaMKII-GluA1 and -NMDAR complexes, respectively, and I show increasing CaMKII-receptor complex formation with increasing alpha-beta CaMKII ratio. Indeed, this result is reasonable given the high affinity of beta-CaMKII for actin binding sites.

To quantify the possible contribution of CaMKII multivalence on protein spatiotemporal dynamics, I modify the spatial-stochastic model to include a rule-based implementation of the CaMKII holoenzyme. Notably, rule-based species in MCell 3.3 cannot diffuse, so my analysis here is limited to interactions between CaMKII and cytosolic proteins such as CaM. Indeed, in Figure 6.9 I show that when CaMKII holoenzymes are uniformly distributed about the spine head, Ca^{2+}/CaM states show somewhat decreased spatial dependence. Specifically, fully-saturated CaM_4 levels are roughly equivalent between the middle and top spine compartments. It appears that in this scenario (Figure 6.9A-C), due to the increased effective affinity of CaMKII for CaM_4, multivalent CaMKII causes CaM_4 to predominate throughout the spine. At least, compared to Figure 6.5F, Figure 6.9C shows a much less steep spatial gradient of CaM_4. Interestingly, when I localize CaMKII holoenzymes to the PSD (Figure 6.9D-F), spatial dependence of Ca^{2+}/CaM becomes much more exaggerated, especially for CaM_4. This result may be significant in light of experimental studies indicating that CaMKII localizes to the PSD in response to LTP. Prior to LTP, uniformly-distributed CaMKII could be responsible for setting high CaM_4 levels throughout the spine head. But, following LTP, it might be preferential for localized CaMKII to localize CaM_4 only to the PSD to ensure that other CaM_4-dependent signaling pathways are activated at that region of the spine.

This study provides a framework for quantifying the effects of CaMKII multivalence. In the future, though, it may be necessary for models to more rigorously define or explore interactions between CaMKII and actin, as I discuss in Chapter 7 of this thesis.

6.5 Methods

All model code and associated files will be made available at the Purdue University Research Repository. The deterministic model is written and evaluated using the software Mathematica. The spatial-stochastic models are written and evaluated using the software MCell 3.3. For the spatial-stochastic models, the dendritic spine geometry is defined using the open-

source software Blender and its plug-in CellBlender, and the relevant geometry files are also provided in the research repository.

For the global sensitivity analysis of the deterministic model output, I use Latin hypercube sampling (LHS) to efficiently vary the model parameter space and subsequently parameter contributions using partial rank correlation coefficients (PRCC). Using LHS-PRCC is a more efficient approach to sampling large parameter spaces than random sampling and has previously been used to analyze complex biological models [208, 314]. In this thesis, I present results for a single objective function against which PRCCs are calculated, which is the end-time concentration of CaMKII-NMDARs. I calculate PRCCs for this objective function at two Ca^{2+} frequencies (10Hz and 100Hz) and at three CaMKII subunit ratios (1:1, 1:0, and 0:1 alpha-beta).

For the spatial-stochastic models, simulations are identical to those implemented in the deterministic model. However, in the spatial-stochastic model proteins are described as individual particles in space rather than bulk concentrations. Thus, individual particles diffuse about a geometry representing the dendritic spine. With the exception of Fig 8, all spatial-stochastic simulations utilize a spine head geometry identical to that used by Keller *et al*. [185], in which the spine head is a 0.5 μm cuboid. For Figure 6.8, I re-scale the spine head dimensions uniformly by 50%, to account for scenarios in which the dendritic spine is much smaller and explore whether spatial gradients of protein activation occur under such conditions. Regardless of geometry, the dendritic spine head contains three equal-volume, equally-spaced compartments distributed along the major axis of the spine head. These compartments are entirely transparent to molecular diffusion and are used to monitor local concentrations of proteins in the top (PSD), middle, and bottom of the spine head. Throughout this chapter, figures denote proteins in the top compartment as red, middle as yellow, and bottom as blue traces. A different color scheme is used in Chapter 4, but the methodology is identical. As in Chapter 4, Ca^{2+} fluxes into the model dendritic spine via NMDARs localized to the synaptic membrane (at the top of the model geometry).

For the spatial-stochastic model with holoenzyme CaMKII, I use the specialized rule-based modeling syntax in MCell 3.3, as described at length in Chapter 5 of this thesis. In these simulations, only CaMKII uses the rule-based syntax. Thus, while CaMKII holoenzymes cannot diffuse in these simulations (due to limitations in MCell), all other protein species can diffuse.

In all models, Ca^{2+} flux proceeds according to time-variable rates informing the reactions $NMDAR \rightarrow NMDAR + Ca^{2+}$ and $Ca^{2+} \rightarrow NULL$. The combined effect of these reactions is to

produce global free Ca^{2+} dynamics obeying the equation $[Ca](t)=12e^{-t/0.012}$ as used by Romano *et al.* [46], and in Chapters 2-4 of this thesis.

7. CONCLUSIONS AND FUTURE DIRECTIONS

Summary

In this thesis I present a series of computational models for quantifying how various molecular mechanisms regulate outputs relevant to synaptic plasticity. First, I present a deterministic, non-spatial model of Ca^{2+} flux, Ca^{2+}/CaM binding, and CaM-binding to multiple explicitly-defined CBPs. By explicitly modeling individual CBPs, I show how competition alone, in the absence of feedback loops or spatial effects, may influence the selection of CBPs by Ca^{2+}/CaM. Indeed, I show that competition is sufficient to set *in vitro* the Ca^{2+} frequency-dependence of CBPs observed *in vivo*. Moreover, shifts in competition may explain counterintuitive experimental results suggesting that reductions in CaM-buffers also reduce CaMKII activity. Second, I extend on the original deterministic model, adding pathways leading to AMPAR phosphorylation by CaMKII and PKA. With this model, I explain that reductions in CaMKII activity, and its phosphorylation of AMPARs, may be compensated for by shifts in competition that increase activation of AC. Third, I adapt the extended deterministic model into a particle-based, spatial-stochastic framework. This third model allows me to quantify how spatial effects influence competitive tuning. Interestingly, I find that spatial effects seem to contribute relatively little to the Ca^{2+} frequency-dependence of CBP activation. However, I observe that when protein states exhibit spatial gradients in the dendritic spine, these spatial gradients are sharpened by the presence of competition. Notably, while exploring why AC-mediated pathways tend not to exhibit spatial gradients, I reveal how the AC8 N-terminus may provide a key function regulating the spatiotemporal dynamics of Ca^{2+}/CaM. Fourth, to more accurately characterize spatiotemporal dynamics in the spine, I show how rule-based modeling can be used to model multivalent proteins such as the CaMKII holoenzyme. Fifth, I incorporate this multivalent CaMKII holoenzyme model into the larger Ca^{2+} signaling network. With this, I begin to quantify how CaMKII multivalence regulates proteins in the spine. Altogether, this thesis demonstrates how competition, spatial effects, multivalence, and other mechanisms may contribute to model outputs relevant to synaptic plasticity.

Further exploration of competition for CaM-binding

The first major result of this thesis is the identification of competition as an emergent property regulating protein activity. Specifically, I explore how competition sets physiological protein activations in response to Ca^{2+} frequency. However, other inputs besides Ca^{2+} frequency are known to determine the response of proteins within the spine, such as Ca^{2+} location, magnitude, and pattern. Indeed, whereas NMDARs are located at the top of the synaptic membrane, Ca^{2+} flux may also occur through voltage-gated channels located about the entire spine surface. The magnitudes of Ca^{2+} flux are also variable depending on the electrochemical input to the spine (EPSP vs AP) and probabilistic membrane channel opening. And during oscillatory Ca^{2+} flux, it is unlikely that Ca^{2+} peaks are uniformly spaced. Thus, it may be important for future work to characterize how competition or other mechanisms set the location-, magnitude-, and pattern-dependence of CBP activation [75].

In addition to adjusting the Ca^{2+} inputs, there may be a need to complement the pool of competitors for CaM-binding. The models presented in this thesis account for at-most nine explicitly-defined CBPs, so chosen because their cumulative concentration (>200μM) is significantly greater than that of CaM (33μM). However, there may be other competitors for CaM-binding yet to be included. For example, CaM binds NMDARs, and although NMDARs are relatively weakly expressed (1-2μM), their localization to the synaptic membrane could have implications for how others CBPs are able to compete for CaM-binding. Also, CaM binds the protein synGAP, which is highly expressed in the spine (tens of micromolar) [223]. Because CaM-synGAP binding may regulate the affinity of synGAP for the structural protein PSD-95, including synGAP into the list of explicit CBPs may be important for future work. In general, it will be important to explore how increasing or decreasing the CaM-CBP ratio, or competitiveness, influences the observations made in Chapter 2 and elsewhere in this thesis.

Although this thesis explores competition strictly in the context of CaM-binding, the strategies employed here may be adapted for studying competition among other regulators of protein signaling. For example, because PKA activation is at least partially Ca^{2+}-dependent (via AC activation by Ca^{2+}/CaM) and PKA has multiple phosphorylation targets [32, 209, 315], it might be interesting to compare output for models in which PKA's targets do or do not compete for PKA-binding. Similarly, the highly non-specific phosphatase PP1 is indirectly Ca^{2+}-dependent (via its interactions with Inh-1) and has multiple de-phosphorylation substrates such as CaMKII,

AMPARs, and NMDARs [104, 280, 316, 317]. Thus, it might also be interesting to compare output for models in which PP1's substrates do or do not compete for PP1-binding. Notably, PP1-binding is even more interesting in light of the possible PP1 exclusion mechanism revealed in Chapter 5, where Ca^{2+}/CaM may significantly out-compete PP1 for CaMKII-binding. Lastly, the structural protein PSD-95 has at least three PDZ binding motifs that are competed for by many proteins such as synGAP, CaMKII, and AMPARs [223]. Because competition for PDZ-binding may regulate the localization of AMPARs to the synaptic membrane, it may be interesting to compare output for models in which PSD-95 has variable numbers of PDZ domains. Furthermore, it is especially relevant to study the synGAP-PSD-95 interaction which has been shown to regulate apparent liquid-liquid phase separation *in vivo*, with possible implications for proteins' abilities to diffuse and/or spatially localize within the dendritic spine [318].

Experimental studies using bench-top technologies may also follow up on the results of Chapter 2. Specifically, it would be important to analyze how Ng knockout influences AC activity *in vivo*. For this, Ng knockout could be achieved in mice using the same strategies as those described by Krucker *et al*. [186]. Next, in addition to quantifying CaMKII activity (by Western blot), future work could also measure activity levels of AC. To measure AC activity, it might be possible to create a FRET-based reporter system for observing binding between CaM and AC. Or, studies can utilize antibodies specific for the cAMP/PKA-dependent phosphorylation sites on AMPAR GluR1 subunits [315]. With these antibodies, Western blot can again be used to observe AMPAR phosphorylation at S831 following neuronal stimulation in the presence and absence of Ng and in the presence and absence of forskolin, which inhibits AC. Using this strategy, future work could determine whether competitive tuning mediates shifts in CaMKII and AC activity upon Ng knockout.

Further exploration of signaling robustness due to shifts in competition

The second major result of this thesis is the characterization of how competition may provide robustness to model output. Specifically, in Chapter 3 I identify that upon knock-down of the CaM-buffer Ng, the resultant decrease in CaMKII activity may be compensated for by a competition-mediated increase in AC activity. As demonstrated in Chapter 3, this compensatory mechanism provides robustness to AMPAR phosphorylation, at least during Ca^{2+} stimulation. Upon termination of Ca^{2+} flux, however, it is unclear whether AMPAR phosphorylation remains

robust. The protein species included in my models do not necessarily regulate AMPAR phosphorylation on long timescales. To better regulate AMPAR phosphorylation, a more detailed or better-parameterized model is required. That is, future work could reconsider how the models in Chapters 3 and 4 regulate AC activation, cAMP generation, and competition for PKA. First, my models assume that AC-CaM binding is sufficient to initiate catalysis of ATP into cAMP, whereas AC's enzymatic activity may also require stimulation by G-protein subunits [319]. Including G-protein-dependence for AC activation may help set physiological cAMP generation levels. Second, my models assume that cAMP exclusively activates PKA and is solely degraded by phosphodiesterases PDE1 and PDE4. Introducing additional phosphodiesterases in future work could help ensure that transient activations of AC result in physiological levels and half-lives of cAMP. Third, my models allow PKA to bind only AMPARs and a generic PKA-inhibitor species. The PKA-inhibitor species is intended to account for non-specific interactions between PKA and its substrates. However, explicitly defining these substrates could more physiologically regulate PKA-AMPAR binding. Moreover, explicitly-defined PKA substrates would allow for a PKA-centric exploration of competition, as mentioned in a previous section of this Chapter.

Experimental studies could also further explore the results of Chapter 3. In the preceding section of this conclusions chapter, I describe a strategy for quantifying how Ng knockout influences AC activity. To quantify AC activity, I suggest using Western blot to measure cAMP/PKA-dependent AMPAR phosphorylation, in a manner similar to Lee *et al*. (2000). This strategy would be also be sufficient to validate my results in Chapter 3 showing that AC pathway-mediated AMPAR phosphorylation increases in the absence of Ng. In Chapter 3, I additionally assert that CaMKII-mediated AMPAR phosphorylation decreases in the absence of Ng. To experimentally quantify CaMKII-mediated AMPAR phosphorylation *in vivo*, it may be possible to generate a FRET-based system that reports binding interactions between CaMKII and AMPARs. However, I suggest using CaMKII phosphorylation site-specific antibodies for subsequent Western blot, as described by Mammen *et al*. (1997) [320]. With this strategy, it may be possible to experimentally validate whether the effects of competitive tuning are transduced downstream of both AC and CaMKII.

Further exploration of spatial effects

The third major result of this thesis is the apparent sharpening of spatial gradients due to competition for CaM-binding. Notably, this competition-sharpened spatial dependence of Ca^{2+}, Ca^{2+}/CaM, and CBP activation is preserved at multiple Ca^{2+} frequencies (Chapter 4) and spine volumes (Chapter 6). In addition to Ca^{2+} frequency and spine volume, however, the spatial dependence reported in this thesis may also depend on descriptions of diffusion, spine geometry, and other factors.

Diffusion of molecules in a dilute medium is, according to the Stokes-Einstein relation, a function of molecular weight, hydrodynamic radius, and the solution viscosity [321]. The spatial models in this thesis generally utilize the Stokes-Einstein relation. Yet dendritic spine proteins are crowded, low in copy number, interact dynamically, and may be subject to convective microfluidics. Thus, the effective diffusion coefficients in the spine may be smaller than the Stokes-Einstein relation predicts. Indeed, experimental results show that diffusion of spine proteins is on average one order of magnitude smaller than simulations predict [38]. Although in Chapter 6 I quantify differences in model output using standard and reduced diffusion coefficients, more can be done to characterize the mechanisms determining effective diffusion in the spine. For example, using the models presented in Chapters 4 and 6, it may be possible to return to the work by Byrne *et al*. to better characterize how diffusion and/or explicit Ca^{2+}-dependent signaling dynamics regulate CaMKII entry and escape from the dendritic spine [245]. Also, it may be valuable to quantify how different descriptions of diffusion influence model output. The spatial models in this thesis all use MCell to describe diffusion as a discrete-time random walk (DTRW). Here, DTRW is effectively a continuous-time random walk (CTRW) process due to my use of a relatively small timestep of 1μsec or less. Although CTRW may be acceptable for my analysis, future work may aim to quantify how alternative representations of diffusion or protein transport influence model output. Using MCell, it is possible to monitor at each time step the three-dimensional spatial coordinates of each protein, making it possible to calculate a particle's effective diffusion at any given point in simulated time. Alternatively, models could use other platforms such as spatialKappa, which describes diffusion using an agent-based grid [322], or COMSOL®, which would describe protein transport in bulk.

Other future studies could explore how this spatial dependence may influence protein translocation into and out of the dendritic spine. For example, Byrne *et al*. use a spatial model to

explore the conditions for CaMKII entry and escape from a single spine, using generic terms to describe CaMKII interactions with CaM and substrates [245]. Future work can modify the Byrne model to include the intracellular signaling pathways modeled throughout this paper, to more rigorously quantify how these pathways may regulate CaMKII translocation. Similarly, proteins entering the spine's plasma membrane can also be studied in more detail. For example, Antunes *et al*. use MCell 3.3 to describe diffusional trapping of AMPARs at the synaptic membrane [228]. Just as Byrne *et al*., Antunes *et al*. describe generalized Ca^{2+}-dependent protein signaling pathways. Thus, using the models presented in this thesis, it is possible to complement the work by Antunes *et al*. and subsequently quantify how specific intracellular signaling mechanisms regulate AMPAR trafficking to the synaptic membrane.

To experimentally validate the results of Chapter 4, I would aim to measure changes to the spatiotemporal dynamics of Ca^{2+} and CaM in response to AC mutation scenarios. For this, studies could use the mouse mutants described by Wong *et al*., who compared learning behaviors between WT, AC1 knock-out, AC8 knock-out, and double knock-out mice [101]. Notably, an additional mouse variant could be created that ensures inhibition of CaM-binding to only the AC8 N-terminus, possibly by introducing some point mutation in AC8. After isolating neuronal slices from each mouse genotype, it could be possible to observe Ca^{2+} and CaM localizations in the spine before, after, or even during electrical stimulation. To observe localizations of Ca^{2+} and/or CaM, super resolution microscopy could be used, assuming appropriate fluorescent reporters are available. If fluorescent reporters for CaM or various Ca^{2+}/CaM states prove unavailable or difficult to design, at minimum it could be possible to utilize the photoactivated localization microscopy (PALM) technique discussed by Lu *et al*. (2014) [38]. Lu *et al*. use PALM to monitor single molecules of CaMKII. Because CaMKII strongly binds fully-saturated Ca^{2+}/CaM, it could be used as a proxy to monitor the dynamic locations of Ca^{2+}/CaM in each of the mouse genotypes. Using this strategy, it may be possible to further explore how the AC8 N-terminus regulates the dynamics of Ca^{2+}/CaM and CaMKII activity.

Experimental results may also be useful for subsequent training or re-parameterization of my spatial models. For instance, I observe in Chapter 4 a 39 percent gradient in activated CaMKII when the spine is stimulated at 100 Hz Ca^{2+} flux in a competitive scenario (Table 4.2). While this 39 percent gradient supports my conclusion that competition sharpens spatial gradients of protein states, it remains unclear whether its numerical value is physiological. *In vivo*, it may be that the

gradient of active CaMKII along the major axis of the spine has a different value, and future computational studies may wish to adopt this different value. To adopt this value, it is first necessary to experimentally quantify the possible spatial gradients of active CaMKII *in vivo*. For this, the PALM microscopy mentioned in the last paragraph may be sufficient, or perhaps a rapid-fixing electron microscopy (EM) technique would be more appropriate. Previous studies such as those by Fera *et al*. and Ding *et al*. have shown that distinct populations of active CaMKII can be identified through EM. If future studies use a similar approach to measure the localizations of active CaMKII at various time points during Ca^{2+} flux, it could be possible to construct an objective function for CaMKII localization against which to train a more physiological computational model [323, 324]. To train this new model, it is easy to use Latin Hypercube Sampling, as described in Chapters 2, 3, and 6, to find parameter sets that cause model output to agree with the physiological localizations of CaMKII activation.

Exploration of CaMKII holoenzyme activation dynamics

The fourth major result of this thesis is the development of the most complete CaMKII holoenzyme model to-date, and with this model I make a series of biophysical analyses. First, I identify a possible threshold of Ca^{2+}/CaM stimulation beyond which CaMKII exhibits a stable state of auto-phosphorylation despite the presence of phosphatase. Second, I characterize a possible regulatory mechanism in which CaMKII-bound CaM may structurally exclude, or out-compete, PP1 for CaMKII-binding. Altogether, this thesis lays the groundwork for future analyses of the CaMKII holoenzyme *in silico*.

The CaMKII holoenzyme stimulation threshold identified in Chapter 5 is reminiscent of the long-hypothesized CaMKII bistable switch [256, 297]. CaMKII bistability refers to the idea that following sufficient Ca^{2+}/CaM stimulation, CaMKII may enter a dynamic steady-state in which its kinase activity exceeds the activity of phosphatases in the dendritic spine. If CaMKII kinase activity can be robust to phosphatase activity for significant timescales, it might be evidence that CaMKII is the bistable switch hypothetically providing a fundamental unit of molecular memory. Notably, a previous and simpler model of CaMKII regulation shows that CaMKII bistability would likely require non-physiologically high kinase activity [280]. However, the CaM-dependent PP1 exclusion mechanism identified in Chapter 5 may, in conjunction with other mechanisms, provide significant reductions to phosphatase activity, reviving the possibility for

CaMKII to function as a bistable switch under physiological conditions. Therefore, an immediate follow-up study for this thesis may be to re-parameterize the previous Lisman and Zhabotinsky model to account for CaM-dependent PP1 exclusion. My laboratory has already begun exploring this project.

Validating my proposed CaM-dependent PP1 exclusion mechanism likely requires more rigorous parameterization through experimental measurements. First, it remains unclear whether my model results are consistent with *in vitro* studies such as by Bradshaw *et al*. [304]. Although Bradshaw *et al*. show no dependence of CaMKII de-phosphorylation by PP1 on the presence of CaM, they do show that CaMKII phosphorylation levels are maintained on relatively long timescales. Critically, CaMKII phosphorylation is only maintained on long timescales in my models when CaM is able to exclude PP1 from CaMKII binding. So, CaMKII phosphorylation levels are likely maintained in the Bradshaw experiments by some regulatory mechanism, either by CaM-dependent exclusion or otherwise. To better identify this mechanism, my immediate next step is to replicate the Bradshaw experiment *in silico*. For this, it is easy to adjust the 9-state-1-step CaMKII holoenzyme model's initial protein concentrations and also their rate parameters to account for 0°C conditions. To adjust the rate parameters, I can use the Arrhenius equation with the assumption that the change in free energy upon protein-protein binding (E = 8 kcal/mol) is temperature-independent and uniform for all interactions [325]. Simulations using this re-parameterization are underway as of the writing of this thesis.

Further analysis of CaM-dependent PP1 exclusion requires further experimental information regarding the structure and kinetics of CaM- and PP1-CaMKII binding. Indeed, the PP1 binding footprint on CaMKII is entirely undetermined. As discussed in the Supplement to Chapter 5, it is likely that even if PP1 binds CaMKII at a site distant from its substrate at Thr-286, the sizes of CaM and PP1 together likely reduce the ability of PP1 to interact with Thr-286. To verify this, structural studies will be essential, especially because my 9-state-1-step CaMKII holoenzyme model suggests that the Ca^{2+}/CaM state predominantly responsible for excluding PP1 (in the absence of Ca^{2+}) is apo-CaM. Although my kinetic parameters of apo-CaM-binding to pThr-286 CaMKII may explain the ability of apo-CaM to out-compete PP1, my kinetic parameters utilize considerable biophysical assumptions as discussed in [42, 46, 97]. It may therefore be necessary for experimental studies to directly quantify the structure and affinity of apo-CaM binding to CaMKII and phosphorylated CaMKII.

Exploring effects of protein multivalence in the dendritic spine

The fifth major result of this thesis is the development of a strategy for quantifying the effect of CaMKII multivalence on Ca^{2+}-dependent signaling pathway activation. Specifically, I present a series of computational models identical except for their descriptions of either deterministic, spatial-stochastic and monomeric, or spatial-stochastic and dodecameric CaMKII. The deterministic model is useful for rapid model validation, global sensitivity analysis, and quantifying non-spatial model behavior. The spatial-stochastic and monomeric CaMKII model, which uses MCell 3.3., is useful for quantifying the spatial dependence of model behavior with monovalent CaMKII. The spatial-stochastic and dodecameric CaMKII model, which also uses MCell 3.3., is useful for quantifying how localized CaMKII holoenzymes influence the spatial dependence of Ca^{2+}/CaM and other CaMKII binding partners. This result, described in Chapter 6, lays the groundwork for rigorously quantifying model dependence on CaMKII multivalence and CaMKII subunit isoform type. To proceed, future work should endeavor to more accurately portray the CaMKII-actin interaction and accommodate diffusion of the multivalent (multi-state) CaMKII holoenzyme.

The CaMKII-actin model presented through Chapter 6 is an extreme case which, though useful for preliminary insight, produces biased model output. That is, in Chapter 6 I describe CaMKII-actin complexes as irreversible, only becoming terminated upon CaM-CaMKII binding. This irreversibility assumption is meant to account for the number of actin binding sites available to CaMKII likely exceeding the number of CaMKII subunits. In other words, even if CaMKII transiently dissociates from actin *in vivo*, CaMKII likely rapidly re-associates with another actin binding site in the absence of Ca^{2+}/CaM. Thus, my irreversibility assumption allows me to reduce the number of explicitly-instantiated actin binding sites, which is helpful for reducing simulation run-times especially when using MCell. Still, it may be important for future studies to quantify the validity of this assumption, and my laboratory is now undertaking simulations with model networks that allow CaMKII and actin to reversibly bind according to kinetics measured by Khan *et al*. [244].

Quantifying the effects of CaMKII multivalence is significantly hindered by the lack of simulation platforms that can acceptably account for diffusion of multiple multi-state molecules. In Chapter 6, I use MCell 3.3 because its rule-based syntax is sufficient for handling the

combinatorial explosion associated with modeling CaMKII holoenzymes. However, MCell 3.3 does not account for diffusion of multi-state molecules such as CaMKII. Thus, it is impossible to quantify the effect of CaMKII multivalence with proteins other than cytosolic species such as Ca^{2+}/CaM and actin binding sites. Moreover, because CaMKII holoenzymes cannot diffuse in MCell 3.3, key interactions between CaMKII and membrane receptors cannot be modeled. And furthermore, other potentially multi-state molecules such as CaM and AC cannot be simultaneously modeled with rules because the lack of multi-state diffusion would abolish their interactions with other multi-state proteins. Problematically, I am aware of no other platform currently ready for the analysis I begin in Chapter 6. NFsim can handle multiple rule-based species, but it is non-spatial [276]. SpatialKappa provides rule-based species and is spatial, but its grid-based handling of diffusion may be inaccurate, and no published models have used it [322].

A new version of MCell, called MCell-R, accounts for diffusion of multiple multi-state molecules [326]. While the developers of MCell-R have seemingly validated their platform, the platform may not be ready to handle large reaction networks, and nor does it preserve all of the functionalities previously available in MCell 3.3. In their validation, MCell-R is shown to reproduce non-rule-based simulation results in a reaction network of three to four molecules. With only three or four particle-based molecules, MCell-R calculates physiological reaction probabilities, even if molecules spatially aggregate during a simulation. Unfortunately, more complex networks such as mine involving CaMKII holoenzymes can lead to large-scale aggregates of CaMKII subunits, CaM, Ca^{2+}, and other CaMKII binding partners. Indeed, Tapia *et al*. warn that such large-scale aggregates may cause reaction probabilities to become non-physiologically high, reducing the accuracy of model output [326]. One solution to this aggregation problem is to reduce simulation time-step, but this solution's effectiveness is limited and my unsuccessful MCell-R trial runs (not shown) use time-steps as small as 0.1μsec. Reducing MCell-R time-steps may be suitable for analyses of very short simulation times, but this analysis may depend on functionalities only available in MCell 3.3. For instance, I would attempt to monitor the spatial coordinates of CaMKII to calculate how the effective diffusivity of CaMKII may depend on its valence. However, similarly to the problem with reaction probabilities, large-scale molecular aggregation prevents MCell-R from reporting spatial coordinates of individual particles. Additionally, MCell-R does not currently accommodate the time-variable parameters used to create dynamic Ca^{2+} flux as I do throughout this thesis using MCell 3.3. Altogether, while MCell-

R may soon be ready for the analysis presented in this thesis, it is not yet. Still, I anticipate future work with MCell-R that directly complements this thesis and also explores exciting new biophysical phenomena in the spine, such as CaMKII subunit exchange [261, 262], synGAP-PSD-95 interactions [223, 318], and actin polymerization [239, 245].

SUPPLEMENT TO CHAPTER 2

Comparison of four-state and nine-state models

The high cooperativity of Ca^{2+} binding at each CaM terminus has led to the development of several models of Ca^{2+} binding to CaM (see [30, 81, 99]). That is, the binding of individual Ca^{2+} ions at each CaM terminus can each be treated as distinct events, resulting in a thermodynamically complete model of all nine possible Ca^{2+}/CaM states (henceforth referred to as the nine-state model). Alternatively, the binding of both Ca^{2+} ions at each CaM terminus can be treated as a single event, resulting in an approximated model (henceforth referred to as the four-state model). The former model is more biophysically accurate, but the latter model is less computationally complex. Therefore, it is important to determine if the nine-state model is truly necessary, or if the four-state model is sufficient.

To test this, isolated and competitive models were each developed as both nine- and four-state models, and the average bound concentrations (C_b) predicted by these models were compared by dividing four-state model's predictions by those of the nine-state model. Red lines correspond to comparisons between isolated models, while blue lines correspond to comparisons between competitive models. All models included 100 Ca^{2+} spikes introduced at frequencies ranging from 0.1 Hz to 1 kHz. All parameters of the four-state model were derived from the parameters of the nine-state model using a steady-state approximation (see [81]).

The level of disagreement between the four-state and nine-state models varied across targets, frequencies, and models (i.e., isolated and competitive). Overall, the four-state model's predictions for the average bound concentrations of CaM targets ranged from 65% to 200% of those for the nine-state model. Compared to the potential cumulative error of experimental values and previously-described model assumptions, this deviation was deemed negligible. Furthermore, if I am to trust that the implications of this study are robust to *in vivo* extrapolation, then these implications should also be robust to such small deviations in model outputs. Therefore, I chose to use the four-state model for all subsequent simulations.

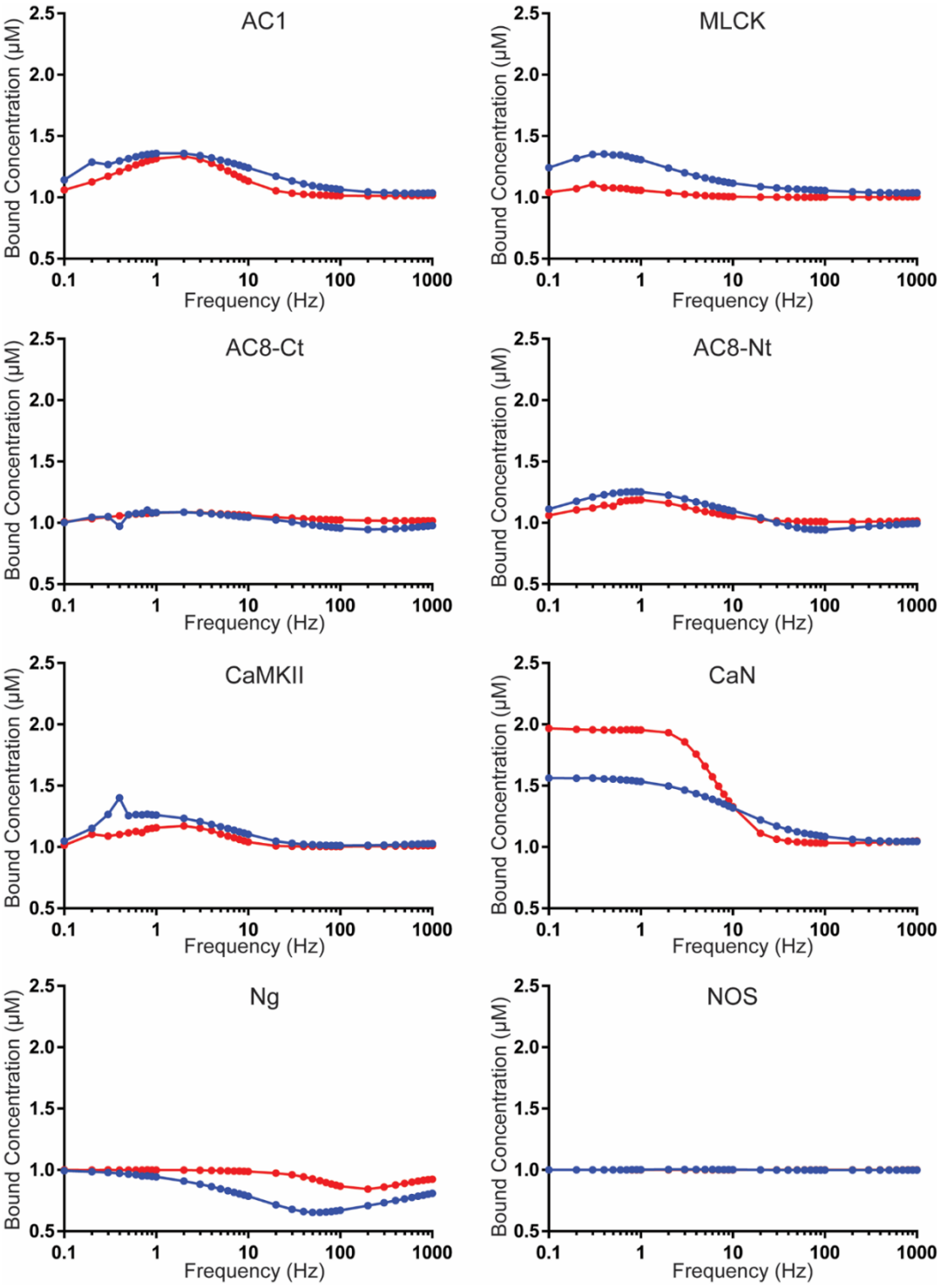

Figure 7.1. Comparison of 4-state and 9-state models of CaM-protein binding. Each panel corresponds to CaM binding to the titled protein as a function of Ca^{2+} frequency. Blue traces are the four-state model; red traces are for nine-state descriptions of CaM. For the purposes of this study, the differences between the two model types are negligible and therefore, I use the four-state model of CaM (with the exception of sensitivity analysis).

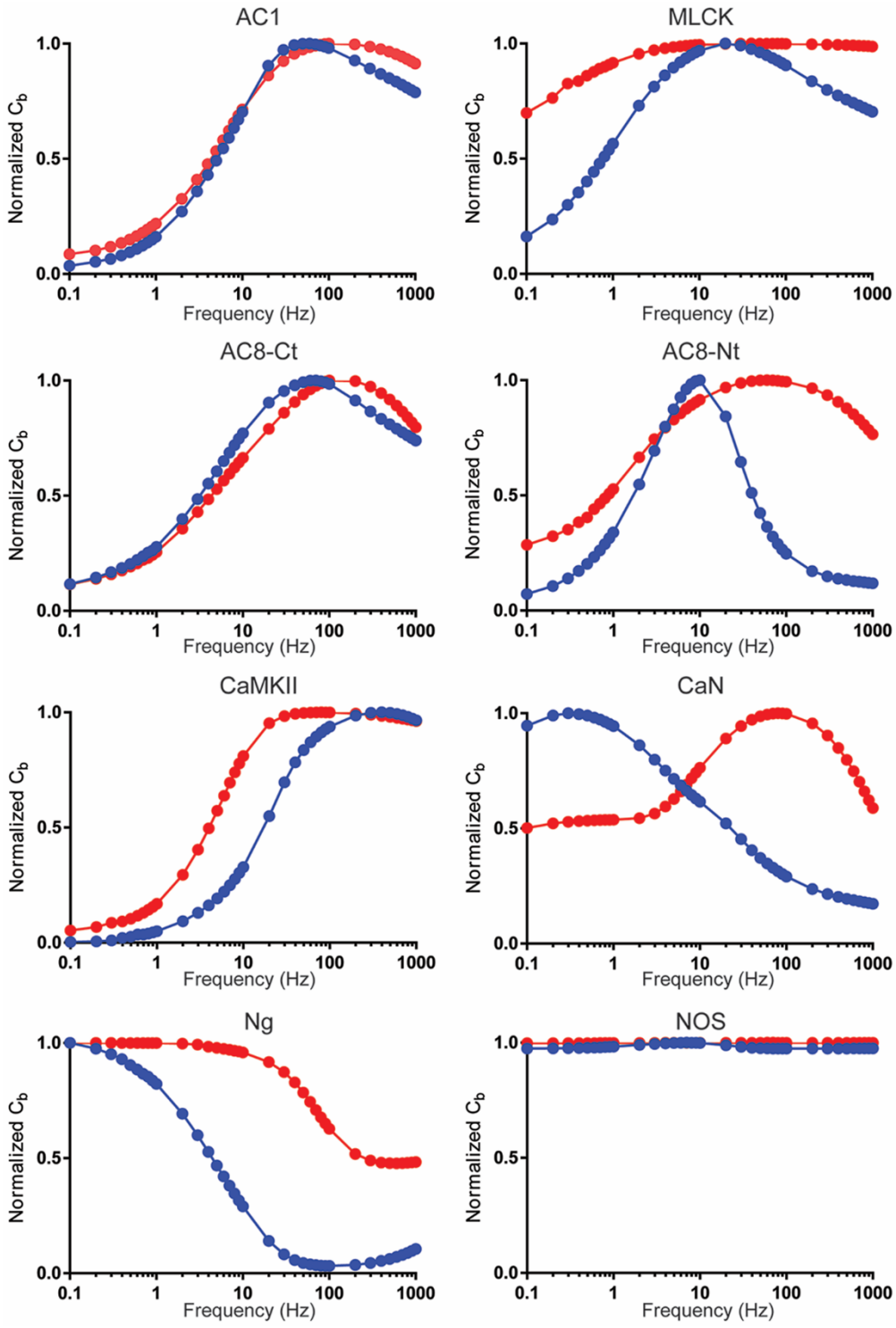

Figure 7.2. Average Bound Concentrations as a Function of Ca^{2+} Frequency. Data is also shown as heatmaps in Fig 4A and Fig 4B. Here, red traces are the output form the competitive models and blue traces are the output from isolated models.

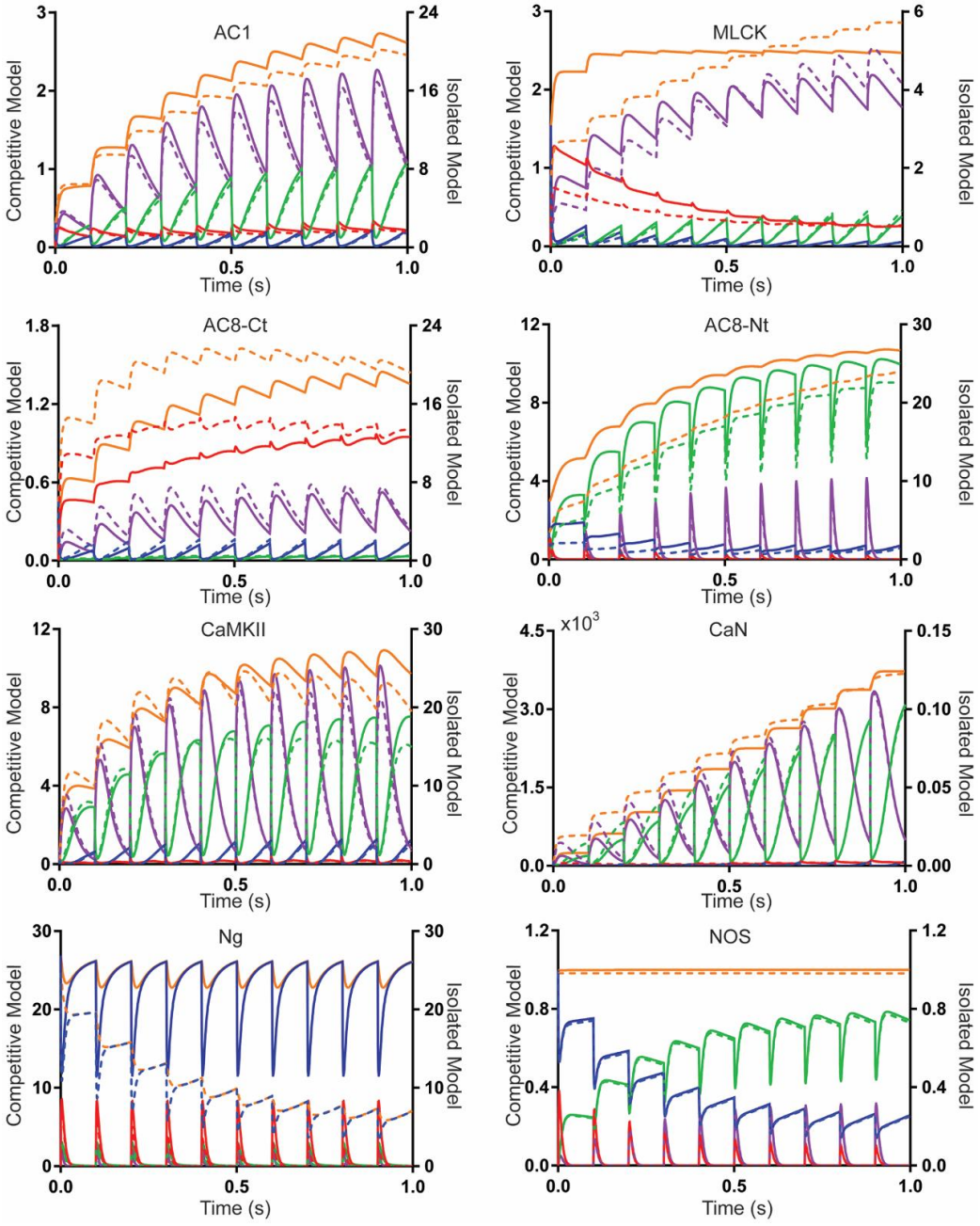

Figure 7.3. Time-course of CaM binding partners bound to various states of CaM (in micromolar) for 1 second of 10 Hz Ca^{2+} flux. Each plot tracks binding of individual CaM states to the indicated binding partner. Note differences in scale. The concentration of indicated binding partner is bound to CaM_0 (blue), CaM_{2N} (red), CaM_{2C} (green), CaM_4 (purple), and CaM_{tot} (orange). Solid lines denote the isolated model plotted against the right axis; dotted lines denote the competitive model plotted against the left axis. The differences between isolated and competitive behavior are more significant for some CaM binding partners than others.

SUPPLEMENT TO CHAPTER 3

Table 7.1. Calmodulin binding proteins and their chemical reaction

Protein	**Description and Chemical Reactions**
Adenylyl Cyclase 1 (AC1)	A prominent, membrane-associated Adenylyl Cyclase isoform in hippocampal neurons. Binds CaM at its C_{1b} domain and, when activated, converts ATP to cAMP. $AC1 + CaM_{iN,jC} \leftrightarrow AC1\_CaM_{iN,jC}$ $2\ Ca^{2+} + AC1\_CaM_{iN,jC} \leftrightarrow AC1\_CaM_{(i+1)N,jC}$ $2\ Ca^{2+} + AC1\_CaM_{iN,jC} \leftrightarrow AC1\_CaM_{iN,(j+1)C}$ $AC1\_CaM_{iN,jC} \rightarrow AC1\_CaM_{iN,jC} + cAMP$
Adenylyl Cyclase 8 (AC8)	A prominent, Adenylyl Cyclase isoform in hippocampal neurons. Binds Ca^{2+}/CaM at both its N- and C-termini, which are explicitly accounted for in this work. Ca^{2+}/CaM-AC8ct (C-terminus-bound AC8) may bind ATP for conversion to cAMP. $AC8nt + CaM_{iN,jC} \leftrightarrow AC8nt\_CaM_{iN,jC}$ $2\ Ca^{2+} + AC8nt\_CaM_{iN,jC} \leftrightarrow AC8nt\_CaM_{(i+1)N,jC}$ $2\ Ca^{2+} + AC8nt\_CaM_{iN,jC} \leftrightarrow AC8nt\_CaM_{iN,(j+1)C}$ $AC8ct + CaM_{iN,jC} \leftrightarrow AC8ct\_CaM_{iN,jC}$ $2\ Ca^{2+} + AC8ct\_CaM_{iN,jC} \leftrightarrow AC8ct\_CaM_{(i+1)N,jC}$ $2\ Ca^{2+} + AC8ct\_CaM_{iN,jC} \leftrightarrow AC8ct\_CaM_{iN,(j+1)C}$ $AC8ct\_CaM_{iN,jC} \rightarrow AC8ct\_CaM_{iN,jC} + cAMP$

Table 7.1. Continued.

Ca^{2+}/CaM-dependent kinase II (CaMKII)	Ca^{2+}/CaM-dependent kinase. Highly expressed in brain, and especially hippocampal tissue. In this work, CaMKII is modeled as monomers which, when active, may dimerize and subsequently become Ca^{2+}/CaM-independent via autophosphorylation. Active CaMKII phosphorylates many downstream proteins such as the GluA1 subunit of AMPA receptors. $CaMKII + CaM_{iN,jC} \leftrightarrow CaMKII\_CaM_{iN,jC}$ $Ca^{2+} + CaMKII\_CaM_{iN,jC} \leftrightarrow CaMKII\_CaM_{(i+1)N,jC}$ $Ca^{2+} + AC8nt\_CaM_{iN,jC} \leftrightarrow AC8nt\_CaM_{iN,(j+1)C}$ $CaMKII\_CaM_{iN,jC} + CaMKII\_CaM_{iN,jC} \leftrightarrow Dimer_{(iN,jC),(iN,jC)} \rightarrow pCaMKII\_CaM_{iN,jC} + CaMKII\_CaM_{iN,jC}$ $CaMKII\_CaM_{iN,jC} + pCaMKII\_CaM_{iN,jC} \leftrightarrow pDimer_{(iN,jC),(iN,jC)} \rightarrow pCaMKII\_CaM_{iN,jC} + pCaMKII\_CaM_{iN,jC}$ $CaMKII\_CaM_{iN,jC} + GluA1 \leftrightarrow CaMKII_{iN,jC}\_GluA1 \rightarrow CaMKII\_CaM_{iN,jC} + GluA1_{p831}$ $CaMKII\_CaM_{iN,jC} + GluA1_{p845} \leftrightarrow CaMKII_{iN,jC}\_GluA1_{p845} \rightarrow CaMKII\_CaM_{iN,jC} + GluA1_{p831p845}$ $pCaMKII\_CaM_{iN,jC} + GluA1 \leftrightarrow pCaMKII_{iN,jC}\_GluA1 \rightarrow pCaMKII\_CaM_{iN,jC} + GluA1_{p831}$ $pCaMKII\_CaM_{iN,jC} + GluA1_{p845} \leftrightarrow pCaMKII_{iN,jC}\_GluA1_{p845} \rightarrow pCaMKII\_CaM_{iN,jC} + GluA1_{p831p845}$
Calcineurin (CaN)	A Ca^{2+}/CaM-dependent serine/threonine phosphatase. For simplicity, my models are restricted only to binding of Ca^{2+}/CaM to the catalytic CaNA subunit. $CaN + CaM_{iN,jC} \leftrightarrow CaN\_CaM_{iN,jC}$ $Ca^{2+} + CaN\_CaM_{iN,jC} \leftrightarrow CaN\_CaM_{(i+1)N,jC}$ $Ca^{2+} + CaN\_CaM_{iN,jC} \leftrightarrow CaN\_CaM_{iN,(j+1)C}$

Table 7.1 Continued.

Myosin Light Chain Kinase (MLCK)	A putatively abundant CBP in dendritic spines, which I model using kinetic parameters derived from studies on smooth muscle. $MLCK + CaM_{iN,jC} \leftrightarrow MLCK\_CaM_{iN,jC}$ $Ca^{2+} + MLCK\_CaM_{iN,jC} \leftrightarrow MLCK\_CaM_{(i+1)N,jC}$ $Ca^{2+} + MLCK\_CaM_{iN,jC} \leftrightarrow MLCK\_CaM_{iN,(j+1)C}$
Neurogranin (Ng)	A membrane-associated protein, and one of the few proteins that strongly binds CaM in absence of Ca^{2+}. $Ng + CaM_{iN,jC} \leftrightarrow Ng\_CaM_{iN,jC}$ $Ca^{2+} + Ng\_CaM_{iN,jC} \leftrightarrow Ng\_CaM_{(i+1)N,jC}$ $Ca^{2+} + Ng\_CaM_{iN,jC} \leftrightarrow Ng\_CaM_{iN,(j+1)C}$
Nitric Oxide Synthetase (NOS)	Typically a membrane-associated protein that binds tightly to CaM and generates Nitric Oxide from citrulline and arginine. $NOS + CaM_{iN,jC} \leftrightarrow NOS\_CaM_{iN,jC}$ $Ca^{2+} + NOS\_CaM_{iN,jC} \leftrightarrow NOS\_CaM_{(i+1)N,jC}$ $Ca^{2+} + NOS\_CaM_{iN,jC} \leftrightarrow NOS\_CaM_{iN,(j+1)C}$
Phosphodiesterase 1 (PDE1)	A Ca^{2+}/CaM dependent phosphodiesterase that cleaves cAMP into AMP. $PDE1 + CaM_{iN,jC} \leftrightarrow PDE1\_CaM_{iN,jC}$ $Ca^{2+} + PDE1\_CaM_{iN,jC} \leftrightarrow PDE1\_CaM_{(i+1)N,jC}$ $Ca^{2+} + PDE1\_CaM_{iN,jC} \leftrightarrow PDE1\_CaM_{iN,(j+1)C}$ $PDE1\_CaM_{iN,jC} + cAMP \rightarrow PDE1\_CaM_{iN,jC} + AMP$

Reaction parameters are provided in Table 7.5. Bidirectional arrows denote reversibility; unidirectional arrows indicate irreversible reactions. Under-scores denote protein complexes. Subscripts i and j pertain to the 4-state model and denote total Ca^{2+} at the CaM N- and C-terminus, respectively. Therefore, in the 4-state model, i and j may be either 0 or 2 independently of each other. In the 2-state model, i and j must both either be 0 or 2. Prefix p denotes phosphorylated players. The corresponding system of differential equations are found in this section entitled "Model Equations".

Table 7.2. Non-calmodulin binding proteins included in model and their respective chemical reactions

Phosphodiesterase 4 (PDE4)	PDE4 is not Ca^{2+}/CaM dependent but plays a significant role in regulating the levels of cAMP in cells by cleaving cAMP into AMP. Phosphorylation by active PKAc increases the enzymatic activity of PDE4 [32]. PDE4 + PKAc ↔ PDE4_PKAc → PKAc + pPDE4 PDE4 + cAMP → PDE4 + AMP pPDE4 + cAMP → pPDE4 + AMP
Protein kinase A (PKA, also known as cAMP-dependent kinase)	Binds up to four cAMP, liberating catalytic subunits that bind and phosphorylate a number of downstream targets such as PDE4 and GluA1 [21, 32]. Reaction subscripts: numbers denote bound cAMP, R denotes auto-inhibition, C denotes a catalytic subunit. PKA + cAMP ↔ R2C2_cAMP R2C2_cAMP + cAMP ↔ $R2C2\_cAMP_2$ $R2C2\_cAMP_2$ + cAMP ↔ $R2C2\_cAMP_3$ $R2C2\_cAMP_3$ + cAMP ↔ $R2C2\_cAMP_4$ $R2C2\_cAMP_4$ ↔ $R2C\_cAMP_4$ + PKAc $R2C\_cAMP_4$ ↔ $R2\_cAMP_4$ + PKAc $R2\_cAMP_4$ ↔ R2 + 4 AMP PKAc + PKAinhibitor ↔ PKAi R2 + PKAi ↔ R2C + PKAinhibitor R2C + PKAi ↔ PKA + PKAinhibitor

Table 7.2 Continued.

Inhibitor 1 (Inh-1 or I1) Protein Phosphatase 1 (PP1)	Inhibitor 1 may become phosphorylated at Ser-35 by PKAc, and phosphorylated Ip35 is able to bind and inhibit the activity of protein phosphatase 1 (PP1). Activated CaN-CaM is able to de-phosphorylate Ip35 back to the original I1 state. $I1 + PKAc \leftrightarrow I1\_PKAc \rightarrow Ip35 + PKAc$ $Ip35 + PP1 \leftrightarrow Ip35\_PP1$ $Ip35 + CaN\_CaM_{iN,jC} \leftrightarrow Ip35\_CaN\_CaM_{iN,jC} \rightarrow I1 + CaN\_CaM_{iN,jC}$ $PP1 + pCaMKII\_CaM_{iN,jC} \leftrightarrow PP1\_ pCaMKII\_CaM_{iN,jC} \rightarrow PP1 + CaMKII\_CaM_{iN,jC}$ $PP1 + GluA1_{p831} \leftrightarrow PP1\_GluA1_{p831} \rightarrow PP1 + GluA1$ $PP1 + GluA1_{p845} \leftrightarrow PP1\_GluA1_{p845} \rightarrow PP1 + GluA1$ $PP1 + GluA1_{p831p845} \leftrightarrow PP1\_GluA1_{p831p845} \rightarrow PP1 + GluA1_{p845}$
GluA1	One of four subunits of α-amino-3-hydroxy-5-methyl-4-isoxazolepropionic acid receptor (AMPA receptor). Is phosphorylated at amino acid residue Ser-831 by CaMKII and residue Ser-845 by PKA [32, 33]. Increase AMPA phosphorylation is implicated in synaptic plasticity, and GluA1-p845 may be necessary for exocytosis of AMPARs to the synaptic membrane [33]. $GluA1 + PKA4 \leftrightarrow GluA1\_PKA4$ $GluA1 + PKAc \leftrightarrow GluA1\_PKAc \rightarrow GluA1_{p845} + PKAc$ $GluA1 + CaMKII\_CaM_{iN,jC} \leftrightarrow GluA1\_CaMKII\_CaM_{iN,jC} \rightarrow GluA1_{p831} + CaMKII\_CaM_{iN,jC}$ $GluA1 + pCaMKII\_CaM_{iN,jC} \leftrightarrow GluA1\_pCaMKII\_CaM_{iN,jC} \rightarrow GluA1_{p831} + pCaMKII\_CaM_{iN,jC}$ $GluA1_{p845} + CaMKII\_CaM_{iN,jC} \leftrightarrow GluA1_{p845}\_CaMKII\_CaM_{iN,jC} \rightarrow GluA1_{p831p845} + CaMKII\_CaM_{iN,jC}$ $GluA1_{p845} + pCaMKII\_CaM_{iN,jC} \leftrightarrow GluA1_{p845}\_pCaMKII\_CaM_{iN,jC} \rightarrow GluA1_{p831p845} + pCaMKII\_CaM_{iN,jC}$ $GluA1_{p831} + PKAc \leftrightarrow GluA1_{p831}\_PKAc \rightarrow GluA1_{p831p845} + PKAc$

Reaction parameters are provided in Table 7.5. Bidirectional arrows denote reversibility; Unidirectional arrows indicate irreversible reactions. Underscores denote protein complexes. Subscripts i and j pertain to the 4-state model and denote total Ca^{2+} at the CaM N- and C-terminus, respectively. Therefore, in the 4-state model, i and j may be either 0 or 2 independently of each other. In the 2-state model, i and j must both either be 0 or 2. Prefix p denotes phosphorylated players. The corresponding system of differential equations are found in Supplemental Material section entitled "Model Equations".

Calculation of C_b for Figure 3.3.

In Figure 3.3, I deploy a metric first utilized in a previous publication (Romano et al. 2017 PLoS Comp Biol). In that publication, the metric C_b is defined as the time-averaged concentration of CaM-bound CBP at a given Ca^{2+} frequency. C_b is mathematically represented in Equation 1 or Equation 2 below. Sometimes, I use Equation 1 which accounts for all CaM_4-bound CBPs, and sometimes I use Equation 2, which accounts for CBPs bound by any Ca^{2+}/CaM state.

$$(1)\ C_b = \frac{1}{t_f - t_0} \int_{t=t_0}^{t_f} \sum_{i=0}^{2} \sum_{j=0}^{2} [T_b CaM4]\, dt$$

$$(2)\ C_b = \frac{1}{t_f - t_0} \int_{t=t_0}^{t_f} \sum_{i=0}^{2} \sum_{j=0}^{2} \left[T_b CaMN_i C_j\right] dt$$

The subscript b indexes the binding partners, so the average bound concentration for a given binding partner (C_b) is found by integrating the total concentration of that binding partner (T_b) bound to each CaM state ($CaMN_iC_j$, i and j = 0, 1, or 2) over the stimulation period (t_o until t_f) and dividing by the stimulus duration (t_f - t_o). Note that dividing by stimulus duration is necessary because I reduce $t_f - t_o$ in order to limit computational expense at high frequencies. To compare relative levels of CaM-binding across various proteins and experimental conditions, for each binding partner I normalize C_b by its peak value from among all the Ca^{2+} frequencies simulated.

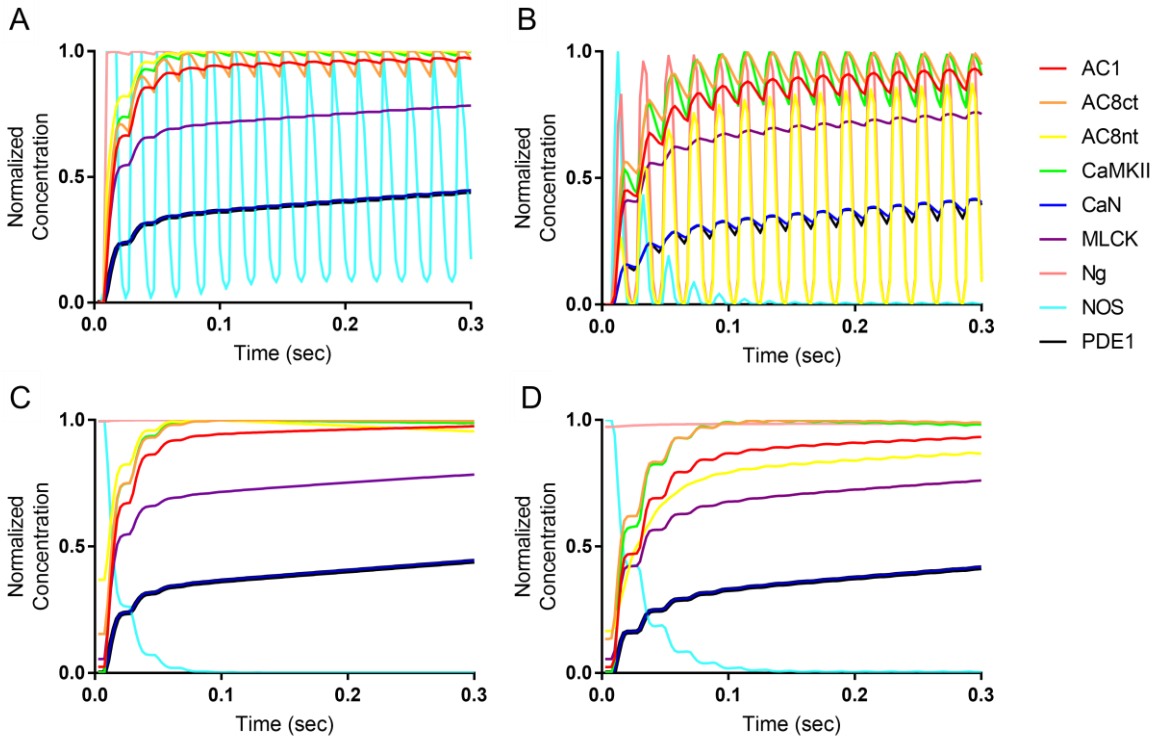

Figure 7.4. 2-state vs 4-state time-course comparison at 50Hz. (A, B) Response of binding models to 50 Hz Ca^{2+} frequency stimulation, monitoring each CBP bound to Ca^{2+}-saturated CaM_4 for the **(A)** 2-state and **(B)** 4-state models. **(C, D)** Response of binding models to 50 Hz Ca^{2+} frequency stimulation, monitoring the cumulative concentration of each CBP bound to any Ca^{2+}/CaM state for the **(C)** 2-state and **(D)** 4-state models.

Table 7.3. Sensitivity Analysis of Kinetic Parameters at 10 Hz Ca^{2+} and WT Ng.

Parameter	PRCC
$k_p^{AC1CaM4}$	0.736
$k_{on}^{AC1CaM4}$	0.568
$k_p^{KCaM4GluA1}$	0.550
$k_{on}^{CaMKIIGluA1}$	0.540
k_{on}^{KCaM4}	-0.560
$k_p^{PDE4cAMP}$	-0.771

Note that both CaMKII- and AC-associated parameters are both implicated as significant in this analysis.

Table 7.4. Sensitivity Analysis of Initial Concentrations at 10 vs 100 Hz Ca^{2+} with WT Ng.

Parameter	PRCC 10 Hz	Parameter	PRCC 100 Hz
$concCaM$	0.898	$concCaM$	0.893
$concGluA1$	0.708	$concGluA1$	0.775
$concAC1$	0.578	$concAC1$	0.632
$concCaMKII$	-0.540	$concPKA$	0.556
$concPDE4$	-0.747	$concCaMKII$	-0.597
		$concPDE4$	-0.758

At both 10 Hz and 100 Hz, that [CaM] and [GluA1] are highly significant lends confidence to my sensitivity analysis results.

Table 7.5. Model parameter values.

Parameter	Description	Value Used
k_{on}^{2N}	2 Ca^{2+} binding to CaM N-terminus	100.0 $\mu M^{-1}s^{-1}$
k_{off}^{2N}	2 Ca^{2+} dissociation from CaM N-terminus	750.0 s^{-1}
K_D^{2N}	Equilibrium binding of 2 Ca^{2+} to CaM N-terminus	7.5 μM
k_{on}^{2C}	2 Ca^{2+} binding to CaM C-terminus	4.0 $\mu M^{-1}s^{-1}$
k_{off}^{2C}	2 Ca^{2+} dissociation from CaM C-terminus	9.25 s^{-1}
K_D^{2C}	Equilibrium binding of 2 Ca^{2+} to CaM C-terminus	2.32 μM
$k_{on}^{AC1CaM0}$	CaM0 binding to AC1	0.00166 $\mu M^{-1}s^{-1}$
$k_{off}^{AC1CaM0}$	CaM0 dissociation from AC1	0.9 s^{-1}
$K_D^{AC1CaM0}$	Equilibrium binding of CaM0 to AC1	542.0 μM
$k_{on}^{AC1CaM2N}$	CaM2N binding to AC1	0.156 $\mu M^{-1}s^{-1}$
$k_{off}^{AC1CaM2N}$	CaM2N dissociation from AC1	0.9 s^{-1}
$K_D^{AC1CaM2N}$	Equilibrium binding of CaM2N to AC1	5.78 μM
$k_{on}^{AC1CaM2C}$	CaM2C binding to AC1	0.064 $\mu M^{-1}s^{-1}$
$k_{off}^{AC1CaM2C}$	CaM2C dissociation from AC1	0.9 s^{-1}
$K_D^{AC1CaM2C}$	Equilibrium binding of CaM2C to AC1	14.1 μM
$k_{on}^{AC1CaM4}$	CaM4 binding to AC1	6.0 $\mu M^{-1}s^{-1}$
$k_{off}^{AC1CaM4}$	CaM4 dissociation from AC1	0.9 s^{-1}
$K_D^{AC1CaM4}$	Equilibrium binding of CaM4 to AC1	0.15 μM
k_{on}^{AC12N}	2 Ca^{2+} binding to AC1-CaM N-terminus	100.0 $\mu M^{-1}s^{-1}$
k_{off}^{AC12N}	2 Ca^{2+} dissociation from AC1-CaM N-terminus	8.0 s^{-1}
K_D^{AC12N}	Equilibrium binding of 2 Ca^{2+} to AC1-CaM N-terminus	0.08 μM
k_{on}^{AC12C}	2 Ca^{2+} binding to AC1-CaM C-terminus	4.0 $\mu M^{-1}s^{-1}$
k_{off}^{AC12C}	2 Ca^{2+} dissociation from AC1-CaM C-terminus	1.2 s^{-1}
K_D^{AC12C}	Equilibrium binding of 2 Ca^{2+} to AC1-CaM C-terminus	0.3 μM
$k_{on}^{AC8ntCaM0}$	CaM0 binding to AC8 N-terminus	0.00828 $\mu M^{-1}s^{-1}$
$k_{off}^{AC8ntCaM0}$	CaM0 dissociation from AC8 N-terminus	1.0 s^{-1}
$K_D^{AC8ntCaM0}$	Equilibrium binding of CaM0 to AC8 N-terminus	121.0 μM
$k_{on}^{AC8ntCaM2N}$	CaM2N binding to AC8 N-terminus	0.00828 $\mu M^{-1}s^{-1}$

Table 7.5 Continued.

$k_{off}^{AC8ntCaM2N}$	CaM2N dissociation from AC8 N-terminus	1.0 s^{-1}
$K_D^{AC8ntCaM2N}$	Equilibrium binding of CaM2N to AC8 N-terminus	121.0 μM
$k_{on}^{AC8ntCaM2C}$	CaM2C binding to AC8 N-terminus	1.25 $\mu M^{-1}s^{-1}$
$k_{off}^{AC8ntCaM2C}$	CaM2C dissociation from AC8 N-terminus	1.0 s^{-1}
$K_D^{AC8ntCaM2C}$	Equilibrium binding of CaM2C to AC8 N-terminus	0.8 μM
$k_{on}^{AC8ntCaM4}$	CaM4 binding to AC8 N-terminus	1.25 $\mu M^{-1}s^{-1}$
$k_{off}^{AC8ntCaM4}$	CaM4 dissociation from AC8 N-terminus	1.0 s^{-1}
$K_D^{AC8ntCaM4}$	Equilibrium binding of CaM4 to AC8 N-terminus	0.8 μM
$k_{on}^{AC8nt2N}$	2 Ca^{2+} binding to AC8(N-terminus)-CaM N-terminus	100.0 $\mu M^{-1}s^{-1}$
$k_{off}^{AC8nt2N}$	2 Ca^{2+} dissociation from AC8(N-terminus)-CaM N-terminus	750.0 s^{-1}
$K_D^{AC8nt2N}$	Equilibrium binding of 2 Ca^{2+} to AC8(N-terminus)-CaM N-terminus	7.5 μM
$k_{on}^{AC8nt2C}$	2 Ca^{2+} binding to AC8(N-terminus)-CaM C-terminus	4.0 $\mu M^{-1}s^{-1}$
$k_{off}^{AC8nt2C}$	2 Ca^{2+} dissociation from AC8(N-terminus)-CaM C-terminus	0.5 s^{-1}
$K_D^{AC8nt2C}$	Equilibrium binding of 2 Ca^{2+} to AC8(N-terminus)-CaM C-terminus	0.125 μM
$k_{on}^{AC8ctCaM0}$	CaM0 binding to AC8 C-terminus	0.00267 $\mu M^{-1}s^{-1}$
$k_{off}^{AC8ctCaM0}$	CaM0 dissociation from AC8 C-terminus	1.0 s^{-1}
$K_D^{AC8ctCaM0}$	Equilibrium binding of CaM0 to AC8 C-terminus	375.0 μM
$k_{on}^{AC8ctCaM2N}$	CaM2N binding to AC8 C-terminus	1.25 $\mu M^{-1}s^{-1}$
$k_{off}^{AC8ctCaM2N}$	CaM2N dissociation from AC8 C-terminus	1.0 s^{-1}
$K_D^{AC8ctCaM2N}$	Equilibrium binding of CaM2N to AC8 C-terminus	0.8 μM
$k_{on}^{AC8ctCaM2C}$	CaM2C binding to AC8 C-terminus	0.00267 $\mu M^{-1}s^{-1}$
$k_{off}^{AC8ctCaM2C}$	CaM2C dissociation from AC8 C-terminus	1.0 s^{-1}
$K_D^{AC8ctCaM2C}$	Equilibrium binding of CaM2C to AC8 C-terminus	375.0 μM
$k_{on}^{AC8ctCaM4}$	CaM4 binding to AC8 C-terminus	1.25 $\mu M^{-1}s^{-1}$

Table 7.5 Continued.

$k_{off}^{AC8ctCaM4}$	CaM4 dissociation from AC8 C-terminus	1.0 s^{-1}
$K_D^{AC8ctCaM4}$	Equilibrium binding of CaM4 to AC8 C-terminus	0.8 μM
$k_{on}^{AC8ct2N}$	2 Ca^{2+} binding to AC8(C-terminus)-CaM N-terminus	100.0 $\mu M^{-1}s^{-1}$
$k_{off}^{AC8ct2N}$	2 Ca^{2+} dissociation from AC8(C-terminus)-CaM N-terminus	1.6 s^{-1}
$K_D^{AC8ct2N}$	Equilibrium binding of 2 Ca^{2+} to AC8(C-terminus)-CaM N-terminus	0.016 μM
$k_{on}^{AC8ct2C}$	2 Ca^{2+} binding to AC8(C-terminus)-CaM C-terminus	4.0 $\mu M^{-1}s^{-1}$
$k_{off}^{AC8ct2C}$	2 Ca^{2+} dissociation from AC8(C-terminus)-CaM C-terminus	9.25 s^{-1}
$K_D^{AC8ct2C}$	Equilibrium binding of 2 Ca^{2+} to AC8(C-terminus)-CaM C-terminus	2.31 μM
k_{on}^{PPCaM0}	CaM0 binding to CaN	0.0000000798 $\mu M^{-1}s^{-1}$
k_{off}^{PPCaM0}	CaM0 dissociation from CaN	0.000319 s^{-1}
K_D^{PPCaM0}	Equilibrium binding of CaM0 to CaN	3999.0 μM
$k_{on}^{PPCaM2N}$	CaM2N binding to CaN	0.000416 $\mu M^{-1}s^{-1}$
$k_{off}^{PPCaM2N}$	CaM2N dissociation from CaN	0.000319 s^{-1}
$K_D^{PPCaM2N}$	Equilibrium binding of CaM2N to CaN	0.768 μM
$k_{on}^{PPCaM2C}$	CaM2C binding to CaN	0.000123 $\mu M^{-1}s^{-1}$
$k_{off}^{PPCaM2C}$	CaM2C dissociation from CaN	0.000319 s^{-1}
$K_D^{PPCaM2C}$	Equilibrium binding of CaM2C to CaN	2.59 μM
k_{on}^{PPCaM4}	CaM4 binding to CaN	0.64 $\mu M^{-1}s^{-1}$
k_{off}^{PPCaM4}	CaM4 dissociation from CaN	0.000319 s^{-1}
K_D^{PPCaM4}	Equilibrium binding of CaM4 to CaN	0.000498 μM
k_{on}^{PP2N}	2 Ca^{2+} binding to CaN-CaM N-terminus	100.0 $\mu M^{-1}s^{-1}$
k_{off}^{PP2N}	2 Ca^{2+} dissociation from CaN-CaM N-terminus	12.0 s^{-1}
K_D^{PP2N}	Equilibrium binding of 2 Ca^{2+} to CaN-CaM N-terminus	0.12 μM
k_{on}^{PP2C}	2 Ca^{2+} binding to CaN-CaM C-terminus	4.0 $\mu M^{-1}s^{-1}$
k_{off}^{PP2C}	2 Ca^{2+} dissociation from CaN-CaM C-terminus	0.6 s^{-1}
K_D^{PP2C}	Equilibrium binding of 2 Ca^{2+} to CaN-CaM C-terminus	0.15 μM
k_{on}^{KCaM0}	CaM0 binding to CaMKII	0.0038 $\mu M^{-1}s^{-1}$
k_{off}^{KCaM0}	CaM0 dissociation from CaMKII	5.5 s^{-1}
K_D^{KCaM0}	Equilibrium binding of CaM0 to CaMKII	1.45 mM

Table 7.5 Continued.

k_{on}^{KCaM2N}	CaM2N binding to CaMKII	0.12 $\mu M^{-1}s^{-1}$
k_{off}^{KCaM2N}	CaM2N dissociation from CaMKII	1.7 s^{-1}
K_D^{KCaM2N}	Equilibrium binding of CaM2N to CaMKII	14.2 μM
k_{on}^{KCaM2C}	CaM2C binding to CaMKII	0.92 $\mu M^{-1}s^{-1}$
k_{off}^{KCaM2C}	CaM2C dissociation from CaMKII	6.8 s^{-1}
K_D^{KCaM2C}	Equilibrium binding of CaM2C to CaMKII	7.39 μM
k_{on}^{KCaM4}	CaM4 binding to CaMKII	30.0 $\mu M^{-1}s^{-1}$
k_{off}^{KCaM4}	CaM4 dissociation from CaMKII	1.7 s^{-1}
K_D^{KCaM4}	Equilibrium binding of CaM4 to CaMKII	0.0567 μM
k_{on}^{K2N}	2 Ca^{2+} binding to CaMKII-CaM N-terminus	76.0 $\mu M^{-1}s^{-1}$
k_{off}^{K2N}	2 Ca^{2+} dissociation from CaMKII-CaM N-terminus	33.0 s^{-1}
K_D^{K2N}	Equilibrium binding of 2 Ca^{2+} to CaMKII-CaM N-terminus	0.43 μM
k_{on}^{K2C}	2 Ca^{2+} binding to CaMKII-CaM C-terminus	44.0 $\mu M^{-1}s^{-1}$
k_{off}^{K2C}	2 Ca^{2+} dissociation from CaMKII-CaM C-terminus	2.7 s^{-1}
K_D^{K2C}	Equilibrium binding of 2 Ca^{2+} to CaMKII-CaM C-terminus	0.0614 μM
k_{on}^{MKCaM0}	CaM0 binding to MLCK	0.00717 $\mu M^{-1}s^{-1}$
k_{off}^{MKCaM0}	CaM0 dissociation from MLCK	0.132 s^{-1}
K_D^{MKCaM0}	Equilibrium binding of CaM0 to MLCK	18.4 μM
$k_{on}^{MKCaM2N}$	CaM2N binding to MLCK	2.34 $\mu M^{-1}s^{-1}$
$k_{off}^{MKCaM2N}$	CaM2N dissociation from MLCK	0.132 s^{-1}
$K_D^{MKCaM2N}$	Equilibrium binding of CaM2N to MLCK	0.0564 μM
$k_{on}^{MKCaM2C}$	CaM2C binding to MLCK	0.170 $\mu M^{-1}s^{-1}$
$k_{off}^{MKCaM2C}$	CaM2C dissociation from MLCK	0.132 s^{-1}
$K_D^{MKCaM2C}$	Equilibrium binding of CaM2C to MLCK	0.776 μM
k_{on}^{MKCaM4}	CaM4 binding to MLCK	55.5 $\mu M^{-1}s^{-1}$
k_{off}^{MKCaM4}	CaM4 dissociation from MLCK	0.132 s^{-1}
K_D^{MKCaM4}	Equilibrium binding of CaM4 to MLCK	0.00238 μM
k_{on}^{MK2N}	2 Ca^{2+} binding to MLCK-CaM N-terminus	100.0 $\mu M^{-1}s^{-1}$
k_{off}^{MK2N}	2 Ca^{2+} dissociation from MLCK-CaM N-terminus	2.3 s^{-1}

Table 7.5 Continued.

K_D^{MK2N}	Equilibrium binding of 2 Ca^{2+} to MLCK-CaM N-terminus	0.023 μM
k_{on}^{MK2C}	2 Ca^{2+} binding to MLCK-CaM C-terminus	4.0 $\mu M^{-1}s^{-1}$
k_{off}^{MK2C}	2 Ca^{2+} dissociation from MLCK-CaM C-terminus	0.39 s^{-1}
K_D^{MK2C}	Equilibrium binding of 2 Ca^{2+} to MLCK-CaM C-terminus	0.098 μM
k_{on}^{NgCaM0}	CaM0 binding to Ng	28.0 $\mu M^{-1}s^{-1}$
k_{off}^{NgCaM0}	CaM0 dissociation from Ng	36.0 s^{-1}
K_D^{NgCaM0}	Equilibrium binding of CaM0 to Ng	1.29 μM
$k_{on}^{NgCaM2N}$	CaM2N binding to Ng	28.0 $\mu M^{-1}s^{-1}$
$k_{off}^{NgCaM2N}$	CaM2N dissociation from Ng	36.0 s^{-1}
$K_D^{NgCaM2N}$	Equilibrium binding of CaM2N to Ng	1.29 μM
$k_{on}^{NgCaM2C}$	CaM2C binding to Ng	2.0 $\mu M^{-1}s^{-1}$
$k_{off}^{NgCaM2C}$	CaM2C dissociation from Ng	136.0 s^{-1}
$K_D^{NgCaM2C}$	Equilibrium binding of CaM2C to Ng	68.0 μM
k_{on}^{NgCaM4}	CaM4 binding to Ng	2.0 $\mu M^{-1}s^{-1}$
k_{off}^{NgCaM4}	CaM4 dissociation from Ng	136.0 s^{-1}
K_D^{NgCaM4}	Equilibrium binding of CaM4 to Ng	68.0 μM
k_{on}^{Ng2N}	2 Ca^{2+} binding to Ng-CaM N-terminus	100.0 $\mu M^{-1}s^{-1}$
k_{off}^{Ng2N}	2 Ca^{2+} dissociation from Ng-CaM N-terminus	750.0 s^{-1}
K_D^{Ng2N}	Equilibrium binding of 2 Ca^{2+} to Ng-CaM N-terminus	7.5 μM
k_{on}^{Ng2C}	2 Ca^{2+} binding to Ng-CaM C-terminus	426.0 $\mu M^{-1}s^{-1}$
k_{off}^{Ng2C}	2 Ca^{2+} dissociation from Ng-CaM C-terminus	418.0 s^{-1}
K_D^{Ng2C}	Equilibrium binding of 2 Ca^{2+} to Ng-CaM C-terminus	0.98 μM
$k_{on}^{NOSCaM0}$	CaM0 binding to NOS	0.135 $\mu M^{-1}s^{-1}$
$k_{off}^{NOSCaM0}$	CaM0 dissociation from NOS	0.01 s^{-1}
$K_D^{NOSCaM0}$	Equilibrium binding of CaM0 to NOS	0.074 μM
$k_{on}^{NOSCaM2N}$	CaM2N binding to NOS	0.135 $\mu M^{-1}s^{-1}$
$k_{off}^{NOSCaM2N}$	CaM2N dissociation from NOS	0.01 s^{-1}
$K_D^{NOSCaM2N}$	Equilibrium binding of CaM2N to NOS	0.074 μM
$k_{on}^{NOSCaM2C}$	CaM2C binding to NOS	1.25 $\mu M^{-1}s^{-1}$
$k_{off}^{NOSCaM2C}$	CaM2C dissociation from NOS	0.01 s^{-1}
$K_D^{NOSCaM2C}$	Equilibrium binding of CaM2C to NOS	0.008 μM
$k_{on}^{NOSCaM4}$	CaM4 binding to NOS	1.25 $\mu M^{-1}s^{-1}$

Table 7.5 Continued.

$k_{off}^{NOSCaM4}$	CaM4 dissociation from NOS	0.01 s^{-1}
$K_D^{NOSCaM4}$	Equilibrium binding of CaM4 to NOS	0.008 μM
k_{on}^{NOS2N}	2 Ca^{2+} binding to NOS-CaM N-terminus	100.0 $\mu M^{-1}s^{-1}$
k_{off}^{NOS2N}	2 Ca^{2+} dissociation from NOS-CaM N-terminus	750.0 s^{-1}
K_D^{NOS2N}	Equilibrium binding of 2nd Ca^{2+} to NOS-CaM N-terminus	7.5 μM
k_{on}^{NOS2C}	2 Ca^{2+} binding to NOS-CaM C-terminus	4.0 $\mu M^{-1}s^{-1}$
k_{off}^{NOS2C}	2 Ca^{2+} dissociation from NOS-CaM C-terminus	1.0 s^{-1}
K_D^{NOS2C}	Equilibrium binding of 2 Ca^{2+} to NOS-CaM C-terminus	0.25 μM
$k_{on}^{PDE1CaM0}$	CaM0 binding to PDE1	0.0000000138 $\mu M^{-1}s^{-1}$
$k_{off}^{PDE1CaM0}$	CaM0 dissociation from PDE1	0.001 s^{-1}
$K_D^{PDE1CaM0}$	Equilibrium binding of CaM0 to PDE1	72463.8 μM
$k_{on}^{PDE1CaM2N}$	CaM2N binding to PDE1	0.00002 $\mu M^{-1}s^{-1}$
$k_{off}^{PDE1CaM2N}$	CaM2N dissociation from PDE1	0.001 s^{-1}
$K_D^{PDE1CaM2N}$	Equilibrium binding of CaM2N to PDE1	50 μM
$k_{on}^{PDE1CaM2C}$	CaM2C binding to PDE1	0.00013 $\mu M^{-1}s^{-1}$
$k_{off}^{PDE1CaM2C}$	CaM2C dissociation from PDE1	0.001 s^{-1}
$K_D^{PDE1CaM2C}$	Equilibrium binding of CaM2C to PDE1	7.69 μM
$k_{on}^{PDE1CaM4}$	CaM4 binding to PDE1	0.18182 $\mu M^{-1}s^{-1}$
$k_{off}^{PDE1CaM4}$	CaM4 dissociation from PDE1	0.001 s^{-1}
$K_D^{PDE1CaM4}$	Equilibrium binding of CaM4 to PDE1	0.0055 μM
k_{on}^{PDE12N}	2 Ca^{2+} binding to PDE1-CaM N-terminus	750.0 $\mu M^{-1}s^{-1}$
k_{off}^{PDE12N}	2 Ca^{2+} dissociation from PDE1-CaM N-terminus	25 s^{-1}
K_D^{PDE12N}	Equilibrium binding of 2 Ca^{2+} to PDE1-CaM N-terminus	0.033 μM
k_{on}^{PDE12C}	2 Ca^{2+} binding to PDE1-CaM C-terminus	204 $\mu M^{-1}s^{-1}$
k_{off}^{PDE12C}	2 Ca^{2+} dissociation from PDE1-CaM C-terminus	1.02 s^{-1}
K_D^{PDE12C}	Equilibrium binding of 2 Ca^{2+} to PDE1-CaM C-terminus	0.005 μM
k_{on}^{CaMKII}	CaMKII binding to CaMKII	45 $\mu M^{-1}s^{-1}$
k_{off}^{CaMKII}	CaMKII dissociation from CaMKII	2250 s^{-1}
K_D^{CaMKII}	Equilibrium binding of CaMKII to CaMKII	50 μM

Table 7.5 Continued.

$k_{on}^{CaMKIIp}$	CaMKII binding pCaMKII	45 $\mu M^{-1}s^{-1}$
$k_{off}^{CaMKIIp}$	CaMKII dissociation from pCaMKII	2250 s^{-1}
$K_D^{CaMKIIp}$	Equilibrium binding of CaMKII to pCaMKII	50 μM
$k_p^{CaMKIICaM0}$	Autophosphorylation of CaMKII-CaM0	0 s^{-1}
$k_p^{CaMKIICaM2N}$	Autophosphorylation of CaMKII-CaM2N	0.120 s^{-1}
$k_p^{CaMKIICaM2C}$	Autophosphorylation of CaMKII-CaM2C	0.064 s^{-1}
$k_p^{CaMKIICaM4}$	Autophosphorylation of CaMKII-CaM4	0.875 s^{-1}
k_{cat}^{AC1CaM}	Catalysis of ATP by AC1-CaM0	0 s^{-1}
$k_{cat}^{AC1CaM2N}$	Catalysis of ATP by AC1-CaM2N	0.77897 s^{-1}
$k_{cat}^{AC1CaM2C}$	Catalysis of ATP by AC1-CaM2C	0.41545 s^{-1}
$k_{cat}^{AC1CaM4}$	Catalysis of ATP by AC1-CaM4	5.68 s^{-1}
$k_{cat}^{AC8ctCaM}$	Catalysis of ATP by AC8ct-CaM0	0 s^{-1}
$k_{cat}^{AC8ctCaM2N}$	Catalysis of ATP by AC8ct-CaM2N	0.3895 s^{-1}
$k_{cat}^{AC8ctCaM2C}$	Catalysis of ATP by AC8ct-CaM2C	0.2077 s^{-1}
$k_{cat}^{AC8ctCaM4}$	Catalysis of ATP by AC8ct-CaM4	2.84 s^{-1}
$k_{cat}^{PDE1cAMP}$	Catalysis of cAMP by PDE1	11.0 s^{-1}
k_{on}^{cAMP1}	Association of first cAMP to PKA	54 $\mu M^{-1}s^{-1}$
k_{off}^{cAMP1}	Dissociation of first cAMP to PKA	33 s^{-1}
k_{on}^{cAMP2}	Association of second cAMP to PKA	54 $\mu M^{-1}s^{-1}$
k_{off}^{cAMP2}	Dissociation of second cAMP to PKA	33 s^{-1}
k_{on}^{cAMP3}	Association of third cAMP to PKA	75 $\mu M^{-1}s^{-1}$
k_{off}^{cAMP3}	Dissociation of third cAMP to PKA	110 s^{-1}
k_{on}^{cAMP4}	Association of fourth cAMP to PKA	75 $\mu M^{-1}s^{-1}$
k_{off}^{cAMP4}	Dissociation of fourth cAMP to PKA	32.05 s^{-1}
k_{split}^{PKAc}	Dissociation of PKAc from R2C2	60 s^{-1}
k_{join}^{PKAc}	Association of PKAc to R2C	18 $\mu M^{-1}s^{-1}$
$k_{on}^{PKAinhib}$	Association of PKA to PKA Inhibitor	59 $\mu M^{-1}s^{-1}$
$k_{off}^{PKAinhib}$	Dissociation of PKAc from PKA Inhibitor	1 s^{-1}
k_p^{PDE4}	PDE4 phosphorylation by PKAc	0.125 s^{-1}
$k_{cat}^{cAMPPDE4}$	PDE4 mediated catalysis of cAMP	17.23 s^{-1}
$k_{cat}^{cAMPpPDE4}$	pPDE4 mediated catalysis of cAMP	34.5 s^{-1}
$k_{on}^{PKA4GluA1}$	PKA4 binding to GluA1	0.402 $\mu M^{-1}s^{-1}$
$k_{off}^{PKA4GluA1}$	PKA4 dissociation from GluA1	24.0 s^{-1}
$K_D^{PKA4GluA1}$	Equilibrium binding of PKA4 to GluA1	59.7 μM
$k_{on}^{PKAc845}$	PKAc binding to GluA1	4.02 $\mu M^{-1}s^{-1}$
$k_{off}^{PKAc845}$	PKAc dissociation to GluA1	24.0 s^{-1}
$K_D^{PKAc845}$	Equilibrium binding of PKAc to GluA1	5.97 μM
$k_p^{PKAc845}$	Phosphorylation of s845 site by PKAc	6.0 s^{-1}

Table 7.5 Continued.

$k_{on}^{CaMKII831}$	CaMKII binding to GluA1	0.02224 $\mu M^{-1}s^{-1}$
$k_{off}^{CaMKII831}$	CaMKII dissociation to GluA1	1.6 s^{-1}
$K_D^{CaMKII831}$	Equilibrium binding of CaMKII to GluA1	71.94 μM
$k_p^{CaMKII831}$	Phosphorylation of s831 site by CaMKII	0.4 s^{-1}
$k_{on}^{pCaMKII831}$	pCaMKII binding to GluA1	0.0278 $\mu M^{-1}s^{-1}$
$k_{off}^{pCaMKII831}$	pCaMKII dissociation to GluA1	2 s^{-1}
$K_D^{pCaMKII831}$	Equilibrium binding of pCaMKII to GluA1	71.94 μM
$k_p^{pCaMKII831}$	Phosphorylation of s831 site by pCaMKII	0.5 s^{-1}
$k_{on}^{PP1CaMKII}$	Association of PP1 to pCaMKII	0.0006 $\mu M^{-1}s^{-1}$
$k_{off}^{PP1CaMKII}$	Dissociation of PP1 to pCaMKII	0.34 s^{-1}
$k_p^{PP1CaMKII}$	De-phosphorylation by PP1 of pCaMKII	0.086 s^{-1}
k_{on}^{I1PKAc}	Association of Inh-1 to PKAc	1.4 $\mu M^{-1}s^{-1}$
k_{off}^{I1PKAc}	Dissociation of Inh-1 from PKAc	5.6 s^{-1}
k_p^{I1PKAc}	Phosphorylation of Inh-1 by PKAc	1.4 s^{-1}
k_{on}^{pI1PP1}	Association of PP1 to pInh-1	1 $\mu M^{-1}s^{-1}$
k_{off}^{pI1PP1}	Dissociation of PP1 from pInh-1	0.0011 s^{-1}
k_{on}^{pI1CaN}	Association of pInh-1 with CaN	2.33 $\mu M^{-1}s^{-1}$
k_{off}^{pI1CaN}	Dissociation of pInh-1 from CaN	11.2 s^{-1}
$k_p^{pI1CaNCaM2C}$	De-phosphorylation of pInh-1 by CaN-CaM2C	0.2048 s^{-1}
$k_p^{pI1CaNCaM2N}$	De-phosphorylation of pInh-1 by CaN-CaM2N	0.384 s^{-1}
$k_p^{pI1CaNCaM4}$	De-phosphorylation of pInh-1 by CaN-CaM4	2.8 s^{-1}
$k_{on}^{p845PP1}$	Association of PP1 with phosphor-S845	0.218 $\mu M^{-1}s^{-1}$
$k_{off}^{p845PP1}$	Dissociation of PP1 from phosphor-S845	0.17 s^{-1}
$k_p^{p845PP1}$	De-phosphorylation by PP1 at phosphor-S845	0.0425 s^{-1}
$k_{on}^{p831PP1}$	Association of PP1 with phosphor-S831	0.219 $\mu M^{-1}s^{-1}$
$k_{off}^{p831PP1}$	Dissociation of PP1 from phosphor-S831	0.35 s^{-1}
$k_p^{p831PP1}$	De-phosphorylation by PP1 at phosphor-S831	0.0875
$k_{on}^{p845CaN}$	Association of CaN with phospho-S845	2.01 $\mu M^{-1}s^{-1}$
$k_{off}^{p845CaN}$	Dissociation of CaN from phospho-S845	8 s^{-1}
$k_p^{p831CaNCaM2C}$	De-phosphorylation of pS845 by CaN-CaM2C	0.274 s^{-1}

Table 7.5 Continued.

$k_p^{p831CaNCaM2N}$	De-phosphorylation of pS845 by CaN-CaM2N	0.146 s^{-1}
$k_p^{p831CaNCaM4}$	De-phosphorylation of pS845 by CaN-CaM4	2 s^{-1}
$[Ca^{2+}]_{t=0}$	Initial concentration of Ca^{2+}	0.005 μM
$[CaM]_{t=0}$	Initial concentration of CaM	33 μM
$[AC1]_{t=0}$	Initial concentration of AC1	42 μM
$[AC8nt]_{t=0}$	Initial concentration of AC8nt	42 μM
$[AC8ct]_{t=0}$	Initial concentration of AC8ct	42 μM
$[CaN]_{t=0}$	Initial concentration of CaN	0.5 μM
$[CaMKII]_{t=0}$	Initial concentration of CaMKII	74 μM
$[MLCK]_{t=0}$	Initial concentration of MLCK	5 μM
$[Ng]_{t=0}$	Initial concentration of Ng	52 μM
$[NOS]_{t=0}$	Initial concentration of NOS	1 μM
$[PDE1]_{t=0}$	Initial concentration of PDE1	2.25 μM
$[PDE4]_{t=0}$	Initial concentration of PDE4	3 μM
$[PP1]_{t=0}$	Initial concentration of ATP	1.47 μM
$[Inh\text{-}1]_{t=0}$	Initial concentration of AMP	1.422 μM
$[PKA]_{t=0}$	Initial concentration of PKA	2.2 μM
$[PKA\ Inhib]_{t=0}$	Initial concentration of PKA Inhibitor	0.259 μM
$[GluA1]_{t=0}$	Initial concentration of GluA1	11.6 μM

References for each parameter value can be found in [165].

SUPPLEMENT TO CHAPTER 4

Calculation of Diffusion Coefficients

Diffusion coefficients are identified from previous literature when available. However, most if not all protein complexes described in this model are un-measured. Therefore, the diffusion coefficients can be estimated from the Stokes-Einstein relation provided below.

$$D = \frac{\mu k_B T}{6\pi\eta r}$$

In the Stokes-Einstein relation, D is the diffusion coefficient and k_B is Boltzmann's constant [233, 321]. For a given protein complex, I assume constant T (human body temperature) and the dynamic viscosity η. The hydrodynamic radius r is assumed to be proportional to molecular weight. Noting that CaM has a molecular weight of approximately 18 kDa and a diffusion coefficient of 6×10^{-6} μm^2/sec, I can calculate the hydrodynamic radius of CaM [327]. Referring to the hydrodynamic radius of CaM, I estimate hydrodynamic radii (and in turn, diffusion coefficients) for other proteins given their molecular weights.

Table 7.6. Sources for diffusion coefficients.

Molecules	MW (kDa)	Diffusion (cm2/s)	Source
ATP	0.5512	2.58527E-07	https://www.neb.com/products/p0756-adenosine-5-triphosphate-atp#Product%20Information
AMP	0.347	4.10663E-07	https://pubchem.ncbi.nlm.nih.gov/compound/5_-adenylic_acid
cAMP	0.329	4.33131E-07	https://pubchem.ncbi.nlm.nih.gov/compound/cAMP
PKAc	38	3.75E-09	https://www.neb.com/products/p6000-camp-dependent-protein-kinase-pka-catalytic-subunit#Product%20Information
PKAr	48	2.96875E-09	calculated
PKA2r	96	1.48438E-09	https://www.sigmaaldrich.com/technical-documents/articles/biology/rbi-handbook/protein-serine-threonine-tyrosine-kinases/pka-and-pkg.html
PKA	134	1.06343E-09	calculated

Table 7.6 Continued.

PDE1	42.006	3.39237E-09	https://www.yeastgenome.org/locus/S000003217
PDE1-CaM	58.796	2.42363E-09	calculated
PDE4	68	2.09559E-09	https://datasheets.scbt.com/sc-25814.pdf
PDE4-PKAc	106	1.34434E-09	calculated
PP1	37.5	3.8E-09	https://www.neb.com/-/media/catalog/datacards-or-manuals/p0754datasheet-lot0111204.pdf
PP1-CaMKII	607.5	2.34568E-10	calculated
I1	19	7.5E-09	http://www.pnas.org/content/pnas/97/11/5824.full.pdf
I1-PP1	56.5	2.52212E-09	calculated
I1-PKAc	57	2.5E-09	calculated
I1-CaMCaN	113.633	1.25404E-09	calculated
Membrane Bound			
AMPAR-CaN	746.83	3.98625E-10	calculated
AMPAR-CaMCaN	763.63	3.89855E-10	calculated
AMPAR-CaMKII	1239	2.40278E-10	calculated
AMPAR-KCaM	1255.79	2.37066E-10	calculated
AMPAR-PKA4	803	3.70741E-10	calculated
AMPAR-PKAc	707	4.21082E-10	calculated
AMPAR-PP1	706.5	4.2138E-10	calculated

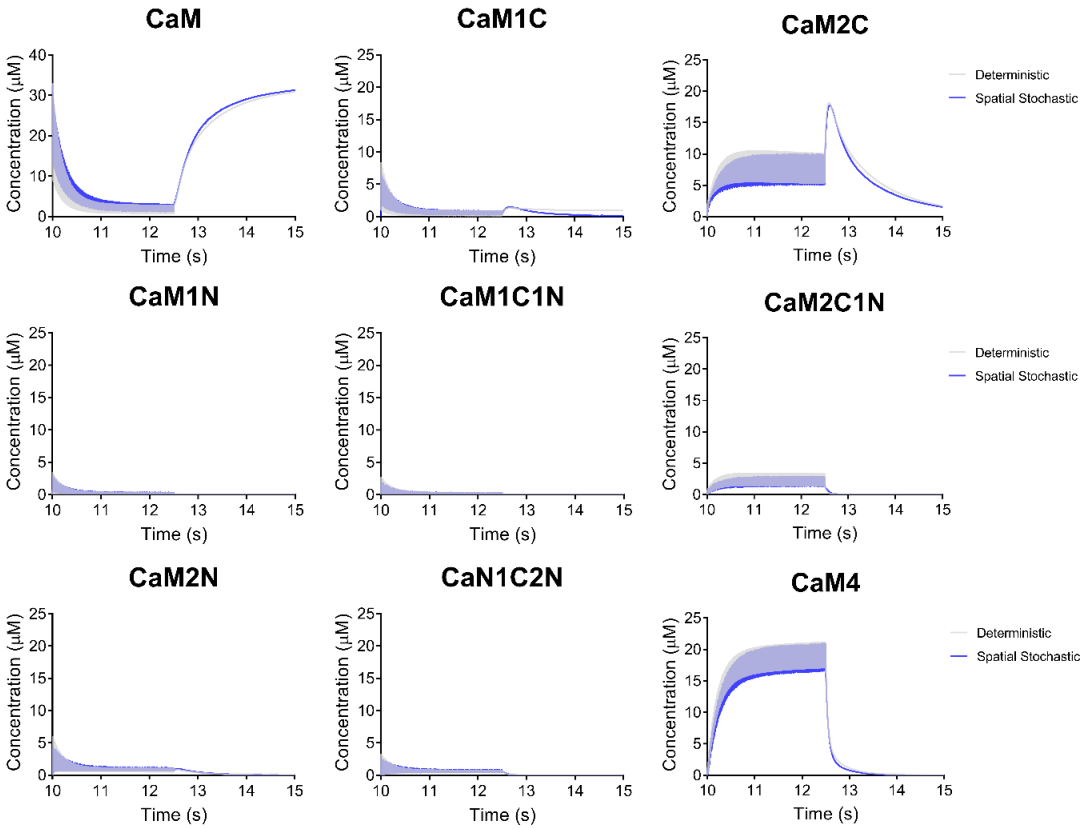

Figure 7.5. Ca^{2+}/CaM states in deterministic vs. spatial-stochastic frameworks at 100Hz Ca^{2+}. Ca^{2+}/CaM activation for 100 Hz Ca^{2+} flux (from t = 10 sec until t = 12.5 sec) in deterministic (grey) and spatial-stochastic (blue) frameworks. Spatial-stochastic traces are the averaged output representative of N=50 executions. Compare to Figure 4.2.

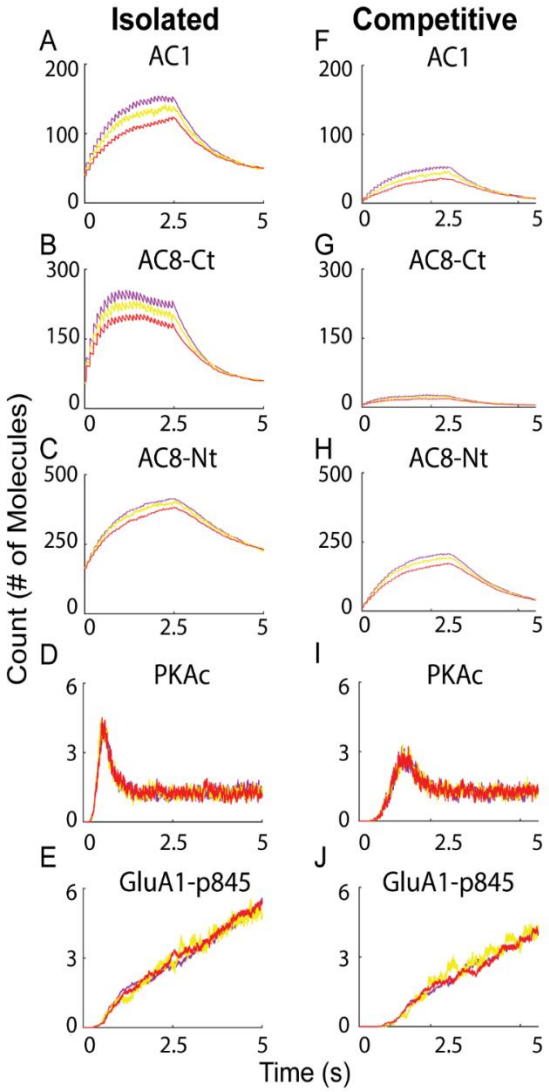

Figure 7.6. AC-associated state gradients in isolated and competitive environments at 10Hz Ca^{2+}. Compare to **Figure 4.6** and **Figure 4.7**. Spatial-stochastic model response to 10Hz Ca^{2+} flux from time t = 0 until t = 2.5 sec. For each protein state, I monitor the number of proteins in the spine head's top (purple), middle (yellow), and bottom (red) compartments. The left-hand columns are the isolated model, and the right-hand columns are the competitive model. All traces are the average of N=50 executions.

Table 7.7 Statistical analysis of AC- and CaMKII-associated spatial gradient formation.

		Isolated				Competitive			
Frequency:		10 Hz		100 Hz		10 Hz		100 Hz	
Protein	Compartment	F-Value	Tukey Groupings	F-Value	Tukey Groupings	F-Value	Tukey Groupings	F-Value	Tukey Groupings
	Top		A		A		A		A
	Middle		B		B		B		B
AC1	Bottom	68.71	C	494.22	C	75.53	C	128.09	C
	Top		A		A		A		A
	Middle		B		B		B		B
AC8ct	Bottom	132.87	C	131.43	C	22.02	C	66.61	C
	Top		A		A		A		A
	Middle		B		A		B		A
AC8nt	Bottom	31.72	C	8.11	B	83.6	C	22.27	B
	Top		A		A		A		A
	Middle		B		B		B		B
CaMKII	Bottom	343.08	C	255.79	C	281.85	C	950.37	C
	Top		A		A		A		A
	Middle		A		B		A		B
CaM	Bottom	4.33	B	11.33	B	9.53	B	94.41	C
	Top		A		A		A		A
	Middle		A		B		B		B
CaM2C	Bottom	10.86	B	367.67	C	280.25	C	8.57	B
	Top		A		A		A		A
	Middle		A		B		A		A
CaM2N	Bottom	7.26	B	16.14	C	7.35	B	19.96	B
	Top		A		A		A		A
	Middle		B		B		B		B
CaM4	Bottom	922.32	C	2456.22	C	244.62	C	2497.58	C
	Top		A		A		A		A
	Middle		A		B		B		B
Ca2+	Bottom	3.91	B	2346.72	C	848.93	C	2971.53	C
	Top						A		A
	Middle						A		B
Ng	Bottom					3.1	A	61.75	C
	Top		A		A		A		A
	Middle		A		A		A		A
PKAc	Bottom	0.44	A	0.56	A	2.49	A	0.02	A
	Top		A		A		A		A
	Middle		B		B		A		B
pKCaM	Bottom	51.97	C	285.31	C	26.76	B	298.54	C
	Top		A		A		A		A
	Middle		A		B		A		B
p831	Bottom	5.11	B	11.69	B	12.28	B	44.44	C
	Top		A		A		A		A
	Middle		A		A		B		A
p845	Bottom	0.57	A	0.17	A	4.06	B	0.56	A

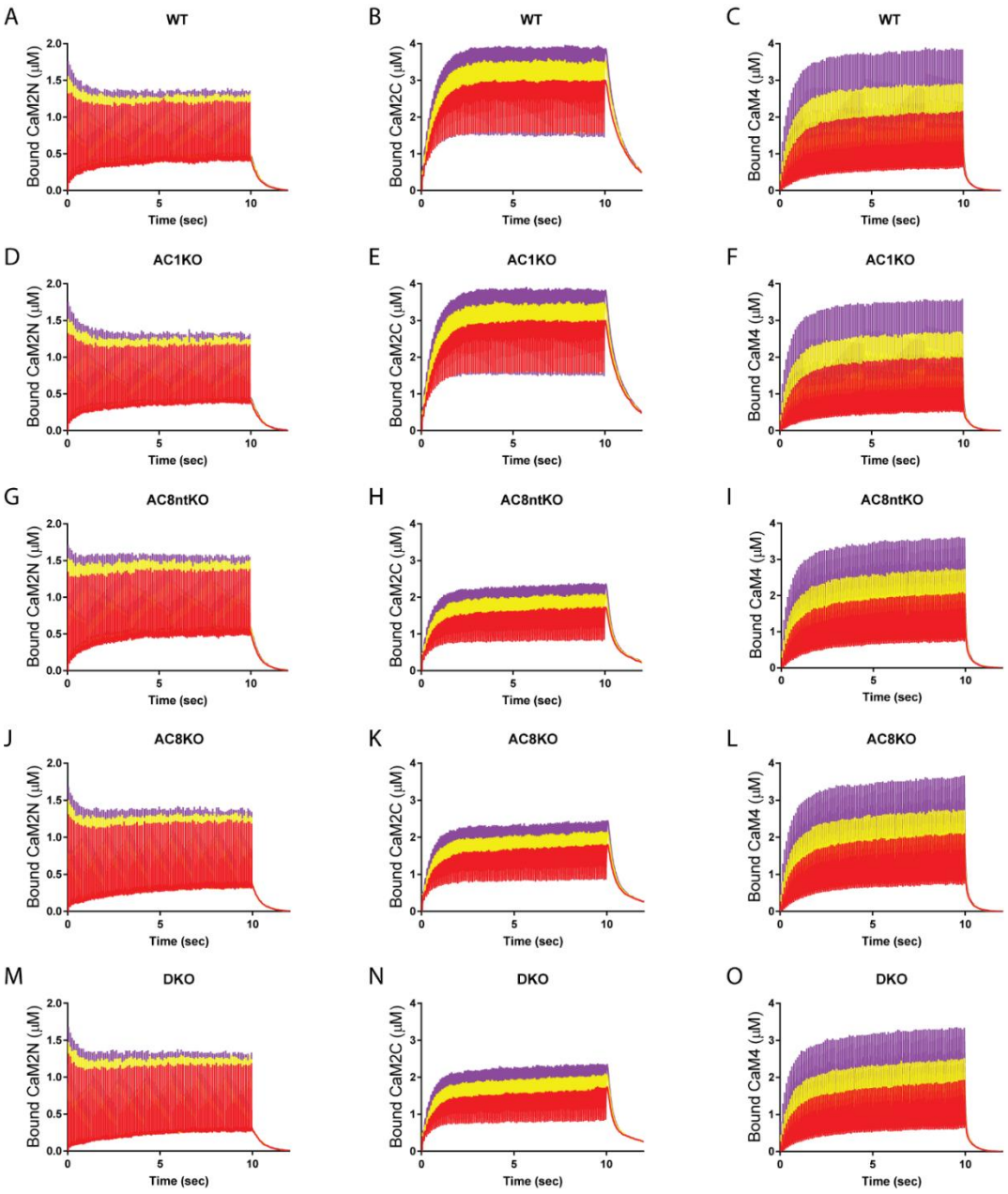

Figure 7.7. CBP-bound Ca^{2+}/CaM states for various AC-knockouts at 10Hz Ca^{2+} flux. CBP-bound Ca^{2+}/CaM states in top (purple), middle (yellow), and bottom (red) compartments of the spine in response to 10Hz Ca^{2+} flux (which terminates at t=10 sec). Ca^{2+}/CaM states are CaM2N (left column), CaM2C (middle column), and fully-saturated CaM4 (right column). Each row is a distinct AC-knockout. All traces are the average of N=50 executions.

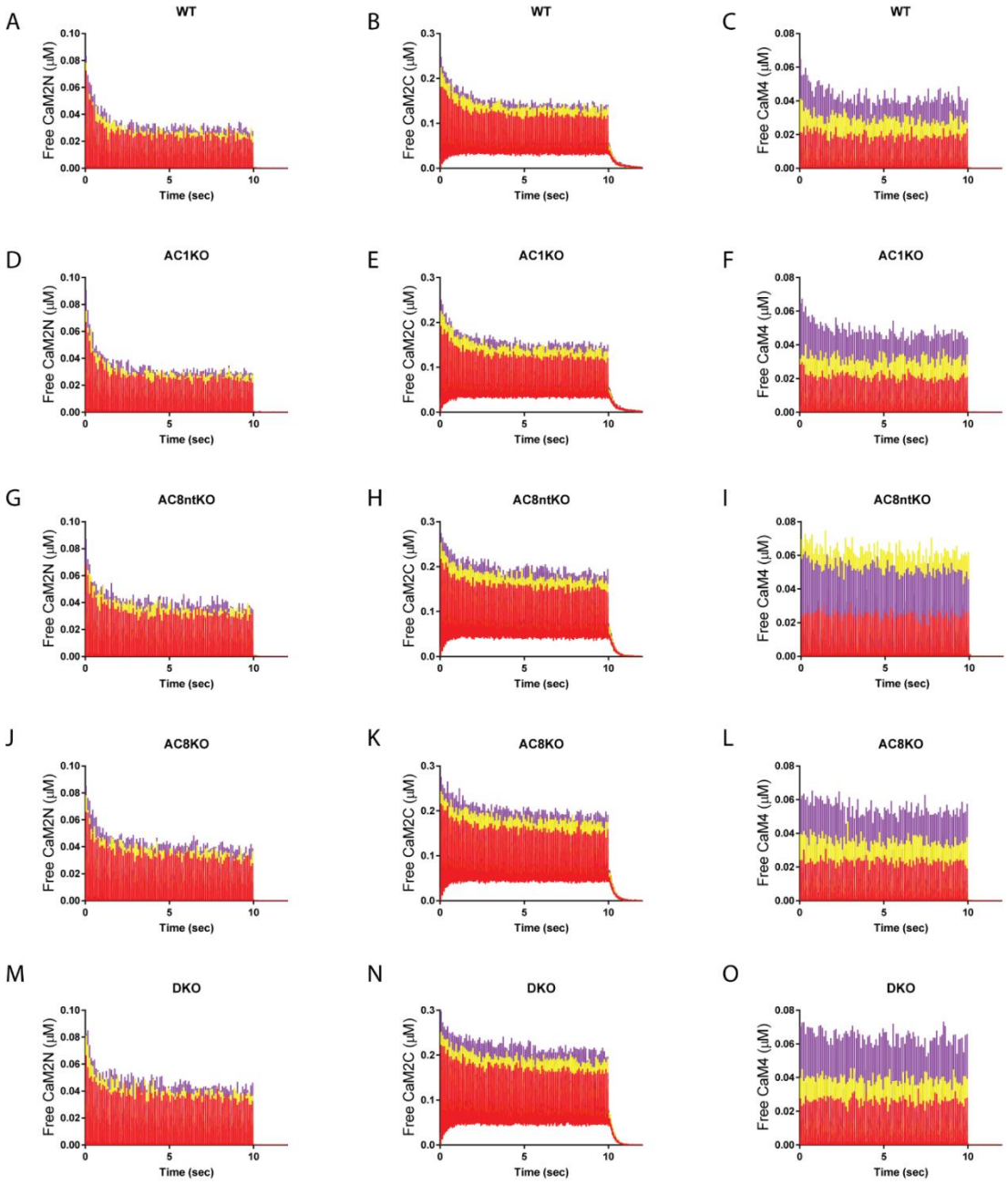

Figure 7.8. Free Ca^{2+}/CaM states for various AC-knockouts at 10Hz Ca^{2+} flux. Free/unbound Ca^{2+}/CaM states in top (purple), middle (yellow), and bottom (red) compartments of the spine in response to 100Hz Ca^{2+} flux (which terminates at t=2.5 sec). Ca^{2+}/CaM states are CaM2N (left column), CaM2C (middle column), and fully-saturated CaM4 (right column). Each row is a distinct AC-knockout. All traces are the average of N=50 executions.

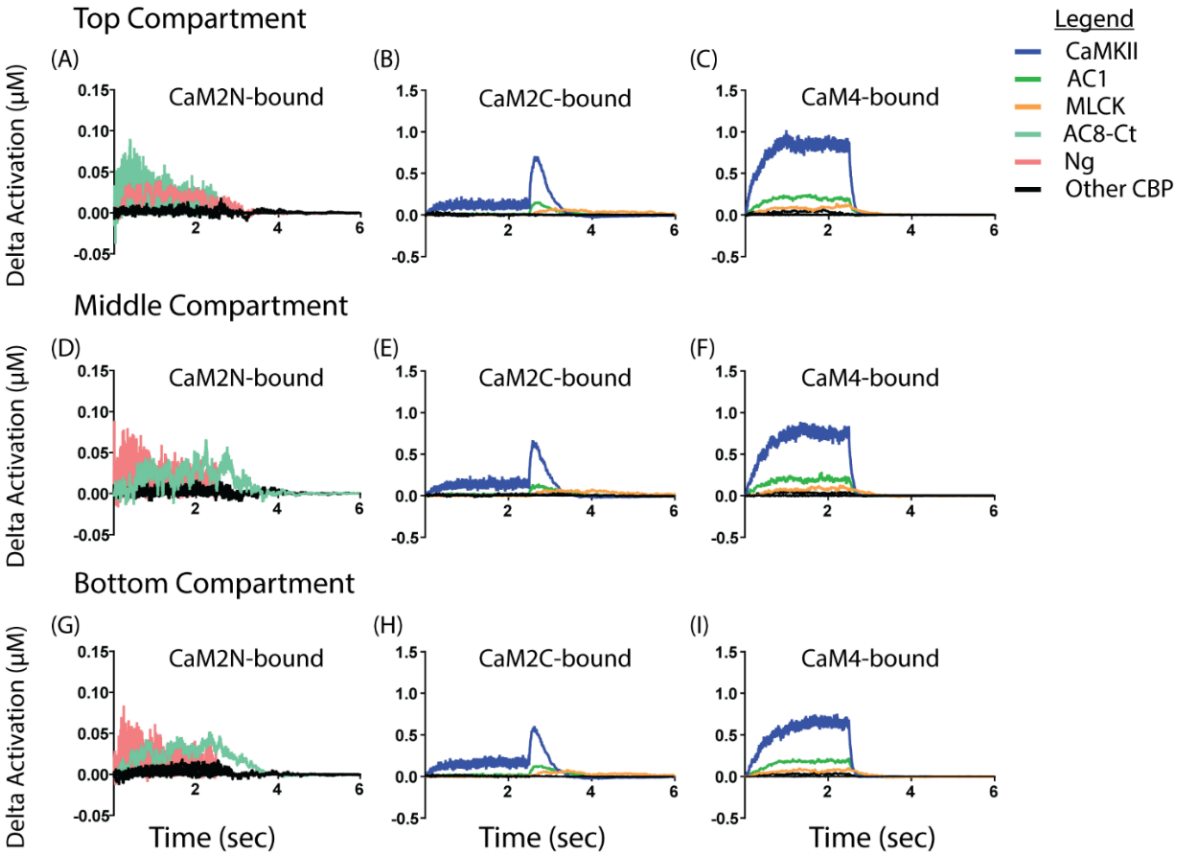

Figure 7.9. Differences in individual CBP activation by Ca^{2+}/CaM states upon AC8-Nt-KO. The change in activation of each CBP upon AC8-Nt-KO (Delta activation(t) = KO(t) – WT(t)) as a function of time in response to 100Hz Ca^{2+} flux. CBPs that change by at least 20% are colored non-black as identified in the legend. Changes are monitored for CBPs activated by CaM2N (left column), CaM2C (middle column), and CaM4 (right column), in the top (A-C), middle (D-F), and bottom (G-I) compartments of the spine. Note differences in scale for CaM2N-activated CBPs. All traces are the average of N=50 executions.

SUPPLEMENT TO CHAPTER 5

Table 7.8. CaMKII model state transitions, grouped by flag, with rates and conditions provided.

Flag	State Transition	Rate	Condition (Rule)	References
1) Docking	Docked → Undocked	0.63 s^{-1}	Subunit Flag 1 == Docked	[218, 281, 282], this paper
	Undocked → Docked	35 s^{-1}	Subunit Flag 3 == Unbound Subunit Flag 5 == uThr-306	[218, 281, 282], this paper
2) Activation	Inactive → Active	2×10^{4} s^{-1}	*None*	[269]
	Active → Inactive	1×10^{7} s^{-1}	Subunit Flag 4 == uThr-286	[116, 265], this paper
Select executions:	Active + K252a → Blocked	1×10^{9} s^{-1}	*None*	Large value
3) Ca^{2+}/CaM Binding	Unbound + CaM_4 → Initially-Bound	1×10^{8} $M^{-1}s^{-1}$	Subunit Flag 1 == Undocked Subunit Flag 4 != PP1-bound Subunit Flag 5 == uThr-306	[269, 281]
	Initially-Bound → Fully-Bound	350 s^{-1}	Subunit Flag 2 == Active	[281]
	Fully-Bound → Initially-Bound	4×10^{-3} s^{-1}	*None*	[281]
	Initially-Bound → Unbound + CaM_4	590 s^{-1}	*None*	[281, 283], this paper
4) Phosphorylation (Thr-286)	uThr-286 → pThr-286	1 s^{-1}	Subunit Flag 1 == Undocked Neighbor Flag 1 == Undocked Subunit Flag 2 == Active Neighbor Flag 2 == Active	[97]
	pThr-286 + PP1→ PP1-bound	3×10^{6} $M^{-1}s^{-1}$	Subunit Flag 3 == Unbound	[216]
	PP1-bound → uThr-286 + PP1	2 s^{-1}	*None*	[216]
	PP1-bound → pThr-286 + PP1	0.5 s^{-1}	*None*	[216]
5) Phosphorylation (Thr-306)	uThr-306 → pThr-306	0.02 s^{-1}	Subunit Flag 1 == Undocked Subunit Flag 2 == Active Subunit Flag 3 == Unbound	[271, 293], this paper

Note: Double equal signs (==) denote the conditional "true" and the exclamation-equal sign (!=) denotes the conditional "false" statement.

Necklace Number Quantification of CaMKII Combinatorial Explosion

In the absence of rules defining the conditions for subunit state transition, CaMKII subunit states are independent, causing combinatorial explosion. To quantify the combinatorial explosion, consider each of the five flags denoting CaMKII subunit states in my model. The docking flag can have one of **two** states. The activation flag can have one of **two** states. The CaM-binding flag can have one of **three** states. The Thr-286 flag can have one of **three** states. Finally, the Thr-306 flag can have one of **two** states. If each flag state is independent, there is a total of **72** possible state combinations that a single subunit can exhibit.

Next, I consider a single ring of six subunits, noting the rotational symmetry. Leveraging this symmetry, I refer to so-called "necklace numbers". Using necklace numbers, the number of fixed arrangements of beads on the necklace is defined as:

$$N(n,a) = \frac{1}{n}\sum_{i=1}^{v(n)} \phi(d_i)\, a^{n/d_i}$$

Where n is the length of the necklace and a is the number of bead types. Phi is Euler's totient function, and d are divisors of n. Thus, for a single CaMKII ring in which n=6 and a=72, the possible number of state combinations is: 23219075544.

To count possible states for a single holoenzyme, I again use necklace numbers. (Squaring the number calculated for a single CaMKII ring fails to account for rare cases in which both rings exhibit identical states.) Thus, I calculate the number of states for the necklace with n=2 and a=23219075544. With this calculation, I determine that in the absence of rules, a twelve-subunit CaMKII holoenzyme as modeled in this paper has **269562734570598985740** possible states.

I emphasize that this value is my estimation. I also acknowledge David Sterratt for his suggestion to use necklace numbers in this calculation.

Exploration of Multiple Degrees of Freedom for Autophosphorylation

To explore the dependence of CaMKII pThr-286 patterns on varying mechanisms of autophosphorylation, I present alternative versions of my model in which autophosphorylation may occur in multiple directions, intra- and/or trans-ring. In these higher-degrees of freedom (DoF) models, autophosphorylation may occur in two directions (2 DoF) or three directions (3 DoF).

	1 DoF	2 DoF A	2 DoF B	3 DoF
Intra-ring (Left)	X	X	X	X
Intra-ring (Right)		X		X
Trans-ring (Across)			X	X

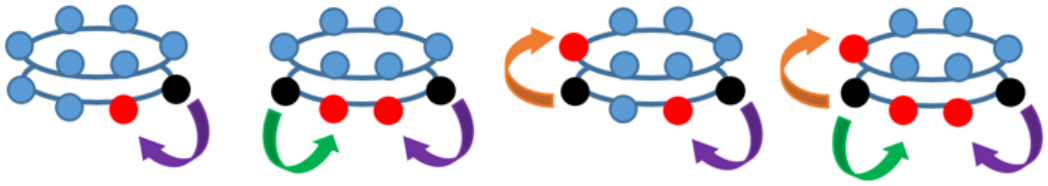

Figure 7.10. Schematic of higher-DoF autophosphorylation of CaMKII subunits (blue). Black circles are the enzymes and red circles are the substrate subunits participating in an autophosphorylation.

I hypothesized that higher DoF's could elicit higher or more robust levels of CaMKII autophosphorylation in the presence of phosphatase. Therefore, in Figure 7.11 below, I monitor pThr-286 in each of the DoF models as a function of time. Each model is subjected to saturating levels of Ca^{2+}/CaM for 20 sec, after which the stimulating Ca^{2+}/CaM is removed. The results in Figure S2.2 indicate that a higher DoF may allow for more rapid formation of pThr-286. For example, the slope of the 3-DoF trace (pink) at t=10sec is noticeably greater than that for the 1-DoF trace (dark blue). Also, following stimulation (after t=20sec) de-phosphorylation rate seems to be independent of DoF. I note that for the models as-simulated and as-parameterized in Figure 7.11, the differences in output between each DoF model may not be experimentally distinguishable.

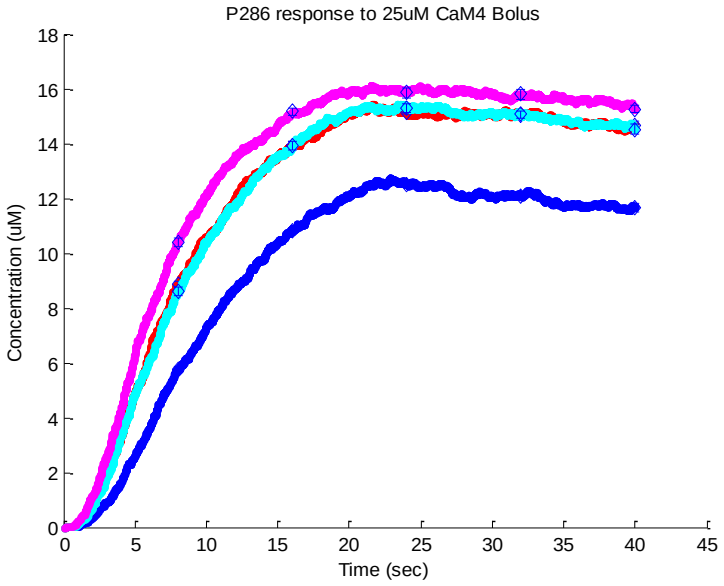

Figure 7.11. Comparing pThr-286 formation for various model DoF for autophosphorylation. For all simulations, holoenzymes were stimulated in the presence of phosphatase with a saturating level of Ca^{2+}/CaM for 20sec, after which Ca^{2+}/CaM was removed. Model output is shown for 1 DoF (blue), 2 DoF (red and cyan), and 3 DoF (violet). Each trace is the average of N=50 executions.

It is also interesting to consider how a higher DoF could accelerate and/or provide redundant paths by which information (e.g. autophosphorylations) flows from one end of a holoenzyme to the opposite. Indeed, intra-holoenzyme information transfer could impact how CaMKII operates as a simultaneous signaling and structural protein, such as when one subunit interacts with Ca^{2+}/CaM while a neighboring subunit binds to actin [280].

To explore the impact of higher DoF autophosphorylation on intra-holoenzyme information transfer, I use the MCell rule-based modeling syntax to monitor individual subunits on an individual holoenzyme. Monitoring individual subunits allows me to identify CaMKII autophosphorylation “chains”, defined as a series of consecutive autophosphorylated subunit neighbors. In Figure 7.12, I monitor individual CaMKII subunit autophosphorylations over time, in the continuous presence of saturating Ca^{2+}/CaM and phosphatase, for various DoFs. In Figure 7.13, I quantify the dependence of autophosphorylation chain formation on DoF number.

Increasing DoF increases the lifetime of autophosphorylation chains (of any length), albeit marginally leading me to suspect experimental measurements would be inconclusive.

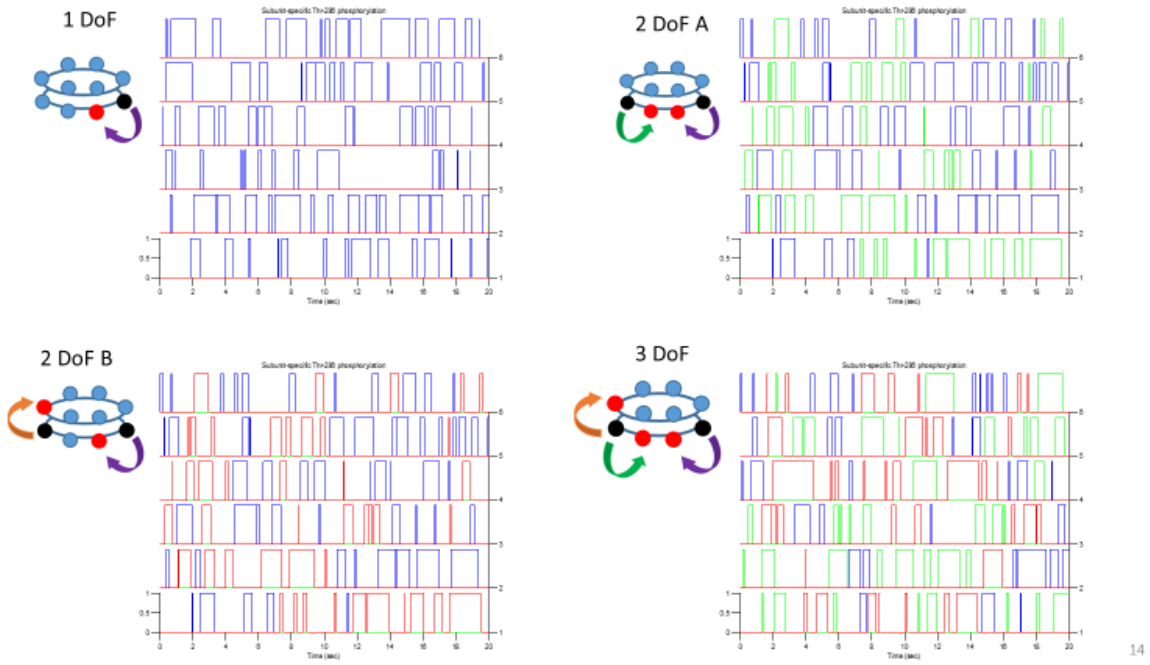

Figure 7.12. Monitoring individual CaMKII subunits at distinct autophosphorylation DoF. In each panel, the horizonal axis is time (up to 20 sec). Each row pertains to one of six subunits in a single holoenzyme ring, and each trace is a binary representation of whether that subunit is pThr-286 (one) or uThr-286 (zero). Depending on the number of DoF, autophosphorylations may proceed clockwise (blue), counter-clockwise (green), and/or trans-ring (red).

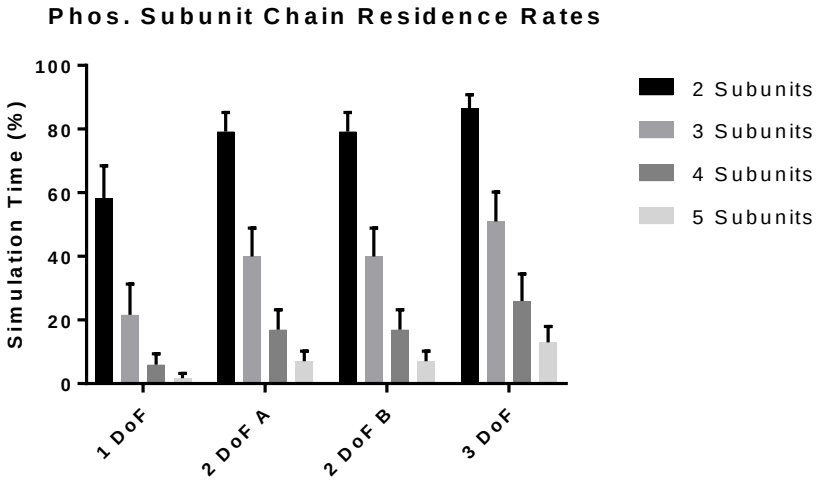

Figure 7.13. pThr-286 chain occurrence increases with increasing DoF. Here, I monitored a single CaMKII holoenzyme over 2min. Each bar denotes the fraction of time that a chain of length n occurs for that number of DoF. Each bar is the average of N=50 executions.

S1 Movie.

Please see this link - https://youtu.be/lUSuv2mWa5g.

Discussion of putative PP1-CaMKII binding site.

Many PP1-binding proteins contain a variable binding motif commonly called the RVxF binding motif [317]. However, no such motif is seen in the alpha-CaMKII subunit amino acid sequence. Furthermore, no structure for the PP1-CaMKII interaction exists, in part because apo-PP1 is unstable in solution [291]. I can instead refer to a crystal structure published by Ragusa *et al*., which shows PP1 binding the neuronal regulatory protein spinophilin (PDB 3EGG) [290].

The 3EGG crystal structure shows an interaction with PP1 spanning the spinophilin residues 417-494. This interaction involves 77 residues (~100 Å, see Figure 7.14), which are necessary and sufficient for PP1 to dephosphorylate spinophilin [292]. This interaction distance is longer than the CaMKII regulatory domain and CaM-binding footprint. Indeed, the CaMKII regulatory domain is only about 39 Å (as in PDB 3SOA, partially shown in Figure 7.15).

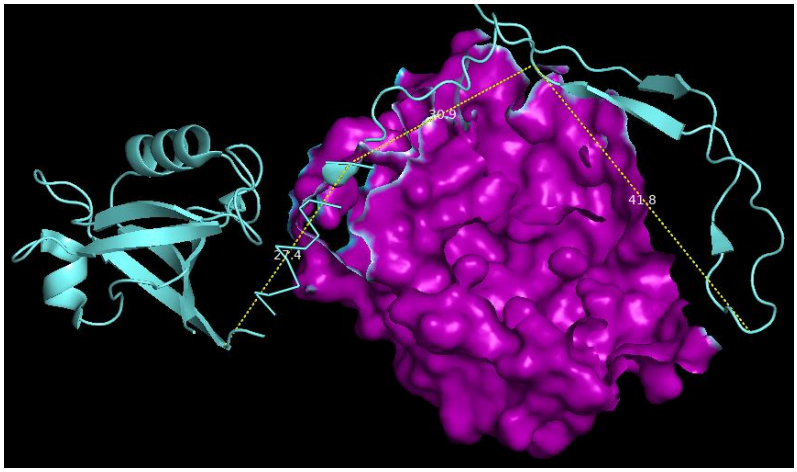

Figure 7.14. Visualization of the spinophilin and PP1 binding interaction (PDB: 3EGG). Some of the PP1 (purple) surface is digitally removed to help visualize the dotted lines, which together approximate the distance spanned by spinophilin (cyan) residues 417-494.

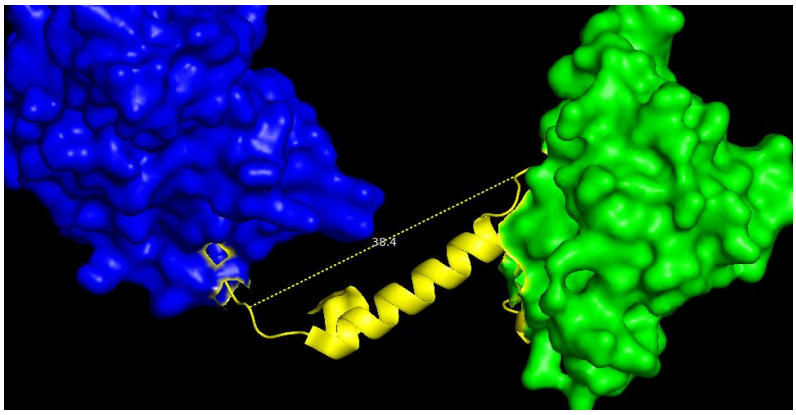

Figure 7.15. Visualization of the CaMKII regulatory domain (yellow) (PDB: 3SOA). The CaMKII hub domain (green) and kinase domain (blue) are also shown. Dotted line measures from residues 280-306.

Note also that the typical PP1 binding motif interacts with PP1 at a site roughly 20 Å from the PP1 active site [292]. Thus, if the PP1 binding footprint does not contain T286, then the furthest CaMKII residue the PP1 footprint could likely be (on the hub domain side of T286) is residue 301, well within the CaM-binding footprint (see Figure 7.16). Admittedly, the furthest likely PP1-binding residue on the kinase domain side of T286 is difficult to ascertain from PDB 3SOA. Still, I believe there is strong evidence that CaM structurally excludes or limits PP1 from binding and/or catalyzing de-phosphorylation at T286.

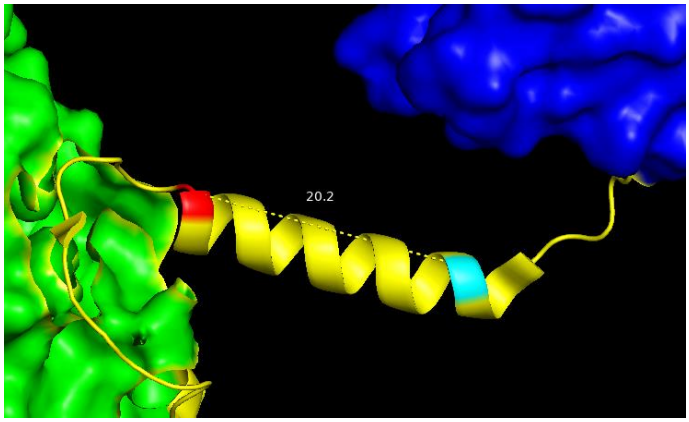

Figure 7.16. Visualization of the furthest likely residue (G301; red) of PP1-binding on the hub domain (green) side of T286 (cyan) (PDB: 3SOA). Dotted line measures from residues 286-301.

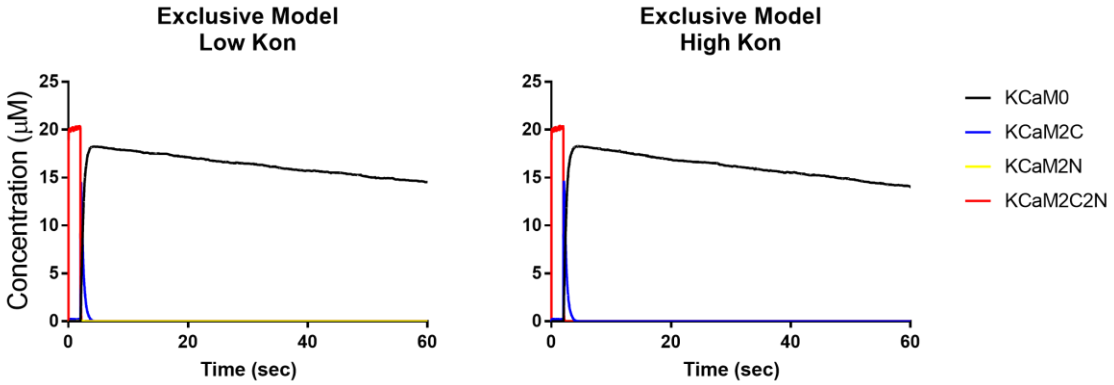

Figure 7.17. Major Ca^{2+}/CaM-CaMKII states following Ca^{2+} bolus in the 9-state-1-step model. Bound Ca^{2+}/CaM states in response to 2 sec Ca^{2+} bolus as-implemented in Fig 7. I monitor the CaMKII-bound Ca^{2+}/CaM states apo-CaM (black), CaM_{2C} (blue), CaM_{2N} (yellow), and CaM_4 (or CaM_{2C2N}, red) in the PP1-exclusive 9-state-1-step model under low (left) and high (right) association rate parameters for PP1-CaMKII binding. Each trace is the average of N=20 executions.

SUPPLEMENT TO CHAPTER 6

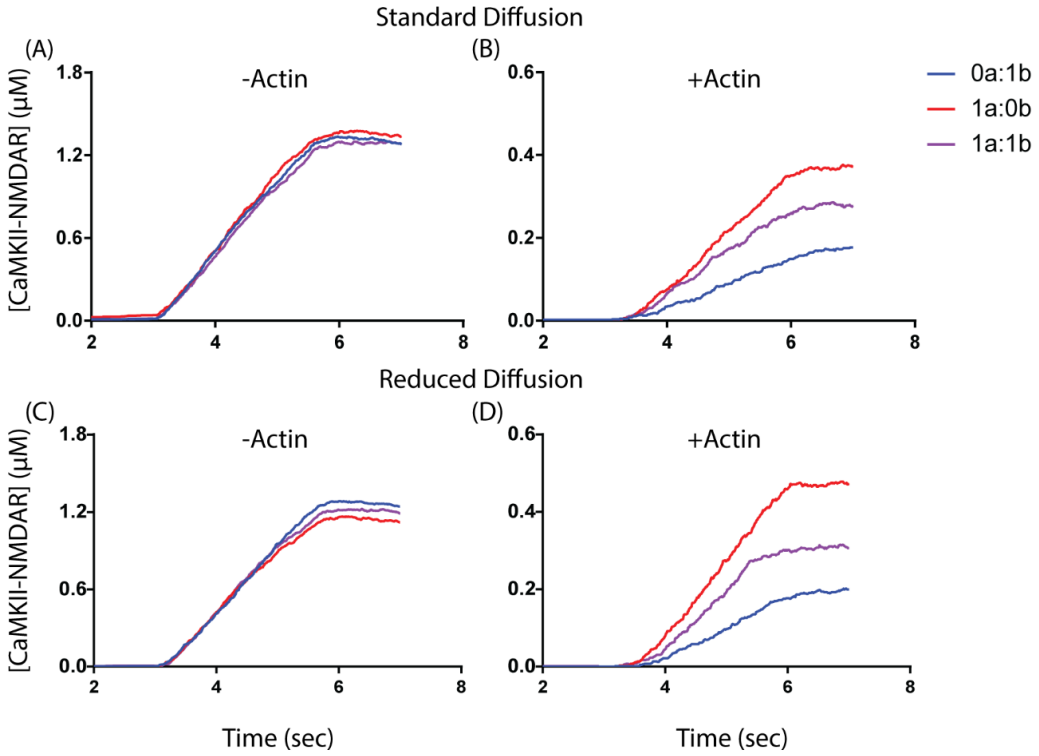

Figure 7.18. CaMKII-NMDARs in the spatial-stochastic monovalent CaMKII model at 10Hz Ca^{2+} flux. CaMKII-bound NMDARs for CaMKII isoform ratios 1:1 (purple), 1:0 (red), and 0:1 (blue) in response to 10Hz Ca^{2+} flux with the standard spine geometry, in the absence (-Actin) or presence (+Actin) of actin binding sites. Model executions using standard diffusion parameters (A & B) are shown, along with executions using diffusion parameters reduced by 1 order of magnitude (C & D). Ca^{2+} flux begins at t=3sec and proceeds for 2.5sec. All traces are the average =50 executions.

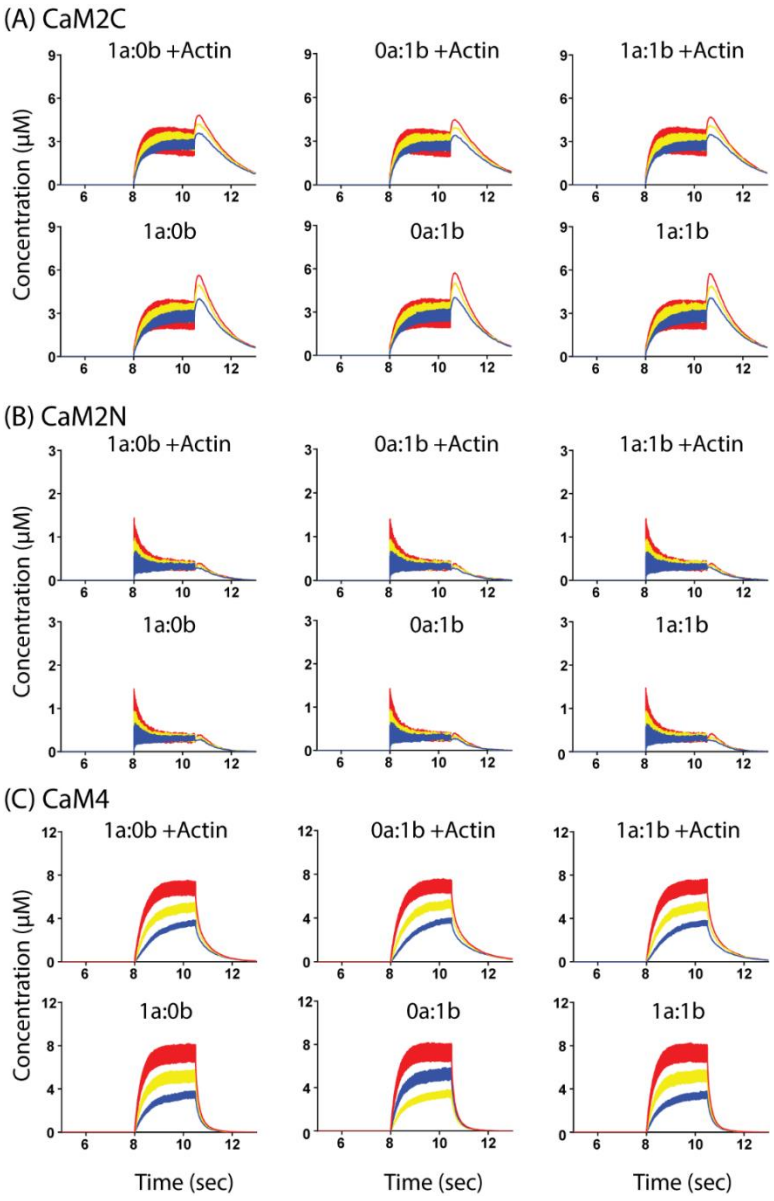

Figure 7.19. Compartmental Ca^{2+}/CaM states in the spatial-stochastic monovalent-CaMKII model. The major Ca^{2+}/CaM states (both bound and unbound) CaM2C (A), CaM2N (B), and CaM4 (C) in the top (red), middle (yellow), and bottom (blue) spine compartments in response to 100Hz Ca^{2+} flux in the standard spine geometry and with standard diffusion coefficients. Ca^{2+} flux begins at t = 8sec and proceeds for 2.5 sec. Each column is a distinct CaMKII alpha:beta subunit ratio. Each row is the model with actin binding sites (+Actin) or without. All traces are the average of N=50 executions.

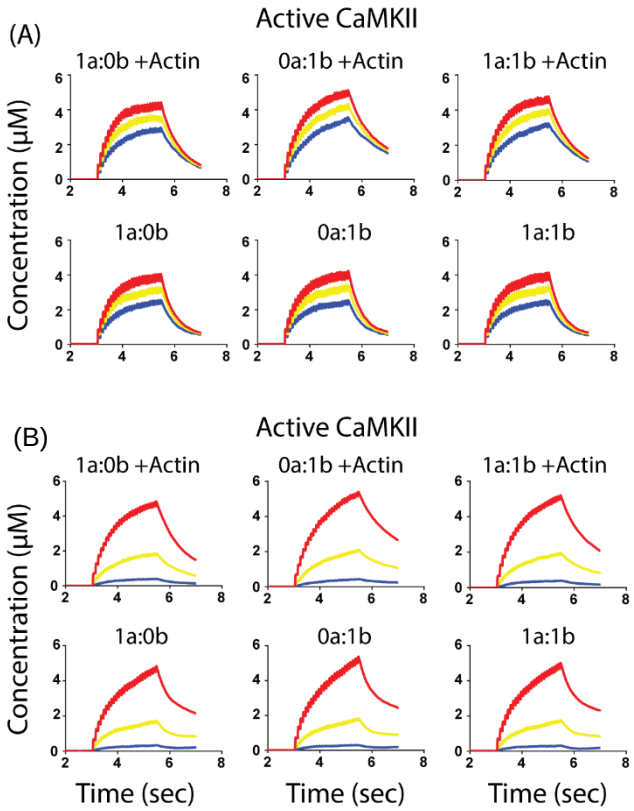

Figure 7.20. Active CaMKII in the spatial-stochastic monomeric model at 10Hz Ca^{2+} flux. Active CaMKII in the top (red), middle (yellow), and bottom (blue) spine compartments in response to 10Hz Ca^{2+} flux with the standard spine geometry, with the presence of actin binding sites (+Actin) or without. Model executions using standard diffusion parameters (A) are shown, along with executions using diffusion parameters reduced by 1 order of magnitude (B). Each column is a distinct CaMKII alpha:beta subunit ratio. Ca^{2+} flux begins at t = 3sec and proceeds for 2.5 sec. All traces are the average =50 executions.

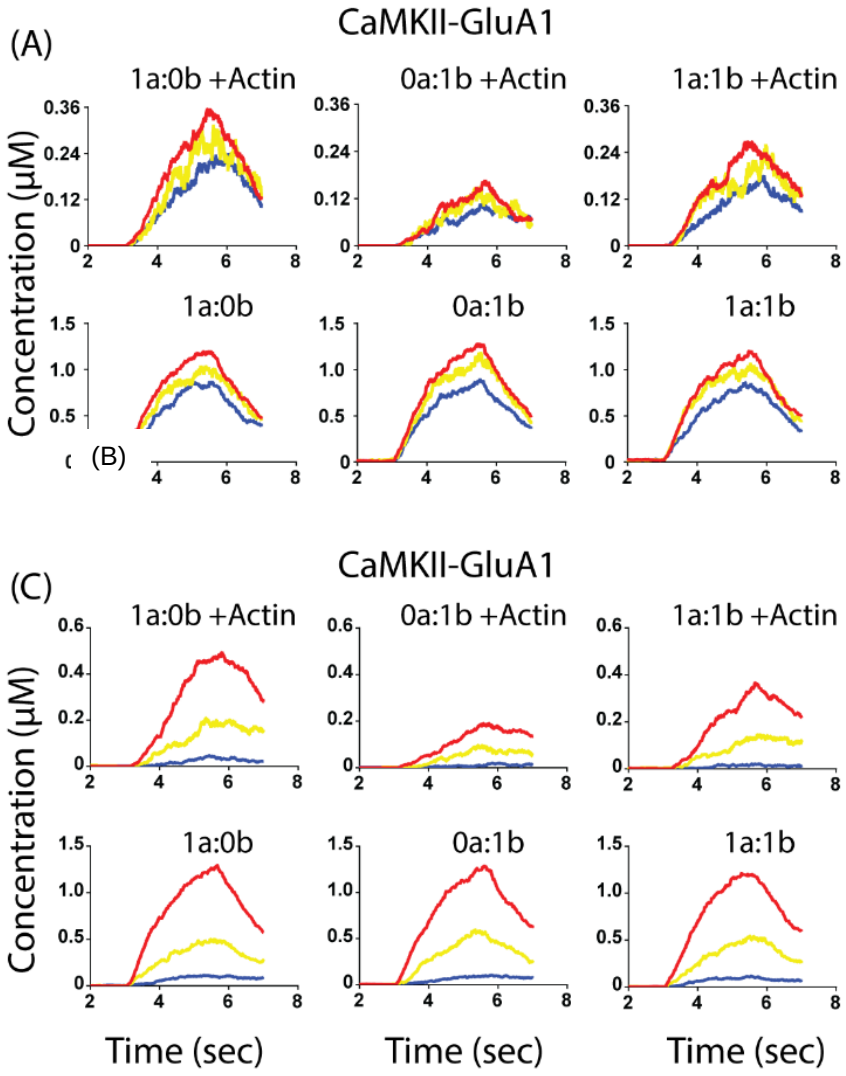

Figure 7.21. Bound GluA1 in the spatial-stochastic monovalent model at 10Hz Ca^{2+} flux. Bound GluA1 in the top (red), middle (yellow), and bottom (blue) spine compartments in response to 10Hz Ca^{2+} flux with the standard spine geometry, with the presence of actin binding sites (+Actin) or without. Model executions using standard diffusion parameters (A) are shown, along with executions using diffusion parameters reduced by 1 order of magnitude (B). Each column is a distinct CaMKII alpha:beta subunit ratio. Ca^{2+} flux begins at t = 3sec and proceeds for 2.5 sec. All traces are the average of N=50 executions.

Table 7.9. Parameters and conditions for models in Chapter 6.

Parameter	Description	Value Used	Reference
Kinetic Parameters			
k_{on}^{actin}	CaMKII association to actin binding site	0.5 $\mu M^{-1}s^{-1}$	[244]
$k_{off}^{alphaActin}$	Alpha-CaMKII dissociation from actin binding site	0.68 s^{-1}	[244]
$k_{off}^{betaActin}$	Beta-CaMKII dissociation from actin binding site	0.23 s^{-1}	[244]
$K_D^{CaMKIIGluN2B}$	Affinity of CaMKII for NMDAR	0.14 μM	[328]
$k_{on}^{CaMKIIGluN2B}$	CaMKII association to NMDAR	0.0278 $\mu M^{-1}s^{-1}$	Assume CaMKII-AMPAR association rate, see Table 7.5
$k_{off}^{CaMKIIGluN2B}$	CaMKII dissociation from NMDAR	0.003892 s^{-1}	$k_{off} = K_D k_{on}$
$k_{cat}^{CaMKIIGluN2B}$	Phosphorylation of NMDAR by CaMKII	0.166 s^{-1}	[329]
Diffusion Coefficients			
D_{actin}	Diffusion of un-bound actin binding sites	8.5 $\mu m^2 s^{-1}$	Assume highly diffuse
Initial Conditions			
$[CaMKII_{alpha}]_{t=0}$	Initial concentration of alpha-CaMKII subunits	37 μM (see footnote)	[42]
$[CaMKII_{beta}]_{t=0}$	Initial concentration of beta-CaMKII subunits	37 μM (see footnote)	[42]
$[Actin]_{t=0}$	Initial concentration of actin binding sites	100 μM	Assume non-limiting
	Localization of all AC isoforms	Plasma membrane	[16, 17]
	Localization of actin binding sites	Cytosol	[36, 258]
	Localization of AMPAR	Plasma membrane	[37, 228, 238]
	Localization of CaM	Cytosol	[14]
	Localization of CaN	Cytosol	[132]
	Localization of CaMKII	Cytosol	[254, 260]
	Localization of MLCK	Cytosol	[188]
	Localization of Ng	Cytosol	[203]
	Localization of NOS	Plasma membrane	[159]
	Localization of NMDAR	Synaptic membrane	[21, 23, 34, 200]
	Localization of PDE1	Cytosol	[21, 198]
	Localization of PP1	Cytosol	[278, 316]

Additional rate parameters not listed are identical to those used in Chapter 4. All model code is available at the Purdue University Research Repository.

REFERENCES

1. Alzheimer's Foundation of America - Alzheimer's Disease Statistics 2016 [cited 2016]. Available from: http://www.alzfdn.org/AboutAlzheimers/statistics.html.
2. Huntington's Disease Genetics. NeuroRx; 2004. p. 255-62.
3. Kennedy MB. Synaptic Signaling in Learning and Memory. Cold Spring Harbor Perspect Biol. 2016;8(2):16. doi: 10.1101/cshperspect.a016824. PubMed PMID: WOS:000371181300004.
4. Zhabotinsky AM, Camp RN, Epstein IR, Lisman JE. Role of the neurogranin concentrated in spines in the induction of long-term potentiation. J Neurosci. 2006;26(28):7337-47.
5. Silva AJ, Stevens CF, Tonegawa S, Wang YY. Deficient hippocampal long-term potentiation in alpha-calcium-calmodulin kinase-II mutant mice. Science. 1992;257(5067):201-6. doi: 10.1126/science.1378648. PubMed PMID: WOS:A1992JC58500026.
6. Baude A, Nusser Z, Molnar E, McIlhinney RAJ, Somogyi P. High-resolution immunogold localization of AMPA type glutamate-receptor subunits at synaptic and nonsynaptic sites in rat hippocampus. Neuroscience. 1995;69(4):1031-55. doi: 10.1016/0306-4522(95)00350-r. PubMed PMID: WOS:A1995TG72600006.
7. Herculano-Houzel S. The human brain in numbers: a linearly scaled-up primate brain. Front Hum Neurosci. 2009;3:11. doi: 10.3389/neuro.09.031.2009. PubMed PMID: WOS:000274619300014.
8. Dosemeci A, Tao-Cheng JH, Vinade L, Winters CA, Pozzo-Miller L, Reese TS. Glutamate-induced transient modification of the postsynaptic density. Proc Natl Acad Sci U S A. 2001;98(18):10428-32. doi: 10.1073/pnas.181336998. PubMed PMID: WOS:000170738000073.
9. Bekkers JM, Stevens CF. Presynaptic mechanism for long-term potentiation in the hippocampus. Nature. 1990;346(6286):724-9. doi: 10.1038/346724a0. PubMed PMID: WOS:A1990DV65200054.
10. Hebb DO. Neurology, 4th edition. Can J Psychol. 1949;3(4):241-2. doi: 10.1037/h0084100. PubMed PMID: WOS:000205056600006.
11. Abraham WC. How long will long-term potentiation last? Philos Trans R Soc B-Biol Sci. 2003;358(1432):735-44. doi: 10.1098/rstb.2002.1222. PubMed PMID: WOS:000182654100019.
12. Kennedy MB. Signal transduction molecules at the glutamatergic postsynaptic membrane. Brain Res Rev. 1998;26(2-3):243-57. doi: 10.1016/s0165-0173(97)00043-x. PubMed PMID: WOS:000074783900016.

13. Bush D, Jin YC. Calcium control of triphasic hippocampal STDP. J Comput Neurosci. 2012;33(3):495-514. doi: 10.1007/s10827-012-0397-5. PubMed PMID: WOS:000310470800005.

14. Babu YS, Bugg CE, Cook WJ. Structure of calmodulin refined at 2.2 A resolution. J Mol Biol. 1988;204(1):191-204.

15. Linse S, Helmersson A, Forsen S. Calcium-binding to calmodulin and its globular domains. Journal of Biological Chemistry. 1991;266(13):8050-4. PubMed PMID: WOS:A1991FK44100017.

16. Mons N, Yoshimura M, Cooper DMF. Discrete expression of Ca2+/calmodulin-sensitive and Ca2+-insensitive adenylyl cyclases in the rat-brain. Synapse. 1993;14(1):51-9. doi: 10.1002/syn.890140108. PubMed PMID: WOS:A1993KZ84600007.

17. Cali JJ, Zwaagstra JC, Mons N, Cooper DMF, Krupinski J. Type-VIII adenylyl-cyclase - a Ca2+/calmodulin-stimulated enzyme expressed in discrete regions of rat-brain. Journal of Biological Chemistry. 1994;269(16):12190-5. PubMed PMID: WOS:A1994NG37700079.

18. Yasuda H, Higashi H, Kudo Y, Inoue T, Hata Y, Mikoshiba K, et al. Imaging of calcineurin activated by long-term depression-inducing synaptic inputs in living neurons of rat visual cortex. Eur J Neurosci. 2003;17(2):287-97. doi: 10.1046/j.1460-9568.2003.02449.x. PubMed PMID: WOS:000180571900011.

19. Anggono V, Huganir RL. Regulation of AMPA receptor trafficking and synaptic plasticity. Curr Opin Neurobiol. 2012;22(3):461-9. doi: 10.1016/j.conb.2011.12.006. PubMed PMID: WOS:000306634700014.

20. Xia ZG, Storm DR. The role of calmodulin as a signal integrator for synaptic plasticity. Nat Rev Neurosci. 2005;6(4):267-76. doi: 10.1038/nrn1647. PubMed PMID: WOS:000228092300010.

21. Chay A, Zamparo I, Koschinski A, Zaccolo M, Blackwell KT. Control of beta AR- and n-methyl-d-aspartate (NMDA) receptor-dependent cAMP dynamics in hippocampal neurons. PLoS Comput Biol. 2016;12(2):32. doi: 10.1371/journal.pcbi.1004735. PubMed PMID: WOS:000376582900018.

22. Zhong L, Gerges NZ. Neurogranin targets calmodulin and lowers the threshold for the induction of long-term potentiation. PLoS One. 2012;7(7):e41275.

23. Evans RC, Morera-Herreras T, Cui YH, Du K, Sheehan T, Kotaleski JH, et al. The effects of NMDA subunit composition on calcium influx and spike timing-dependent plasticity in striatal medium spiny neurons. PLoS Comput Biol. 2012;8(4):13. doi: 10.1371/journal.pcbi.1002493. PubMed PMID: WOS:000303440400042.

24. Li L, Stefan MI, Le Novere N. Calcium input frequency, duration and amplitude differentially modulate the relative activation of calcineurin and CaMKII. PLoS One. 2012;7(9):17. doi: 10.1371/journal.pone.0043810. PubMed PMID: WOS:000308577600017.

25. Doyere V, Laroche S. Linear relationship between the maintenance of hippocampal long-term potentiation and retention of an associative memory. Hippocampus. 1992;2(1):39-48. doi: 10.1002/hipo.450020106. PubMed PMID: WOS:A1992HD52200005.

26. Giese KP, Fedorov NB, Filipkowski RK, Silva AJ. Autophosphorylation at Thr(286) of the alpha calcium-calmodulin kinase II in LTP and learning. Science. 1998;279(5352):870-3. doi: 10.1126/science.279.5352.870. PubMed PMID: WOS:000071923500046.

27. Herring BE, Nicoll RA. Long-term potentiation: From CaMKII to AMPA receptor trafficking. In: Julius D, editor. Annual Review of Physiology, Vol 78. Annual Review of Physiology. 78. Palo Alto: Annual Reviews; 2016. p. 351-65.

28. Malinow R, Schulman H, Tsien RW. Inhibition of postsynaptic PKC or CaMKII blocks induction but not expression of LTP. Science. 1989;245(4920):862-6. doi: 10.1126/science.2549638. PubMed PMID: WOS:A1989AM10100035.

29. He Y, Kulasiri D, Samarasinghe S. Systems biology of synaptic plasticity: A review on N-methyl-D-aspartate receptor mediated biochemical pathways and related mathematical models. Biosystems. 2014;122:7-18. doi: 10.1016/j.biosystems.2014.06.005. PubMed PMID: WOS:000342531400002.

30. Slavov N, Carey J, Linse S. Calmodulin transduces Ca2+ oscillations into differential regulation of its target proteins. ACS Chem Neurosci. 2013;4(4):601-12. doi: 10.1021/cn300218d. PubMed PMID: WOS:000317873000010.

31. Diering GH, Heo S, Hussain NK, Liu B, Huganir RL. Extensive phosphorylation of AMPA receptors in neurons. Proc Natl Acad Sci U S A. 2016;113(33):E4920-E7. doi: 10.1073/pnas.1610631113. PubMed PMID: WOS:000381399200022.

32. Oliveira RF, Kim M, Blackwell KT. Subcellular location of PKA controls striatal plasticity: stochastic simulations in spiny dendrites. PLoS Comput Biol. 2012;8(2):19. doi: 10.1371/journal.pcbi.1002383. PubMed PMID: WOS:000300729900027.

33. Hayer A, Bhalla US. Molecular switches at the synapse emerge from receptor and kinase traffic. PLoS Comput Biol. 2005;1(2):137-54. doi: 10.1371/journal.pcbi.0010020. PubMed PMID: WOS:000234712600006.

34. Nabavi S, Kessels HW, Alfonso S, Aow J, Fox R, Malinow R. Metabotropic NMDA receptor function is required for NMDA receptor-dependent long-term depression. Proc Natl Acad Sci U S A. 2013;110(10):4027-32. doi: 10.1073/pnas.1219454110. PubMed PMID: WOS:000316377400075.

35. Huang KP, Huang FL, Chen HC. Characterization of a 7.5-kDa protein-kinase-c substrate (RC3 protein, neurogranin) from rat-brain. Arch Biochem Biophys. 1993;305(2):570-80. doi: 10.1006/abbi.1993.1463. PubMed PMID: WOS:A1993LY02200051.

36. Matus A. Actin-based plasticity in dendritic spines. Science. 2000;290(5492):754-8. doi: 10.1126/science.290.5492.754. PubMed PMID: WOS:000090067600037.

37. Opazo P, Labrecque S, Tigaret CM, Frouin A, Wiseman PW, De Koninck P, et al. CaMKII triggers the diffusional trapping of surface AMPARs through phosphorylation of stargazin. Neuron. 2010;67(2):239-52. doi: 10.1016/j.neuron.2010.06.007. PubMed PMID: WOS:000280461500009.

38. Lu HME, MacGillavry HD, Frost NA, Blanpied TA. Multiple spatial and kinetic subpopulations of CaMKII in spines and dendrites as resolved by single-molecule tracking PALM. J Neurosci. 2014;34(22):7600-10. doi: 10.1523/jneurosci.4364-13.2014. PubMed PMID: WOS:000337131800020.

39. Hayashi Y, Shi SH, Esteban JA, Piccini A, Poncer JC, Malinow R. Driving AMPA receptors into synapses by LTP and CaMKII: Requirement for GluR1 and PDZ domain interaction. Science. 2000;287(5461):2262-7. doi: 10.1126/science.287.5461.2262. PubMed PMID: WOS:000086049100051.

40. Chen L, Chetkovich DM, Petralia RS, Sweeney NT, Kawasaki Y, Wenthold RJ, et al. Stargazin regulates synaptic targeting of AMPA receptors by two distinct mechanisms. Nature. 2000;408(6815):936-43. PubMed PMID: WOS:000165951100039.

41. Griffith T, Tsaneva-Atanasova K, Mellor JR. Control of Ca2+ influx and calmodulin activation by SK-Channels in dendritic spines. PLoS Comput Biol. 2016;12(5):19. doi: 10.1371/journal.pcbi.1004949. PubMed PMID: WOS:000379348100038.

42. Pepke S, Kinzer-Ursem T, Mihalas S, Kennedy MB. A dynamic model of interactions of Ca2+, calmodulin, and catalytic subunits of Ca2+/calmodulin-dependent protein kinase II. PLoS Comput Biol. 2010;6(2):15. doi: 10.1371/journal.pcbi.1000675. PubMed PMID: WOS:000275260000022.

43. Bartol T, Dittrich M, Faeder J. MCell. Encyclopedia of computational neuroscience; 2015. p. 1673-76.

44. Michalski PJ, Loew LM. CaMKII activation and dynamics are independent of the holoenzyme structure: an infinite subunit holoenzyme approximation. Phys Biol. 2012;9(3):13. doi: 10.1088/1478-3975/9/3/036010. PubMed PMID: WOS:000306003700011.

45. Li X, Holmes W. Biophysical attributes that affect CaMKII activation deduced with a novel spatial stochastic simulation approach. PLOS Computational Biology; 2018.

46. Romano DR, Pharris MC, Patel NM, Kinzer-Ursem TL. Competitive tuning: Competition's role in setting the frequency-dependence of Ca2+-dependent proteins. PLoS Comput Biol. 2017;13(11):26. doi: 10.1371/journal.pcbi.1005820. PubMed PMID: WOS:000416838500012.

47. Ando K. Calmodulin-dependent regulation of neurotransmitter release differs in subsets of neuronal cells. Brain Res. 2013;1535:1–13.

48. Tabuchi H, Yamamoto H, Matsumoto K, Ebihara K, Takeuchi Y, Fukunaga K, et al. Regulation of insulin secretion by overexpression of Ca2+/calmodulin-dependent protein kinase II in insulinoma MIN6 cells. Endocrinology. 2000;141(7):2350-60. Epub JUL 2000.

49. Torok K, Trentham DR. Mechanism of 2-chloro-(epsilon-Lys75)-(6-(N,N-diethylamino)phenyl)-(1,3,5-triazin-4-yl)calmodulin interactions with smooth muscle myosin light chain kinase and derived peptides. Biochemistry. 1994;33(43):12807-14.

50. Masada N, Schaks S, Jackson SE, Sinz A, Cooper DM. Distinct mechanisms of calmodulin binding and regulation of adenylyl cyclases 1 and 8. Biochemistry. 2012;51(40):7917-29.

51. Quintana AR, Wang D, Forbes JE, Waxham MN. Kinetics of calmodulin binding to calcineurin. Biochem Biophys Res Commun. 2005;334(2):674-80.

52. Hubbard MJ, Klee CB. Calmodulin binding by calcineurin: Ligand-induced renaturation of protein immobilized on nitrocellulose. J Biol Chem. 1987;262(31):15062-70.

53. Takano E, Hatanaka M, Maki M. Real-time analysis of the calcium-dependent interaction between calmodulin and a synthetic oligopeptide of calcineurin by a surface plasmon resonance biosensor. FEBS Lett. 1994;352(2):247-50.

54. Stemmer PM, Klee CB. Dual calcium ion regulation of calcineurin by calmodulin and calcineurin B. Biochemistry. 1994;33(22):6859-66.

55. Kasturi R, Vasulka C, Johnson JD. Ca2+, caldesmon, and myosin light chain kinase exchange with calmodulin. J Biol Chem. 1993;268(11):7958-64.

56. Tsvetkov PO, Protasevich II, Gilli R, Lafitte D, Lobachov VM, Haiech J, et al. Apocalmodulin binds to the myosin light chain kinase calmodulin target site. J Biol Chem. 1999;274(26):18161-4.

57. Johnson JD, Snyder C, Walsh M, Flynn M. Effects of myosin light chain kinase and peptides on Ca2+ exchange with the N- and C-terminal Ca2+ binding sites of calmodulin. J Biol Chem. 1996;271(2):761-7.

58. Peersen OB, Madsen TS, Falke JJ. Intermolecular tuning of calmodulin by target peptides and proteins: Differential effects on Ca2+ binding and implications for kinase activation. Protein Sci. 1997;6(4):794-807.

59. McMurry JL, Chrestensen CA, Scott IM, Lee EW, Rahn AM, Johansen AM, et al. Rate, affinity and calcium dependence of nitric oxide synthase isoform binding to the primary physiological regulator calmodulin. FEBS J. 2011;278(24):4943-54.

60. Wu G, Berka V, Tsai A-L. Binding kinetics of calmodulin with target peptides of three nitric oxide synthase isozymes. J Inorg Biochem. 2011;105(9):1226-37.

61. Zoche M, Bienert M, Beyermann M, Koch K-W. Distinct molecular recognition of calmodulin-binding sites in the neuronal and macrophage nitric oxide synthases: a surface plasmon resonance study. Biochemistry. 1996;35(26):8742-6.

62. Sheta EA, McMillan K, Masters BS. Evidence for a bidomain structure of constitutive cerebellar nitric oxide synthase. J Biol Chem. 1994;269(21):15147-53.

63. Weissman BA, Jones CL, Liu Q, Gross SS. Activation and inactivation of neuronal nitric oxide synthase: Characterization of Ca2+-dependent [125I]calmodulin binding. Eur J Pharmacol. 2002;435(1):9-18.

64. Censarek P, Beyermann M, Koch K-W. Target recognition of apocalmodulin by nitric oxide synthase I peptides. Biochemistry. 2002;41(27):8598-7.

65. Persechini A, White HD, Gansz KJ. Different mechanisms for Ca2+ dissociation from complexes of calmodulin with nitric oxide synthase or myosin light chain kinase. J Biol Chem. 1996;271(1):62-7.

66. Zucker RS. Calcium- and activity-dependent synaptic plasticity. Curr Opin Neurobiol. 1999;9(3):305-13.

67. Whitlock JR, Heynen AJ, Shuler MG, Bear MF. Learning induces long-term potentiation in the hippocampus. Science. 2006;313(5790):1093-7.

68. Maren S. Long-term potentiation in the amygdala: A mechanism for emotional learning and memory. Trends Neurosci. 1999;22(12):561-7.

69. Ge Y, Dong Z, Bagot RC, Howland JG, Phillips AG, Wong TP, et al. Hippocampal long-term depression is required for the consolidation of spatial memory. Proc Natl Acad Sci U S A. 2010;107(38):16697-702.

70. Kemp A, Manahan-Vaughan D. Hippocampal long-term depression: Master or minion in declarative memory processes? Trends Neurosci. 2007;30(3):111-8.

71. Platenik J, Kuramoto N, Yoneda Y. Molecular mechanisms associated with long-term consolidation of the NMDA signals. Life Sci. 2000;67(4):335-64.

72. Carlisle HJ, Kennedy MB. Spine architecture and synaptic plasticity. Trends Neurosci. 2005;28(4):182-7.

73. Xia Z, Storm DR. The role of calmodulin as a signal integrator for synaptic plasticity. Nature Reviews Neuroscience. 2005;6(4):267-76.

74. Mayford M, Wang J, Kandel ER, O'Dell TJ. CaMKII regulates the frequency-response function of hippocampal synapses for the production of both LTD and LTP. Cell. 1995;81(6):891-904.

75. Evans RC, Blackwell KT. Calcium: Amplitude, duration, or location? Biological Bulletin. 2015;228(1):75-83.

76. Dudek SM, Bear MF. Homosynaptic long-term depression in area CA1 of hippocampus and effects of N-methyl-D-aspartate receptor blockade. Proc Natl Acad Sci U S A. 1992;89(10):4363-7.

77. Giese KP, Fedorov NB, Filipkowski RK, Silva AJ. Autophosphorylation at Thr286 of the alpha calcium-calmodulin kinase II in LTP and learning. Science. 1998;279(5352):870-3.

78. Lee H-K. Synaptic plasticity and phosphorylation. Pharmacol Ther. 2006;112(3):810-32.

79. Lu Y-F, Hayashi Y, Moriwaki A, Tomizawa K, Matsui H. FK506, a Ca2+/calmodulin-dependent phosphatase inhibitor, inhibits the induction of long-term potentiation in the rat hippocampus. Neurosci Lett. 1996;205(2):103-6.

80. Pi HJ, Otmakhov N, Lemelin D, De Koninck P, Lisman J. Autonomous CaMKII can promote either long-term potentiation or long-term depression, depending on the state of T305/T306 phosphorylation. J Neurosci. 2010;30(26):8704-9.

81. Pepke S, Kinzer-Ursem T, Mihalas S, Kennedy MB. A dynamic model of interactions of Ca2+, calmodulin, and catalytic subunits of Ca2+/calmodulin-dependent protein kinase II. PLoS Comput Biol. 2010;6(2):e1000675.

82. Bhalla US, Iyengar R. Emergent properties of networks of biological signaling pathways. Science. 1999;283(5400):381-7.

83. Kim M, Park AJ, Havekes R, Chay A, Guercio LA, Oliveira RF, et al. Colocalization of protein kinase A with adenylyl cyclase enhances protein kinase A activity during induction of long-lasting long-term-potentiation. PLoS Comput Biol. 2011;7(6):e1002084.

84. Sanabria H, Digman MA, Gratton E, Waxham NM. Spatial diffusivity and availability of intracellular calmodulin. Biophys J. 2008;95(12):6002-15.

85. Martzen MR, Slemmon JR. The dendritic peptide neurogranin can regulate a calmodulin-dependent target. J Neurochem. 1995;64(1):92-100.

86. Tran Q, Black DJ, Persechini A. Intracellular coupling via limiting calmodulin. J Biol Chem. 2003;278(27):24247-50.

87. Blumenthal DK, Charbonneau H, Edelman AM, Hinds TR, Rosenberg GB, Storm DR, et al. Synthetic peptides based on the calmodulin-binding domain of myosin light chain kinase inhibit activation of other calmodulin-dependent enzymes. Biochem Biophys Res Commun. 1988;156(2):860-5.

88. Antunes G, Roque AC, Simoes de Souza FM. Modelling intracellular competition for calcium: kinetic and thermodynamic control of different molecular modes of signal decoding. Sci Rep. 2016;6:23730.

89. Li L, Stefan MI, Le Novere N. Calcium input frequency, duration and amplitude differentially modulate the relative activation of calcineurin and CaMKII. PLoS One. 2012;7(9):e43810.

90. Hayer A, Bhalla US, Friston KJ. Molecular switches at the synapse emerge from receptor and kinase traffic. PLoS Comput Biol. 2005;1(2):e20.

91. He Y, Kulasiri D, Samarasinghe S. Modelling bidirectional modulations in synaptic plasticity: A biochemical pathway model to understand the emergence of long term potentiation (LTP) and long term depression (LTD). J Theor Biol. 2016;403:159-77. doi: 10.1016/j.jtbi.2016.05.015. PubMed PMID: WOS:000378987100015.

92. Saucerman JJ, Bers DM. Calmodulin mediates differential sensitivity of CaMKII and calcineurin to local Ca2+ in cardiac myocytes. Biophys J. 2008;95(10):4597-612. doi: 10.1529/biophysj.108.128728. PubMed PMID: WOS:000260519300013.

93. Saucerman JJ, Bers DM. Calmodulin binding proteins provide domains of local Ca2+ signaling in cardiac myocytes. J Mol Cell Cardiol. 2012;52(2):312-6. doi: 10.1016/j.yjmcc.2011.06.005. PubMed PMID: WOS:000299801600004.

94. Song Q, Saucerman JJ, Bossuyt J, Bers DM. Differential integration of Ca2+-calmodulin signal in intact ventricular mocytes at low and high affinity Ca2+-calmodulin targets. Biol Chem. 2008;283(46).

95. Onal B, Unudurthi S, Hund TJ. Modeling CaMKII in cardiac physiology: from molecule to tissue. Front Pharmacol. 2014;5(1).

96. Lakatta E, Maltsev V, Vinogradova T. A coupled system of intracellular Ca2+ clocks and surface membrane voltage controls the timekeeping mechanism of the heart's pacemaker. Circ Res. 2010;106(4).

97. Shifman JM, Choi MH, Mihalas S, Mayo SL, Kennedy MB. Ca2+/calmodulin-dependent protein kinase II (CaMKII) is activated by calmodulin with two bound calciums. Proc Natl Acad Sci U S A. 2006;103(38):13968-73. doi: 10.1073/pnas.0606433103. PubMed PMID: WOS:000240746600014.

98. Linse S, Helmersson A, Forsen S. Calcium binding to calmodulin and its globular domains. J Biol Chem. 1991;266(13):8050-4.

99. Kubota Y, Putkey J, Waxham M. Neurogranin controls the spatiotemporal pattern of postsynaptic Ca2+/CaM signaling. Biophys J. 2007;93(11):3848-59.

100. Wu Z-L, Thomas SA, Villacres EC, Xia Z, Simmons ML, Chavkin C, et al. Altered behavior and long-term potentiation in type I adenylyl cyclase mutant mice. Proc Natl Acad Sci U S A. 1995;92(1):220-4.

101. Wong ST, Athos J, Figueroa XA, Pineda VV. Calcium-stimulated adenylyl cyclase activity is critical for hippocampus-dependent long-term memory and late phase LTP. Neuron. 1999;23(4):787-98.

102. Schaefer ML, Wong ST, Wozniak DF, Muglia LM, Liauw JA, Zhuo M, et al. Altered stress-induced anxiety in adenylyl cyclase type VIII-deficient mice. J Neurosci. 2000;20(13):4809-20.

103. Wang JH, Kelly PT. Postsynaptic calcineurin activity downregulates synaptic transmission by weakening intracellular Ca2+ signaling mechanisms in hippocampal CA1 neurons. J Neurosci. 1997;17(12):4600-11.

104. Mulkey RM, Endo S, Shenolikar S, Malenka RC. Involvement of a calcineurin/inhibitor-1 phosphatase cascade in hippocampal long-term depression. Nature. 1994;369(6480):486-8.

105. Malleret G, Haditsch U, Genoux DJ, M.W., Bliss TV, Vanhoose AM, Weitlauf C, et al. Inducible and reversible enhancement of learning, memory, and long-term potentiation by genetic inhibition of calcineurin. Cell. 2001;104(5):675-86.

106. Otmakhov N, Griffith LC, Lisman JE. Postsynaptic inhibitors of calcium/calmodulin-dependent protein kinase type II block induction but not maintenance of pairing-induced long-term potentiation. J Neurosci. 1997;17(14):5357-65.

107. Silva AJ, Paylor R, Wehner JM, Tonegawa S. Impaired spatial learning in alpha-calcium-calmodulin kinase II mutant mice. Science. 1992;257(5067):206-11.

108. Silva AJ, Stevens CF, Tonegawa S, Wang Y. Deficient hippocampal long-term potentiation in alpha-calcium-calmodulin kinase II mutant mice. Science. 1992;257(5067):201-6.

109. Lei S, Czerwinska E, Czerwinski W, Walsh MP, MacDonald JF. Regulation of NMDA receptor activity by F-actin and myosin light chain kinase. J Neurosci. 2001;21(21):8464-72.

110. Rex CS, Gavin CF, Rubio MD, Kramar EA, Chen LY, Jia Y, et al. Myosin IIb regulates actin dynamics during synaptic plasticity and memory formation. Neuron. 2010;67(4):603-17.

111. Fedorov NB, Pasinelli P, Oestreicher AB, Degraan PN, Reymann KG. Antibodies to postsynaptic PKC substrate neurogranin prevent long-term potentiation in hippocampal CA1 neurons. Eur J Neurosci. 1995;7(4):819-22.

112. Zhong L, Cherry T, Bies CE, Florence MA, Gerges NZ. Neurogranin enhances synaptic strength through its interaction with calmodulin. Embo J. 2009;28(19):3027-39. doi: 10.1038/emboj.2009.236. PubMed PMID: WOS:000270514000016.

113. Huang K-P, Huang FL, Jager T, Li J, Reymann KG, Balschun D. Neurogranin/RC3 enhances long-term potentiation and learning by promoting calcium-mediated signaling. J Neurosci. 2004;24(47):10660-9.

114. Bohme GA, Bon C, Lemaire M, Reibaud M, Piot O, Stutzmann JM, et al. Altered synaptic plasticity and memory formation in nitric oxide synthase inhibitor-treated rats. Proc Natl Acad Sci U S A. 1993;90(19):9191-4.

115. Kinzer-Ursem TL, Linderman JJ. Both ligand- and cell-specific parameters control ligand agonism in a kinetic model of G protein-coupled receptor signaling. PLoS Comput Biol. 2007;3(1):e6.

116. Hoffman L, Chandrasekar A, Wang X, Putkey JA, Waxham MN. Neurogranin Alters the Structure and Calcium Binding Properties of Calmodulin. Journal of Biological Chemistry. 2014;289(21):14644-55. doi: 10.1074/jbc.M114.560656. PubMed PMID: WOS:000337248100021.

117. Olwin BB, Edelman AM, Krebs EG, Storm DR. Quantitation of energy coupling between Ca2+, calmodulin, skeletal-muscle myosin light chain kinase, and kinase substrates. J Biol Chem. 1984;259(17):949-55. PubMed PMID: WOS:A1984TH57900049.

118. Olwin B, Storm D. Calcium binding to complexes of calmodulin and calmodulin binding proteins. Biochemistry. 1985;24(27).

119. Brown SE, Martin SR, Bayley PM. Kinetic control of the dissociation pathway of calmodulin-peptide complexes. Journal of Biological Chemistry. 1997;272(6):3389-97. doi: 10.1074/jbc.272.6.3389. PubMed PMID: WOS:A1997WG19200041.

120. Chattopadhyaya R, Meador W, Means A, Quiocho F. Calmodulin structure refined at 1.7 A resolution. J Mol Biol. 1992;228(4).

121. Ikura M, Clore G, Gronenborn A, Zhu G, Klee C, Bax A. Solution structure of a calmodulin-target peptide complex by multidimensional NMR. Science. 1992;256(5057).

122. Conti AC, Maas JW, Muglia LM, Dave BA, Vogt SK, Tran TT, et al. Distinct regional and subcellular localization of adenylyl cyclases type 1 and 8 in mouse brain. Neuroscience. 2007;146(2):713-29.

123. Mons N, Yoshimura M, Cooper DM. Discrete expression of Ca2+/calmodulin-sensitive and Ca2+-insensitive adenylyl cyclases in the rat brain. Synapse. 1993;14(1):51-9.

124. Cali JJ, Zwaagstra JC, Mons N, Cooper DM, Krupinski J. Type VIII adenylyl cyclase: A Ca2+/calmodulin-stimulated enzyme expressed in discrete regions of rat brain. J Biol Chem. 1994;269(16):12190-5.

125. Swislocki NI, Tierney J. Solubilization, stabilization, and partial purification of brain adenylate cyclase from rat. Biochemistry. 1973;12(10):1862-6.

126. Brostrom CO, Huang Y-C, Wolff DJ. Identification of a calcium-binding protein as a calcium-dependent regulator of brain adenylate cyclase. Proc Natl Acad Sci U S A. 1975;72(1):64-8.

127. Levin LR, Reed RR. Identification of functional domains of adenylyl cyclase using in vivo chimeras. J Biol Chem. 1995;270(13):7573-9.

128. Masada N, Ciruela A, MacDougall DA, Cooper DMF. Distinct Mechanisms of Regulation by Ca(2+)/Calmodulin of Type 1 and 8 Adenylyl Cyclases Support Their Different Physiological Roles. J Biol Chem. 2009;284(7):4451-63. doi: 10.1074/jbc.M807359200. PubMed PMID: PMC2640985.

129. Gu C, Cooper DM. Calmodulin-binding sites on adenylyl cyclase type VIII. J Biol Chem. 1999;274(12):8012-21.

130. Herbst S, Masada N, Pfennig S, Ihling C, Cooper D, Sinz A. Structural insights into calmodulin/adenylyl cyclase 8 interaction. Anal Bioanal Chem. 2013;405(429):9333-42.

131. Lilly SM, Alvarez FJ, Tietz EI. Synaptic and subcellular localization of A-kinase anchoring protein 150 in rat hippocampal CA1 pyramidal cells: Co-localization with excitatory synaptic markers. Neuroscience. 2005;134(1):155-63.

132. Morioka M, Nagahiro S, Fukunaga K, Miyamoto E, Ushio Y. Calcineurin in the adult rat hippocampus: Different distribution in CA1 and CA3 subfields. Neuroscience. 1997;78(3):673-84. doi: 10.1016/s0306-4522(96)00626-4. PubMed PMID: WOS:A1997WX54000006.

133. Klee CB, Crouch TH, Krinks MH. Calcineurin: A calcium- and calmodulin-binding protein of the nervous system. Proc Natl Acad Sci U S A. 1979;76(12):6270-3.

134. Dunlap TB, Guo H-F, Cook EC, Holbrook E, Rumi-Masante J, Lester TE, et al. Stoichiometry of the calcineurin regulatory domain-calmodulin complex. Biochemistry. 2014;53(36):5779-90.

135. Huiming L, Rao A, Hogan PG. Interaction of calcineurin with substrates and targeting proteins. Trends Cell Biol. 2011;21(2):91-103.

136. Wallace RW, Tallant EA, Cheung WY. High levels of a heat-labile calmodulin-binding protein (CaM-BP80) in bovine neostriatum. Biochemistry. 1980;19(9):1831-7.

137. Miller SG, Kennedy MB. Distinct forebrain and cerebellar isozymes of type II calcium/calmodulin-dependent protein kinase associate differently with the postsynaptic density fraction. J Biol Chem. 1985;260(15):9039-46.

138. Benson DL, Gall CM, Isackson PJ. Dendritic localization of type II calcium calmodulin-dependent protein kinase mRNA in normal and reinnervated rat hippocampus. Neuroscience. 1992;46(4):851-7.

139. Bennett MK, Erondu NE, Kennedy MB. Purification and characterization of a calmodulin-dependent protein kinase that is highly concentrated in brain. J Biol Chem. 1983;258(20):12735-44.

140. Kuret J, Schulman H. Mechanism of autophosphorylation of the multifunctional Ca2+/calmodulin-dependent protein kinase. J Biol Chem. 1985;260(10):6427-33.

141. Katoh T, Fujisawa H. Calmodulin-dependent protein kinase II: Kinetic studies on the interaction with substrates and calmodulin. Biochim Biophys Acta. 1991;1091(2):205-12.

142. Kim SA, Heinze KG, Bacia K, Waxham MN, Schwille P. Two-photon cross-correlation analysis of intracellular reactions with variable stoichiometry. Biophys J. 2005;88(6):4319-36.

143. Hanson PI, Schulman H. Neuronal Ca2+/calmodulin-dependent protein kinases. Annu Rev Biochem. 1992;61:559-601.

144. Irvine EE, von Hertzen LS, Plattner F, Peter K. alphaCaMKII autophosphorylation: A fast track to memory. Trends Neurosci. 2006;29(8):459.

145. Meyer T, Hanson P. Calmodulin trapping by calcium-calmodulin-dependent protein kinase. Science. 1992;256(5060):1199-202.

146. Edelman AM, Higgins DM, Bowman CL, Haber SN, Rabin RA, Cho-Lee J. Myosin light chain kinase is expressed in neurons and glia: Immunoblotting and immunocytochemical studies. Mol Brain Res. 1992;14(1):27-34.

147. Dabrowska R, Sherry JM, Aromatorio DK, Hartshorne DJ. Modulator protein as a component of the myosin light chain kinase from chicken gizzard. Biochemistry. 1978;17(2):253-8.

148. Lukas TJ, Burgess WH, Prendergast FG, Lau W, Watterson DM. Calmodulin binding domains: Characterization of a phosphorylation and calmodulin binding site from myosin light chain kinase. Biochemistry. 1986;25(6):1458-64.

149. Conti MA, Adelstein RS. The relationship between calmodulin binding and phosphorylation of smooth muscle myosin kinase by the catalytic subunit of 3':5' cAMP-dependent protein kinase. J Biol Chem. 1981;256(7):3178-81.

150. Potier M-C, Chelot E, Pekarsky Y, Gardiner K, Rossier J. The human myosin light chain kinase (MLCK) from hippocampus: Cloning, sequencing, expression, and localization to 3qcen-q21. Genomics. 1995;29(3):562-70.

151. Szymanski P, Szymanska G, Goyal R. Differences in calmodulin and calmodulin-binding proteins in phasic and tonic smooth muscle. Am J Physiol. 2002;51(1):C94-C104.

152. Baudier J, Deloulme JC, Van Dorsselaer A, Black D, Matthes HW. Purification and characterization of a brain-specific protein kinase C substrate, neurogranin (p17). J Biol Chem. 1991;266(1):229-37.

153. Dominguez-Gonzalez I, Vazquez-Cuesta SN, Algaba A, Diez-Guerra FJ. Neurogranin binds to phosphatidic acid and associates to cellular membranes. Biochem J. 2007;404(1):31-43.

154. Represa A, Deloulme JC, Sensenbrenner M, Ben-Ari Y, Baudier J. Neurogranin: Immunocytochemical localization of a brain-specific protein kinase C substrate. J Neurosci. 1990;10(12):3782-92.

155. Gerendasy DD, Herron SR, Watson JB, Sutcliffe JG. Mutational and biophysical studies suggest RC3/neurogranin regulates calmodulin availability. J Biol Chem. 1994;269(35):22420-6.

156. Huang K-P, Huang FL, Chen HC. Characterization of a 7.5-kDa protein kinase C substrate (RC3 protein, neurogranin) from rat brain. Arch Biochem Biophys. 1993;305(2):570-80.

157. Herbison AE, Simonian SX, Norris PJ, Emson PC. Relationship of neuronal nitric oxide synthase immunoreactivity to GnRH neurons in the ovariectomized and intact female rat. J Neuroendocrinol. 1996;8(1):73-82.

158. Burette A, Zabel U, Weinberg RJ, Schmidt HH, Valtschanoff JG. Synaptic localization of nitric oxide synthase and soluble guanylyl cyclase in the hippocampus. J Neurosci. 2002;22(20):8961-70.

159. Doyle CA, Slater P. Localization of neuronal and endothelial nitric oxide synthase isoforms in human hippocampus. Neuroscience. 1997;76(2):387-95. doi: 10.1016/s0306-4522(96)00297-7. PubMed PMID: WOS:A1997WB59200008.

160. Bredt DS, Snyder SH. Isolation of nitric oxide synthetase, a calmodulin-requiring enzyme. Proc Natl Acad Sci U S A. 1990;87(2):682-5.

161. Panda K, Ghosh S, Stuehr DJ. Calmodulin activates intersubunit electron transfer in the neuronal nitric-oxide synthase dimer. Journal of Biological Chemistry. 2001;276(26):23349-56. doi: 10.1074/jbc.M100687200. PubMed PMID: WOS:000169531100019.

162. Koh WC, Choe ES, Lee DK, Chang S-C, Shim Y-B. Monitoring the activation of neuronal nitric oxide synthase in brain tissue and cells with a potentiometric immunosensor. Biosensors Bioelectron. 2009;25(1):211-7.

163. Lourenco CF, Ferreira NR, Santos RM, Lukacova N, Barbosa RM, Laranjinha J. The pattern of glutamate-induced nitric oxide dynamics in vivo and its correlation with nNOS expression in rat hippocampus, cerebral cortext and striatum. Brain Res. 2014;1554:1-11.

164. Sabatini BL, Oertner TG, Svoboda K. The life cycle of Ca2+ ions in dendritic spines. Neuron. 2002;33(3):439-52. doi: 10.1016/s0896-6273(02)00573-1. PubMed PMID: WOS:000173643200013.

165. Pharris MC, Patel NM, Kinzer-Ursem TL. Competitive Tuning Among Ca2+ Calmodulin-Dependent Proteins: Analysis of In Silico Model Robustness and Parameter Variability. Cell Mol Bioeng. 2018;11(5):353-65. doi: 10.1007/s12195-018-0549-4. PubMed PMID: WOS:000444812000005.

166. Pak JH, Huang FL, Li J, Balschun D, Reymann K, Chiang C, et al. Involvement of neurogranin in the modulation of calcium/calmodulin-dependent protein kinase II, synaptic plasticity, and spatial learning: A study with knockout mice. Proc Natl Acad Sci U S A. 2000;97(21):11232-7.

167. Krucker T, Siggins GR, NcNamara RK, Lindsley KA, Dao A, Allison DW, et al. Targeted disruption of RC3 reveals a calmodulin-based mechanism for regulating metaplasticity in the hippocampus. J Neurosci. 2002;22(13):5525-35.

168. Edelstein SJ, Stefan MI, Le Novere N. Ligand depletion in vivo modulates the dynamic range and cooperativity of signal transduction. PLoS One. 2010;5(1):10. doi: 10.1371/journal.pone.0008449. PubMed PMID: WOS:000273338500003.

169. Bazzazi H, Sang L, Dick IE, Joshi-Mukherjee R, Yang W, Yue DT. Novel fluorescence resonance energy transfer-based reporter reveals differential calcineurin activation in neonatal and adult cardiomyocytes. J Physiol. 2015;593(17):3865-84. PubMed PMID: 26096996.

170. Sanderson JL, Gorski JA, Gibson ES, Lam P, Freund RK, Chick WS, et al. AKAP150-anchored calcineurin regulates synaptic plasticity by limiting synaptic incorporation of Ca2+-permeable AMPA receptors. J Neurosci. 2012;32(43):15036-52. Epub 2012/10/27. doi: 10.1523/jneurosci.3326-12.2012. PubMed PMID: 23100425; PubMed Central PMCID: PMCPMC3504485.

171. Sanderson JL, Dell'Acqua ML. AKAP signaling complexes in regulation of excitatory synaptic plasticity. Neuroscientist. 2011;17(3):321-36. PubMed PMID: 21498812.

172. Dell'Acqua ML, Dodge KL, Tavalin SJ, Scott JD. Mapping the protein phosphatase-2B anchoring site on AKAP79. Binding and inhibition of phosphatase activity are mediated by residues 315-360. J Biol Chem. 2002;277(50):48796-802. Epub 2002/10/02. doi: 10.1074/jbc.M207833200. PubMed PMID: 12354762; PubMed Central PMCID: PMCPMC3923414.

173. Research W. Mathematica Edition 10.0 Champaign, IL: 2016.

174. Shapiro B, Levchenko A, Meyerowitz E, Wold B, Mjolsness E. Cellerator: Extending a computer algebra system to include biochemical arrows for signal transduction simulations. Bioinformatics. 2002;19:677-8.

175. Chelliah V, Juty N, Ajmera I, Ali R, Dumousseau M, Glont M, et al. BioModels: ten-year anniversary. Nucleic Acids Res. 2015;43(D1):D542-D8. doi: 10.1093/nar/gku1181. PubMed PMID: WOS:000350210400081.

176. Li C, Donizelli M, Rodriguez N, Dharuri H, Endler L, Chelliah V, et al. BioModels Database: An enhanced, curated and annotated resource for published quantitative kinetic models. BMC Syst Biol. 2010;4:14. doi: 10.1186/1752-0509-4-92. PubMed PMID: WOS:000282255800003.

177. Le Novere N, Bornstein B, Broicher A, Courtot M, Donizelli M, Dharuri H, et al. BioModels Database: a free, centralized database of curated, published, quantitative kinetic models of biochemical and cellular systems. Nucleic Acids Res. 2006;34:D689-D91. doi: 10.1093/nar/gkj092. PubMed PMID: WOS:000239307700145.

178. WH O. Neurological Disorders: Public Health Challenges. Geneva, Switzerland: WHO Press; 2006. p. 232.

179. Borlongan CV, Burns K, Tajiri N, Stahl CE,Wweinbren NL, et al. Epidemiological survey-based formulae to approximate incidence and prevalence of neurological disorders in the United States: a meta-analysis. e78490 ed: PLoS One; 2013.

180. Huganir RL, Nicoll RA. AMPARs and synaptic plasticity: The last 25 years. Neuron. 2013;80(3):704-17. doi: 10.1016/j.neuron.2013.10.025. PubMed PMID: WOS:000326609900015.

181. Ghosh A, Greenberg ME. Calcium signaling in neurons - molecular mechanisms and cellular consequences. Science. 1995;268(5208):239-47. doi: 10.1126/science.7716515. PubMed PMID: WOS:A1995QT18500023.

182. Chin D, Means AR. Calmodulin: a prototypical calcium sensor. Trends Cell Biol. 2000;10(8):322-8. doi: 10.1016/s0962-8924(00)01800-6. PubMed PMID: WOS:000088382600004.

183. Kulkami C, Lo M, Fraseur JG, Tirrell DA, Kinzer-Ursem TL. Bioorthogonal chemoenzymatic functionalization of calmodulin for bioconjugation applications. Bioconjugate Chem. 2015;26(10):2153-60. doi: 10.1021/acs.bioconjchem.5b00449. PubMed PMID: WOS:000363438100020.

184. Romano DR, Pharris MC, Patel NM, Kinzer-Ursem TL. Competitive tuning: Competition's role in setting the frequency-dependence of Ca2+-dependent proteins. PLoS computational biology. 2017;13(11):e1005820. Epub 2017/11/07. doi: 10.1371/journal.pcbi.1005820. PubMed PMID: 29107982; PubMed Central PMCID: PMCPMC5690689.

185. Keller DX, Franks KM, Bartol TM, Sejnowski TJ. Calmodulin activation by calcium transients in the postsynaptic density of dendritic spines. PLoS One. 2008;3(4):16. doi: 10.1371/journal.pone.0002045. PubMed PMID: WOS:000261572300017.

186. Krucker T, Siggins GR, McNamara RK, Lindsley KA, Dao A, Allison DW, et al. Targeted disruption of RC3 reveals a calmodulin-based mechanism for regulating metaplasticity in the hippocampus. J Neurosci. 2002;22(13):5525-35. PubMed PMID: WOS:000176599100032.

187. Malenka RC, Lancaster B, Zucker RS. Temporal limits on the rise in postsynaptic calcium required for the induction of long-term potentiation. Neuron. 1992;9(1):121-8. doi: 10.1016/0896-6273(92)90227-5. PubMed PMID: WOS:A1992JE75600013.

188. Olwin BB, Edelman AM, Krebs EG, Storm DR. Quantitation of energy coupling between Ca-2+, calmodulin, skeletal-muscle myosin light chain kinase, and kinase substrates. Journal of Biological Chemistry. 1984;259(17):949-55. PubMed PMID: WOS:A1984TH57900049.

189. Masada N, Schaks S, Jackson SE, Sinz A, Cooper DMF. Distinct Mechanisms of Calmodulin Binding and Regulation of Adenylyl Cyclases 1 and 8. Biochemistry. 2012;51(40):7917-29. doi: 10.1021/bi300646y. PubMed PMID: WOS:000309505300012.

190. Forest A, Swulius MT, Tse JKY, Bradshaw JM, Gaertner T, Waxham MN. Role of the N- and C-lobes of calmodulin in the activation of Ca(2+)/calmodulin-dependent protein kinase II. Biochemistry. 2008;47(40):10587-99. doi: 10.1021/bi8007033. PubMed PMID: WOS:000259603600008.

191. Swislocki NI, Tierney J. Solubilization, stabilization, and partial-purification of brain adenylate cyclase from rat. Biochemistry. 1973;12(10):1862-6. doi: 10.1021/bi00734a004. PubMed PMID: WOS:A1973P562700004.

192. Brostrom CO, Huang YC, Breckenridge BM, Wolff DJ. Identification of a calcium-binding protein as a calcium-dependent regulator of brain adenylate cyclase. Proc Natl Acad Sci U S A. 1975;72(1):64-8. doi: 10.1073/pnas.72.1.64. PubMed PMID: WOS:A1975V479600015.

193. Gu C, Cooper DMF. Calmodulin-binding sites on adenylyl cyclase type VIII. Journal of Biological Chemistry. 1999;274(12):8012-21. doi: 10.1074/jbc.274.12.8012. PubMed PMID: WOS:000079268100059.

194. Miller SG, Kennedy MB. Distinct forebrain and cerebellar isozymes of type II Ca2+/calmodulin-dependent protein kinase associate differently with the postsynaptic density fraction. J Biol Chem. 1985;260(15):9039-46.

195. Miller SG, Kennedy MB. Regulation of brain type-II Ca-2+ calmodulin-dependent protein-kinase by autophosphorylation - a Ca-2+-triggered molecular switch. Cell. 1986;44(6):861-70. doi: 10.1016/0092-8674(86)90008-5. PubMed PMID: WOS:A1986A741800006.

196. Barria A, Derkach V, Soderling T. Identification of the Ca2+/calmodulin-dependent protein kinase II regulatory phosphorylation site in the alpha-amino-3-hydroxyl-5-methyl-4-isoxazole-propionate-type glutamate receptor. Journal of Biological Chemistry. 1997.

197. Stemmer PM, Klee CB. Dual calcium ion regulation of calcineurin by calmodulin and calcineurin B. Biochemistry. 1994;33(22):6859-66. Epub 1994/06/07. PubMed PMID: 8204620.

198. Klee CB, Krinks MH. Purification of cyclic 3',5'-nucleotide phosphodiesterase inhibitory protein by affinity chromatography on activator protein coupled to sepharose. Biochemistry. 1978;17(1):120-6. doi: 10.1021/bi00594a017. PubMed PMID: WOS:A1978EG71400017.

199. Beattie EC, Carroll RC, Yu X, Morishita W, Yasuda H, von Zastrow M, et al. Regulation of AMPA receptor endocytosis by a signaling mechanism shared with LTD. Nat Neurosci. 2000;3(12):1291-300. PubMed PMID: WOS:000167177900015.

200. Lei SB, Czerwinska E, Czerwinski W, Walsh MP, MacDonald JF. Regulation of NMDA receptor activity by F-actin and myosin light chain kinase. J Neurosci. 2001;21(21):8464-72. PubMed PMID: WOS:000171608600026.

201. Dabrowska R, Sherry JMF, Aromatorio DK, Hartshorne DJ. Modulator protein as a component of myosin light chain kinase from chicken gizzard. Biochemistry. 1978;17(2):253-8. doi: 10.1021/bi00595a010. PubMed PMID: WOS:A1978EH77300010.

202. Lukas TJ, Burgess WH, Prendergast FG, Lau W, Watterson DM. Calmodulin binding domains - characterization of a phosphorylation and calmodulin binding-site from myosin light chain kinase. Biochemistry. 1986;25(6):1458-64. doi: 10.1021/bi00354a041. PubMed PMID: WOS:A1986A562900041.

203. Represa A, Deloulme JC, Sensenbrenner M, Benari Y, Baudier J. Neurogranin - immunocytochemical localization of a brain-specific protein-kinase-C substrate. J Neurosci. 1990;10(12):3782-92. PubMed PMID: WOS:A1990EP04200003.

204. Zhong L, Gerges NZ. Neurogranin targets calmodulin and lowers the threshold for the induction of long-term potentiation. PLoS One. 2012;7(7):8. doi: 10.1371/journal.pone.0041275. PubMed PMID: WOS:000306806600048.

205. Bredt DS, Snyder SH. Isolation of nitric-oxide synthetase, a calmodulin-requiring enzyme. Proc Natl Acad Sci U S A. 1990;87(2):682-5. doi: 10.1073/pnas.87.2.682. PubMed PMID: WOS:A1990CK37800037.

206. Oliveira RF, Kim M, Blackwell KT. Subcellular location of PKA controls striatal plasticity: stochastic simulations in spiny dendrites. PLoS computational biology. 2012;8(2):e1002383. Epub 2012/02/22. doi: 10.1371/journal.pcbi.1002383. PubMed PMID: 22346744; PubMed Central PMCID: PMCPMC3276550.

207. Hao HP, Zak DE, Sauter T, Schwaber J, Ogunnaike BA. Modeling the VPAC(2)-activated cAMP/PKA signaling pathway: From receptor to circadian clock gene induction. Biophys J. 2006;90(5):1560-71. doi: 10.1529/biophysj.105.065250. PubMed PMID: WOS:000235235600010.

208. Kinzer-Ursem TL, Linderman JJ. Both ligand- and cell-specific parameters control ligand agonism in a kinetic model of G protein-coupled receptor signaling. PLoS Comput Biol. 2007;3(1):84-94. doi: 10.1371/journal.pcbi.0030006. PubMed PMID: WOS:000243838700009.

209. Kim M, Park AJ, Havekes R, Chay A, Guercio LA, Oliveira RF, et al. Colocalization of Protein Kinase A with Adenylyl Cyclase Enhances Protein Kinase A Activity during Induction of Long-Lasting Long-Term-Potentiation. PLoS Comput Biol. 2011;7(6):18. doi: 10.1371/journal.pcbi.1002084. PubMed PMID: WOS:000292381900028.

210. Maravall M, Mainen ZF, Sabatini BL, Svoboda K. Estimating intracellular calcium concentrations and buffering without wavelength ratioing. Biophys J. 2000;78(5):2655-67. doi: 10.1016/s0006-3495(00)76809-3. PubMed PMID: WOS:000086892500043.

211. Antunes G, Roque AC, de Souza FMS. Modelling intracellular competition for calcium: kinetic and thermodynamic control of different molecular modes of signal decoding. Sci Rep. 2016;6:12. doi: 10.1038/srep23730. PubMed PMID: WOS:000373324800001.

212. Shapiro BE, Levchenko A, Meyerowitz EM, Wold BJ, Mjolsness ED. Cellerator: extending a computer algebra system to include biochemical arrows for signal transduction simulations. Bioinformatics. 2003;19(5):677-8. doi: 10.1093/bioinformatics/btg042. PubMed PMID: WOS:000181964600027.

213. Anand KS, Dhikav V. Hippocampus in health and disease: An overview. Ann Indian Acad Neurol. 2012;15(4):239-46. doi: 10.4103/0972-2327.104323. PubMed PMID: WOS:000313288300001.

214. Broadhead MJ, Horrocks MH, Zhu F, Muresan L, Benavides-Piccione R, DeFelipe J, et al. PSD95 nanoclusters are postsynaptic building blocks in hippocampus circuits. Sci Rep. 2016;6:14. doi: 10.1038/srep24626. PubMed PMID: WOS:000374639800001.

215. Blackwell KT. Approaches and tools for modeling signaling pathways and calcium dynamics in neurons. J Neurosci Methods. 2013;220(2):131-40. doi: 10.1016/j.jneumeth.2013.05.008. PubMed PMID: WOS:000327921800004.

216. Zhabotinsky AM. Bistability in the Ca2+/calmodulin-dependent protein kinase-phosphatase system. Biophys J. 2000;79(5):2211-21. doi: 10.1016/s0006-3495(00)76469-1. PubMed PMID: WOS:000165104500001.

217. Mayford M, Wang J, Kandel ER, Odell TJ. CAMKII regulates the frequency-response function of hippocampal synapses for the production of both LTD and LTP. Cell. 1995;81(6):891-904. doi: 10.1016/0092-8674(95)90009-8. PubMed PMID: WOS:A1995RD76800010.

218. Chao LH, Stratton MM, Lee IH, Rosenberg OS, Levitz J, Mandell DJ, et al. A mechanism for tunable autoinhibition in the structure of a human Ca2+/calmodulin-dependent kinase II holoenzyme. Cell. 2011;146(5):732-45. doi: 10.1016/j.cell.2011.07.038. PubMed PMID: WOS:000294477500014.

219. Lisman J, Yasuda R, Raghavachari S. Mechanisms of CaMKII action in long-term potentiation. Nat Rev Neurosci. 2012;13(3):169-82. doi: 10.1038/nrn3192. PubMed PMID: WOS:000300636500011.

220. Lee HK. Synaptic plasticity and phosphorylation. Pharmacol Ther. 2006;112(3):810-32. doi: 10.1016/j.pharmthera.2006.06.003. PubMed PMID: WOS:000242054400015.

221. Song RS, Tolentino R, Sobie EA, Neves-Zaph SR. Cross-regulation of phosphodiesterase 1 and phosphodiesterase 2 activities controls dopamine-mediated striatal alpha-amino-3-hydroxy-5-methyl-4-isoxazolepropionic acid (AMPA) receptor trafficking. Journal of Biological Chemistry. 2016;291(44):23257-67. doi: 10.1074/jbc.M116.749747. PubMed PMID: WOS:000387224800034.

222. Lu YF, Hayashi Y, Moriwaki A, Tomizawa K, Matsui H. FK506 a Ca2+/calmodulin-dependent phosphatase inhibitor inhibits the induction of long-term potentiation in the rat hippocampus. Neurosci Lett. 1996;205(2):103-6. doi: 10.1016/0304-3940(96)12384-3. PubMed PMID: WOS:A1996TX75800009.

223. Walkup W, Mastro TL, Schenker LT, Vielmetter J, Hu R, Iancu A, et al. A model for regulation by SynGAP-alpha1 of binding of synaptic proteins to PDZ-domain 'Slots' in the postsynaptic density. eLife; 2017.

224. Benson DL, Gall CM, Isackson PJ. Dendritic localization of type-II calcium calmodulin-dependent protein-kinase messenger-rna in normal and reinnervated rat hippocampus. Neuroscience. 1992;46(4):851-7. doi: 10.1016/0306-4522(92)90189-9. PubMed PMID: WOS:A1992HB52600006.

225. Ramirez-Amaya V, Vazdarjanova A, Mikhael D, Rosi S, Worley PF, Barnes CA. Spatial exploration-induced Arc mRNA and protein expression: Evidence for selective, network-specific reactivation. J Neurosci. 2005;25(7):1761-8. doi: 10.1523/jneurosci.4342-04.2005. PubMed PMID: WOS:000227064000017.

226. Matt L, Kim K, Chowdhury D, Hell JW. Role of palmitoylation of postsynaptic proteins in promoting synaptic plasticity. Front Molec Neurosci. 2019;12:19. doi: 10.3389/fnmol.2019.00008. PubMed PMID: WOS:000457405900001.

227. Woolfrey KM, Dell'Acqua ML. Coordination of protein phosphorylation and dephosphorylation in synaptic plasticity. Journal of Biological Chemistry. 2015;290(48):28604-12. doi: 10.1074/jbc.R115.657262. PubMed PMID: WOS:000365762300003.

228. Antunes G, Simoes-de-Souza FM. AMPA receptor trafficking and its role in heterosynaptic plasticity. Sci Rep. 2018;8:14. doi: 10.1038/s41598-018-28581-w. PubMed PMID: WOS:000437830200045.

229. Kerr RA, Bartol TM, Kaminsky B, Dittrich M, Chang JCJ, Baden SB, et al. Fast monte carlo simulation methods for biological reaction-diffusion systems in solution and on surfaces. SIAM J Sci Comput. 2008;30(6):3126-49. doi: 10.1137/070692017. PubMed PMID: WOS:000260850200021.

230. Bartol TM, Keller DX, Kinney JP, Bajaj CL, Harris KM, Sejnowski TJ, et al. Computational reconstitution of spine calcium transients from individual proteins. Frontiers in synaptic neuroscience. 2015;7:17. doi: 10.3389/fnsyn.2015.00017. PubMed PMID: MEDLINE:26500546.

231. Ikura M, Barbato G, Klee CB, Bax A. Solution structure of calmodulin and its complex with a myosin light chain kinase fragment. Cell Calcium. 1992;13(6-7):391-400. doi: 10.1016/0143-4160(92)90052-t. PubMed PMID: WOS:A1992JF05300005.

232. Pecora R. Dynamic light scattering measurement of nanometer particles in liquids. J Nanopart Res. 2000;2(2):123-31. doi: 10.1023/a:1010067107182. PubMed PMID: WOS:000208067200002.

233. Clayton KN, Salameh JW, Wereley ST, Kinzer-Ursem TL. Physical characterization of nanoparticle size and surface modification using particle scattering diffusometry. Biomicrofluidics. 2016;10(5):14. doi: 10.1063/1.4962992. PubMed PMID: WOS:000387577400007.

234. Stemmer PM, Klee CB. Dual calcium-ion regulation of calcineurin by calmodulin and calcineurin-B. Biochemistry. 1994;33(22):6859-66. doi: 10.1021/bi00188a015. PubMed PMID: WOS:A1994NQ73000015.

235. Wong ST, Athos J, Figueroa XA, Pineda VV, Schaefer ML, Chavkin CC, et al. Calcium-stimulated adenylyl cyclase activity is critical for hippocampus-dependent long-term memory and late phase LTP. Neuron. 1999;23(4):787-98. doi: 10.1016/s0896-6273(01)80036-2. PubMed PMID: WOS:000082280900021.

236. Leonard AS, Bayer KU, Merrill MA, Lim IA, Shea MA, Schulman H, et al. Regulation of calcium/calmodulin-dependent protein kinase II docking to N-methyl-D-aspartate receptors by calcium/calmodulin and alpha-actinin. Journal of Biological Chemistry. 2002;277(50):48441-8. doi: 10.1074/jbc.M205164200. PubMed PMID: WOS:000179789600063.

237. Shen K, Meyer T. Dynamic control of CaMKII translocation and localization in hippocampal neurons by NMDA receptor stimulation. Science. 1999;284(5411):162-6. doi: 10.1126/science.284.5411.162. PubMed PMID: WOS:000079509000059.

238. Opazo P, Sainlos M, Choquet D. Regulation of AMPA receptor surface diffusion by PSD-95 slots. Curr Opin Neurobiol. 2012;22(3):453-60. doi: 10.1016/j.conb.2011.10.010. PubMed PMID: WOS:000306634700013.

239. Sanabria H, Swulius MT, Kolodziej SJ, Liu J, Waxham MN. Beta CaMKII regulates actin assembly and structure. Journal of Biological Chemistry. 2009;284(15):9770-80. doi: 10.1074/jbc.M809518200. PubMed PMID: WOS:000264892900017.

240. Ohta Y, Nishida E, Sakai H. Type-II Ca-2+ calmodulin-dependent protein-kinase binds to actin-filaments in a calmodulin-sensitive manner. Febs Letters. 1986;208(2):423-6. doi: 10.1016/0014-5793(86)81061-4. PubMed PMID: WOS:A1986F119500048.

241. Kim K, Saneyoshi T, Hosokawa T, Okamoto K, Hayashi Y. Interplay of enzymatic and structural functions of CaMKII in long-term potentiation. Journal of Neurochemistry. 2016;139(6):959-72. doi: 10.1111/jnc.13672. PubMed PMID: WOS:000393038700004.

242. Okamoto KI, Narayanan R, Lee SH, Murata K, Hayashi Y. The role of CaMKII as an F-actin-bundling protein crucial for maintenance of dendritic spine structure. Proc Natl Acad Sci U S A. 2007;104(15):6418-23. doi: 10.1073/pnas.0701656104. PubMed PMID: WOS:000245737500058.

243. Yamanaka M, Matsuura T, Pan HL, Zhuo M. Calcium-stimulated adenylyl cyclase subtype 1 (AC1) contributes to LTP in the insular cortex of adult mice. Heliyon. 2017;3(7):20. doi: 10.1016/j.heliyon.2017.e00338. PubMed PMID: WOS:000432023900028.

244. Khan S, Conte I, Carter T, Bayer KU, Molloy JE. Multiple CaMKII binding modes to the actin cytoskeleton revealed by single-molecule imaging. Biophys J. 2016;111(2):395-408. doi: 10.1016/j.bpj.2016.06.007. PubMed PMID: WOS:000380371500016.

245. Byrne MJ, Waxham MN, Kubota Y. The impacts of geometry and binding on CaMKII diffusion and retention in dendritic spines. J Comput Neurosci. 2011;31(1):1-12. doi: 10.1007/s10827-010-0293-9. PubMed PMID: WOS:000293646600001.

246. Regner BM, Vucinic D, Domnisoru C, Bartol TM, Hetzer MW, Tartakovsky DM, et al. Anomalous diffusion of single particles in cytoplasm. Biophys J. 2013;104(8):1652-60. doi: 10.1016/j.bpj.2013.01.049. PubMed PMID: WOS:000318262300006.

247. Halls ML, Cooper DMF. Regulation by Ca2+-signaling pathways of adenylyl cyclases. Cold Spring Harbor Perspect Biol. 2011;3(1):22. doi: 10.1101/cshperspect.a004143. PubMed PMID: WOS:000285866500009.

248. Masada N, Ciruela A, MacDougall DA, Cooper DMF. Distinct mechanisms of regulation by Ca2+/calmodulin of type 1 and 8 adenylyl cyclases support their different physiological roles. Journal of Biological Chemistry. 2009;284(7):4451-63. doi: 10.1074/jbc.M807359200. PubMed PMID: WOS:000263134400045.

249. Garelick MG, Chan GCK, DiRocco DP, Storm DR. Overexpression of type I adenylyl cyclase in the forebrain impairs spatial memory in aged but not young mice. J Neurosci. 2009;29(35):10835-42. doi: 10.1523/jneurosci.0553-09.2009. PubMed PMID: WOS:000269518500007.

250. Xia ZG, Storm DR. Role of signal transduction crosstalk between adenylyl cyclase and MAP kinase in hippocampus-dependent memory. Learn Mem. 2012;19(9):369-74. doi: 10.1101/lm.027128.112. PubMed PMID: WOS:000309170200003.

251. Bazwinsky-Wutschke I, Muhlbauer E, Albrecht E, Peschke E. Calcium- signaling components in rat insulinoma b- cells (INS-1) and pancreatic islets are differentially influenced by melatonin. J Pineal Res. 2014;56(4):439-49. doi: 10.1111/jpi.12135. PubMed PMID: WOS:000334678500008.

252. Pan W, Yang ZQ, Cheng J, Qian C, Wang YG. Contractile heterogeneity in ventricular myocardium. J Cell Physiol. 2018;233(8):6273-9. doi: 10.1002/jcp.26512. PubMed PMID: WOS:000430797600068.

253. Wei J, Wayman G, Storm DR. Phosphorylation and inhibition of type III adenylyl cyclase by calmodulin-dependent protein kinase II in vivo. Journal of Biological Chemistry. 1996;271(39):24231-5. doi: 10.1074/jbc.271.39.24231. PubMed PMID: WOS:A1996VJ44200096.

254. Erondu NE, Kennedy MB. Regional distribution of type-II Ca-2+ calmodulin-dependent protein-kinase in rat-brain. J Neurosci. 1985;5(12):3270-7. PubMed PMID: WOS:A1985AXC3000016.

255. Kennedy MB. Regulation of synaptic transmission in the central nervous-system - long-term potentiation. Cell. 1989;59(5):777-87. doi: 10.1016/0092-8674(89)90601-6. PubMed PMID: WOS:A1989CC79800003.

256. Lisman J, Schulman H, Cline H. The molecular basis of CaMKII function in synaptic and behavioural memory. Nat Rev Neurosci. 2002;3(3):175-90. doi: 10.1038/nrn753. PubMed PMID: WOS:000174207900014.

257. Kennedy MB. Synaptic signaling in learning and memory. Cold Spring Harbor Perspect Biol. 2013;8. doi: 10.1101/cshperspect.a016824.

258. Harris KM. Structure, development, and plasticity of dendritic spines. Curr Opin Neurobiol. 1999;9(3):343-8. doi: 10.1016/s0959-4388(99)80050-6. PubMed PMID: WOS:000080942500013.

259. Sjostrom PJ, Nelson SB. Spike timing, calcium signals and synaptic plasticity. Curr Opin Neurobiol. 2002;12(3):305-14. doi: 10.1016/s0959-4388(02)00325-2. PubMed PMID: WOS:000176180800011.

260. Bennett MK, Erondu NE, Kennedy MB. Purification and characterization of a calmodulin-dependent protein-kinase that is highly concentrated in brain. Journal of Biological Chemistry. 1983;258(20):2735-44. PubMed PMID: WOS:A1983RN36300109.

261. Stratton M, Lee IH, Bhattacharyya M, Christensen SM, Chao LH, Schulman H, et al. Activation-triggered subunit exchange between CaMKII holoenzymes facilitates the spread of kinase activity. eLife. 2014;3:28. doi: 10.7554/eLife.01610. PubMed PMID: WOS:000331145800007.

262. Bhattacharyya M, Stratton MM, Going CC, McSpadden ED, Huang Y, Susa AC, et al. Molecular mechanism of activation-triggered subunit exchange in Ca2+/ calmodulin-dependent protein kinase II. eLife. 2016;5:32. doi: 10.7554/eLife.13045. PubMed PMID: WOS:000376257400001.

263. Rosenberg OS, Deindl S, Sung RJ, Nairn AC, Kuriyan J. Structure of the autoinhibited kinase domain of CaMKII and SAXS analysis of the holoenzyme. Cell. 2005;123(5):849-60. doi: 10.1016/j.cell.2005.10.029. PubMed PMID: WOS:000233814100018.

264. Myers JB, Zaegel V, Coultrap SJ, Miller AP, Bayer KU, Reichow SL. The CaMKII holoenzyme structure in activation-competent conformations. Nat Commun. 2017;8:14. doi: 10.1038/ncomms15742. PubMed PMID: WOS:000402806800001.

265. Hoffman L, Stein RA, Colbran RJ, McHaourab HS. Conformational changes underlying calcium/calmodulin-dependent protein kinase II activation. Embo J. 2011;30(7):1251-62. doi: 10.1038/emboj.2011.40. PubMed PMID: WOS:000290305200010.

266. Colbran RJ, Fong YL, Schworer CM, Soderling TR. Regulatory interactions of the calmodulin-binding, inhibitory, and autophosphorylation domains of Ca2+/calmodulin-dependent protein kinase-II. Journal of Biological Chemistry. 1988;263(34):18145-51. PubMed PMID: WOS:A1988R162300042.

267. Hudmon A, Schulman H. Neuronal Ca2+/calmodulin-dependent protein kinase II: The role of structure and autoregulation in cellular function. Annual Review of Biochemistry. 2002;71:473-510. doi: 10.1146/annurev.biochem.71.110601.135410. PubMed PMID: WOS:000177352600018.

268. Li Y, Holmes WR. Comparison of CaMKinase II activation in a dendritic spine computed with deterministic and stochastic models of the NMDA synaptic conductance. Neurocomputing. 2000;32:1-7. doi: 10.1016/s0925-2312(00)00137-5. PubMed PMID: WOS:000087897800003.

269. Stefan MI, Marshall DP, Le Novere N. Structural analysis and stochastic modelling suggest a mechanism for calmodulin trapping by CaMKII. PLoS One. 2012;7(1):14. doi: 10.1371/journal.pone.0029406. PubMed PMID: WOS:000299771900013.

270. Stefan MI, Bartol TM, Sejnowski TJ, Kennedy MB. Multi-state modeling of biomolecules. PLoS Comput Biol. 2014;10(9):9. doi: 10.1371/journal.pcbi.1003844. PubMed PMID: WOS:000343011700039.

271. Lucic V, Greif GJ, Kennedy MB. Detailed state model of CaMKII activation and autophosphorylation. Eur Biophys J Biophys Lett. 2008;38(1):83-98. doi: 10.1007/s00249-008-0362-4. PubMed PMID: WOS:000260525000009.

272. Johnson T, Bartol T, Sejnowski T, Mjolsness E. Model reduction for stochastic CaMKII reaction kinetics in synapses by graph-constrained correlation dynamics. Phys Biol. 2015;12(4):16. doi: 10.1088/1478-3975/12/4/045005. PubMed PMID: WOS:000361837200005.

273. Chylek LA, Harris LA, Tung CS, Faeder JR, Lopez CF, Hlavacek WS. Rule-based modeling: a computational approach for studying biomolecular site dynamics in cell signaling systems. Wiley Interdiscip Rev-Syst Biol. 2014;6(1):13-36. doi: 10.1002/wsbm.1245. PubMed PMID: WOS:000328558500002.

274. Sejnowski TJ, Poggio T. Computational modeling methods for neuroscientists foreword. In: DeSchutter E, editor. Computational Modeling Methods for Neuroscientists. Computational Neuroscience-MIT. Cambridge: Mit Press; 2009. p. VII-+.

275. Blinov ML, Faeder JR, Goldstein B, Hlavacek WS. BioNetGen: software for rule-based modeling of signal transduction based on the interactions of molecular domains. Bioinformatics. 2004;20(17):3289-91. doi: 10.1093/bioinformatics/bth378. PubMed PMID: WOS:000225361400053.

276. Sneddon MW, Faeder JR, Emonet T. Efficient modeling, simulation and coarse-graining of biological complexity with NFsim. Nat Methods. 2011;8(2):177-U12. doi: 10.1038/nmeth.1546. PubMed PMID: WOS:000286654600017.

277. Strack S, Barban MA, Wadzinski BE, Colbran RJ. Differential inactivation of postsynaptic density-associated and soluble Ca2+/calmodulin-dependent protein kinase II by protein phosphatases 1 and 2A. Journal of Neurochemistry. 1997;68(5):2119-28. PubMed PMID: WOS:A1997WU24800039.

278. Strack S, Kini S, Ebner FF, Wadzinski BE, Colbran RJ. Differential cellular and subcellular localization of protein phosphatase 1 isoforms in brain. J Comp Neurol. 1999;413(3):373-84. PubMed PMID: WOS:000082661800002.

279. Schworer CM, Colbran RJ, Soderling TR. Reversible generation of a Ca-2+-independent form of Ca-2+(calmodulin)-dependent protein kinase-II by an autophosphorylation mechanism. Journal of Biological Chemistry. 1986;261(19):8581-4. PubMed PMID: WOS:A1986D026600002.

280. Lisman JE, Zhabotinsky AM. A model of synaptic memory: A CaMKII/PP1 switch that potentiates transmission by organizing an AMPA receptor anchoring assembly. Neuron. 2001;31(2):191-201. doi: 10.1016/s0896-6273(01)00364-6. PubMed PMID: WOS:000170277700006.

281. Torok K, Tzortzopoulos A, Grabarek Z, Best SL, Thorogate R. Dual effect of ATP in the activation mechanism of brain Ca2+/calmodulin-dependent protein kinase II by Ca2+/calmodulin. Biochemistry. 2001;40(49):14878-90. doi: 10.1021/bi010920+. PubMed PMID: WOS:000172608100018.

282. Tzortzopoulos A, Torok K. Mechanism of the T286A-mutant alpha CaMKII interactions with Ca2+/calmodulin and ATP. Biochemistry. 2004;43(21):6404-14. doi: 10.1021/bi036224m. PubMed PMID: WOS:000221658000006.

283. Tse JKY, Giannetti AM, Bradshaw JM. Thermodynamics of calmodulin trapping by Ca2+/calmodulin-dependent protein kinase II: Subpicomolar K-d determined using competition titration calorimetry. Biochemistry. 2007;46(13):4017-27. doi: 10.1021/bi700013y. PubMed PMID: WOS:000245207800009.

284. Hanson PI, Meyer T, Stryer L, Schulman H. Dual role of calmodulin in autophosphorylation of multifunctional cam kinase may underlie decoding of calcium signals. Neuron. 1994;12(5):943-56. doi: 10.1016/0896-6273(94)90306-9. PubMed PMID: WOS:A1994NM83100002.

285. Bradshaw JM, Hudmon A, Schulman H. Chemical quenched flow kinetic studies indicate an intraholoenzyme autophosphorylation mechanism for Ca2+/calmodulin-dependent protein kinase II. Journal of Biological Chemistry. 2002;277(23):20991-8. doi: 10.1074/jbc.M202154200. PubMed PMID: WOS:000176204500114.

286. Shields SM, Ingebritsen TS, Kelly PT. Identification of protein phosphatase-1 in synaptic junctions - dephosphorylaton of endogenous calmodulin-dependent kinase-II and synapse-enriched phosphoproteins. J Neurosci. 1985;5(12):3414-22. PubMed PMID: WOS:A1985AXC3000029.

287. Dosemeci A, Reese TS. Inhibition of endogenous phosphatase in a postsynaptic density fraction allows extensive phosphorylation of the major postsynaptic density protein. Journal of Neurochemistry. 1993;61(2):550-5. PubMed PMID: WOS:A1993LM75300019.

288. Waxham MN, Tsai AL, Putkey JA. A mechanism for calmodulin (CaM) trapping by CaM-kinase II defined by a family of CaM-binding peptides. Journal of Biological Chemistry. 1998;273(28):17579-84. doi: 10.1074/jbc.273.28.17579. PubMed PMID: WOS:000074816100045.

289. Meador WE, Means AR, Quiocho FA. Target enzyme recognition by calmodulin - 2.4-angstrom structure of a calmodulin-peptide complex. Science. 1992;257(5074):1251-5. doi: 10.1126/science.1519061. PubMed PMID: WOS:A1992JL05000025.

290. Ragusa MJ, Dancheck B, Critton DA, Nairn AC, Page R, Peti W. Spinophilin directs protein phosphatase 1 specificity by blocking substrate binding sites. Nat Struct Mol Biol. 2010;17(4):459-U100. doi: 10.1038/nsmb.1786. PubMed PMID: WOS:000276416800014.

291. Kelker MS, Page R, Peti W. Crystal Structures of Protein Phosphatase-1 Bound to Nodularin-R and Tautomycin: A Novel Scaffold for Structure-based Drug Design of Serine/Threonine Phosphatase Inhibitors. J Mol Biol. 2009;385(1):11-21. doi: 10.1016/j.jmb.2008.10.053. PubMed PMID: WOS:000262870200004.

292. Hsieh-Wilson LC, Allen PB, Watanabe T, Nairn AC, Greengard P. Characterization of the neuronal targeting protein spinophilin and its interactions with protein phosphatase-1. Biochemistry. 1999;38(14):4365-73. doi: 10.1021/bi982900m. PubMed PMID: WOS:000079834100015.

293. Payne ME, Fong YL, Ono T, Colbran RJ, Kemp BE, Soderling TR, et al. Calcium calmodulin-dependent protein kinase-II - characterization of distinct calmodulin binding and inhibitory domains. Journal of Biological Chemistry. 1988;263(15):7190-5. PubMed PMID: WOS:A1988N454900043.

294. Miller P, Zhabotinsky AM, Lisman JE, Wang XJ. The stability of a stochastic CaMKII switch: Dependence on the number of enzyme molecules and protein turnover. PLoS Biol. 2005;3(4):705-17. doi: 10.1371/journal.pbio.0030107. PubMed PMID: WOS:000228279900017.

295. Kolodziej SJ, Hudmon A, Waxham MN, Stoops JK. Three-dimensional reconstructions of calcium/calmodulin dependent (CaM) kinase II alpha and truncated CaM kinase II alpha reveal a unique organization for its structural core and functional domains. Journal of Biological Chemistry. 2000;275(19):14354-9. doi: 10.1074/jbc.275.19.14354. PubMed PMID: WOS:000087006900048.

296. De Koninck P, Schulman H. Sensitivity of CaM kinase II to the frequency of Ca2+ oscillations. Science. 1998;279(5348):227-30. doi: 10.1126/science.279.5348.227. PubMed PMID: WOS:000071408100042.

297. Lisman JE. A mechanism for memory storage insensitive to molecular turnover - a bistable autophosphorylating kinase. Proc Natl Acad Sci U S A. 1985;82(9):3055-7. doi: 10.1073/pnas.82.9.3055. PubMed PMID: WOS:A1985AGW3200104.

298. Mullasseril P, Dosemeci A, Lisman JE, Griffith LC. A structural mechanism for maintaining the 'on-state' of the CaMKII memory switch in the post-synaptic density. Journal of Neurochemistry. 2007;103(1):357-64. doi: 10.1111/j.1471-4159.2007.04744.x. PubMed PMID: WOS:000249949700032.

299. Urakubo H, Sato M, Ishii S, Kuroda S. In vitro reconstitution of a CaMKII memory switch by an NMDA receptor-derived peptide. Biophys J. 2014;106(6):1414-20. doi: 10.1016/j.bpj.2014.01.026. PubMed PMID: WOS:000333226900024.

300. Meyer T, Hanson PI, Stryer L, Schulman H. Calmodulin trapping by calcium-calmodulin dependent protein-kinase. Science. 1992;256(5060):1199-202. doi: 10.1126/science.256.5060.1199. PubMed PMID: WOS:A1992HV19200035.

301. Le Novere N, Shimizu TS. STOCHSIM: modelling of stochastic biomolecular processes. Bioinformatics. 2001;17(6):575-6. doi: 10.1093/bioinformatics/17.6.575. PubMed PMID: WOS:000169404700018.

302. Slepchenko BM, Schaff JC, Macara I, Loew LM. Quantitative cell biology with the virtual cell. Trends Cell Biol. 2003;13(11):570-6. doi: 10.1016/j.tcb.2003.09.003. PubMed PMID: WOS:000186311300006.

303. Harris LA, Hogg JS, Tapia JJ, Sekar JAP, Gupta S, Korsunsky I, et al. BioNetGen 2.2: advances in rule-based modeling. Bioinformatics. 2016;32(21):3366-8. doi: 10.1093/bioinformatics/btw469. PubMed PMID: WOS:000387983700029.

304. Bradshaw JM, Kubota Y, Meyer T, Schulman H. An ultrasensitive Ca2+/calmodulin-dependent protein kinase II-protein phosphatase 1 switch facilitates specificity in postsynaptic calcium signaling. Proc Natl Acad Sci U S A. 2003;100(18):10512-7. doi: 10.1073/pnas.1932759100. PubMed PMID: WOS:000185119300068.

305. Bliss TVP, Lomo T. Long-lasting potentiation of synaptic transmission in dentate area of anesthetized rabbit following stimulation of perforant path. J Physiol-London. 1973;232(2):331-56. doi: 10.1113/jphysiol.1973.sp010273. PubMed PMID: WOS:A1973Q266100009.

306. Kennedy MB, Bennett MK, Erondu NE. Biochemical and immunochemical evidence that the major postsynaptic density protein is a subunit of a calmodulin-dependent protein-kinase. Proceedings of the National Academy of Sciences of the United States of America-Biological Sciences. 1983;80(23):7357-61. doi: 10.1073/pnas.80.23.7357. PubMed PMID: WOS:A1983RT73300064.

307. Kennedy MB, McGuinness T, Greengard P. A calcium calmodulin-dependent protein-kinase from mammalian brain that phosphorylates synapsin-I - partial-purification and characterization. J Neurosci. 1983;3(4):818-31. PubMed PMID: WOS:A1983QL11900014.

308. Coultrap SJ, Bayer KU. CaMKII regulation in information processing and storage. Trends in Neurosciences. 2012;35(10):607-18. doi: 10.1016/j.tins.2012.05.003. PubMed PMID: WOS:000309848600003.

309. Hotulainen P, Hoogenraad CC. Actin in dendritic spines: connecting dynamics to function. J Cell Biol. 2010;189(4):619-29. doi: 10.1083/jcb.201003008. PubMed PMID: WOS:000277777700003.

310. Hoffman L, Farley MM, Waxham MN. Calcium-Calmodulin-Dependent Protein Kinase II Isoforms Differentially Impact the Dynamics and Structure of the Actin Cytoskeleton. Biochemistry. 2013;52(7):1198-207. doi: 10.1021/bi3016586. PubMed PMID: WOS:000315326600009.

311. Naoki H, Sakumura Y, Ishii S. Local signaling with molecular diffusion as a decoder of Ca2+ signals in synaptic plasticity. Mol Syst Biol. 2005;1:12. doi: 10.1038/msb4100035. PubMed PMID: WOS:000243244500028.

312. Ando K, Kudo Y, Aoyagi K, Ishikawa R, Igarashi M, Takahashi M. Calmodulin-dependent regulation of neurotransmitter release differs in subsets of neuronal cells. Brain Res. 2013;1535:1-13. doi: 10.1016/j.brainres.2013.08.018. PubMed PMID: WOS:000325831400001.

313. Heidarinejad M, Nakamura H, Inoue T. Stimulation-induced changes in diffusion and structure of calmodulin and calmodulin-dependent protein kinase II proteins in neurons. Neurosci Res. 2018;136:13-32. doi: 10.1016/j.neures.2018.01.003. PubMed PMID: WOS:000447153300003.

314. Iman RL, Helton JC. An investigation of uncertainty and sensitivity analysis techniques for computer-models. Risk Anal. 1988;8(1):71-90. doi: 10.1111/j.1539-6924.1988.tb01155.x. PubMed PMID: WOS:A1988N161900012.

315. Lee HK, Barbarosie M, Kameyama K, Bear MF, Huganir RL. Regulation of distinct AMPA receptor phosphorylation sites during bidirectional synaptic plasticity. Nature. 2000;405(6789):955-9. PubMed PMID: WOS:000087732700052.

316. Alessi DR, Street AJ, Cohen P, Cohen PTW. Inhibitor-2 functions like a chaperone to fold 3 expressed isoforms of mammalian protein phosphatase-1 into a conformation with the specificity and regulatory properties of the native enzyme. Eur J Biochem. 1993;213(3):1055-66. doi: 10.1111/j.1432-1033.1993.tb17853.x. PubMed PMID: WOS:A1993LB74500020.

317. Cohen PTW. Protein phosphatase 1 - targeted in many directions. J Cell Sci. 2002;115(2):241-56. PubMed PMID: WOS:000173768800002.

318. Zeng ML, Shang Y, Araki Y, Guo TF, Huganir RL, Zhang MJ. Phase transition in postsynaptic densities underlies formation of synaptic complexes and synaptic plasticity. Cell. 2016;166(5):1163-75. doi: 10.1016/j.cell.2016.07.008. PubMed PMID: WOS:000382259500014.

319. Sadana R, Dessauer CW. Physiological roles for G protein-regulated adenylyl cyclase isoforms: insights from knockout and overexpression studies. Neurosignals. 2009;17(1):5-22. doi: 10.1159/000166277. PubMed PMID: WOS:000263609000002.

320. Mammen AL, Kameyama K, Roche KW, Huganir RL. Phosphorylation of the alpha-amino-3-hydroxy-5-methylisoxazole-4-propionic acid receptor GluR1 subunit by calcium/calmodulin-dependent kinase II. Journal of Biological Chemistry. 1997;272(51):32528-33. doi: 10.1074/jbc.272.51.32528. PubMed PMID: WOS:000071108000084.

321. Einstein A. The motion of elements suspended in static liquids as claimed in the molecular kinetic theory of heat. Ann Phys-Berlin. 1905;17(8):549-60. PubMed PMID: WOS:000201991500005.

322. Sorokina O, Sorokin A, Armstrong JD, Danos V. A simulator for spatially extended kappa models. Bioinformatics. 2013;29(23):3105-6. doi: 10.1093/bioinformatics/btt523. PubMed PMID: WOS:000327508300024.

323. Fera A, Dosemeci A, Sousa AA, Yang C, Leapman RD, Reese TS. Direct visualization of CaMKII at postsynaptic densities by electron microscopy tomography. J Comp Neurol. 2012;520(18):4218-25. doi: 10.1002/cne.23151. PubMed PMID: WOS:000310073200009.

324. Ding JD, Kennedy MB, Weinberg RJ. Subcellular organization of camkii in rat hippocampal pyramidal neurons. J Comp Neurol. 2013;521(15):3570-83. doi: 10.1002/cne.23372. PubMed PMID: WOS:000323383800014.

325. Sklar LA, Finney DA, Oades ZG, Jesaitis AJ, Painter RG, Cochrane CG. The dynamics of ligand-receptor interactions - real-time analyses of association, dissociation, and internalization of an n-formyl peptide and its receptors on the human neutrophil. Journal of Biological Chemistry. 1984;259(9):5661-9. PubMed PMID: WOS:A1984SR55200055.

326. Tapia JJ, Saglam AS, Czech J, Kuczewski R, Bartol T, Sejnowski T, et al. MCell-R: A particle-resolution network-free spatial modeling framework. 2018.

327. Clayton KN, Lee D, Wereley ST, Kinzer-Ursem TL. Measuring biotherapeutic viscosity and degradation on-chip with particle diffusometry. Lab Chip. 2017;17(23):4148-59. doi: 10.1039/c7lc00507e. PubMed PMID: WOS:000415989600020.

328. Strack S, Colbran RJ. Autophosphorylation-dependent targeting of calcium/calmodulin-dependent protein kinase II by the NR2B subunit of the N-methyl-D-aspartate receptor. Journal of Biological Chemistry. 1998;273(33):20689-92. doi: 10.1074/jbc.273.33.20689. PubMed PMID: WOS:000075386100002.

329. Strack S, McNeill RB, Colbran RJ. Mechanism and regulation of calcium/calmodulin-dependent protein kinase II targeting to the NR2B subunit of the N-methyl-D-aspartate receptor. Journal of Biological Chemistry. 2000;275(31):23798-806. doi: 10.1074/jbc.M001471200. PubMed PMID: WOS:000088564200055.